INFLUENCE OF GRAIN CHARACTERISTICS ON STRESS-DILATANCY RELATIONSHIP AND FAILURE SURFACE GEOMETRY

by

Çağdaş Arda

B.S., Civil Engineering, Yıldız Technical University, 2007

M.S., Civil Engineering, Boğaziçi University, 2009

Submitted to the Institute for Graduate Studies in
Science and Engineering in partial fulfillment of
the requirements for the degree of
Doctor of Philosophy

Graduate Program in Civil Engineering

Boğaziçi University

2019

INFLUENCE OF GRAIN CHARACTERISTICS ON STRESS-DILATANCY RELATIONSHIP AND FAILURE SURFACE GEOMETRY

APPROVED BY:

Assoc. Prof. Özer ÇİNİCİOĞLU (Thesis Supervisor)	……...
Prof. Erol GÜLER	……...
Prof. Gökhan BAYKAL	……...
Prof. İlknur BOZBEY	……...
Assoc. Prof. Kubilay KELEŞOĞLU	……...

DEDICATION

Before all else, this dissertation is dedicated to the memory of my beloved mother, Tülin Gürşans who dedicated her life to me for my education but passed away on the first year of my doctoral study. Without her enormous personal sacrifice and unconditional love, I would never have become the individual that I am today.

I also thank my wife, Emine and my family for their endless patience and encouragement during dead ends through my study.

ACKNOWLEDGEMENTS

I would like to express my sincere gratitude to my thesis supervisor, Assoc. Prof. Özer Çinicioğlu, for his precious guidance and support through my study. His innovative ideas and technical knowledge eased the way during development of this thesis.

I would like to thank the members of the thesis committee, Prof. Gökhan Baykal and Prof. İlknur Bozbey for their valuable suggestions.

I would also thank my aunt, Dilek Tokay for her valuable support during writing of my thesis.

Finally, I would like to express my appreciation and thanks to the Turkish Scientific and Technical Researchers Institute (TUBITAK) for supporting me financially during my Ph.D. studies. This research was supported by Turkish Scientific and Technical Researchers Institute (TUBITAK), Project Number: 114M329.

ABSTRACT

INFLUENCE OF GRAIN CHARACTERISTICS ON STRESS-DILATANCY RELATIONSHIP AND FAILURE SURFACE GEOMETRY

Stress-dilatancy relationships of granular soils are influenced by both mechanical and physical soil properties. However, existing empirical correlations which define the influence of dilatant behavior on soil strength depend only on the interpretation of shear test data conducted at different relative density and confining pressure ranges. Therefore in this study a wide range of consolidated, drained triaxial testing program was carried out on granular materials consisting of varying gradation and grain shapes in order to reveal the effect of physical grain characteristics on existing stress-dilatancy and strength correlations available in literature. In addition, soil specimens were shared with different stress paths in order to observe the influence of loading condition on dilatant behavior. In the end, unique empirical correlations were proposed which link initial physical characteristics of granular materials with line-fitting stress-dilatancy correlation parameters and stress-dilatancy relationship constants. Within the scope of this research, influence of dilatant behavior on the evaluation of shear band geometry at active failure state of granular backfills were also investigated. For this purpose, small-scale physical retaining wall model experiments were conducted in 1g conditions. Tests were applied on variant graded granular materials of distinct grain characteristics. Arching effects on shear band generation were eliminated by proper selection of model width. Failure surfaces were revealed by particle image velocimetry (PIV) method. Mechanical properties of tested soils were evaluated by positioning pressure sensors at vertical and horizontal walls of the physical model. Consequently, variance on the slip surface geometry and peak friction angles of granular materials which were composed of different grain size and shapes were investigated. Actual results were compared with existing empirical equations which proposed the coordinates of any point located on the failure surface of the backfill. It was revealed that physical grain characteristics have a considerable effect on the dilatancy of granular soils especially under high surcharge pressures. Hence, existing correlations were modified to take grain size and grain shape effects into account.

ÖZET

TANE ÖZELLİKLERİNİN GERİLME-GENLEŞİM BAĞINTILARI VE GÖÇME YÜZEYİ GEOMETRİSİNE ETKİLERİ

Kohezyonsuz zeminlerin gerilme-genleşim ilişkileri, zeminlerin mekanik ve fiziksel özelliklerinden etkilenmektedir. Fakat, literatürdeki genleşim davranışının zemin mukavemetine etkilerini belirten ampirik bağıntılar, sadece farklı başlangıç sıkılık ve hücre basıncı koşullarında gerçekleştirilmiş kesme deneylerinin sonuçları baz alınarak türetilmiştir. Bu nedenle, mevcut çalışmada fiziksel tane özelliklerinin, literatürde yer alan mevcut gerilme-genleşim ve kayma mukavemeti bağıntılarına etkilerini araştırmak adına farklı tane boyutu ve tane şekline sahip zeminler üzerinde geniş ölçekli bir konsolidasyonlu, drenajlı üç eksenli kesme deneyi programı gerçekleştirilmiştir. Ayrıca, farklı gerilme izleri ile deneyler tekrarlanarak gerilme izinin maksimum kayma mukavemetine etkileri araştırılmıştır. Sonuç olarak granüler zeminlerin fiziksel karakteristiklerini, gerilme-genleşim bağıntısı parametreleri ve gerilme–kayma mukavemeti ilişkisi sabitleri ile ilişkilendiren ampirik bağıntılar önerilmiştir. Çalışma kapsamında, hacimsel genleşim davranışının granüler dolguların aktif göçme durumundaki kayma düzlemi geometrisine etkileri de araştırılmıştır. Bu amaçla, küçük ölçekli, 1g koşullarında fiziksel istinat duvar deneyleri gerçekleştirilmiştir. Deneyler, farklı başlangıç göreceli yoğunluk ve sürşarj yükü kademelerinde, değişken dane dağılımına ve ayrı dane şekline sahip kohezyonsuz zeminler üzerinde uygulanmıştır. Fiziksel model genişliği uygun büyüklükte tutularak, kayma düzlemi oluşumuna kemerlenme etkisi bertaraf edilmiştir. Göçme yüzeyleri, parçacık görüntüleme odaklı hız ölçümü (PGHÖ) metodu kullanılarak meydana çıkartılmıştır. Test edilen zeminlerin mekanik özellikleri, fiziksel modelin yatay ve düşey duvarlarına basınç sensörleri yerleştirilerek hesaplanmıştır. Böylece, farklı tane boyutu ve tane şekline sahip granüler zeminlerin kayma yüzeyi geometrileri ve maksimum sürtünme açılarındaki farklılıklar incelenmiştir. Tanelerin fiziksel karakteristiklerinin, özellikle yüksek sürşarj yükleri altında granüler zeminlerin hacimsel genleşim davranışına oldukça etki ettiği tespit edilmiştir. Bu nedenle, mevcut ampirik bağıntılar, dane boyutu ve tane şekli etkilerini de ihtiva edecek şekilde genişletilmiştir.

TABLE OF CONTENTS

DEDICATION iii

ACKNOWLEDGEMENTS iv

ABSTRACT v

ÖZET vi

LIST OF FIGURES ix

LIST OF TABLES xviii

LIST OF SYMBOLS xxi

LIST OF ACRONYMS/ABBREVIATIONS xxiv

1. INTRODUCTION 1

2. LITERATURE REVIEW 4

2.1. Previous Research on Stress-Dilatancy Relationship 4

2.2. Previous Research on the Influence of Grain Size and Shape on Dilatancy 14

2.3. Previous Research on Failure Surface Geometry and PIV 27

3. METHODOLOGY 38

3.1. Scope of the Research 38

3.2. Research Objectives and Approach 42

3.3. Determination of Physical Soil Properties 45

3.3.1. Index Properties of Soils 46

3.3.2. Grain Shape Properties 49

3.4. Determination of Mechanical Soil Properties 52

3.4.1. Saturation Phase 59

3.4.2. Consolidation Phase 60

3.4.3. Shearing Phase 61

3.5. Determination of Failure Surface Geometry 63

4. EVALUATION OF THE TEST RESULTS 72

4.1. Triaxial Tests 72
4.1.1. Influence of Grain Size on Stress-Dilatancy Coefficients 89
4.1.2. Influence of Grain Shape on Stress-Dilatancy Coefficients 94
4.2. Physical Model Tests 100
4.2.1. Experimental Visualization of Active Failure Surfaces 116
4.2.2. Proposing an Equation to Define Failure Surface Geometry 128
5. CONCLUSION 143
REFERENCES 147

LIST OF FIGURES

Figure 2.1. Stress-strain relationship of a granular soil at varying confining pressure and relative density ranges. 6

Figure 2.2. The saw blades model of dilatancy. 7

Figure 2.3. Dilatancy mechanism. 7

Figure 2.4. Mohr Circle at failure state. 8

Figure 2.5. Dilatancy factor versus stress ratio at failure (Hanna, 2001). 12

Figure 2.6. Roundness and Sphericity determination by H. Wadell (1935). 14

Figure 2.7. Grain shape determination chart (Powers, 1953). 15

Figure 2.8. Sphericity and Roundness chart presented by Krumbein and Sloss (1963). 16

Figure 2.9. Effect of particle shape on angle of internal friction (Holubec and Appolonia, 1973). 16

Figure 2.10. Asperity index – interparticle friction angle relationship (E. Frossard, 1979). 17

Figure 2.11. View of soil grains obtained by SEM analysis (Alshibli and Alsaleh, 2004). 18

Figure 2.12. A view of Scion Image Analysis Software outcome (Alshibli and Alsaleh, 2004). 19

Figure 2.13. Influence of particle size on friction angle (Latha and Sitharam, 2008) 21

Figure 2.14. Influence of grain distribution on friction (Latha and Sitharam, 2008). 21

Figure 2.15. Variation of friction angle with void ratio (Latha and Sitharam, 2008)..... 22

Figure 2.16. Variance of Bolton's 'a' parameter with median grain size (D_{50}) and angularity (Amirpour *et al*. 2017). 24

Figure 2.17. Variance of '*r*' with median grain size and angularity (Amirpour *et al*. 2017). 25

Figure 2.18. Coulomb failure wedge. 27

Figure 2.19. Slip planes within a soil mass near a retaining wall. 28

Figure 2.20. Measured vs. computed shear band inclination (Vardoulakis, 1980). 30

Figure 2.21. Variation in lateral earth pressures by retaining wall tilting (S. Bang, 1985). 31

Figure 2.22. Physical model apparatus designed by Lesniewska and Wood (2009). 32

Figure 2.23. Imperfections and strain localization zones revealed by GeoPIV (Lesniewska and Wood, 2009). 33

Figure 2.24. Dilatancy angle – failure surface relationship (Altunbas *et al*., 2017). 34

Figure 2.25. Geometrical parameters of the shear band (Altunbas *et al.,* 2017). 35

Figure 2.26. Variation of α with $\emptyset p'$ as obtained from model test results (Vardoulakis, 1980). 36

Figure 2.27. Comparison of estimated and experimentally visualized failure surfaces (Altunbas *et al.,* 2017).....37

Figure 3.1. View of tested granular soils: S1, S2, S3 sand and GB.....45

Figure 3.2. Grain size distributions of the granular soils used in the research. 48

Figure 3.3. View of digital microscope and a picture of the grains taken by Mshot camera. 49

Figure 3.4. Transformation of pictures into black & white color. 49

Figure 3.5. Determination of geometrical properties of soil grains by ImageJ. 50

Figure 3.6. Sphericity – Roundness chart proposed by Krumbein and Sloss (1963). 51

Figure 3.7. Triaxial tests under K_o conditions. 53

Figure 3.8. Equipment used in dry pluvation technique. 57

Figure 3.9. View of the test specimen held stable by vacuum pump. 58

Figure 3.10. Overview of triaxial sample during saturation phase. 59

Figure 3.11. View of failed samples after shearing phase. 61

Figure 3.12. q – p relationship for AC and LE stress path. 62

Figure 3.13. Front view of the physical retaining wall model. 63

Figure 3.14. View of measure gauge and air hose connecting to pneumatic pistons. 64

Figure 3.15. View of vertical and horizontal sensors in the model box. 65

Figure 3.16. Plot of vertical and horizontal sensor readings through wall transition. 66

Figure 3.17. Plot of deviatoric stress – displacement graph during wall transition. 66

Figure 3.18. Direct shear tests to calculate internal friction between polyethylene sheet and granular soils. 67

Figure 3.19. The physical test model used in retaining tests. 68

Figure 3.20. View of the generated mesh of square patches and the displacement vector field of the deformed mesh. 70

Figure 3.21. Shear strain distribution generated by PIV behind retaining of S2 sand. 71

Figure 4.1. $\psi p'$ and $\phi p'$ relationship for AC stress path triaxial testing of S1 sand. 77

Figure 4.2. $\psi p'$ and $\phi p'$ relationship for LE stress path triaxial testing of S1 sand. 77

Figure 4.3. $\psi p'$ and $\phi p'$ relationship for AC stress path triaxial testing of S3 sand. 78

Figure 4.4. $\psi p'$ and $\phi p'$ relationship for LE stress path triaxial testing of S3 sand. 78

Figure 4.5. $\psi p'$ and $\phi p'$ relationship for AC stress path triaxial testing of GB. 79

Figure 4.6. $\psi p'$ and $\phi p'$ relationship for LE stress path triaxial testing of GB. 79

Figure 4.7. $\psi p'$ and $\phi p'$ relationship for AC stress path triaxial tests of SW-S2. 80

Figure 4.8. $\psi p'$ and $\phi p'$ relationship for AC stress path triaxial tests of SP-S2. 80

Figure 4.9. Summary of $\psi p'$ and $\phi p'$ relationships for AC - LE conditions. 81

Figure 4.10. Determination of Q and R parameter from AC stress path of S1 sand. 83

Figure 4.11. Determination of Q and R parameter from LE stress path of S1 sand. 83

Figure 4.12. Determination of Q and R parameter from AC stress path of S3 sand. 84

Figure 4.13. Determination of Q and R parameter from LE stress path of S3 sand. 84

Figure 4.14. Determination of Q and R parameter from AC stress path of GB. 85

Figure 4.15. Determination of Q and R parameter from LE stress path of GB. 85

Figure 4.16. Determination of Q and R parameter from AC stress path of SW-S2. 86

Figure 4.17. Determination of Q and R parameter from AC stress path of SP-S2. 86

Figure 4.18. Evaluation of line fitting Q parameter when R = 1 for AC-LE conditions. ... 87

Figure 4.19. C_u – *r* relationship of tested soils together with literature data. 90

Figure 4.20. C_u - Q relationship of tested soils together with literature data. 90

Figure 4.21. C_u – $Ø_{cs}$ relationship. 91

Figure 4.22. D_{50} - *r* relationship for all tested soils in AC and LE stress path and literature. 92

Figure 4.23. D_{50} - *r* relationship for rounded-subrounded quartz sand. 92

Figure 4.24. D_{50} - *r* relationship for subangular quartz sand. 93

Figure 4.25. D_{50} - Q relationship. 93

Figure 4.26. D_{50} - $Ø_{cs}$ relationship. 94

Figure 4.27. S_{ave} - r relationship. 95

Figure 4.28. S_{ave} – Q relationship provided that R =1. 95

Figure 4.29. S_{ave} – $Ø_{cs}$ and R_{ave} – $Ø_{cs}$ relationship.. 96

Figure 4.30. Grain shape - $Ø_{cs}$ relationship. 97

Figure 4.31. Effect of loading condition on strength properties. 99

Figure 4.32. PIV analysis results for S1 sand. 100

Figure 4.33. PIV analysis results for S3 sand. 101

Figure 4.34. PIV analysis results for SW-S2. 102

Figure 4.35. PIV analysis results for SP-S2..... 104

Figure 4.36. PIV analysis results for GB. 104

Figure 4.37. Deviatoric stress – wall displacement graph for a particular physical model experiment. 106

Figure 4.38. Visualization of friction forces between shear wedge and model frame. 107

Figure 4.39. Comparison of calculated ‘r’ and ‘a’ stress-dilatancy coefficients from triaxial tests and actual ‘r’ and ‘a’ from physical model tests..... 114

Figure 4.40. Relative density – Friction angle relationship at 100 kPa surcharge pressure for tested soils. 115

Figure 4.41. Selection of X-Y coordinate points using PlotDigitizer software. 117

Figure 4.42. Active failure surface geometries of SW- S2 sand..... 118

Figure 4.43. Active failure surface geometries of SP- S2 sand. 119

Figure 4.44. Active failure surface geometries of GB at varying surcharge and densities. 120

Figure 4.45. Active failure surface geometries of S1 at varying surcharge and densities. 120

Figure 4.46. Active failure surface geometries of S3 at varying surcharge and densities. 121

Figure 4.47. Influence of dilatancy on slip surface geometry. 122

Figure 4.48. Comparison of failure surface geometries of tested granular materials at varying dilatancy angle values. 124

Figure 4.49. Relationship between inclination of initial part of the failure surface and peak friction angle for tested granular backfills..... 125

Figure 4.50. Influence of dilatancy on experimentally measured values of a_b for S1 Sand. 126

Figure 4.51. Influence of dilatancy on experimentally measured values of a_b for S3 Sand. 126

Figure 4.52. Influence of dilatancy on experimentally measured values of a_b for S2-SW..... 127

Figure 4.53. Influence of dilatancy on experimentally measured values of ab for S2-SP. 127

Figure 4.54. Geometric properties of failure surface geometry. 129

Figure 4.55. Comparison between plots of estimated and actual failure surfaces on normalized coordinate system for varying dilatancy values of physical model experiment data of SW-S2. 131

Figure 4.56. Comparison between plots of estimated and actual failure surfaces on normalized coordinate system for varying dilatancy values of physical model experiment data of S1 Sand..... 132

Figure 4.57. Comparison between plots of estimated and actual failure surfaces on normalized coordinate system for varying dilatancy values of physical model experiment data of SP-S2..... 133

Figure 4.58. Comparison between plots of estimated and actual failure surfaces on normalized coordinate system for varying dilatancy values of physical model experiment data of S3 Sand..... 134

Figure 4.59. Comparison between plots of estimated and actual failure surfaces on normalized coordinate system for varying dilatancy values of physical model experiment data of GB. 135

Figure 4.60. Comparison of actual failure surface geometries with empirical method (Altunbas *et al*., 2017) of tested soils..... 138

Figure 4.61. Actual - empirical failure surface geometry relationship of different sands at similar initial conditions..... 139

Figure 4.62. Change of "*n*" coefficient with respect to surcharge pressure. 142

LIST OF TABLES

Table 2.1. Variance of stress-dilatancy parameter ‘Q’ with grain type (Bolton, 1986). 11

Table 2.2. Stress-dilatancy correlation coefficients derived from literature.....26

Table 3.1. Relative density and vertical confining stress ranges for drained triaxial tests..45

Table 3.2. Average sphericity and roundness values of the soil grains for each sand.....51

Table 3.3. Physical properties of the S1, S2, S3 sands and GB.....52

Table 3.4. Testing program for sand specimens 54

Table 3.5. Testing program of each sand for the physical model experiments 69

Table 4.1. Calculated peak dilatancy rate, $\psi p'$ and $\phi p'$ for S1 Sand (AC Stress Path) 72

Table 4.2. Calculated peak dilatancy rate, $\psi p'$ and $\phi p'$ for S1 Sand (LE Stress Path).....73

Table 4.3. Calculated peak dilatancy rate, $\psi p'$ and $\phi p'$ for S3 Sand (AC Stress Path) 73

Table 4.4. Calculated peak dilatancy rate, $\psi p'$ and $\phi p'$ for S3 Sand (LE Stress Path).....74

Table 4.5. Calculated peak dilatancy rate, $\psi p'$ and $\phi p'$ for GB (AC Stress Path).....74

Table 4.6. Calculated peak dilatancy rate, $\psi p'$ and $\phi p'$ for GB (LE Stress Path)..... 75

Table 4.7. Calculated peak dilatancy rate, $\psi p'$ and $\phi p'$ for SW-S2 (AC Stress Path)..... 75

Table 4.8. Calculated peak dilatancy rate, $\psi p'$ and $\phi p'$ for SP-S2 (AC Stress Path)..... 75

Table 4.9. Stress-dilatancy coefficients calculated for each test under AC stress path..... 88

Table 4.10. Stress-dilatancy coefficients calculated for each test under LE stress path..... 88

Table 4.11. Measured vs. actual principal stresses of S1 sand..... 109

Table 4.12. Actual vs. calculated strength – dilatancy parameters of S1 sand..... 109

Table 4.13. Measured vs. actual principal stresses of S2-SW sand..... 110

Table 4.14. Actual vs. calculated strength – dilatancy parameters of S2-SW sand..... 110

Table 4.15. Measured vs. actual principal stresses of S2-SP sand..... 111

Table 4.16. Actual vs. calculated strength – dilatancy parameters of S2-SP sand..... 111

Table 4.17. Measured vs. actual principal stresses of S3 sand..... 112

Table 4.18. Actual vs. calculated strength – dilatancy parameters of S3 sand..... 112

Table 4.19. Measured vs. actual principal stresses of GB sand..... 113

Table 4.20. Actual vs. calculated strength – dilatancy parameters of GB sand.....113

Table 4.21. '*n*' coefficient derived by SPSS analysis for varying density and surcharge .141

Table 4.22. Standard deviations of '*n*' for different density and surcharge ranges.....141

Table 5.1. Summary of proposed correlations between grain characteristics and stress-dilatancy and strength parameters.....144

LIST OF SYMBOLS

a	Contribution of dilatancy index on frictional strength (Amirpour *et al.* 2017)
a_b	B_f / X ratio (Altunbas *et al.*, 2017)
A_{sf}	Side frame area of the physical model box
A_{sw}	Area of the shear wedge
a_ψ	Stress-based Çinicioğlu (2012) stress-dilatancy constant
A_ψ	Contribution of dilatancy index on frictional strength (Bolton, 1986)
B	The horizontal distance from the retaining wall to the failure surface at a particular depth *z* (Altunbas *et al.*, 2017)
B	Skempton's parameter for saturation
B_f	Distance of shear band to wall at ground surface (Altunbas *et al.*, 2017)
c'	Cohesion
C_c	Coefficient of curvature
C_u	Coefficient of uniformity
D	Dilatancy factor (Hanna, 2001)
D_{50}	Median particle size
e_{cr}	Critical state void ratio
e_{max}	Maximum void ratio
e_{min}	Minimum void ratio
G_s	Specific gravity
H_w	Height of the retaining wall (Altunbas *et al.*, 2017)
I_a	Asperity index
I_D	Relative density
I_R	Dilatancy index
k	Constant representing loading condition
K	Lateral earth pressure coefficient for critical state (Hanna, 2001)
K_a	Lateral earth pressure at active failure state
K_o	Lateral earth pressure at-rest condition

m_ψ	Density-based Çinicioğlu (2012) stress-dilatancy constant
n	Coefficient for proposed failure surface geometry correlation
p'	Mean effective stress
p_a	Atmospheric pressure
p'_i	Initial mean effective stress
p'_{peak}	Peak mean effective stress
q	Deviatoric stress
Q	Line-fitting Bolton (1986) stress-dilatancy constant
r	Contribution coefficient of dilatancy on strength
R	Line-fitting Bolton (1986) stress-dilatancy constant
R_{ave}	Average roundness
r_{ps}	Dilatancy effect parameter on friction for plane strain conditions
r_{tx}	Dilatancy effect parameter on friction for axisymmetric conditions
S_{ave}	Average sphericity
SP	Poor graded soil
SW	Well graded soil
X	Distance of the linear extrapolated line to wall at ground surface which is tangent to initial part of shear band at toe level (Altunbas *et al.*, 2017)
z	The vertical coordinate (Altunbas *et al.*, 2017)

α	Inclination of the initial section of the shear band at the toe level (Altunbas *et al.*, 2017)
γ	Total unit weight
δ	Side wall-soil friction angle measured by simple shear tests
ε_a	Axial strain
ε_r	Radial strain
ε_v	Volumetric strain
$d\varepsilon_1$	Vertical strain change
$d\varepsilon_3$	Horizontal strain change
$d\varepsilon_v$	Volumetric strain change
θ	Inclination of slip surface to horizontal (Coulomb, 1776)

μ	Interparticle friction
σ'	Vertical effective stress
σ'_{1f}	Effective vertical stress at failure
σ'_{2f}	Effective intermediate stress at failure
σ'_{3f}	Effective horizontal stress at failure
σ'_c	Effective confining pressure
σ'_{cs}	Effective critical stress
σ'_{nf}	Effective normal stress at failure
τ	Shear stress
τ_f	Shear stress at failure
ϕ'	Drained internal friction angle
ϕ'_{cs}	Drained critical state friction angle
ϕ'_p	Drained peak friction angle
ϕ'_{ps}	Plane strain angle of shearing resistance
ψ	Dilatancy angle
ψ'_p	Peak dilatancy angle

LIST OF ACRONYMS/ABBREVIATIONS

AC	Axial compression
ASTM	American society of testing materials
CK_0D	Consolidated drained in K_0 condition
CSL	Critical state line
DEM	Discrete element modelling
FPSA	Flexible boundary plane strain test
LE	Lateral extension
OCR	Overconsolidation ratio
PIV	Particle image velocimetry
SEM	Scanned electron microscopy
SIAS	Scion Image Analysis Software

1. INTRODUCTION

Earth crust is composed of various soil types originated from different geological origins. In addition, it is proved that lithology have a strong influence on soil properties. Therefore, physical and mechanical soil properties investigated during soil exploration for the design of geotechnical structures in civil engineering consist of very different grain characteristics. Moreover, related to the type of engineering application, soils may be under different loading conditions.

For both fine and coarse-grained soils, dilatancy influences strength, but for coarse grained soils it has an effect on shear plane formation; so it controls the geometry of failure mechanism. Moreover, for coarse grained soils dilatant behavior is physically apparent and can be measured by soil tests. Therefore, researchers prefer to study the dilatant behavior of coarse-grained soils. In line with this, stress-dilatancy relationships are proposed by researchers according to experimental data of shear tests conducted on soil samples under varying relative density and confining pressure ranges. The aim of the researchers is to reveal the contribution of dilatancy on soil strength and to mathematically denote the correlation of obtained strength properties with strains generated during any stress change on soils.

The effect of soil mineralogical composition on the strength of granular soils were experimentally exposed in the former century, however experimental work was not adequate and sufficient to reveal the effect of particle geometry such as grain size and shape in soil strength. For this reason, numerical solutions such as the DEM method was adapted by numerous researchers to investigate the microstructure of granular soils. However, it was suggested that variance in line-fitting stress-dilatancy parameters such as Q, R and r were caused by differences in soil microstructure. Recently the influence of micro-scale soil properties on existing stress-dilatancy correlations have started to be quantified, because only latest advances in digital microscopy and software programming enabled fast and accurate procession of grain size and shape characteristics.

Former century scientists relied on conventional axisymmetric and plane strain shear test data to propose stress-dilatancy correlation constants. In this respect, modified stress-dilatancy correlations which include grain size and shape effects were a function of consolidated, drained axial compression (AC) stress path data under K_o loading conditions and were applicable for a soil element under increasing vertical stress such as foundation loading. On the other hand, a soil element behind a retaining wall which translates laterally through the active side would definitely follow a lateral extension (LE) stress path, where horizontal stresses decrease with wall displacement while vertical stresses are constant.

Design of retaining walls is a major and elder research field in geotechnical engineering. The location, inclination, thickness, and geometry of shear wedge and slip surfaces forming on the granular soil located behind translating retaining walls during and after excavation which takes place on the front wall had been widely investigated. Formerly, the evaluation of strain localizations during shearing phase of triaxial testing within the specimen which leads to slip surface and consequently failure were investigated to locate the inclination of the shear bands. It was suggested that the failure plane during triaxial testing was oriented roughly at 45+ Ø/2 degrees against the horizontal plane. However, effective visualization of strain localizations and formation of slip surface would not be possible due to physical restrictions such as the presence of membrane around the specimen. For this reason, latter research has concantrated on physical model retaining wall experiments in order to observe the strain and stress variances on the backfill soil and visualize the evaluation of strain localization and shear bands with wall rotation.

Following this research, many scientists have proposed empirical equations correlated with soil-wall interface, soil arching and soil strength to define shear band geometry. However, the research exposed that physically, quantifying the arching mechanism was rather difficult by experimental study, and provided that experimental retaining wall set-up was designed to physically restrain any arching pressure generation and minimize soil-wall friction, the only intrinsic soil parameters which primarily influence the shear band formation were observed to be friction and dilation. By this way, estimating the failure surface geometries of granular soils standing behind laterally translating retaining walls by physical model experiments would be a function of macro and micro scale soil properties which influences dilatant behavior.

To sum up, this PhD research initially aimed to investigate and quantify the coupled effects of soil density, initial stress state, loading condition, grain size, and shape properties on existing stress-dilatancy correlations available in literature. Second, since the formation of shear band geometry behind retaining walls is a function of dilatancy; the coupled influence of these parameters on existing geometrical functions which estimates the geometry of slip surfaces at failure state was investigated within this study. For this purpose, a wide range of experimental study was conducted, including both triaxial testing and physical model testing on four types of granular material with different grain characteristics.

Triaxial tests were conducted following two different stress paths (axial compression and lateral extension) to observe the influence of loading condition on soil dilatancy. Stress-dilatancy equation coefficients of both stress paths were calculated. Next, physical retaining wall experiments were conducted on the soils to experimentally visualize the failure surface geometries by particle image velocimetry analysis. Physical model tests were executed under varying relative density range and surcharge pressures so that effect of high initial stress on shear band generation would be observed. Moreover, tested soils consisted of different grain size and shapes, therefore, influence of macro scale physical properties could also be investigated. The dilation and friction angles of all tests were calculated using the stress-dilatancy coefficients calculated within triaxial the testing program. Finally, the experimentally visualized failure surface geometries were compared with the estimated geometries obtained by quantitative correlations, and a modified correlation which considers the coupled influence of grain size and shape on evaluation of shear band geometry was proposed.

2. LITERATURE REVIEW

Due to the high variability of sand types, there are many factors influencing their mechanical properties. However, in existing empirical correlations in literature only a few of these factors are taken into consideration.

2.1. Previous Research on Stress-Dilatancy Relationship

All major constructive materials such as steel and concrete typically exhibit an elastoplastic stress-strain relationship. After an initial elastic linear portion ending up to some percent of ultimate load, the curve becomes non-linear due to formation of micro cracks at aggregate-cement interface, with large strains being registered for small increments of stress. Therefore, for concrete, the behavior after peak is strain-softening, which indicates a reduction in stress beyond the peak value with an increase in deformation. On the other hand, steel exhibits strain-hardening behavior after yielding. Similarly, soils have got an elastoplastic stress-strain relationship as their hardening or softening behavior is attributed to their initial relative density. Primary researchers on soil engineering have investigated the frictional strength of granular soils as a construction material and revealed that relative density of a granular material directly influences the stress-strain behavior; denser soils having larger frictional strength than loose soils.

As a pioneer, Coulomb (1776) formulated an equation which have two parameters to identify the soil strength:

$$\tau = c' + (\sigma' tan\emptyset') \tag{2.1}$$

Here *c*' is the cohesion and ∅' is the internal friction angle for soil. In this model, if shear stress on a body element is high enough, it overcomes both the adhesion forces between soil particles and internal friction resistance. Consequently, the soil element is divided into two rigid bodies that could slip relative to each other along that interface, which is referred as the slip surface, leading to failure. Since grain size of granular materials are large enough

to avoid any adhesive behavior, the only strength parameter for a non-cohesive soil is the friction angle. The formula also states that the more a soil is under a vertical effective stress, the higher is its shear strength.

Reynolds (1885) is the first researcher who revealed the physical presence of 'dilatancy' for granular soils, which is the volumetric increase of a soil mass under shear. Theoretically, dilatancy is the ratio of volumetric strain to shear strain:

$$sin\psi = \frac{d\varepsilon_1 + kd\varepsilon_3}{d\varepsilon_1 - kd\varepsilon_3} \tag{2.2}$$

Here, ε_1 and ε_3 are the vertical and horizontal strain increments for a soil element; and '*k*' represents the loading condition, where k = 2 for triaxial and k = 1 for plane strain conditions.

Subsequently, many researchers investigated the effect of dilatancy on soil strength experimentally by conducting strain-controlled laboratory tests initially with simple shear and then with conventional triaxial apparatus (Terzaghi, Skempton, Bishop, Roscoe, Penman etc.). The studies revealed that density and dilatancy are proportional. Hence, it was concluded by the early 20th century researchers that dilatancy was the result of particle interlocking which ultimately increases the peak shear strength of the soil.

During these strain-controlled experiments, vertical effective stress had been applied on soil samples. It had been observed that at the initial stage of shear tests, dense samples compress slightly by small strain increment, until all voids were compressed. When axial strain on soil specimen was increased, soil grains interlock in order to continue shearing under increasing vertical stress, increase in volume, and this additional work sustained an additional strength to the soil. When the influence of dilatant behavior is at its maximum, the soil reaches its peak shear strength (ϕ'_p). However, when this additional interlocking stress is overcome by the increasing strain, the effect of interlocking terminates and soil strength reduces to its critical state strength. In such a case, the strength parameter of the soil sample becomes the critical state friction angle (ϕ'_{cs}) which is located on the critical state line (Figure 2.1).

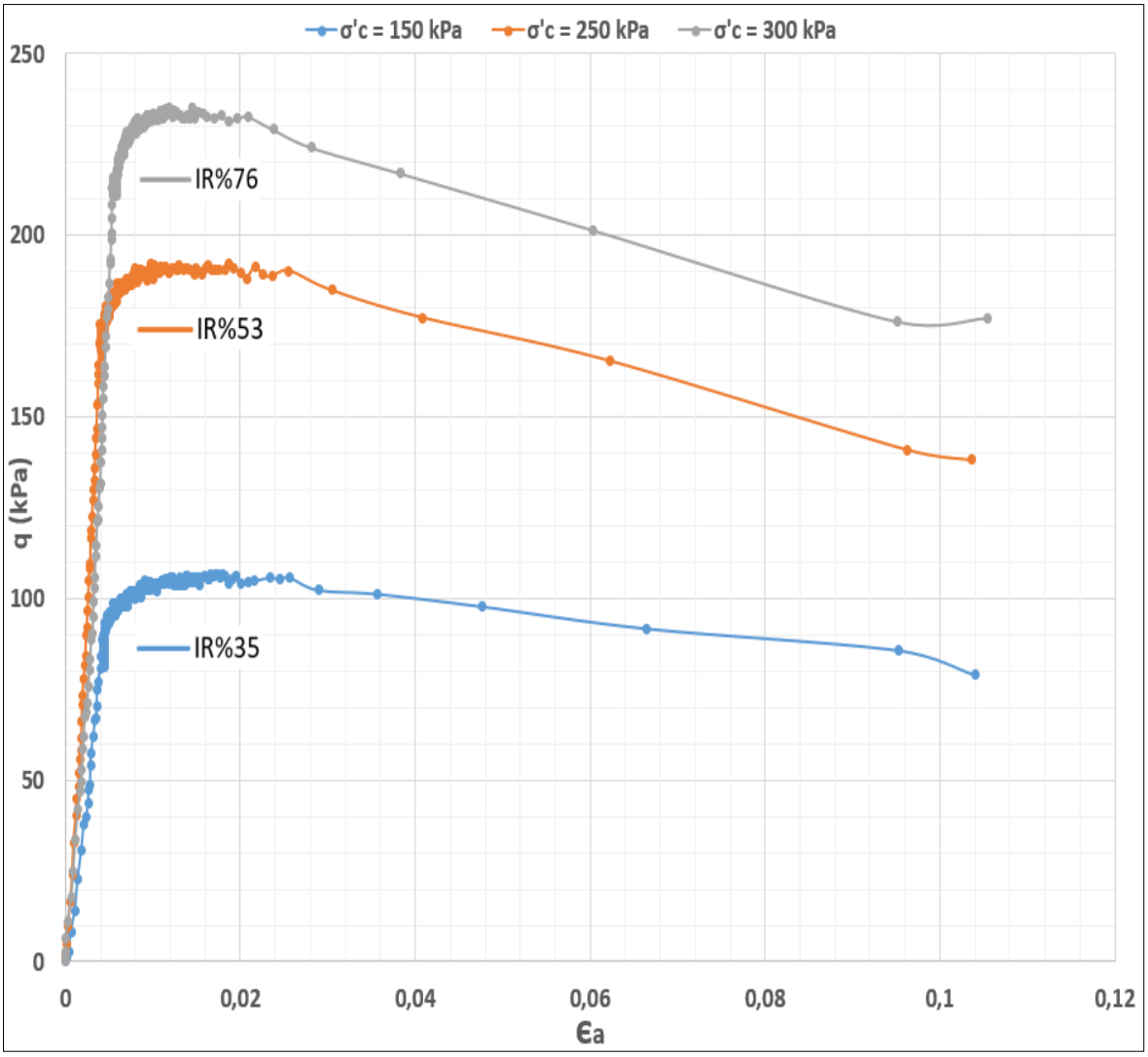


Figure 2.1. Stress-strain relationship of a granular soil at varying confining pressure and relative density ranges.

On the other hand, if the saturated granular soil is loose, the soil compresses until it bears all the stress applied on it since it has many voids to be compressed. After a specific strain value, there is no more additional increase on the shear stress with increasing strain meaning that the sample has reached to its failure state. Another important outcome of these tests was that whether the sample is loose or dense, after a specific strain value the void ratio of the sample becomes the same and is termed as the critical void ratio (e_{cr}). Figure 2.1 summarizes a typical stress-strain relationship for dense and loose granular soils respectively.

Taylor (1948) conducted many simple shear tests to investigate the influence of dilatancy on soil strength for cohesionless soils using saw-tooth frictional model (Figure 2.2).

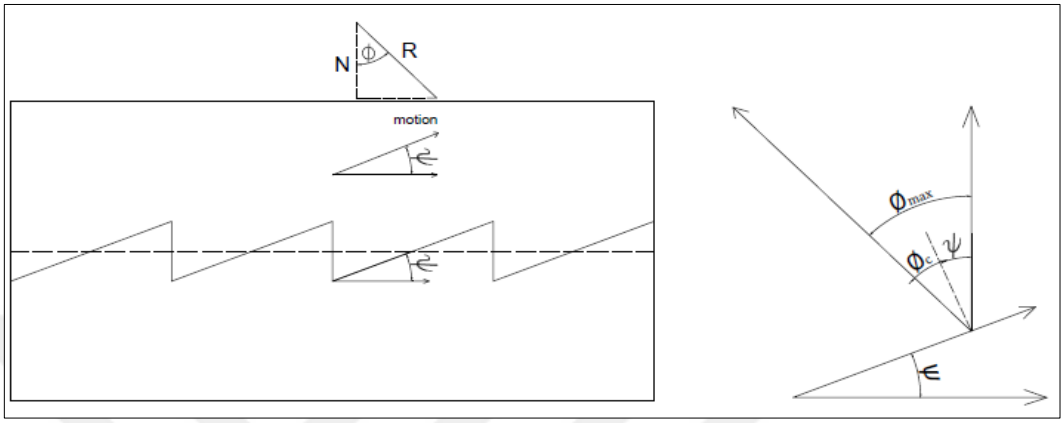


Figure 2.2. The saw blades model of dilatancy.

When tests were conducted on a flat, smooth plane, no volume expansion took place and dilatancy was zero, hence soil strength was equal to the critical state strength. On the other hand if sliding occurred in a rough, angular plane like the saw-tooth model as the case in simple shear box device, particle interlocking was observed during shearing which was the underlying mechanism of dilatant behavior (Figure 2.3).

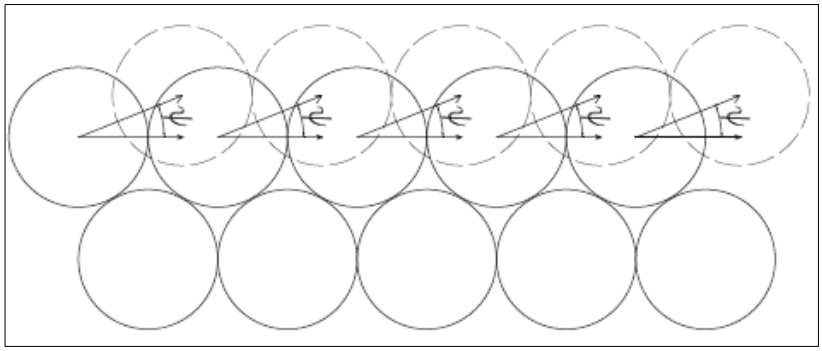


Figure 2.3. Dilatancy mechanism.

Accordingly, traditional Coulomb strength criterion was modified for rough, angular shear surfaces where volumetric expansion and particle interlocking took place. So, an empirical relationship between friction angle and dilation angle was proposed (Taylor, 1948):

$$\tau_f = \sigma'_{nf} \tan(\emptyset'_{cs} + \psi'_p) \quad (2.3)$$

$$tan\,\emptyset'_p = tan\emptyset'_{cs} + tan\psi'_p \quad (2.4)$$

In this modified Coulomb strength criterion, at failure state shear strength of soil specimen is dependent on vertical effective stress at the failure state, critical state friction angle and peak dilation angle. The sum of critical state friction angle and peak dilation angle is equal to peak friction angle of the soil. For a dense soil, dilation angle is higher; and so its peak strength. For a loose soil, no dilation occurs due to high void ratio, hence its critical strength is also its peak strength. However, regardless of its initial soil density, at intense shearing any granular soil extends to a specific critical void ratio value therefore critical state strength of a soil does not depend on soil compressibility. The peak friction angle of a granular soil by Mohr-Coulomb's frictional law is (Figure 2.4):

$$\phi'_p = sin^{-1} \frac{(\sigma'_{1f} - \sigma'_{3f})}{(\sigma'_{1f} + \sigma'_{3f})} \quad (2.5)$$

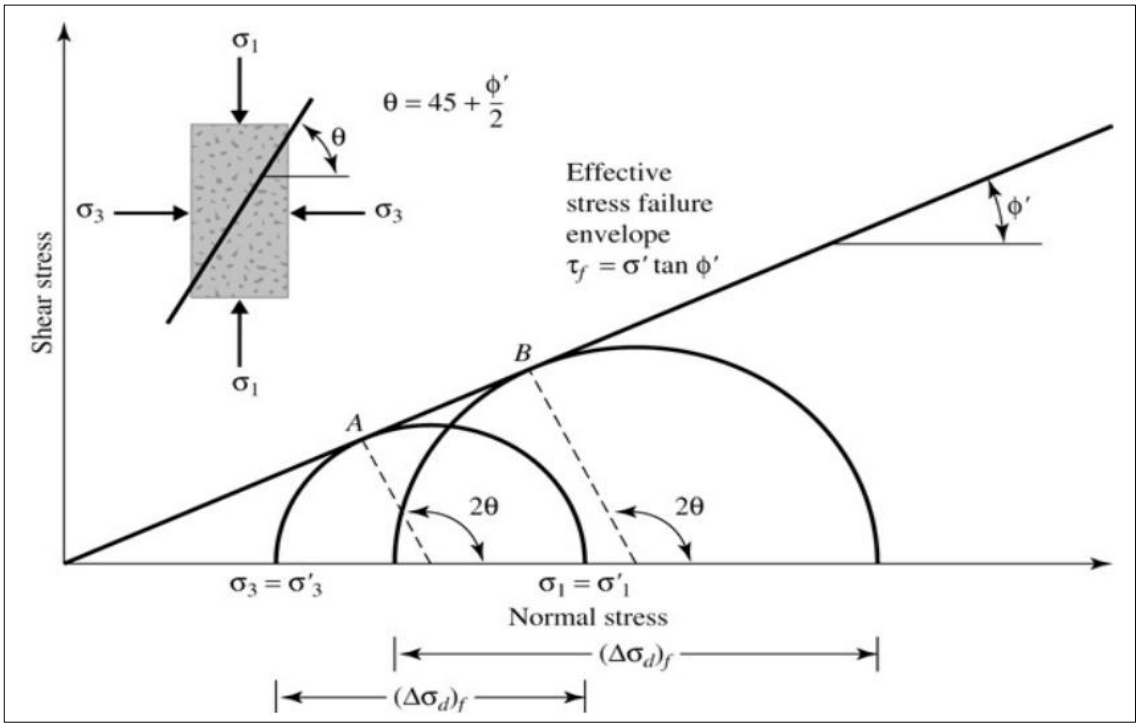


Figure 2.4. Mohr Circle at failure state.

where Ø' is friction angle, σ'_{1f} and σ'_{3f} are major and minor principal stresses at failure.

As a result, by combination of Mohr-Coulomb strength criterion and work dissipation theory, a link between stress and dilatancy was generated and called as stress – dilatancy relationship. Rowe (1962) proposed a stress-dilatancy correlation based on minimum energy ratio principle in a dense packing of granular assemblies, linking the stress rate with strain rate by internal friction.

$$\frac{\sigma'_{1f}}{\sigma'_{3f}} = tan^2\left(\frac{\pi}{4} + \frac{\phi'_p}{2}\right)\left(\frac{d\varepsilon_3}{d\varepsilon_1}\right) \tag{2.6}$$

Here, ε_3 and ε_1 are the horizontal and vertical strain respectively. In this approach, dilation is linked with friction and stress at failure state.

De Josselin de Jong (1976) derived a toothed separation plane model and showed that Rowe's equation is valid until the peak state by applying rules of friction only.

The following studies regarding dilatancy revealed that only some percent of volumetric dilation influences grain interlocking and consequently soil strength. Bishop (1971) proved experimentally that only some part of dilatancy is attributed to particle interlocking due to the geometry of the volumetric expansion which is different from Taylor and Rowe's model which gives no attempt to optimize the failure mechanism or to correlate the principal stress and strain increments directions.

$$r = \frac{\phi'_p - \phi'_{cs}}{\psi'_p} \tag{2.7}$$

Bolton (1986) investigated the parameters which affect dilatancy. He conducted many conventional triaxial tests with 17 different sand types under varying relative densities and vertical effective stresses (he consolidated the specimen under various consolidation pressures). He did both plane strain and axisymmetric tests. He figured out that if the granular soil is denser, its dilatancy is higher; and so is its peak strength. Moreover, increased

vertical effective stress on a granular soil decreases its dilatancy. After he analyzed the tests, he proposed a relationship where dilatancy is related to relative density and effective stress:

$$I_R = I_D(Q - lnp') - R \tag{2.8}$$

Q = 10 and R = 1

In this equation, I_R refers to dilatancy index which is a function of relative density (I_D) and mean effective stress at failure (p_f') state. Q and R are the coefficients which are derived from experimental work and proposed to be constant.

As follows, Bolton (1986) figured out that below equation gives a better estimation of Rowe's stress dilatancy correlation based on work dissipation theory. He offered that the influence of dilatancy attributed to interlocking is a constant paramater depending on many triaxial results.

$$\phi'_p = \phi'_{cs} + 0.8\psi' \tag{2.9}$$

Bolton (1986) observed that there is a linear relationship between the dilatancy index and rate of dilation which is the peak gradient of the volumetric strain – axial strain curve of the triaxial tests during the shearing phase. According to his experiments, averagely he proposed as:

$$\left(-\frac{d\varepsilon_v}{d\varepsilon_1}\right)_{max} = 0.3I_R \tag{2.10}$$

$$\phi'_p - \phi'_{cs} = 0.8\psi = 3I_R\ (triaxial) \tag{2.11}$$

$$\phi'_p - \phi'_{cs} = 0.8\psi = 5I_R\ (plane\ strain) \tag{2.12}$$

However, the proposed stress-dilatancy coefficients for the correlation were obtained from the test results of quartz sand, and for soils consisting of weaker grains different Q coefficient values were proposed (Table 2.1).

Table 2.1. Variance of stress-dilatancy parameter 'Q' with grain type (Bolton, 1986).

Q	Grain Type
10	Quartz and feldspar
8	Limestone
7	Anthracite
5.5	Chalk

Schanz and Vermeer (1996) proposed that dilatancy angle concept can be extended to include triaxial test conditions:

$$sin\psi' = -\frac{\frac{\varepsilon_v}{\varepsilon_1}}{2-\frac{\varepsilon_v}{\varepsilon_1}} \tag{2.13}$$

and they included Bolton (1986) expression into triaxial conditions as:

$$sin\psi' = \frac{0.3I_R}{2+0.3I_R} = \frac{I_R}{6.7+I_R} \tag{2.14}$$

Vaid and Sasitharan (1992) studied the accuracy of stress-dilatancy theories under varying relative density, vertical stress (consolidation pressure), and stress path. They conducted some K_0 tests as well as isotropic tests on a specific sand type. From test results, peak friction angle – peak dilation angle graphs were generated and they showed that there is a unique (linear) relationship between peak friction angle and dilation angle regardless of stress path, relative density, confining pressure (between 100 – 2400 kPa), and mode of loading (compression or extension).

Hanna (2001) conducted many axisymmetric and plane strain triaxial drained tests to create a correlation and suggested a method to convert conventional triaxial test friction angles into plane strain conditions. Accordingly, below equation was suggested to predict the value of plane-strain angle of shearing resistance (ϕ'_{ps}):

$$\tan \emptyset'_{ps} \cos \emptyset'_{cs} = \frac{(KD-1)\sqrt{12D-3D^2}}{4KD-KD^2+3D} \quad (2.15)$$

where,

$$K = tan^2(45 + \frac{\emptyset_{cs}}{2}) \quad (2.16)$$

D is the dilatancy factor varying with porosity which can be derived from Figure 2.5.

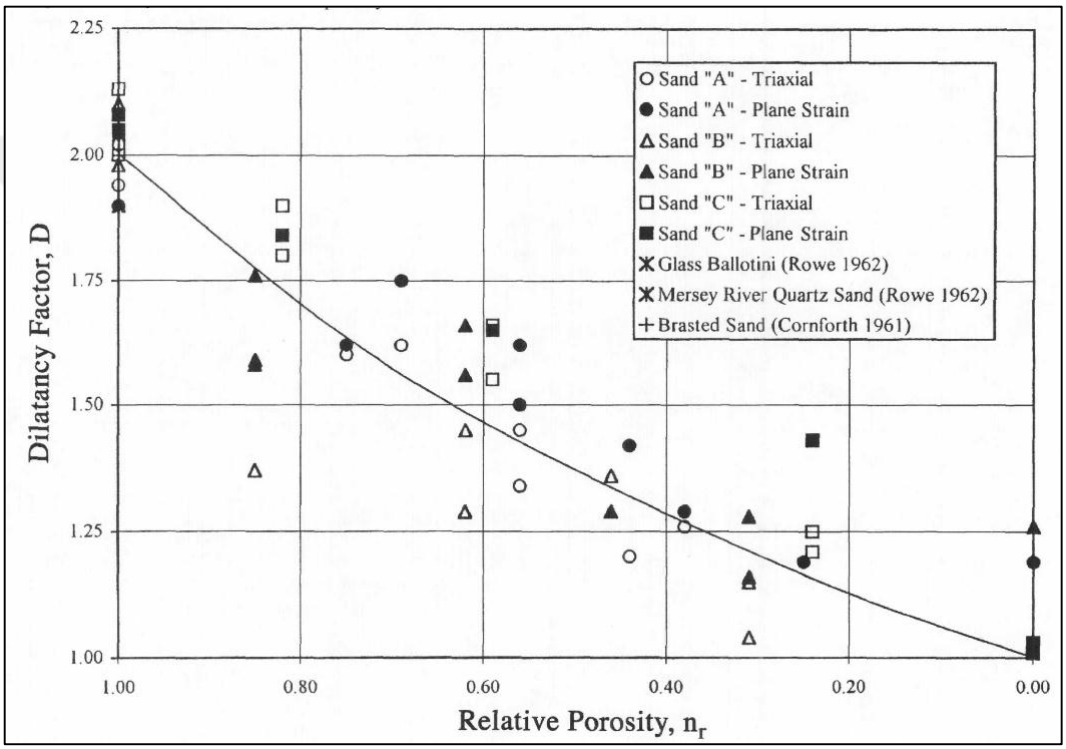


Figure 2.5. Dilatancy factor versus stress ratio at failure (after Hanna, 2001).

Subsequently, Nanda and Petra (2015) proposed a unique method to calculate mechanical soil properties for plane strain conditions from axisymmetric conditions.

Chakraborty and Salgado (2010) conducted triaxial tests on a single sand type but under very low confining stresses (<50 kPa) in order to compare the accuracy of Bolton (1986) relationship at low pressures. They revealed that at low stresses Q and R values change and for R=1, Q decreases following a parabolic relationship with initial confining stress as given below:

$$Q = 7.4 + 0.6 \ln \sigma_c' \quad (2.17)$$

$$\emptyset'_p = \emptyset'_{cs} + 0.62\psi'_p \quad (2.18)$$

$$\phi_p' - \phi_{cs}' = 3.8 I_R \quad (2.19)$$

However, conducting triaxial shear tests at low pressures were difficult, as demonstrated by Fukushima and Tatsuoka (1984).

Çinicioğlu and Abadkon (2014) proposed a unique stress-dilatancy equation which is based on initial soil properties rather than peak states, because dilatancy rates calculated by these functions are dependent on the failure states of the soil and therefore impractical. Many CK_0D triaxial tests were conducted on a specific granular soil at different $p_i' - I_D$ combinations to define $p_i' - \psi$ relationship for every change in relative density. Here, p'_i and I_D are the in-situ (before shearing) mean effective stress and relative density values. Several tests were conducted at different OCR values (1,2,4,8) to consider the influence of unloading on dilation. Overconsolidated samples were unloaded under K_o conditions. Dilatancy angle was calculated from test results using Schanz and Vermeer equation (1996) of triaxial conditions. When results are analyzed, it is revealed that unloading has no effect on the dilatant behavior, hence it is concluded that OCR does not affect the proposed equations.

During the evaluation of triaxial tests, tangent of dilatancy angle ($tan\psi$) values were plotted against corresponding end of consolidation (in-situ) mean effective stresses which were normalized by p_a. It is revealed that $tan\psi_p - (p_i'/p_a)$ relationships were linear. Consequently, following equation was proposed:

$$tan\psi_p = \alpha_\psi \left(\frac{p_i'}{p_a}\right) + m_\psi I_D \quad (2.20)$$

At the end of the research, the validity of the proposed equation was verified for different sand types whose data were available in literature. Results showed that there is a linear relationship for all sands but line-fitting parameters were different (α_ψ and m_ψ). Finally, researchers concluded that this difference was possibly due to differences in the grain shape, size and distribution characteristics between these types of sand.

The proposed stress-dilatancy coefficients available in the literature were all derived according to shear tests conducted on granular soils. However, the varying parameters in these experiments are density and the stress state. The influence of grain shape, size, distribution and loading condition on these coefficients should be investigated in order to enhance the applicability of these equations.

2.2. Previous Research on the Influence of Grain Size and Shape on Dilatancy

The determination of the size and shape characteristics of soil grains were initially a research area for geology. C.K. Wentworth (1922) investigated the shape of beach pebbles, which have varying flatness and roundness values according to their geological origin. H. Wadell (1935) studied the volume, shape, and roundness of quartz particles, however his research was concentrated on the geological reasons on the formation of particle shape factors rather than their influence on strength. He defined roundness as the ratio of the average of radii of corners of the grain image ($\sum r_i/N$) and the maximum radius of the inscribed circle (r_{max-in}), and sphericity as the ratio of the surface area of a sphere of the same volume as the fragment in question to the actual surface area of the grain (Figure 2.6).

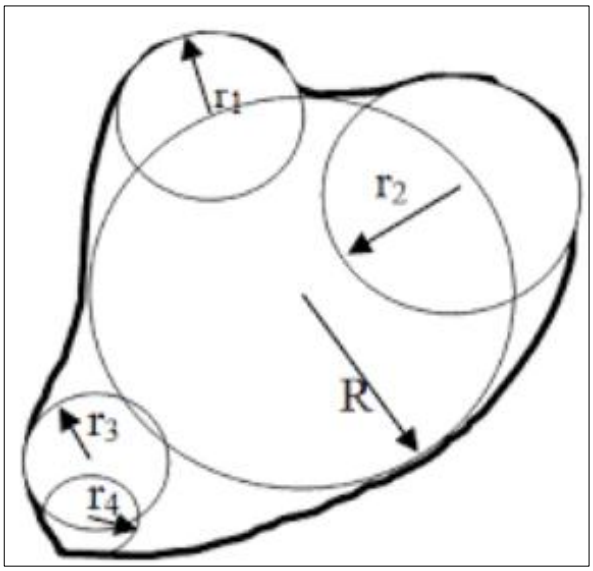


Figure 2.6. Roundness and Sphericity determination by H. Wadell (1935).

where,

$$\text{Roundness} = \frac{\sum r_i/N}{r_{max-in}} = \frac{4A}{\pi L^2} \tag{2.21}$$

$$\text{Sphericity} = \frac{r_{max-in}}{r_{min-cir}} = \frac{4\pi A}{p^2} \tag{2.22}$$

and as particle becomes round and sphere, value approaches to one. In these equations, *A* is the area of the soil particle, *L* is the average radius of the grain and *p* is the perimeter of the grain.

G. Rittenhouse (1943) presented a two-dimensional chart to estimate the sphericity value of a granular material by visual comparison only. M.C. Powers (1953) discussed that roundness of particles depend on the sharpness of grain edges, and developed a visual comparison chart to estimate the two-dimensional roundness and sphericity values of sedimentary particles (Figure 2.7).

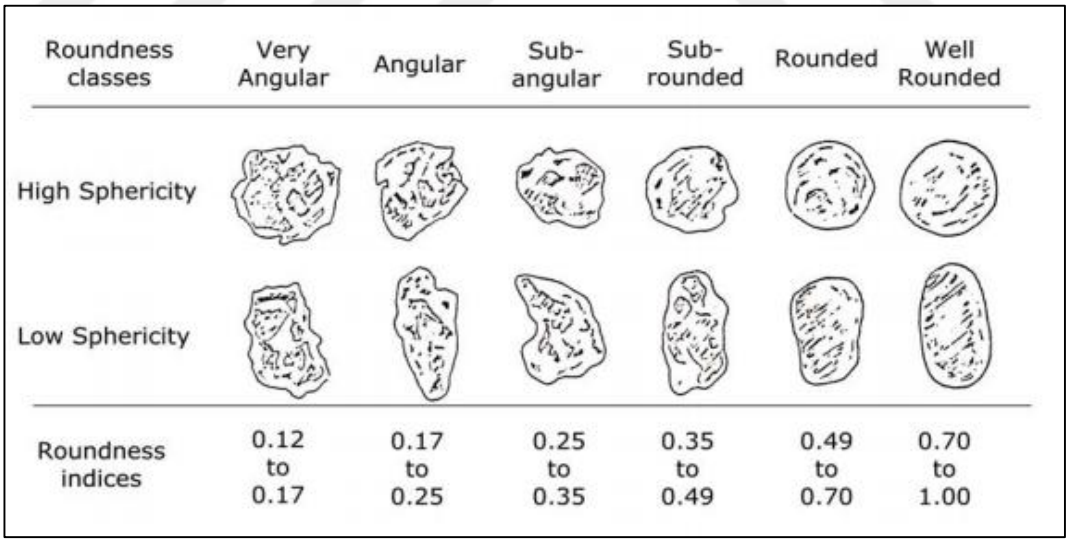


Figure 2.7. Grain shape determination chart (Powers, 1953).

Finally, Krumbein and Sloss (1963) published a chart to visually determine the sphericity and roundness values of any type of granular soil in their book *Stratigraphy and Sedimentation*, (Figure 2.8) which is still widely used in geological and geotechnical practice.

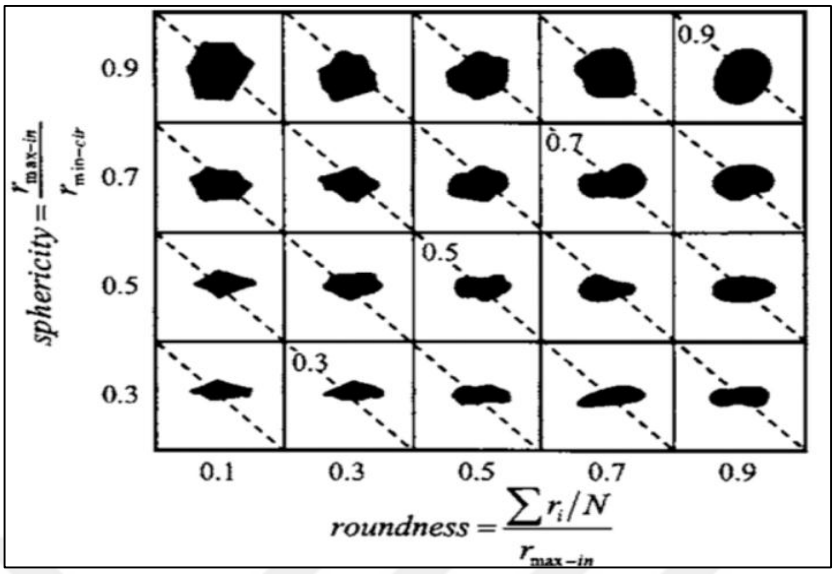


Figure 2.8. Sphericity and Roundness chart presented by Krumbein and Sloss (1963).

Holubec and Appolonia (1973) revealed the considerable varience at engineering properties of granular soils which have the same relative densities by conducting several strength tests on GB and sand samples of different shape.

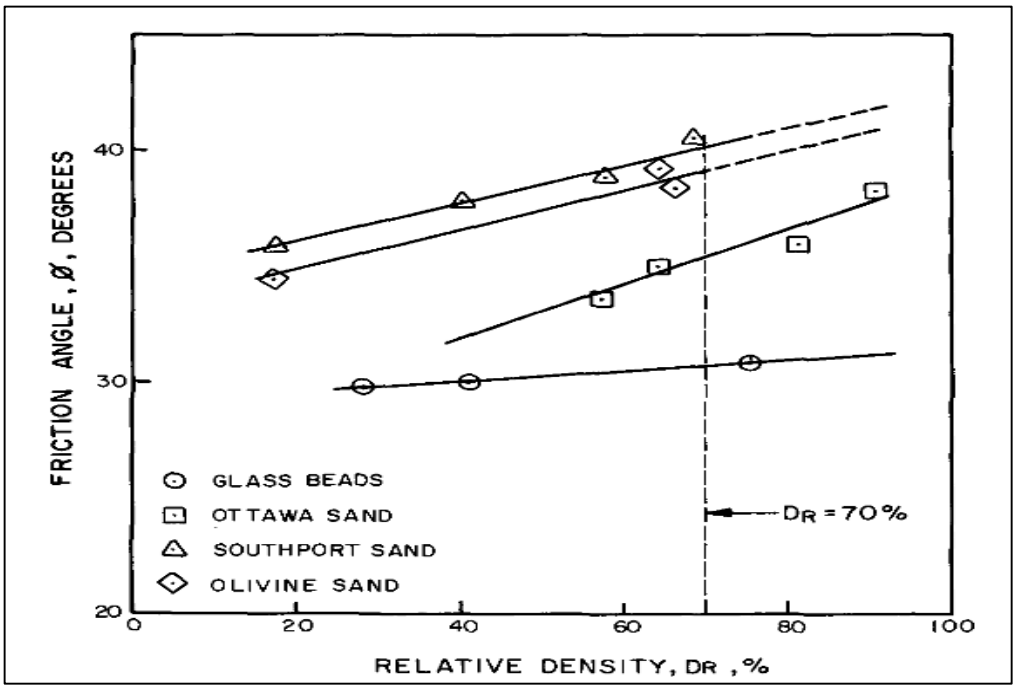


Figure 2.9. Effect of particle shape on angle of internal friction (Holubec and Appolonia, 1973).

Moreover, their study exposed that sands which consist of more angular grains are more deformable and have higher internal friction angles (Figure 2.9). Therefore, the use of existing stress-dilatancy equations which only take the relative density into account to calculate soil strength became misleading and not accurate.

E. Frossard (1979) investigated the effect of grain angularity on interparticle friction. In his work, the author defined the roundness of soil grains by an asperity index (I_a), and has worked with four different sand types and two granulometric classes (2 to 1 mm and 1 to 0.5 mm). Standard consolidated, drained triaxial tests were conducted on specimens under 50 kPa lateral pressure. The results revealed that soils having low asperity index values denote strong interparticle friction angles independent from mineralogical nature of soil grains (Figure 2.10). Additionally, sphericity influences the dilatancy rate. Consequently, the study proved that Rowe's and Horne's theoretical stress-dilatancy theories based on interparticle friction should also consider angularity and sphericity effects of sand grains.

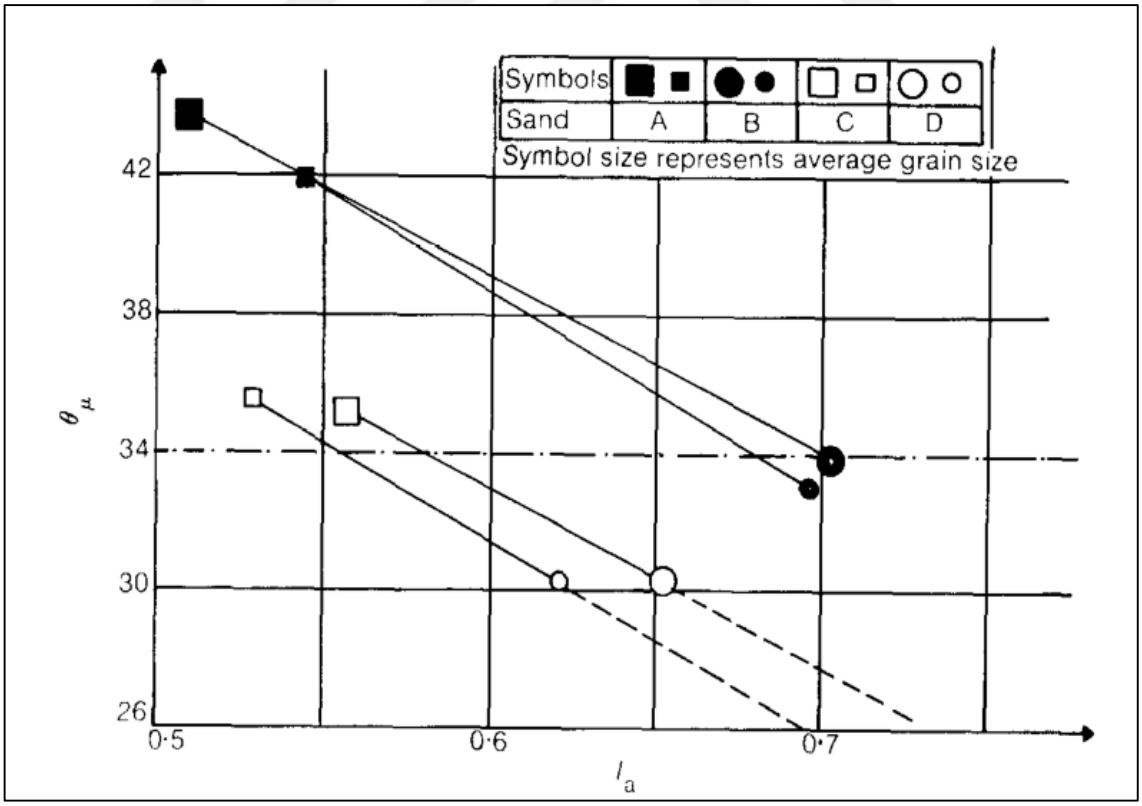


Figure 2.10. Asperity index – interparticle friction angle relationship (E. Frossard, 1979).

At the beginning of the 21th century, advances in digital microscopy have lead researches to intensively focus on the investigation of grain surface roughness and geometry for their effects on soil strength. Formerly, the observations could only be done visually, however the improved computational science software programs helped researchers to obtain particle shape characteristics faster and more accurately.

K.A. Alshibli and M.I. Alsaleh (2004) investigated the infleunce of surface rougness, roundness and sphericity of three different silica sand grains into friction and dilation angle of sands. In the study, researchers employed scanning electron microscopy (SEM) technique to obtain pictures of soil particles. A view of soil grains obtained by SEM analysis is presented in Figure 2.11 to indicate the accuracy and quality achieved by the advances in digital microscopy.

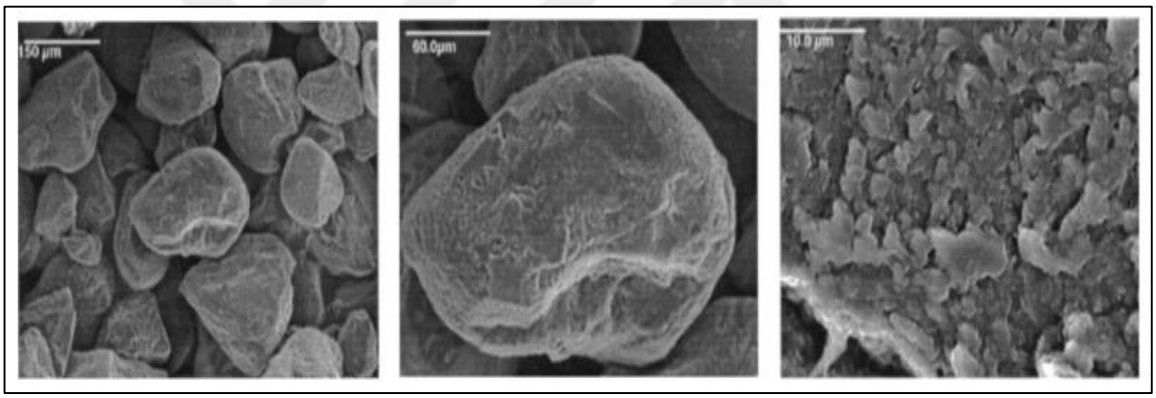


Figure 2.11. View of soil grains obtained by SEM analysis (Alshibli and Alsaleh, 2004).

Surface roundness measurements were done by *Vision 32* software program. In addition, *Scion Image Analysis Software (SIAS)* is used to measure the area, perimeter and shortest-longest axes of 25 particles of each of the three sand types. Figure 2.12 presents the outcome of SIAS showing particle analysis.

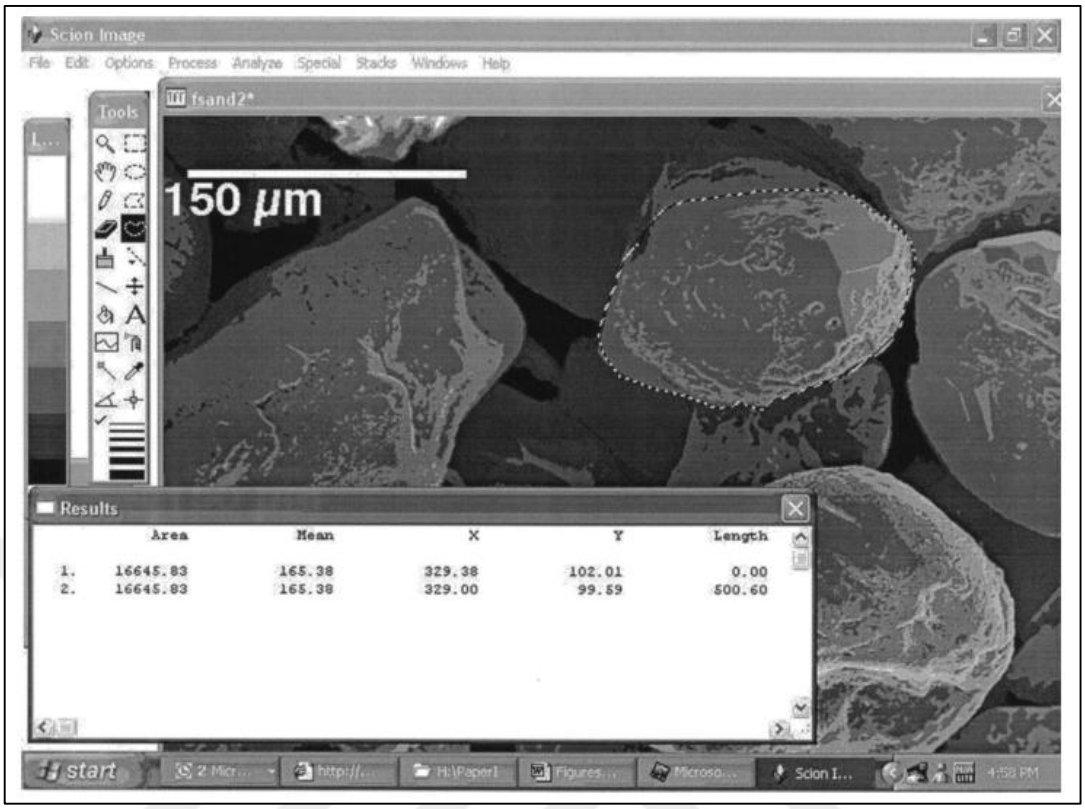


Figure 2.12. A view of Scion Image Analysis Software outcome (Alshibli and Alsaleh, 2004).

Moreover, authors also converted the particles listed in Powers (1953) chart into image format and analysed using the same software in order to compare the results. In conclusion, it was revealed that as the surface roughness increases, the friction and dilatancy angles of the soils increase.

Santamarina and Cho (2004) implemented a wide study to calculate the particle shape and mechanical properties of various natural and crushed sands using both their own data and Ashmawy et al., (2003) data. The soils used in the study were gathered from various places around the world. Also tests on GB were conducted for comparison. In this study stereomicroscope (Leica MZ6) was used to take microphotographs of the soil grains. Spherity and roundness values were determined by Krumbein and Sloss (1963) chart.

According to their study, particle shape had a major effect on the critical state mechanical soil parameters (V_s, C_c, C_s, $\boldsymbol{\Gamma}$, $\boldsymbol{\lambda}$, Φ_{cs}) as well as maximum void ratio and small

strain stiffness. Therefore it was concluded that macroscale soil behavior reflects particle level characteristics and processes.

When it comes to grain size and gradation, literature seldom presents clear and accurate outcome. Some of the experimental studies based on strength tests indicated that particle size has no considerable effect on shear strength of granular soils (Bishop, 1948; Holtz and Gibbs, 1956; Vallerga *et al*.; 1956 and Selig and Roner, 1987). However, researchers like Lewis (1956), Dunn and Bora (1972), Chattopadhya and Saha (1981) observed in their studies that an increase in particle size increases shear strength of soils. On the other hand, Rowe (1962), Kirkpatrick (1965), Marsal (1965), Koerner (1970) and Marachi *et al*. (1972) indicated that soils consisting of higher particle sizes have lower shear strengths. Regarding the effect of particle distribution, researchers like Rico *et.al*. (1977), Marsal (1965), Marachi *et al.*, (1972) observed that well graded soils have higher strengths; whereas Leslie (1963) and Susan (1999) proposed that soils having a broader gradation posess lower friction angles.

G.M. Latha and T.G. Sitharam (2008) used discrete element modelling method (DEM) to investigate the effect of particle size and gradation on the behaviour of granular materials. DEM includes particulate modelling which takes into account the interaction of individual particles at inter-particle contact points. This way, the effect of grain size and gradation can be more realistically modelled. On the other hand, constitutive modelling which is derived from continuum mechanics and widely used in geotechnical design like finite element analysis can not model the micro scale, grain level properties. Therefore, the researchers preferred the DEM method in their study. The modified version of the TRUBAL (1989) software program was used for modeling granular soils. Four different assemblies of uniform size spheres and seven different assemblies of graded spheres, both having varying diameters had been used in numerical experiments. The reason to model spheres was to elimiante shape factor effects and concentrate on the influence of grain size and distribution. Next, coefficient of curvature (C_c) and coefficient of uniformity (C_u) values were calculated for each soil. The experiments were grouped into four categories: Soils with equal C_u values, soils having the same maximum particle sizes, soils having the same minimum particle sizes and soils consisting of equal, uniform sized particles only. Samples were prepared under different confining pressure, relative density and interparticle friction (μ) values for

comparison. The results indicated that particle size has no considerable influence on strength behavior of granular soils (Figure 2.13).

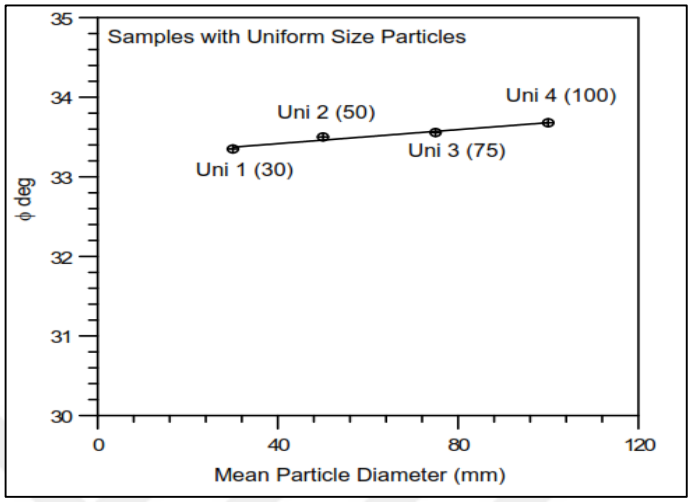


Figure 2.13. Influence of particle size on friction angle (Latha and Sitharam, 2008)

Additionally, it was observed that samples having higher particle sizes had lower initial void ratio and higher compressibility characteristics. In terms of granulometry, it was observed that the shear strength of granular materials was higher if their grains have a wider gradation of particle sizes (Figure 2.14). It meant that well graded soils have more strength than that of poorly graded soils.

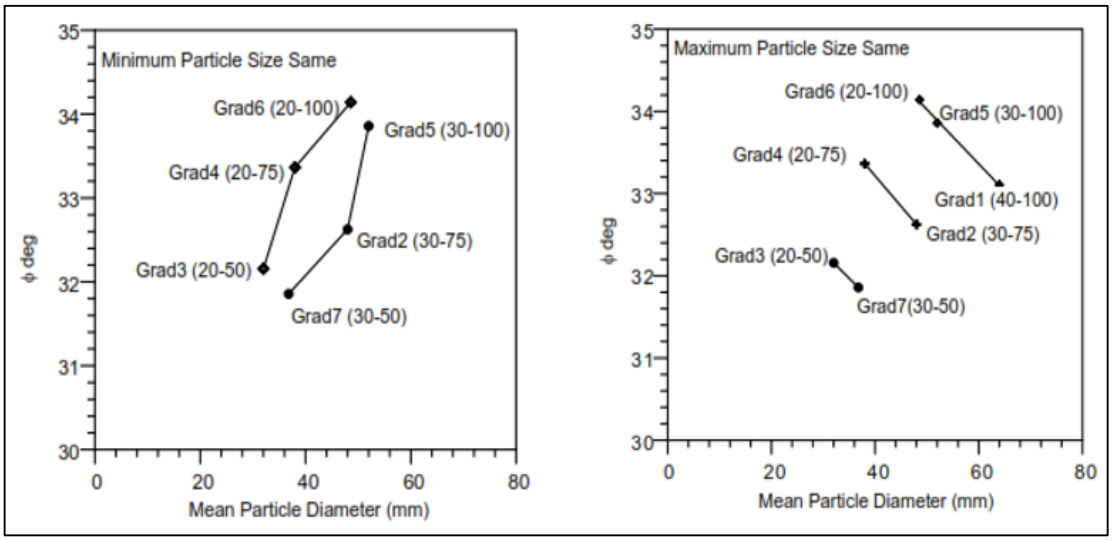


Figure 2.14. Influence of grain distribution on friction (Latha and Sitharam, 2008).

Finally, the relationship between friction angle and initial void ratio of the samples indicated that the volume change behaviour was slightly affected with the variation in the size of particles (Figure 2.15).

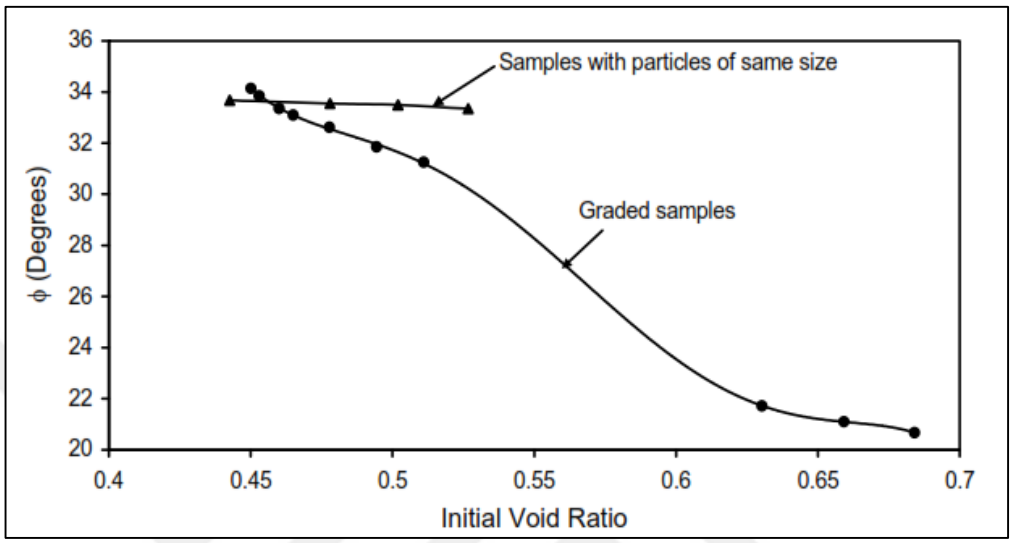


Figure 2.15. Variation of friction angle with void ratio (Latha and Sitharam, 2008).

Hence, it was concluded from the research that particle size has no considerable effect on the strength of granular materials, however granulometry significantly influences the strength and volume change behavior of granular soils.

Siang *et al.* (2012) investigated the effects of particle morphology on engineering properties of granular materials. For this purpose, physical properties of various sand types were collected from literature. Next, laboratory tests were conducted on two different sand types named as Buzzard and Kahang sand in order to reveal their grain size, shape, granulometry and mineralogical composition. In addition, direct shear tests were conducted to calculate friction and dilation angle of the sands. Dilation angle – relative density correlation was investigated. Finally, they proposed comparison charts regarding uniformity coefficient and shape factors with critical friction angle. The study revealed that grain shape influences maximum and minimum void ratio of the sands, and particle gradation significantly affect peak and critical friction angles. Finally, sands consisting of rounded and sphere grains possess lower dilation behavior.

J. Lee *et al.* (2013) experimentally investigated the values of K_o for different types of granular materials, GB and etched GB. For this purpose initially triaxial and other basic property tests were conducted to reveal strength properties of sands. Next, inter-particle stress analysis was presented to analyze and validate the correlation of K_o to soil strength. Angular sand particles showed lower K_o values compared with GB. The effect of particle surface roughness was relatively small. Jacy's equation was found to be valid and critical state friction angle can be used to calculate K_o for uniform, round GB; however for soils having irregular, angular particles the friction angle parameter had to be taken more than critical state friction angle due to particle interlocking, but less than the peak friction angle due to particle angularity. It was proposed that,

$$K_o = \frac{1-\sin(\beta\emptyset'_{cs})}{1+\sin(\beta\emptyset'_{cs})} \tag{2.23}$$

where,

$$\beta = a[I_D(\%)]^b \tag{2.24}$$

In the equation a and b are correlation parameters and according to Lee *et al*. (2013), β is between 0.4 and 0.9.

Amirpour *et al.* (2017) investigated the influence of particle size and gradation on the stress-dilatancy behavior of granular materials by conducting consolidated, drained triaxal tests on GB and a granular soil having seven different grain-size distribution curves. Tests were done under varying confining stress and relative densities. The comparison of test results showed that shear strength and volumetric response of tested materials were independent of C_u coefficient but significantly influenced by median particle size, D_{50}. As a result, they proposed a unique coefficient (a) to be replaced by Bolton's stress-dilatancy equation constant of 0.3 which increases with increasing angularity and decreases with particle size:

$$(-d\varepsilon_v/d\varepsilon_1)_{max} = aI_R \tag{2.25}$$

$$a = c_1 / (D_{50})^{c_2} \tag{2.26}$$

Soil specific c_1 and c_2 constants which determine grain size and shape effect into dilatancy respectively were calculated by plotting $(-d\varepsilon_v/d\varepsilon_1)_{max}$ and dilatancy index (I_R) relationship for each sand. Consequently, the decrease of '*a*' value with increasing D_{50} was described by a power function, with constant c_1 =0.49 and c_2 = 0.12 for material made up of rounded particles. The constant c_2 decreased to 0.03 by increasing angularity (Figure 2.16). Additionally, the contribution of dilatancy on soil strength in peak friction angle – peak dilatancy angle relationship had also been investigated by Amirpour et al. (2017). They have considered Bishop (1971)'s 'r' coefficient as 'b'; and proposed that 'b' varies with grain size and angularity.

$$\emptyset'_{max} - \emptyset'_{cv} = r\psi_{max} \tag{2.27}$$

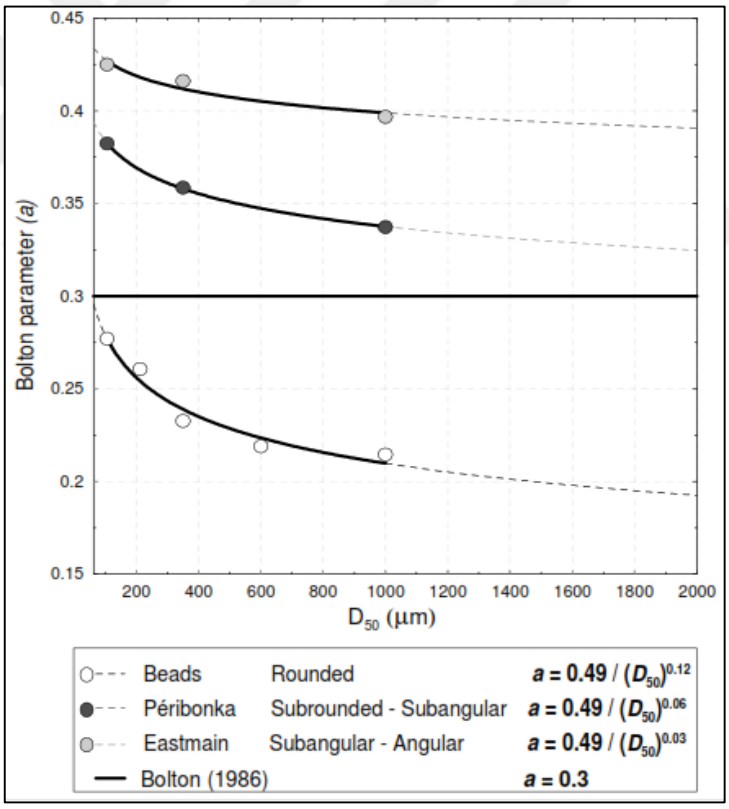


Figure 2.16. Variance of Bolton's 'a' parameter with median grain size (D_{50}) and angularity (Amirpour *et al.*, 2017).

They revealed by conventional triaxial tests conducted on particularly uniform graded sand with different grain size ranges that if grain size was higher, '*r*' coefficient was less.

Moreover, they also conducted shear tests on glass beads, plus they have used literature triaxial data of granular soils with different angularity to reveal that granular soils with angular grains have more contribution of dilatancy into soil strength (Figure 2.17).

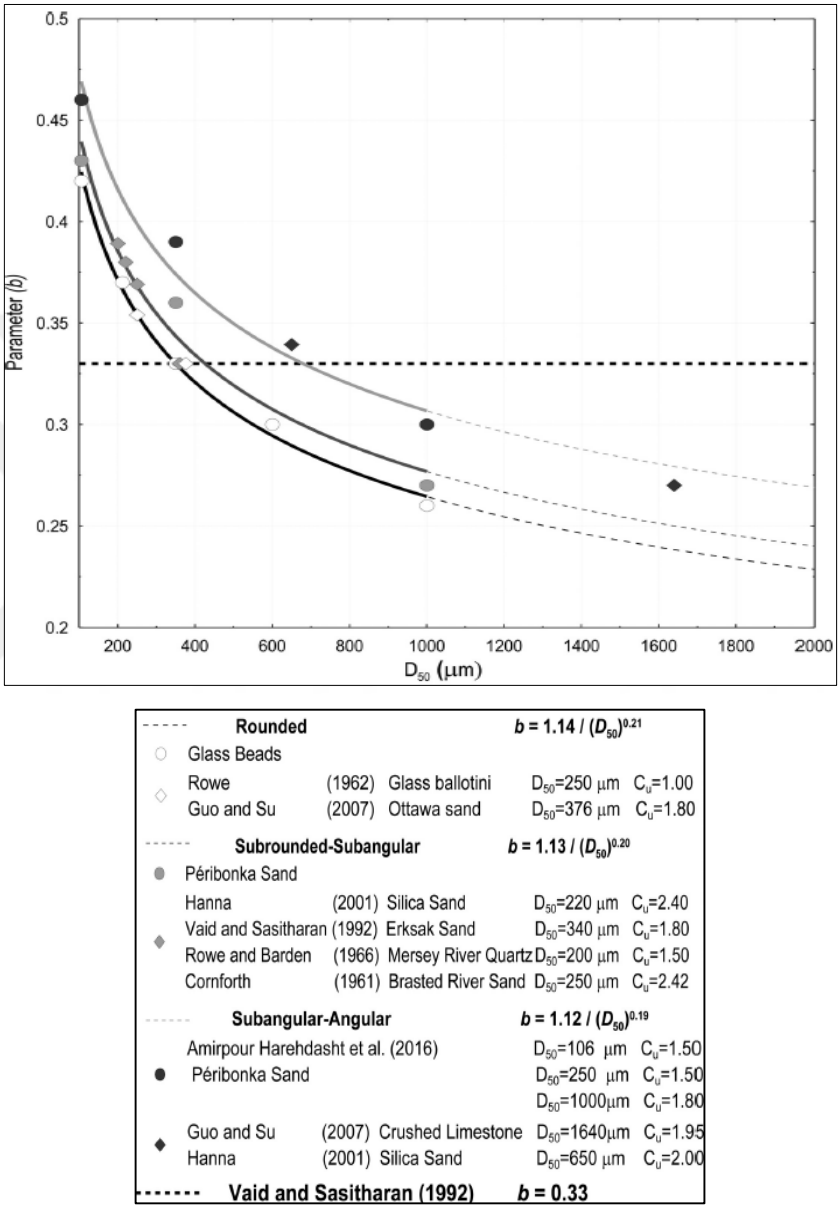


Figure 2.17. Variance of '*r*' with median grain size and angularity (Amirpour *et al*., 2017).

Giampa and Bradshaw (2017) proposed an experimental method to evaluate the peak friction angle of sands at very low confining pressures by conducting triaxial tests to find friction and dilation angles of two different soils. Table 2.2 summarizes all physical and mechanical properties of soils gathered from literature and used in this study.

Table 2.2. Stress-dilatancy correlation coefficients derived from literature.

Author(s)	Sand	Minerology	S_{ave}	R_{ave}	C_u	D_{50}	r	$Ø_{cs}$	Q	R	A_ϕ
Bolton (1986)	Varies	Varies					0.50		10.0	1.0	3.0
Hanna (2001)	Sand A	Silica	Rounded	Rounded	2.40	0.22	0.43	31.9			
	Sand B	Silica	Angular	Angular	2.33	0.65	0.41	34.2			
	Sand C	Silica	Angular	Angular	2.00	0.65	0.40	35.5			
Vaid and Sashitarian (1992)	Erksak	Quartz	Subround	Subround	1.80	0.34	0.33	32.0			
Guo and Su (2007)	Sand O	Quartz	0.691	0.572	1.80	0.38	0.63	30.0			
	Sand L	Limestone	0.405	0.144	1.95	1.64	0.91	39.0			
Chakraborty and Salgado (2010)	Toyoura	Quartz	Subangular	Subangular	1.46	0.16	0.83	31.7	9.7	1.0	3.8
Siang et al. (2012)	SPu Buzzard		0.730	0.680	1.48	0.65	0.49	27.0			
	SPu Kahang	River	0.640	0.410	1.86	0.60	0.70	34.8			
	SW Kahang	River			3.95	1.20	0.61	38.0			
	SPg Kahang	River			11.5	1.30	0.90	37.0			
Lee et. al. (2013)	Jumunjin	Quartz				0.56		37.8	8.73	1.27	3.0
	Glass Beads	Soda Lime				0.50		27.1	6.89	0.78	3.0
	Etched GB	Soda Lime				0.50		30.8	8.42	1.23	3.0
Çinicioğlu (2014)	Akpınar	Quartz	0.700	0.500	1.23	0.27	0.39	33.0	9.0	1.0	
Amirpour et. al. (2016)	Peribonka	Quartz	0.60	0.44	1.50	0.11	0.43				
	Peribonka	Quartz	0.60	0.44	1.50	0.35	0.36				
	Peribonka	Quartz	0.60	0.44	5.00	0.35					
	Peribonka	Quartz	0.60	0.44	1.50	1.00	0.27				
Amirpour et. al. (2016)	Glass Beads	Glass	1.00	1.00	1.50	0.11	0.42				
	Glass Beads	Glass	1.00	1.00	1.50	0.21	0.37				
	Glass Beads	Glass	1.00	1.00	1.50	0.35	0.32				
	Glass Beads	Glass	1.00	1.00	1.50	0.60	0.30				
	Glass Beads	Glass	1.00	1.00	1.50	1.00	0.26				
Bradshaw et. al. (2017)	Westerly	Quartz	0.60		1.63	0.30	0.69	32.3	10.2	1.0	4.8
	Goldonflint	Quartz	0.80		1.61	0.25	0.64	33.9	13.2	1.0	3.6
Cho et. al. (2006)	Nevada		0.85	0.60	1.8	0.15		31			
	Ticino		0.80	0.40	1.5	0.58		37			
	M.River		0.70	0.70	1.9	0.49		33			
	ASTM 20/30		0.90	0.80	1.4	0.60		32			
	Ponte Vedra		0.85	0.30	1.8	0.18		39			
	8M8 Crushed		0.70	0.20	3.3	0.38		40			
	9C1 Crushed		0.70	0.25	2.3	0.52		39			
	Jekyll Island		0.85	0.30	1.7	0.17		40			
	ASTM graded		0.90	0.80	1.7	0.35		30			
	Blasting		0.55	0.30	1.9	0.71		34			
	Glass Beads		1.00	1.00	1.4	0.32		21			
	Granite powder		0.24	0.24	6.2	0.09		34			
	Ottowa 20/30		0.90	0.90	1.2	0.72		27			
	Ottowa F-110		0.70	0.70	1.7	0.12		31			

2.3. Previous Research on Failure Surface Geometry and PIV

Coulomb (1776) proposed that a soil mass behind a rigid retaining wall slips along a plane inclined with an inclination to the horizontal in terms of limit equilibrium. By drawing the free-body diagram and using statistics (Figure 2.18), he proposed:

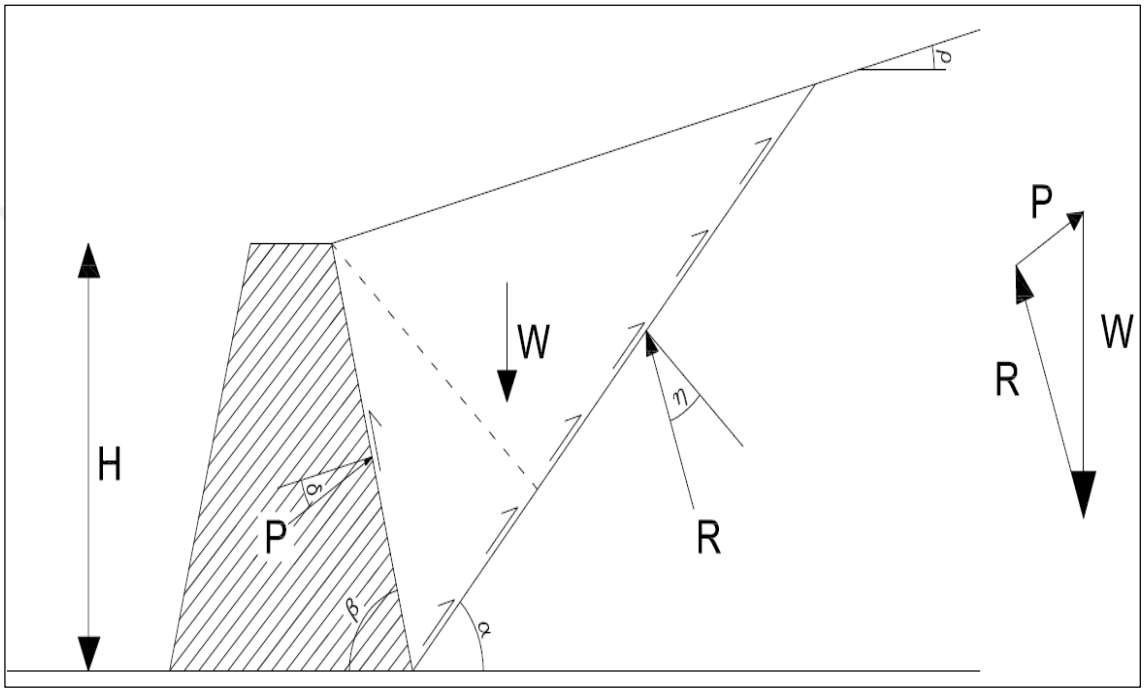


Figure 2.18. Coulomb failure wedge.

$$P_a = \frac{W \cdot \sin(\alpha - \eta)}{\sin(180^0 - \beta - \alpha + \eta + \delta)} \tag{2.28}$$

where,

$$W = \frac{\gamma H^2}{2sin^2\beta}[\sin(\beta + \alpha)] \times \frac{\sin(\beta + i)}{\sin(\alpha - i)} \tag{2.29}$$

Rankine (1857) investigated the stress states of a soil element behind a rigid retaining wall for active state and in front of the wall for passive state. He termed the sum of all slip planes occurring behind and in front of the wall during transition until the failure state as the 'Active zone' and 'Passive zone' respectively (Figure 2.19).

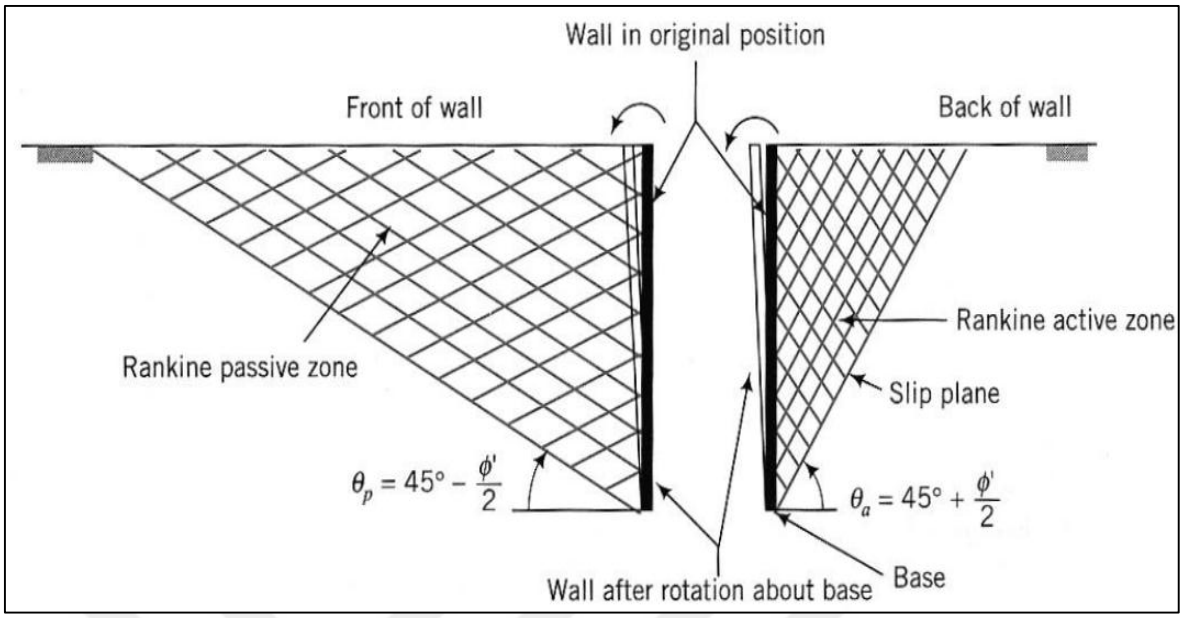


Figure 2.19. Slip planes within a soil mass near a retaining wall.

Hence, active and passive lateral earth pressures would be calculated at Rankine active and passive states respectively.

The Coulomb and Rankine theories are based on several assumptions. First, the geometry of the shear band tracks a linear path; assuming that the angle of the slip surface to horizontal is only proportional to friction angle of granular soil. The reason behind this proposal was that the soil resistance against sliding would be only its inherent shear strength. Moreover, if tension cracks occur on the slip plane the failure geometry modifies, but this condition mostly exists in cohesive soils.

However, research that followed has revealed that for granular backfills, the geometry of the shear band behind retaining walls are influenced from interface friction generated between wall and the soil. The wall-soil interface leads to soil arching which causes the slip surface geometry to become non-linear. Therefore, distribution of stresses on the slip plane are not uniform. Caquot and Kerisel (1948) used nonplanar, logarithm spiral slip surfaces, whereas Packshaw (1969) proposed circular failure surfaces. Researchers such as Y.S. Fang and I. Ishibashi (1986), R. Salgado (2003), S. Goel and N.R. Patra (2008), P.P. Rao *et al.*, (2015) investigated the influence of soil-wall interface and soil arching on active earth

pressures and slip surface geometries for rigid retaining walls transiting laterally. Through this research, it was revealed that due to frictional resistance between wall and the soil, arching mechanism occurs resulting in non-linear pressure distribution and failure surface geometry behind rigid retaining walls. However, since numerical modelling of arching mechanism was difficult to interpret, theoretical assumptions could not directly figure out the actual geometry of shear bands. Therefore, most study concentrated on the physical appearance of dilative behavior on slip surface rather than the arching effect.

Following these experimentations, Z.V. Tsagareli (1965) experimentally investigated the generation of earth pressures and character of pressure distribution of a cohesionless soil behind a retaining wall. In his research different wall heights and wall inclinations were used. The deformation of sliding sand during wall transition was photographed. At the end, different slip surface geometries were obtained for varying wall heights and soil friction angles; however the geometry of the shear band was parabolic in all cases. Finally, he proposed a geometric power function to calculate failure surface geometry:

$$Y = C(3.6\emptyset + 0.5)^{x/c} \tag{2.30}$$

Where Ø is the internal friction angle of soil in radians, X is the horizontal distance between retaining wall and the shear band at ground surface and C is a coefficient having dimensionality in length units (c= 1 m).

J.R. Arthur *et al*., (1977) have conducted many simple shear, direct shear and flexible boundary plane strain tests to investigate the orientations of the rupture layers at local simple shears at failure state and revealed that orientations from the major principal stress direction are between 45^0-$1/2\emptyset'$ and 45^0- $1/2\psi'$ due to plastic, plane strain hardening and softening behavior of granular soil at pre-failure. These values were selected as upper and lower bound values respectively. Amongst the shear tests, the FPSA tests were best a representative of a plane strain retaining wall model due to boundary conditions and at all tests conducted by FPSA, the thin rupture layers formed with orientations to the major principal stress of:

$$\alpha = \frac{\pi + \emptyset'_p + \psi'_p}{4} \tag{2.31}$$

and were symmetrical. This study clearly demonstrated the influence of dilatant behavior of granular soils on the formation of shear band geometry.

Vardoulakis (1980) studied the generation of shear band formations on biaxial tests of dry sand samples as a function of dilatancy. He selected the upper bound (45^0+1/2Ø') as Coulomb solution and lower bound (45^0+1/2ψ') as the Roscoe solution referring to inclination of initial part of the failure surface into horizontal. Finally, he showed that the measured shear band inclinations were in good agreement with the computed values by the equation proposed by Arthur *et al.,* (1977), both of which were in between Coulomb and Roscoe solutions (Figure 2.20).

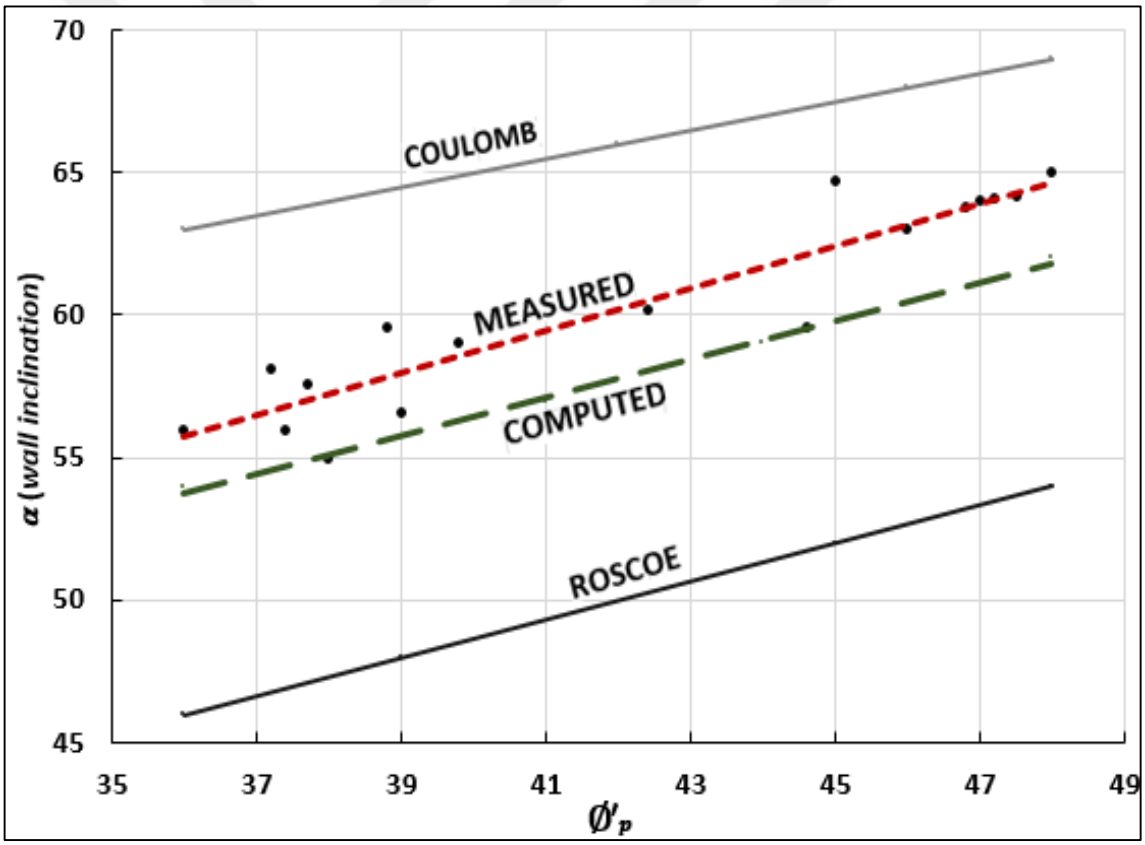


Figure 2.20. Measured vs. computed shear band inclination (Vardoulakis, 1980).

M. Toulios (1984) discussed the process of formation and propagation of a shear band on a nonlinear elastic material under shear deformation. An imperfection was modelled on the element so that the concentration of strains around the imperfection which eventually

cause a propagation of the crack and formation of the shear band could be observed. Also the influence of the strength of the initial imperfection on the evaluation of the shear layer was investigated. It was found that the speed of the shear band propagation, once formed, was independent of the background strain at which the band has formed. However, the growth of the shear band was sustained by the natural strain concentration at the edge of the band. This study showed that the one-dimensional shear models which assume a global instability criterion in order for a bond to form become inapplicable; since for the bond to evolve, only a local instability criterion would be sufficient.

S. Bang (1985) investigated active earth pressure generation behind a retaining wall between initial and full active state of a granular soil through wall tilting about the base. He considered the full active case with a coefficient β=1.0 and initial case as β=0 in the analysis. He used Coulomb's theory to calculate lateral earth pressures for each case; however the effect of wall tilting was also considered in calculations. He found that wall tilting significantly influences lateral earth pressure values especially when wall tilts through the active state (Figure 2.21).

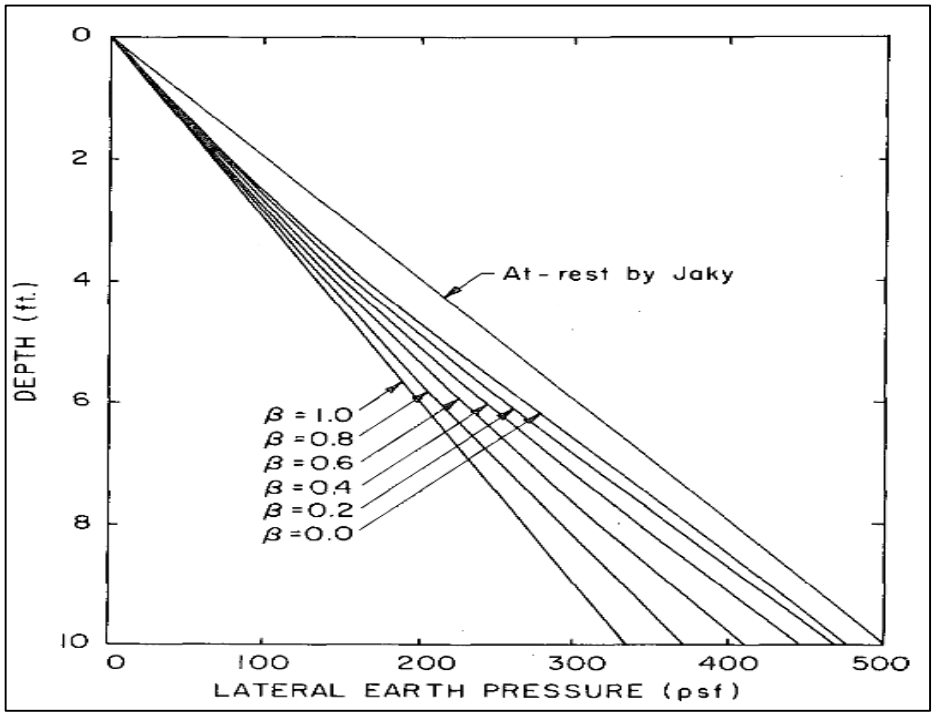


Figure 2.21. Variation in lateral earth pressures by retaining wall tilting (S. Bang, 1985).

In 2000s the advances in computational science and graphics allowed researchers to work on photoelastic and photographic study on granular materials. This enabled the investigation of strain localization and shear band formation behind retaining walls to be held more intensely and accurately. Most recent advance in geomechanics is the particle image velocimetry method (PIV) where the flow of grains between a reference image and a sequence of deformed images are tracked by evaluation of displacement fields (White *et al.*, 2003). This software was initially programmed for fluid mechanics, however the availability to observe the displacement of soil grains by tracking of consecutive pictures enabled researchers to use this software in geotechnical engineering field. It operates by tracking spatial variations of brightness within an image (divided into a mesh of PIV patches) by comparing successive images so that displacement data can be extracted from sequences of images, and strains, then calculated from gradients of measured displacements. In 2015, the GeoPIV was upgraded to GeoPIV-RG module by S. Stanier, A. Take and D. White, so that more accurate shear and volumetric strain fields would be generated by the software. Owing to this fact, in this Ph.D. research the most recent GeoPIV-RG software was used in the analysis. Lesniewska and Wood (2009) examined the advantages of photoelastic technique (PIV) on analysis of incremental stress, displacement and strain fields for model retaining walls. For this purpose, a physical retaining wall model was manufactured in their study as shown in Figure 2.22.

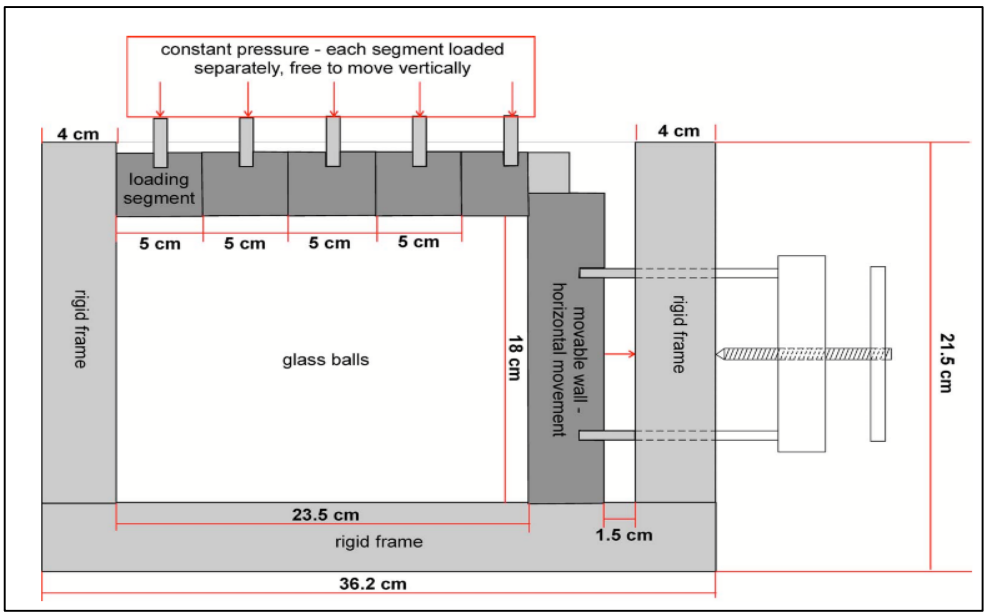


Figure 2.22. Physical model apparatus designed by Lesniewska and Wood (2009).

The researchers have used glass ballotini as backfill material and the wall transition process were photographed by a digital camera by using polarized light as the lightening source. The analysis of the pictures by PIV revealed the change in stress conditions on the backfill material during wall transition. All strain localization zones, slip surfaces, imperfections would be elaborately visualized by volumetric strain maps generated in MATLAB by GeoPIV software (Figure 2.23).

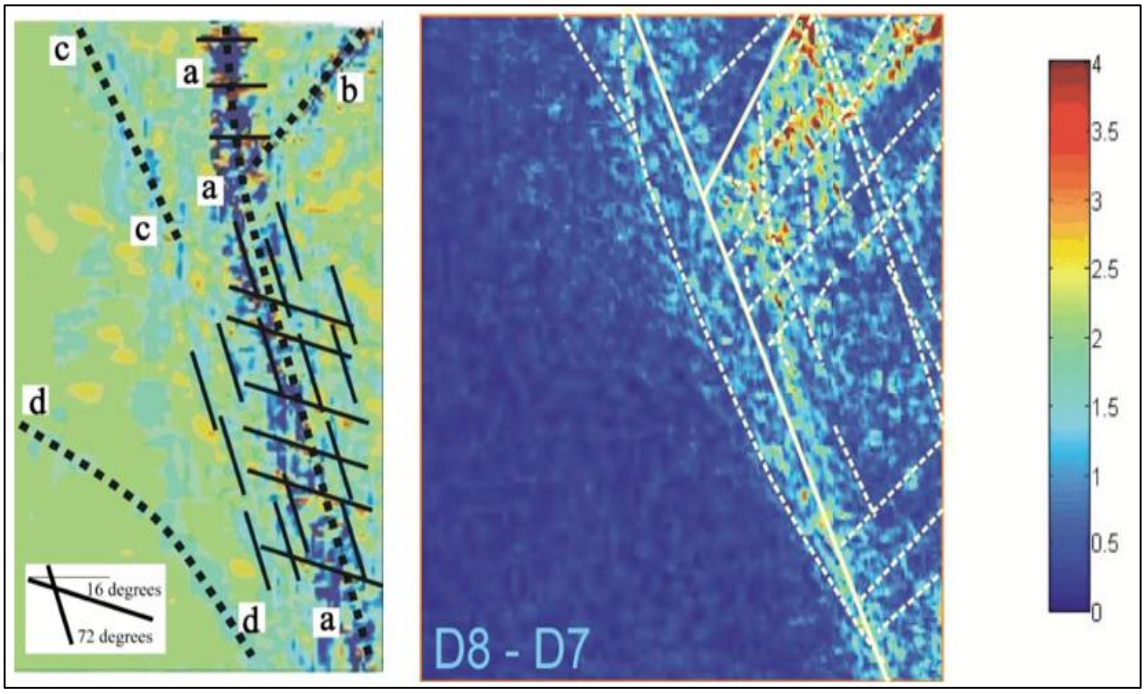


Figure 2.23. Imperfections and strain localization zones revealed by GeoPIV (Lesniewska and Wood, 2009).

Niedostatkiewicz *et al.*, (2011) analyzed the shear band patterns in cohesionless soils for active and passive cases using PIV method and experimentally produced slip surfaces. The study evaluated the influence of initial relative density on shear band geometry. Pietrzak and Lesniewska (2012) conducted physical model tests at varying surcharge pressures and relative densities however their study was focused on stress localization, generation of volumetric and shear strains and macro scale behavior of granular material rather than formation of shear bands.

Altunbas *et al.,* (2017) conducted physical model tests on a granular backfill of varying initial densities to quantify the influence of dilatancy on shear band geometry using PIV method. In their experiments, PIV analysis revealed that shear band begins from the bottom corner of the retaining wall and follows a parabolic path until it reaches to the ground surface where the distance between the wall and slip surface is the widest. To obtain the influence of dilatant behavior on failure surface geometry; consolidated, drained triaxial tests were conducted on the granular soil at varying density and surcharge pressures. As a result, mechanical soil properties such as critical state friction angle (ϕ'_{cs}), Bolton's stress-dilatancy equation coefficients Q and R, dilatancy effect parameter on friction for axisymmetric conditions (r_{tx}), dilatancy effect parameter on friction for plane strain conditions (r_{ps}) were all calculated. These parameters were used to evaluate the dilatancy angle of the tested soils for each physical model test.

The evaluated failure surface geometries for each test were compared by the dilatancy angle of tested soils (Figure 2.24). The study revealed that the magnitudes of dilatancy angles influence the shapes of the failure surfaces.

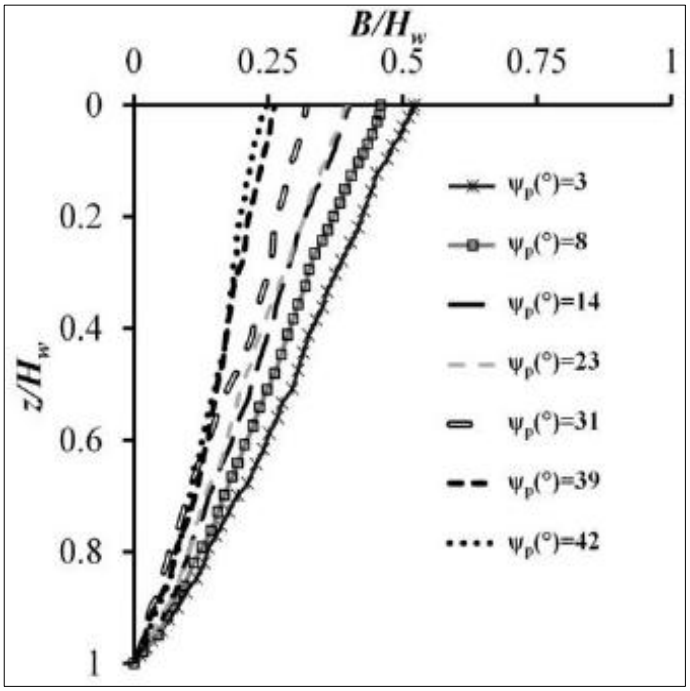


Figure 2.24. Dilatancy angle – failure surface relationship (Altunbas *et al*., 2017).

Next, researchers proposed a unique geometrical correlation to define the failure surface geometry:

$$z = aB^2 + bB + c \tag{2.32}$$

$$a = [(a_b - 1)/(a_b^2 H_w)]tan^2(\alpha) \tag{2.33}$$

$$b = -\tan(\alpha) \tag{2.34}$$

$$c = H_w \tag{2.35}$$

where H_w is the wall height, B_f is the distance of shear band to wall at ground surface, X is the distance of the linear extrapolated line to wall at ground surface which is tangent to initial part of shear band at toe level; α is the inclination of the initial section of the shear band at the toe level, *z* is the vertical coordinate, and B is the horizontal distance from the retaining wall to the failure surface at a particular depth *z* (Figure 2.25).

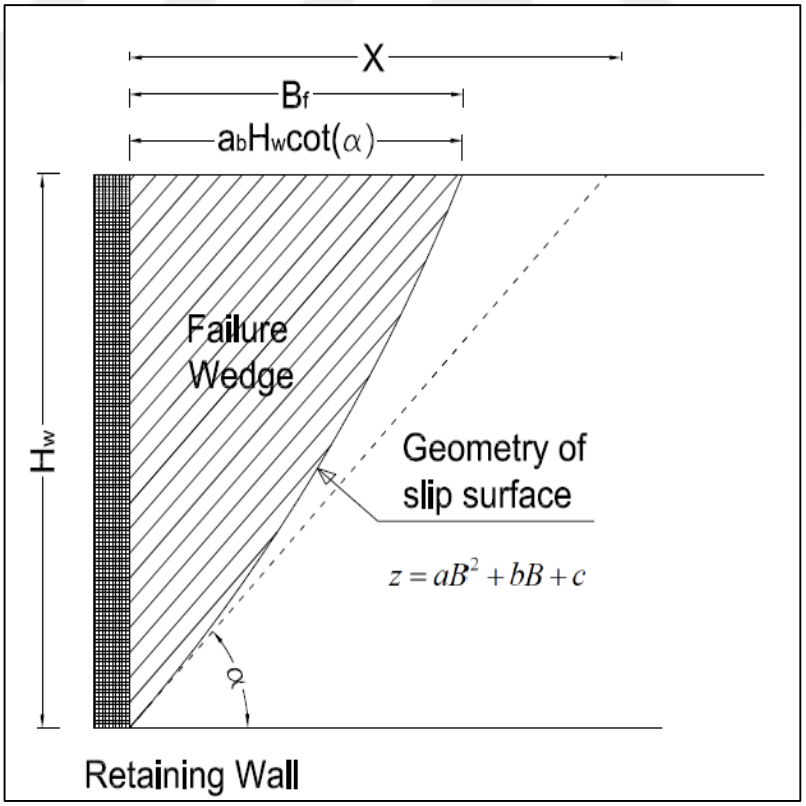


Figure 2.25. Geometrical parameters of the shear band (Altunbas *et al.*, 2017).

To derive a unitless parameter to be used in comparison of failure geometry of backfills consisting of various dilatancy angles, B_f / X ratio was selected as the 'a_b' parameter.

$$z = \left(\left[{}^{(a_b - 1)} \Big/ {}_{(a_b^2 H_w)} \right] tan^2(\alpha) \right) B^2 - \tan(\alpha)\, B + H_w \qquad (2.36)$$

The variation of α with $\emptyset'_p$ was investigated as proposed by Vardoulakis (1980):

$$\alpha = \frac{\pi + \emptyset'_p + \psi'_p}{4} \qquad (2.37)$$

The results showed that measured α values were in a good match with Vardoulakis (1980) and when soil density increases, strength and α values also increase, meaning that shear band becomes steeper and closer to the retaining wall (Figure 2.26).

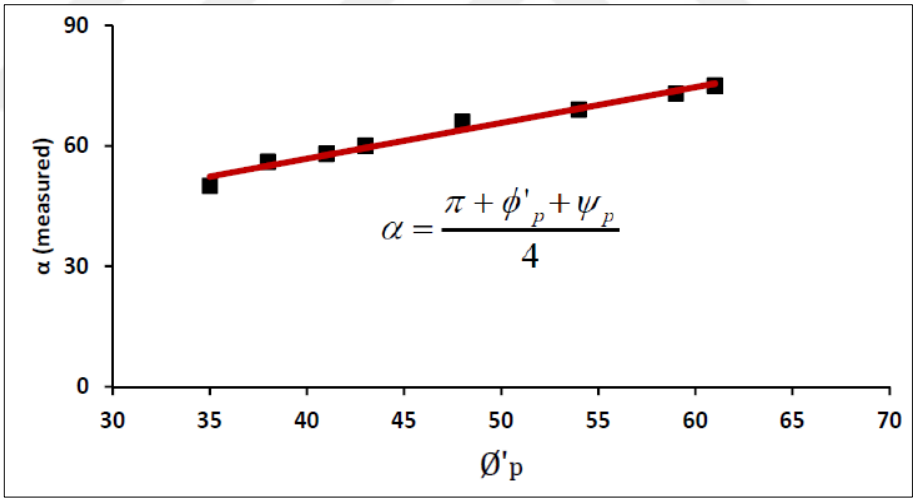


Figure 2.26. Variation of α with $\emptyset'_p$ as obtained from model test results (Vardoulakis, 1980).

These results fit well with the proposal that when dilatant behavior increases, the strength of the granular soil also increases.

Finally, the actual failure surface geometries obtained by PIV analysis is compared with the proposed geometrical correlation and existing Tsagareli (1965) and Arthur *et al.*, (1977) correlation in literature (Figure 2.27).

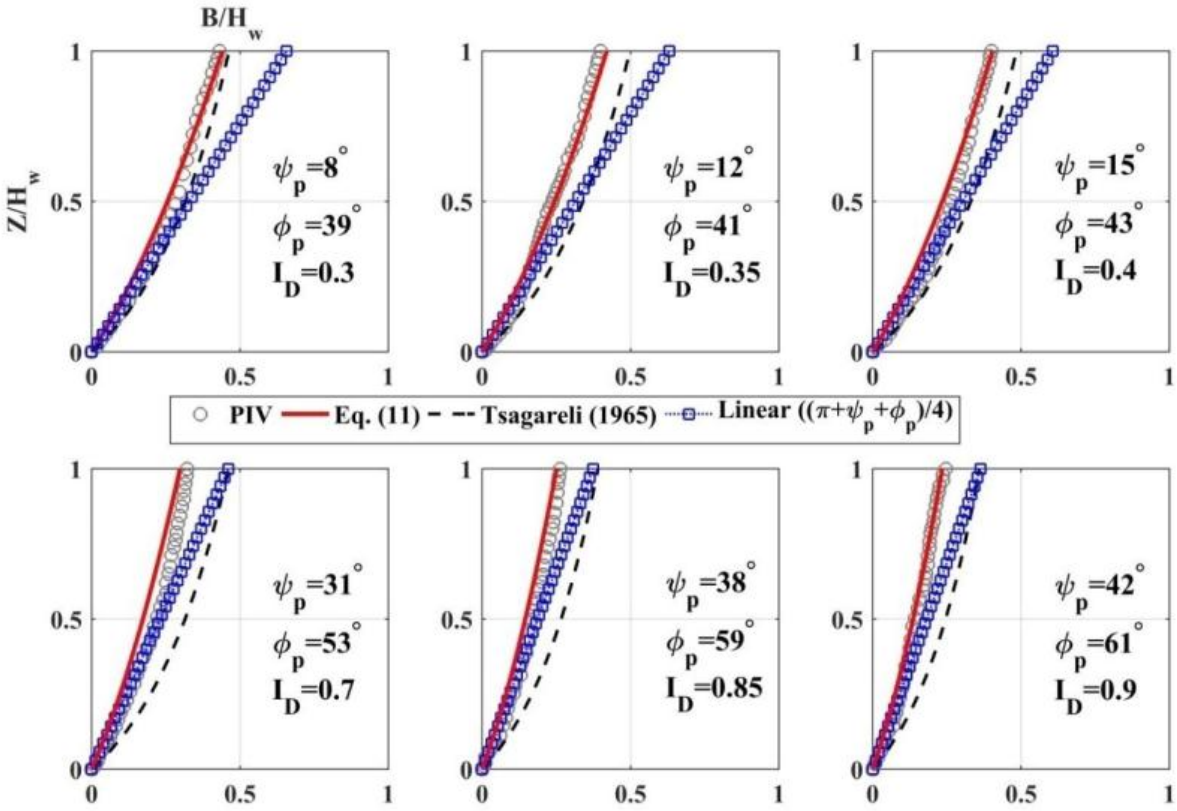


Figure 2.27. Comparison of estimated and experimentally visualized failure surfaces (Altunbas *et al.*, 2017).

As a result, researchers proposed that their proposed equation is valid for actual failure surface geometry evaluation behind any retaining wall translating laterally through active side. However, their research had some assumptions:

(i) No surcharge pressure was applied during physical model experiments, hence influence of high stress state into dilatant behavior was not considered.

(ii) Research was conducted with a single type of granular soil. Therefore, effect of macro-scale soil properties such as grain shape, size and granulometry which are variables for different sands could not be investigated.

Consequently, in order to enhance the applicability of the proposed equation, further experimental research is needed with different granular soil types and under high effective stresses. This would stand out as one of the research objectives of this thesis.

3. METHODOLOGY

3.1. Scope of the Research

The aim of this PhD research is to investigate experimentally the coupled influence of grain size, shape and loading condition on stress-dilatancy behaviour and the shear band geometry evaluation of granular soils, and propose unique correlations between physical grain properties and stress-dilatancy parameters. In addition, it is aimed to enhance the existing geometrical formulations which were proposed to formulate failure surface geometries. Literature review revealed that wall friction, soil arching, and dilatancy were the main properties which affect soil strength and therefore played a key role on formation of shear bands behind retaining walls. Wall friction and arching are physical effects and can be eliminated during experimental study. However, dilatant behavior is an intrinsic soil property and is influenced by many micro and macro scale effects. Existing correlations available in literature are based on experimental studies which do not comprise the combined influence of all these variables.

In order that the proposed functions in this research would be more applicable, all known variables which influence dilatant behavior were considered in the physical model generated during this study. The variables investigated in this research thesis which influence dilatancy and shear band formation are summarized below.

(i) Influence on stress-dilatancy relationship:

For Bolton (1986) stress-dilatancy correlation,

- Influence of grain shape
- Influence of granulometry
- Influence of stress path

(ii) Influence on $\phi_p' - \psi_p'$ relationship:

- Influence of grain shape
- Influence of granulometry
- Influence of stress path

(iii) Influence on failure surface geometry:

- Characteristics of shear bands
- Investigation of shear band evaluation
- Calculation of lateral earth pressure coefficients

(iv) Influence of soil properties such as,

- Friction angle
- Dilatancy
- Gradation
- Grain shape

The range of the proposed equations available in the literature are limited, because previous research did not consider the coupled effect of macro scale physical soil properties on all the above mentioned subjects. Therefore, the initial approach in this study was to expose the limitation of existing theories by conducting several triaxial tests and physical retaining wall model tests to reveal stress-dilatancy constants and actual slip surface geometries of tested granular materials. The next aim of the study was to extend the range of existing correlations which calculates the strength-dilatancy parameters and coordinates of the slip surface geometries by modification of existing equations. Therefore, an extensive testing program was established. The mechanical properties of the granular soils such as peak dilatancy and friction angle were determined for each test. 80 drained and K_0 consolidated triaxial tests were conducted at geotechnical laboratory in order to calculate the coefficients which define the dilatant behavior of tested soils. Stress path tests (axial compression and lateral extension) were conducted to expose the effect of loading condition

on peak states and dilatancy. Physical model tests were conducted on a wide variety of sand types consisting of distinct grain shapes and grain sizes. Model experiments were performed with backfill soils under different relative densities and surcharge pressures. The actual shear band formations and failure surface geometries behind retaining wall were revealed by particle image velocimetry (PIV) method.

An extensive literature review was implemented before commencement of laboratory experiments in order to drive an effective procedure for defining the scope and aim of the research. First, it was crucial to totally eliminate the arching effects in the physical model which influences slip surface geometry behind retaining walls as proposed by Salgado (2003) and Rao *et al.* (2015). The physical model width was selected to be wide enough to avoid soil arching. In addition, lubricant silicon grease was applied on both model walls and frame and polyethylene sheets were used at both side walls in order to minimize interface friction which also influences the shear band evaluation. Using this methodology, in this study it was aimed that the only remnant parameter which would affect the evaluation of the shear band geometry would be the dilatant behavior.

Critical state strength of a soil is independent from the loading condition, density and vertical stress; it only changes with mineralogical composition of soil grains and grain characteristics (grain size, shape, distribution). Eventually only different types of sand expose different critical state strengths. Therefore, the only parameter affecting the peak strength of a particular granular soil is its interparticle locking and dilatant behavior. Thus, by changing the factors for a specific sand which can affect its dilatant properties such as relative density, vertical stress, loading condition; validity of a stress-dilatancy relationship can be investigated and its strength properties can be evaluated. It is empirically proven that dilatancy is independent from the stress-history of a granular soil (Abadkon, 2012); maximum dilatancy rate does not change whether a soil is normal consolidated or over-consolidated, therefore in this research investigation of the effect of stress-history on maximum dilatancy was neglected.

On the other hand, soils of distinct mineralogical composition possess different critical strengths. In addition, the contribution of their dilatant behavior to strength is different due to variability in grain size and shape. For example, types of sand consisting of more angular

particles are more suitable for packing and expand more volumetrically, exposing higher dilatancy and consequently higher peak strengths. Therefore, their peak strengths are both a function of grain size and shape as well as their relative density, stress state, and loading condition. Hence, validity and applicability of any proposed stress-dilatancy equation is questionable in case it does not consider grain size and shape effects.

Investigating and analyzing the influence of all these parameters separately is rather difficult by triaxial testing. The reason is that the observation of the evaluation of strain localization, discontinuities and shear zones in triaxial apparatus is not accurate due to the effect of grain characteristics on dilatant behavior. Hence, a more proper and accurate way to observe the influence of dilatancy on shear band characteristics is to use physical models where any change in the stress state of the soil can be associated with the lateral transition of a model retaining wall. In this way, strength properties of a granular soil evaluated by triaxial testing can be linked with the evaluation of the geometry of shear bands forming behind the retaining wall during wall transition at the failure state. Provided that soil arching and wall friction are prevented, the proportional relationship between the dilatant behavior of the backfill soil in the physical model and the triaxial apparatus will reveal the validity of proposed stress-dilatancy correlation by physical modelling.

Finally, testing with different graded soils which consist of same mineralogical composition of soil grains or testing with soils having different grain shape but similar grain size distribution will separately reveal the influence of grain size and shape into the dilatant behavior. Accordingly, the effect of grain size, shape and gradation should be represented by a soil-specific constant to any stress-dilatancy relationship available in the literature, which is one of the major research objectives of this study.

As mentioned, dilatancy is influenced by soil macro and micro mechanical properties. Relative density, stress state, grain size, grain shape, and loading condition are the major parameters which control the dilatant behavior. Therefore, the experiments in this PhD research considered all these variables as a function of dilatancy angle evaluation. Items presented below summarize the methods followed in this thesis to embody all mentioned soil parameters:

(i) The experiments were conducted with three different clean sands and glass beads which contained different grain characteristics so that their particle shapes differ from each other.

(ii) The gradation of the sands were calibrated so that their D_{50}, C_u and/or C_c values were compatible with each other. e.g. sands of same mineralogical composition, but different grain size distribution were used to investigate the effect of grain size on dilatancy.

(iii) Glass beads of 400-600 μm grain size range were used in shear tests and physical model experiments which were totally circular and spherical so that their mechanical behavior would be comparable with other tested sands consisting of varying grain shapes. As a result, the influence of grain shape at dilatant behavior was analyzed.

(iv) CK_oD Triaxial tests were conducted under varying relative density and confining pressures to derive stress-dilatancy coefficients such as Q, R, r and ϕ'_{cs} according to proposed up-to-date stress-dilatancy equations.

(v) CK_oD Triaxial stress path tests (AC and LE) were conducted to investigate the influence of loading condition on stress-dilatancy parameters and critical state friction angle.

(vi) Physical model experiments on granular soils were conducted under equal relative density and surcharge ranges in order to reveal the macro mechanical properties on soil strength evaluation. e.g. The difference in shear band geometries of the sands and glass beads having different grain size and/or grain shape tested in the same initial density and surcharge value exposed the effect of macro scale soil properties on soil dilatancy.

3.2. Research Objectives and Approach

The first objective of the research is to propose new correlations to calculate line-fitting parameters of existing stress-dilatancy theories and strength-dilatancy relationship

from physical properties of granular soils to enhance applicability of existing equations. Therefore all the impacts on dilatant behavior were examined by conducting triaxial tests; relative density, confining pressure, grain size, grain shape, grain distribution and loading condition. Triaxial tests revealed the influence of preshear physical soil properties and loading conditions on dilatant behavior of granular soils.

The second objective of the research is to propose an equation which defines the coordinates of any point located on the shear band geometry generating behind the retaining wall. For this purpose, small-scale physical retaining wall model tests in 1G conditions were conducted. Physical model consisted of pressure transducers which measured the vertical and horizontal stresses through initial (K_o) and active failure (K_a) state. Failure surfaces were generated, and the shape and geometry of shear bands at failure were exposed which corresponded to different dilatancy angle values of soils by particle image velocimetry (PIV) analysis. Therefore, physical model tests disclosed the effect of dilatancy on engineering properties of soils at failure state. As a result, a relationship between preshear physical soil properties and engineering properties at failure were generated by utilization of empirical coefficients which include density, confining pressure, grain size, and shape. In addition, verification of proposed correlations under different loading conditions was provided.

Hence; the research approach consisted of a wide range of laboratory experiments. These included several triaxial shear tests for discrete sands of varying grain shapes under different stress paths and small-scale physical retaining wall model tests to evaluate the dilatant effect on slip surface geometry. For both tests, getting precise data at failure state was important. Accordingly, the work plan was divided into three main categories:

(i) Finding and bringing sands to geotechnical laboratory from different sand pits located at Istanbul province and implementing laboratory tests to evaluate their physical properties such as minimum and maximum void ratio, specific gravity, shape factors (circularity and roundness), grain size distribution and mineralogical composition. It was crucial that physical and mechanical properties of these sands differed from each other so that experimental work would cover a wide range of soil parameters. Care had to be given that sand samples were clean, free of fines and gravel so that the results were not affected.

(ii) Conducting K_o consolidated and drained tests (CK_oD) on the sand specimens under 2 different stress paths: AC (axial compression) and LE (lateral extension). At each stress path, the variables would be the relative density range and confining pressure. Table 3.1 below gives a summary of proposed testing program for each stress path. A relative density range was achieved instead of a specific relative density value due to the fact that obtaining equal density value for each sand was very difficult due to lack of accuracy in air pluvation method. The confining pressures were selected in a wide range so that the results did interfere with each other. In addition, very high confining stress ranges were avoided to prevent particle crushing during shearing because particle crushing affect the dilatant behavior of soils.

(iii) Physical model tests representing a soil element on the active side of a retaining wall. The tests would be conducted under varying relative densities and vertical stresses. Vertical and horizontal pressure sensors would measure the stresses on the soil element during wall displacement and when vertical loading or unloading was applied to sample via pistons located at the top of the model. To represent a stressed soil element behind a retaining wall, pressure would be applied to specimen prior to testing. Physical model tests were conducted by moving the retaining wall laterally with a measurable speed so that active failure on the shear band could be visualized. All the testing would be recorded by a digital camera, and by a program which could read and save the data received by the pressure transducers. At the end of the test, the shear band mobilized by the failure of the specimen with the wall movement or external loading would be obtained. The geometry of the shear band at failure by the GeoPIV-RG program would be interpreted to determine the difference in shear band shapes of the sand types under different dilatancy values. It would not be possible to apply more than 150 kPa surcharge pressure on backfill material due to the limit of the pneumatic pistons.

In conclusion, in this PhD research it is aimed to propose:

- Unique correlations to calculate stress-dilatancy correlation and strength-dilatancy correlation coefficients from initial physical properties of granular soils.

- A geometric equation which defines the coordinates of any point located on the shear band geometry generating behind the retaining wall.

Table 3.1. Relative density and vertical confining stress ranges for drained triaxial tests.

Relative Density Range (%)	Vertical Confining Stress Variables
35 – 45 (loose)	50 kPa, 150 kPa, 250 kPa, 300 kPa
55 – 65 (medium dense)	50 kPa, 150 kPa, 250 kPa, 300 kPa
75 – 90 (dense)	50 kPa, 150 kPa, 250 kPa, 300 kPa

3.3. Determination of Physical Soil Properties

Within the scope of the PhD project, four types of granular material were gathered in soil mechanics laboratory. General view of the tested soils are given in Figure 3.1 below.

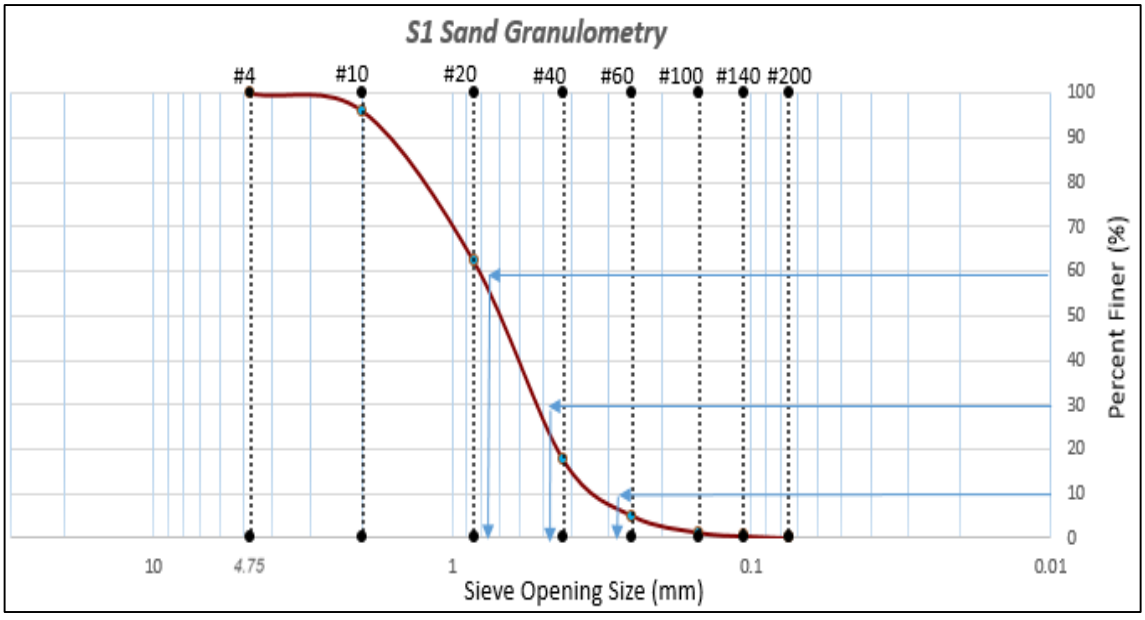


Figure 3.1. View of tested granular soils: S1, S2, S3 sand and GB.

Sand samples were taken from sand pits located at different provinces of Istanbul. Moreover, GB with 400-600μm grain size range were taken from a glass workshop. The granular soils were washed initially to be removed from dust, dirt, and cohesive material. The sand samples were named as S1 (Şile Sand), S2 (Çerkezköy Sand), S3 (Kilyos Sand) and GB (Glass Beads) respectively. To obtain different granulometry, S2 was separated into its grain sizes as determined by ASTM D422-63 standard. Next, two different gradations were composed by adequate portioning of its grain size weights as well graded S2 (SW-S2) and poorly graded S2 (SP-S2).

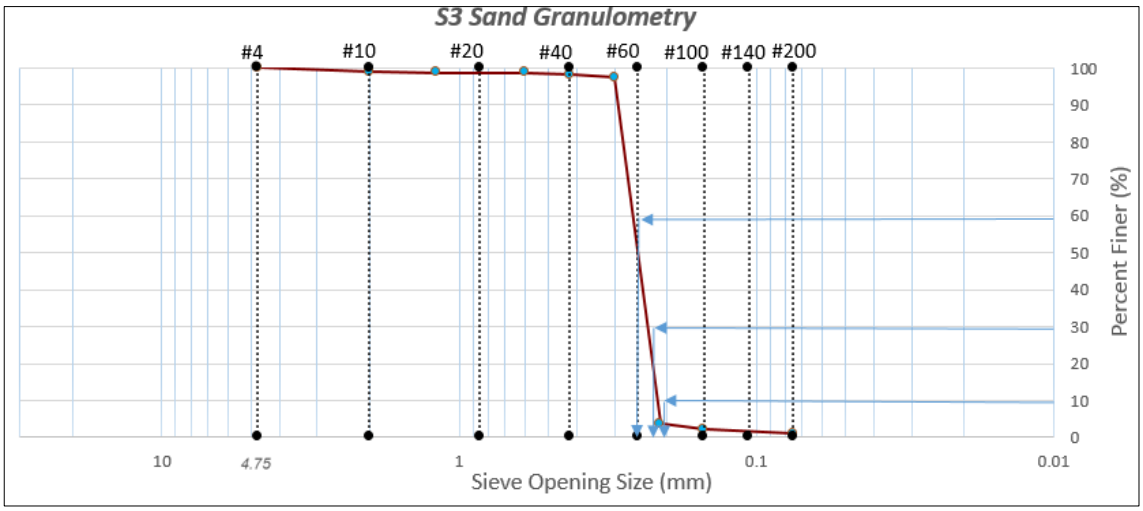
3.3.1. Index Properties of Soils

Sieve analysis was conducted to determine the grain size distribution of the tested soils. Index density tests, specific gravity tests were conducted to detect e_{max}, e_{min}, G_s values for each sand. ASTM standards of D854-14, D4253-00 and D4254-00 were used as references. After sieve analysis, uniformity coefficient (C_u), gradation coefficient (C_c), median particle size (D_{50}) values were calculated. Grain size distribution of the sand types are given in Figure 3.2.

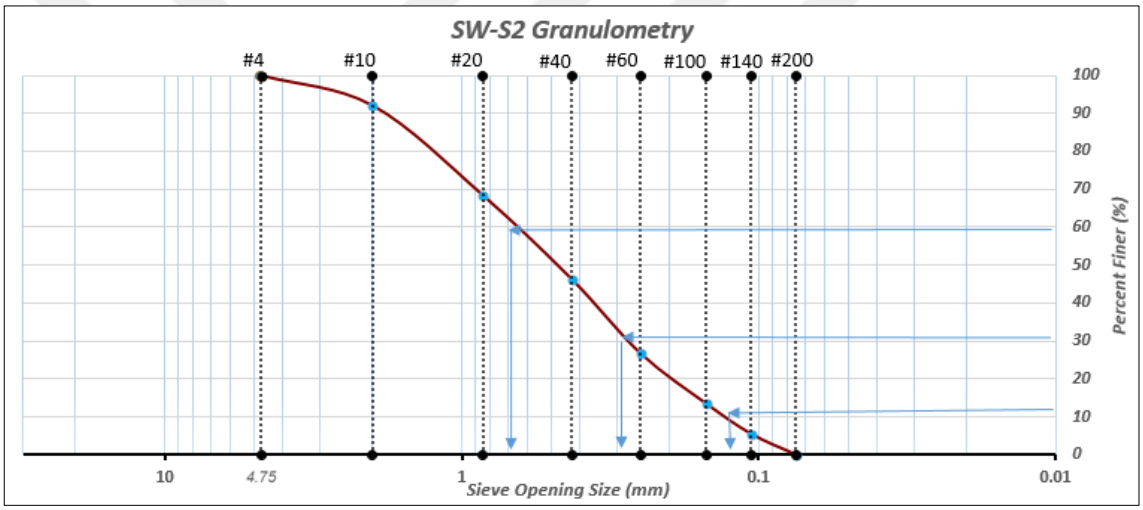


(a) S1 Sand

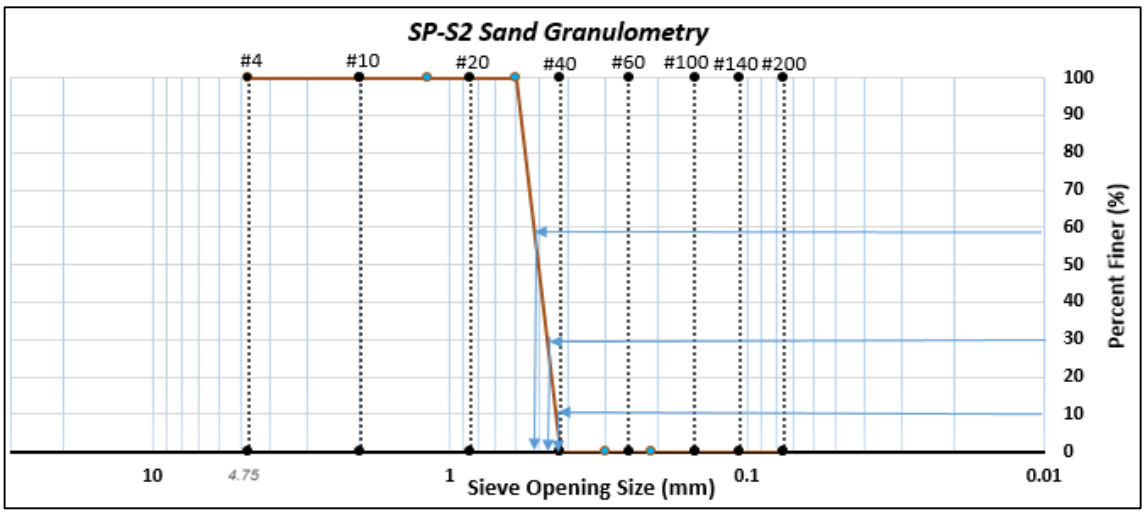
Figure 3.2. Grain size distributions of the granular soils used in the research.



(b) S3 Sand

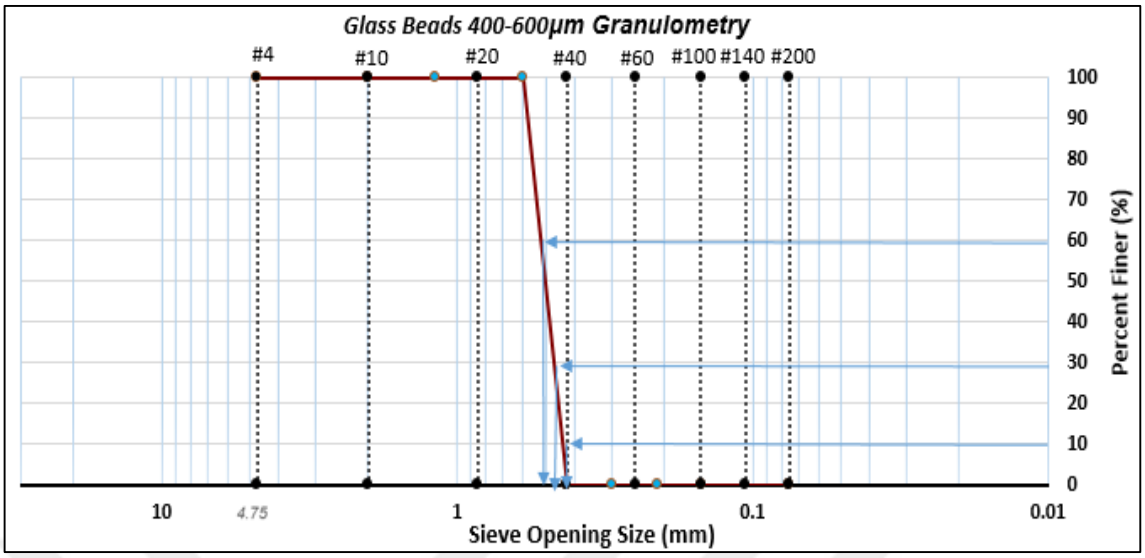


(c) SW-S2 Sand



(d) SP-S2 Sand

Figure 3.3. Grain size distributions of the granular soils used in the research (cont.)



(e) GB Sand

Figure 3.4. Grain size distributions of the granular soils used in the research (cont.)

According to their C_c and C_u values, S1 and S3 sands are poorly graded. However, S1 sand has a more variety of grain distribution and is used as concrete aggregate. S1 sand is completely quartz, and gray-brownish in color. S3 sand is a beach sand and is uniform graded. S3 sand is brown-yellowish colored, and its mineralogical composition is of predominantly quartz origin. However, it also consists of sandstone and andesite. GB are also uniformly graded. S2 is light greenish gray colored, consisting of subangular-subrounded grain shapes. Mineralogical composition of S2 is a mixture of quartz-sandstone-claystone origin where quartz is dominant, and all the bedrocks were subjected to several phases of metamorphism and deformation. S2 was separated into its all grain sizes between passing No.4 and retaining No.200 grains by sieve analysis, and two different graded S2 were comprised. First one is totally uniformly graded; only consisting of sand grains passing No.40 sieve and retained on No.60 sieve. Second one consists of all its grain sizes with selected weights so that a well-graded granulometry is achieved.

As a result, mineralogical composition of all granular materials used in research were dominantly quartz.

3.3.2. Grain Shape Properties

To determine the average grain shape characteristics of the sands, pictures of the grains were taken by an Mshot brand, MD50 model digital microscope camera (Figure 3.3). Next, the pictures were analyzed using ImageJ software to evaluate the sphericity and roundness values of the grains. The pictures were transferred into black & white color in order to be analyzed by ImageJ program (Figure 3.4).



Figure 3.5. View of digital microscope and a picture of the grains taken by Mshot camera.

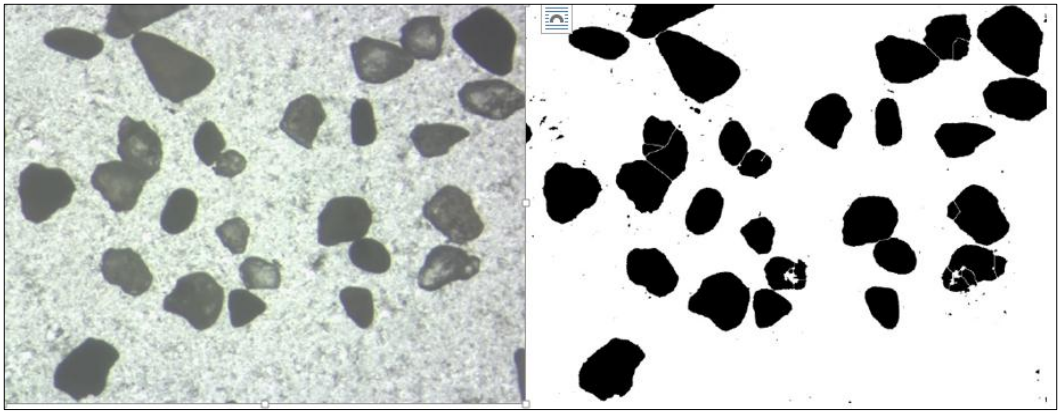
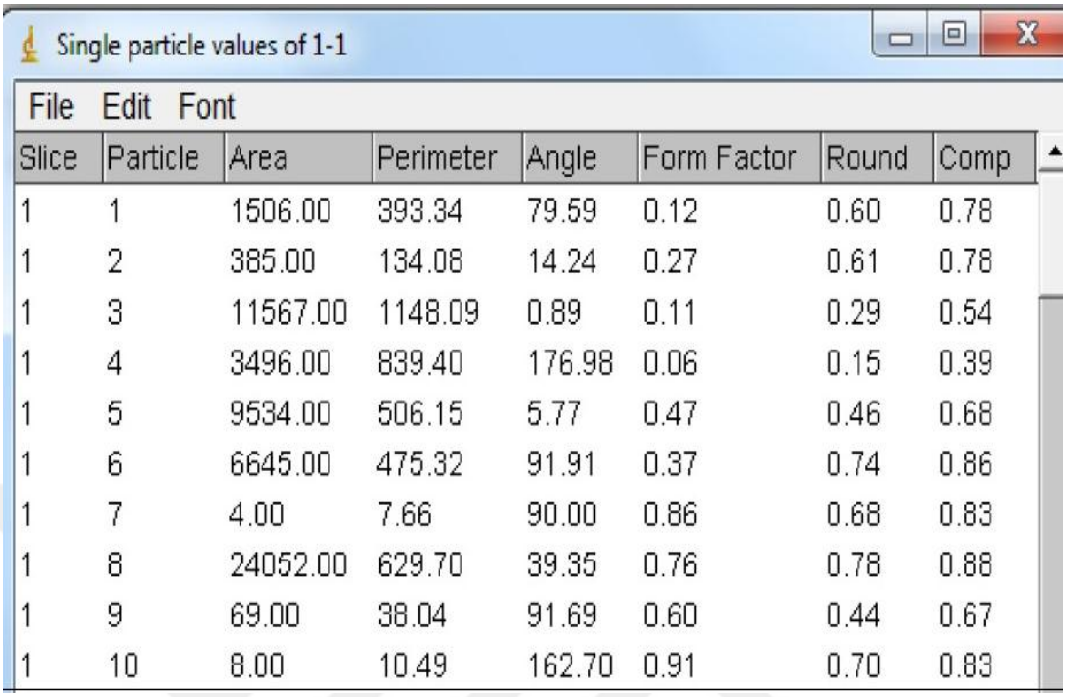


Figure 3.6. Transformation of pictures into black & white color.

ImageJ program automatically detects and calculates the area, perimeter and roundness of the grain particles within the monochrome picture (Figure 3.5).


Single particle values of 1-1

File Edit Font

Slice	Particle	Area	Perimeter	Angle	Form Factor	Round	Comp
1	1	1506.00	393.34	79.59	0.12	0.60	0.78
1	2	385.00	134.08	14.24	0.27	0.61	0.78
1	3	11567.00	1148.09	0.89	0.11	0.29	0.54
1	4	3496.00	839.40	176.98	0.06	0.15	0.39
1	5	9534.00	506.15	5.77	0.47	0.46	0.68
1	6	6645.00	475.32	91.91	0.37	0.74	0.86
1	7	4.00	7.66	90.00	0.86	0.68	0.83
1	8	24052.00	629.70	39.35	0.76	0.78	0.88
1	9	69.00	38.04	91.69	0.60	0.44	0.67
1	10	8.00	10.49	162.70	0.91	0.70	0.83

Figure 3.7. Determination of geometrical properties of soil grains by ImageJ.

Sphericity (S) and roundness (R) values were calculated by the given equation using the geometrical properties by ImageJ program:

$$S = \frac{4\pi A}{P^2} \quad \text{and} \quad R = \frac{4A}{\pi L^2} \tag{3.1}$$

In the equations P is the grain perimeter, A is the grain area and L is the length of the main axis of the grain.

A total of 50 Mshot pictures of the grains which were selected from separate sections of the sand samples were taken by camera so that an average shape factor value could be determined for each sand. The average sphericity and roundness values were calculated for S1, S3 and S2 sands and are given in Table 3.2.

Table 3.2. Average sphericity and roundness values of the soil grains for each sand

Sand Type	Ave. Sphericity (S_{ave})	Ave. Roundness (R_{ave})
S1	0.551	0.757
S3	0.743	0.759
S2	0.569	0.741
GB	1.000	1.000

Krumbein and Sloss (1963) proposed a chart of roundness and sphericity values in the range of 0-1 based on laboratory anaysis (Figure 3.6).

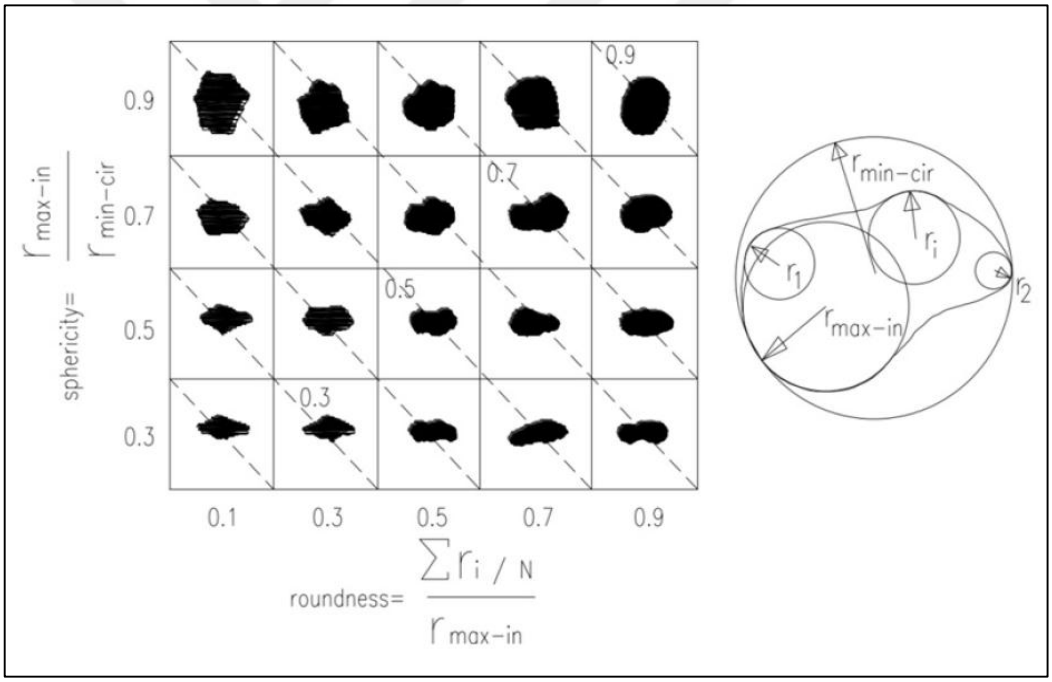


Figure 3.8. Sphericity – Roundness chart proposed by Krumbein and Sloss (1963).

Acccording to grain shape values and the chart, S3 sand is the poorest graded soil, consisting of the roundest and most circular grains, and is a beach sand. Adversely, S1 and S2 particles are more angular. S1 sand comprises wider assortment of particle sizes and is being used as a concrete aggregate. S1 and S2 sands have similar grain shapes but their grain size distribution and median particle sizes (D_{50}) are pretty different. On the other hand, poor

graded S2 and GB have totally the same grain size distribution, however the grain shape factors are different. GB are totally circular and sphere, therefore their dilatant behavior while shearing will be a good comparison of the influence of grain shape with soils consisting of angular grains. Results reveal that most sphere and round GB have lowest e_{max} and e_{min} values as proposed by Cho and Santamarina (2006). Table 3.3 below summarizes the obtained physical parameters of the tested granular soils.

Table 3.3. Physical properties of the S1, S2, S3 sands and GB

Property	**SW S2**	**S1**	**SP S2**	**S3**	**GB**
Classification	SW	SP	SP	SP	SP
Median Particle Size (D_{50})	0.48	0.71	0.60	0.26	0.50
Uniformity Coefficient (C_u)	6.00	2.80	1.43	1.24	1.23
Coefficient of Gradation (C_c)	1.08	1.12	0.94	0.97	0.89
Specific Gravity (G_s)	2.62	2.61	2.62	2.66	2.45
Maximum Void Ratio (e_{max})	0.77	0.78	0.92	0.77	0.67
Minimum Void Ratio (e_{min})	0.38	0.52	0.56	0.44	0.34
Average Sphericity (S_{ave})	0.569	0.551	0.548	0.743	1.000
Average Roundness (R_{ave})	0.741	0.757	0.718	0.759	1.000

3.4. Determination of Mechanical Soil Properties

To determine the mechanical properties of the granular soils investigated within the research, consolidated and drained (CD) triaxial shear tests were conducted. GEOCOMP Triaxial testing device was used to conduct triaxial tests under K_0 conditions for S1, S2, S3 sands and GB following the ASTM-D7181 standard. Figure 3.7 presents the overview of triaxial testing apparatus. In the field, under vertical stress horizontal displacements are relatively small in comparison with vertical displacements. Hence, in order to represent the field conditions, specimens were consolidated under K_o conditions, coherent with the oedometric state. Specimens were prepared under different initial relative densities and were consolidated under varying confining pressures. Moreover tests were conducted under two stress paths; axial compression (AC) and lateral extension (LE), respectively. In this way,

the coupled influence of density and pressure on the strength of sand samples were observed within two different loading conditions.



Figure 3.9. Triaxial tests under K_o conditions.

In this study an experimental testing program was followed to calculate the dilation ratio affecting the soil strength for S1, S2, S3 sands and GB respectively. Table 3.4 below summarizes the triaxial testing program for the sand samples.

Table 3.4. Testing program for sand specimens

Test No	Soil Type	Stress Path	Consolidation Pressure (σ'_3)	Relative density (I_D) (%)
1	S1 Sand	AC	150	40
2	S1 Sand	AC	250	32
3	S1 Sand	AC	300	29
4	S1 Sand	AC	250	45
5	S1 Sand	AC	150	67
6	S1 Sand	AC	300	50
7	S1 Sand	AC	150	74
8	S1 Sand	AC	150	50
9	S1 Sand	AC	250	73
10	S1 Sand	AC	300	83
11	S1 Sand	AC	50	37
12	S1 Sand	AC	50	85
13	S1 Sand	LE	150	38
14	S1 Sand	LE	150	53
15	S1 Sand	LE	250	37
16	S1 Sand	LE	250	57
17	S1 Sand	LE	300	51
18	S1 Sand	LE	150	66
19	S1 Sand	LE	250	65
20	S1 Sand	LE	300	65
21	S1 Sand	LE	150	84
22	S1 Sand	LE	250	57
23	S1 Sand	LE	250	88
24	S1 Sand	LE	300	39
25	S1 Sand	LE	150	94

Table 3.4. Testing program for sand specimens (cont.)

Test No	Soil Type	Stress Path	Consolidation Pressure (σ'_3)	Relative density (I_D) (%)
26	S1 Sand	LE	300	92
27	S3 Sand	AC	50	59
28	S3 Sand	AC	300	55
29	S3 Sand	AC	250	43
30	S3 Sand	AC	250	24
31	S3 Sand	AC	150	75
32	S3 Sand	AC	250	60
33	S3 Sand	AC	150	56
34	S3 Sand	AC	150	34
35	S3 Sand	AC	300	45
36	S3 Sand	AC	150	43
37	S3 Sand	AC	300	32
38	S3 Sand	AC	250	60
39	S3 Sand	AC	150	60
40	S3 Sand	LE	150	43
41	S3 Sand	LE	150	57
42	S3 Sand	LE	150	69
43	S3 Sand	LE	250	37
44	S3 Sand	LE	250	58
45	S3 Sand	LE	250	72
46	S3 Sand	LE	300	40
47	S3 Sand	LE	300	60
48	GB	AC	50	30
49	GB	AC	150	30
50	GB	AC	300	30
51	GB	AC	50	46
52	GB	AC	400	33
53	GB	AC	150	25
54	GB	AC	50	17

Table 3.4. Testing program for sand specimens (cont.)

Test No	Soil Type	Stress Path	Consolidation Pressure (σ'_3)	Relative density (I_D) (%)
55	GB	AC	150	48
56	GB	AC	300	46
57	GB	AC	50	48
58	GB	AC	50	28
59	GB	AC	300	20
60	GB	LE	150	30
61	GB	LE	50	30
62	GB	LE	300	30
63	GB	LE	50	48
64	GB	LE	150	45
65	GB	LE	300	46
66	SW-S2	AC	50	46
67	SW-S2	AC	150	51
68	SW-S2	AC	50	21
69	SW-S2	AC	300	46
70	SW-S2	AC	150	25
71	SW-S2	AC	300	25
72	SW-S2	AC	150	72
73	SW-S2	AC	300	72
74	SP-S2	AC	50	43
75	SP-S2	AC	50	57
76	SP-S2	AC	20	58
77	SP-S2	AC	50	70
78	SP-S2	AC	150	42
79	SP-S2	AC	150	70
80	SP-S2	AC	300	40

Consolidation pressures varied between 50 kPa and 300 kPa. Higher vertical effective pressures were inhibited to avoid any grain crushing during shear testing because this would effect grain size distribution of the specimens. Sieve analysis was conducted prior to testing and after testing to control if there was any change in soil granulometry, and in the end no major change was observed.

Test specimens were prepared using dry pluvation method so that different sand densities could be achieved (Figure 3.8). In this method, sand is dropped into the triaxial cell from varying heights but with a constant speed in order to control soil density. When the drop height is low, less sand volume is fit into the test chamber, so a looser soil density is achieved. After the cell is filled with sand, the total weight of sand filled into rubber membrane is calculated.

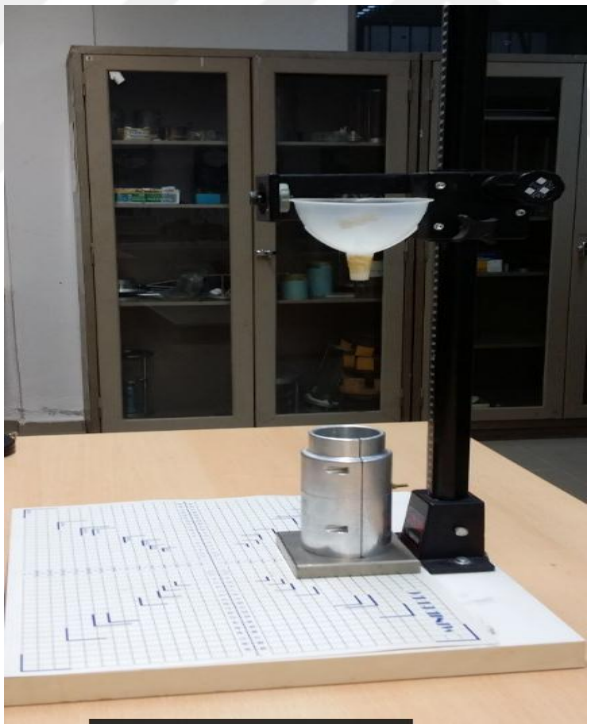


Figure 3.10. Equipment used in dry pluvation technique.

It is not possible to conduct a shear test with a disturbed dry granular soil due to lack of adhesion forces between soil grains. Therefore, to maintain stability of sand specimen prior to inserting into triaxial chamber, air inside the specimen was withdrawn by a vacuum pump so that the specimen remained stable after removal of side supports (Figure 3.9). Next,

the height and width of the test specimen was measured to calculate the unit weight and the initial void ratio for each specimen. Using these values the initial relative density of soil specimen was calculated and recorded for each test.

The second variable in triaxial testing program is the effective confining pressure (σ'_3) applied to the sample. Here, according to Mohr-Coulomb principle the specimen possesses lower internal friction angle under higher confining stresses:

$$\phi'_p = sin^{-1} \frac{(\sigma'_{1f} - \sigma'_{3f})}{(\sigma'_{1f} + \sigma'_{3f})} \tag{3.2}$$



Figure 3.11. View of the test specimen held stable by vacuum pump.

Therefore, triaxial test specimens were prepared with different initial density ranges and were consolidated under varying confining pressures.

The consolidated – drained triaxial tests were conducted following the saturation phase, consolidation and shearing phases respectively. Below is the summary of the procedure followed during triaxial testing and the interpretation of the sensor readings:

3.4.1. Saturation Phase

In laboratory conditions it is very difficult to create dry samples for shearing. It is known that (Schofield, 1968) sand specimens exhibit similar behavior with voids either completely empty or completely full of water, provided that drainage conditions are the same. Therefore, all the samples were saturated until Skempton parameter 'B' is equal or higher than 0.95. During the initialization phase, instead of air, the void spaces were filled by CO_2 to fasten the saturation process. CO_2 is more soluble than air, so the process of pore water entrance and fill to the voids of the specimen due to the pressure difference between pore and cell pressures is faster.

To saturate the specimen, initially 20 kPa of cell pressure was applied to deaired water inside the triaxial chamber. To avoid deformation of sample due to pressure variance, 10 kPa pore pressure was also applied inside the sample. Next, within 10 minutes interval cell pressure and sample pressure was increased by 10 kPa respectively in order to maintain the saturation phase until all voids were filled with deaired water (Figure 3.10).



Figure 3.12. Overview of triaxial sample during saturation phase.

3.4.2. Consolidation Phase

Several consolidated, drained triaxial tests were conducted in the geotechnical laboratory. To represent the site conditions, K_o consolidation was applied to specimens, because at in-situ conditions, under a vertical stress, the majority of deformations is vertical. Lateral deformations can be assumed zero since horizontally the field condition can be considered as oedometer testing. In triaxial conditions it is represented by maintaining the lateral strain (radial strain) in a minimal range of +-0.005 mm which is considered as zero. In the consolidation phase of the specimen, the total stress acting to the sample was increased. With increasing stress, the sample compresses, volumetric change occurs on the specimen, leading to increased volumetric strain ($\varepsilon_v=\Delta V/V$) and decreased void ratio. Height of sample also decreases, hence axial straining ($\varepsilon_a=\Delta L/L$) occurs within the specimen. However, radial strain $\varepsilon_r= (\varepsilon_v - \varepsilon_a)/2$ should be kept within the range of +-0.005 mm, so that axial and volumetric strains stand the same. To achieve this, automatically *GeoComp* triaxial software acts different stresses vertically and horizontally to the specimen.

During the consolidation phase, cell pressure was increased. The total increase on the cell pressure was equally the same as the increase on the horizontal effective stress since pore pressure is constant (the drainage valve is open). Cell pressure acted both vertically and horizontally to the specimen, applying an isotropic stress. In addition to this increase, a deviatoric stress (q) was also applied by the piston vertically so that the vertical stress become higher than the horizontal stress. This demonstrated the condition of a vertical load increase to an isotropically consolidating soil in the field. The sum of the vertical effective stresses of cell pressure increase and deviatoric pressure increase was the desired vertical effective stress value which was given as an input to the triaxial device. The proportion between vertical and horizontal effective stress increase had to be so accurate that the axial and volumetric strains were equal, so radial strain was zero. The ratio between these two was called the earth pressure coefficient at rest (K_0). Therefore, this precise work was automatically maintained by *GeoComp* triaxial software during testing.

3.4.3. Shearing Phase

During the shearing phase of the triaxial tests, the specimens were sheared with both AC and LE stress path respectively. During a LE test to keep vertical stress constant, GeoComp software automatically increases deviatoric stress in relation with the reduction in cell pressure value during shearing because any reduction in horizontal stress equally causes a decrease in vertical stress. During the shearing phase, effective deviatoric stress (q'=q) was applied vertically keeping horizontal stress (σ'_3) constant for axial compression (AC) stress path. Tranversely, during lateral extension (LE) stress path, horizontal stress was decreased while keeping vertical stress constant so that strains are tensile and specimen fails at higher deviatoric stress (q), but at lower mean effective stress (p'). The pictures of the failed samples after shearing phase are given in Figure 3.11.

$$q = \sigma'_1 - \sigma'_3 \tag{3.3}$$

$$p' = (\sigma'_1 + 2\sigma'_3)/3 \tag{3.4}$$



Figure 3.13. View of failed samples after shearing phase.

Sample p' – q relationship for consolidation and shearing phases are presented for AC and LE stress paths respectively in Figure 3.12. It is seen from figures that stress variance followed different paths for AC and LE tests until both reached to critical state line (CSL). Since 20 kPa of confining pressure (σ_3') was applied to specimens before replacing air in specimen voids with CO_2 during the saturation phase to avoid collapse of the specimen, mean effective stress values were not zero at the beginning of the consolidation phase.

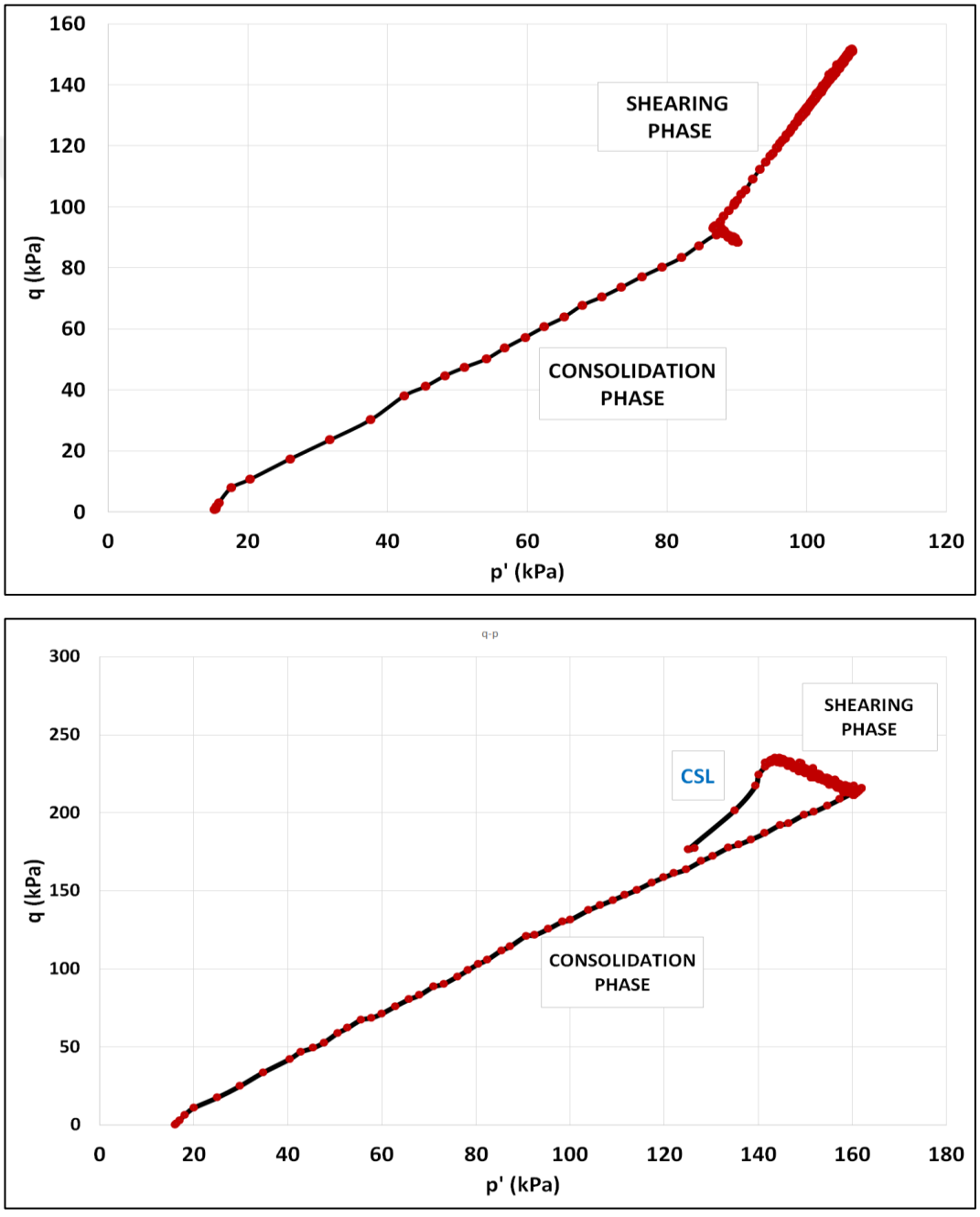


Figure 3.14. q – p relationship for AC and LE stress path.

3.5. Determination of Failure Surface Geometry

One of the major scope of this research is to visualize the influence of dilatant behavior on actual failure surface geometry. It is more accurate and widely accepted by researchers to observe shear bands and slip surfaces by digital photogrammetry. Due to its adequate size and convenient set-up, retaining wall models provide an easy method to visualize the failure strains on granular samples. For this reason for this research a physical model box representing 1g conditions had been manufactured. The physical model was composed of a rectangular, aluminum frame. The height of the frame was 20 cm, and the length was 25cm. Inside of the frame had empty space to fill the granular soil. The front and back walls of the frame were made from thick, transparent plexiglass so that the filled soil was visible. One side of the model was designed to act as a retaining wall which can translate laterally. The displacement of the wall was achieved by a manually rotating wheel attached on the wall and was displayed by a digital sensor. General view of the model box is shown in Figure 3.13.

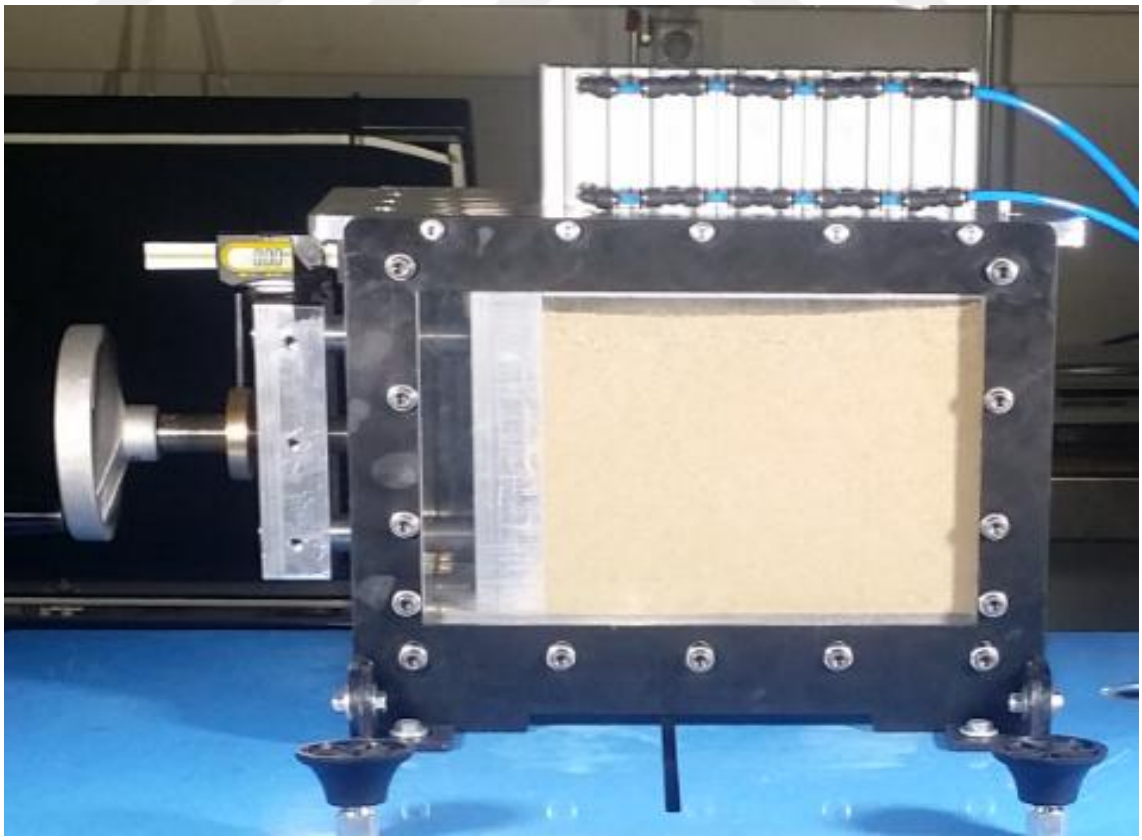


Figure 3.15. Front view of the physical retaining wall model.

On the top of the frame, there were five equally sized pneumatic pistons. These pistons were able to move vertically to compress the soil filled inside the box. They represented the surcharge pressure acting on a backfill soil behind a retaining wall insitu. There was a bar measure gauge behind the table which carries the physical model frame with a capacity of eight bars (Figure 3.14). This gauge was connected to the central air system which was supplied by a compressor by an air hose. Also, another air hose connected the gauge to pneumatic pistons.

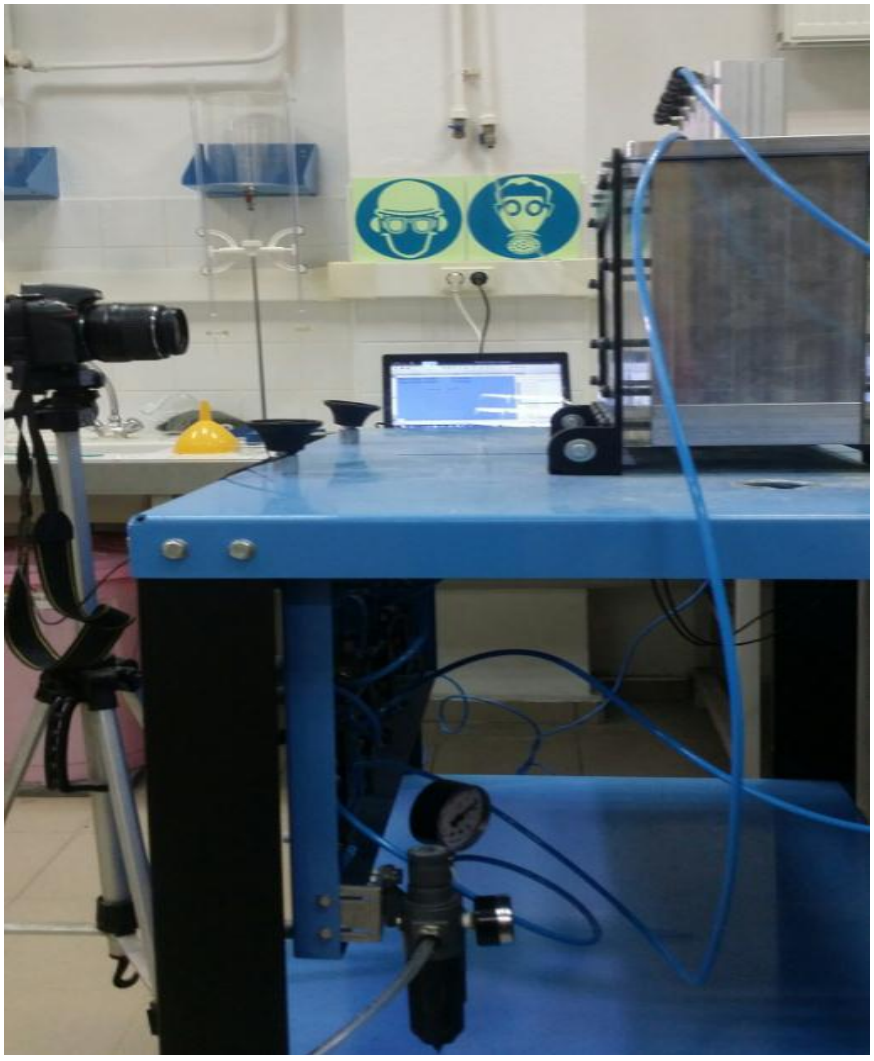


Figure 3.16. View of measure gauge and air hose connecting to pneumatic pistons.

There were two pressure sensors in the model box. One was situated at the inner central bottom of the frame and reads the vertical pressure. The other one was located in the middle of the retaining wall and reads the horizontal pressures (Figure 3.15).

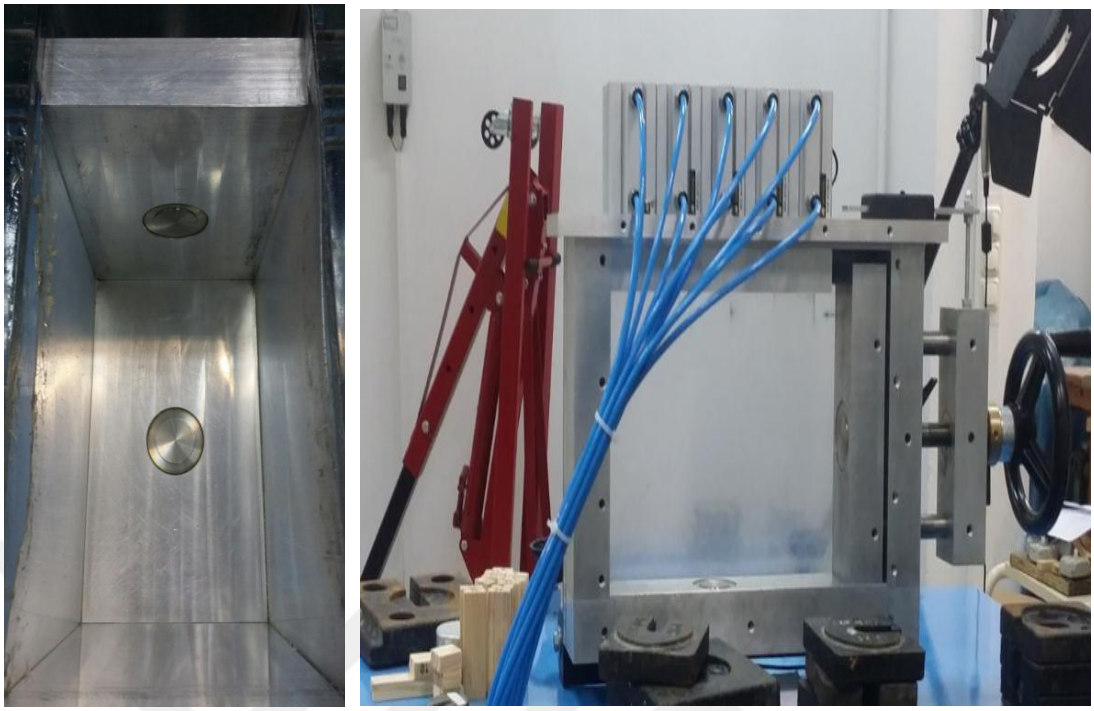


Figure 3.17. View of vertical and horizontal sensors in the model box.

The pressure sensors were connected to a software named as *IMC-Studio* where the time-pressure graphs could be generated and plotted. By this way, when the model retaining wall was laterally displaced through active failure side, the vertical and horizontal principle stresses generated on the tested soil were recorded from initial state until active failure state (Figure 3.16). The evaluation of stress states provided the researcher to calculate strength properties of the granular soil. Using the vertical and horizontal stress variables, deviatoric stresses ($q = \sigma'_1 - \sigma'_3$) were calculated and deviatoric stress – displacement graphs were plotted for each test (Figure 3.17).

The width of the pistons were designed to be 15 cm long in order to avoid any arching effect. To test the evaluation of arching mechanism, the applied surcharge pressure and the vertical pressures obtained via sensors were compared. Consequently, there were no stress loss due to arching within the tested soil, therefore it was proved that no arching mechanism occurs within the physical model while testing.

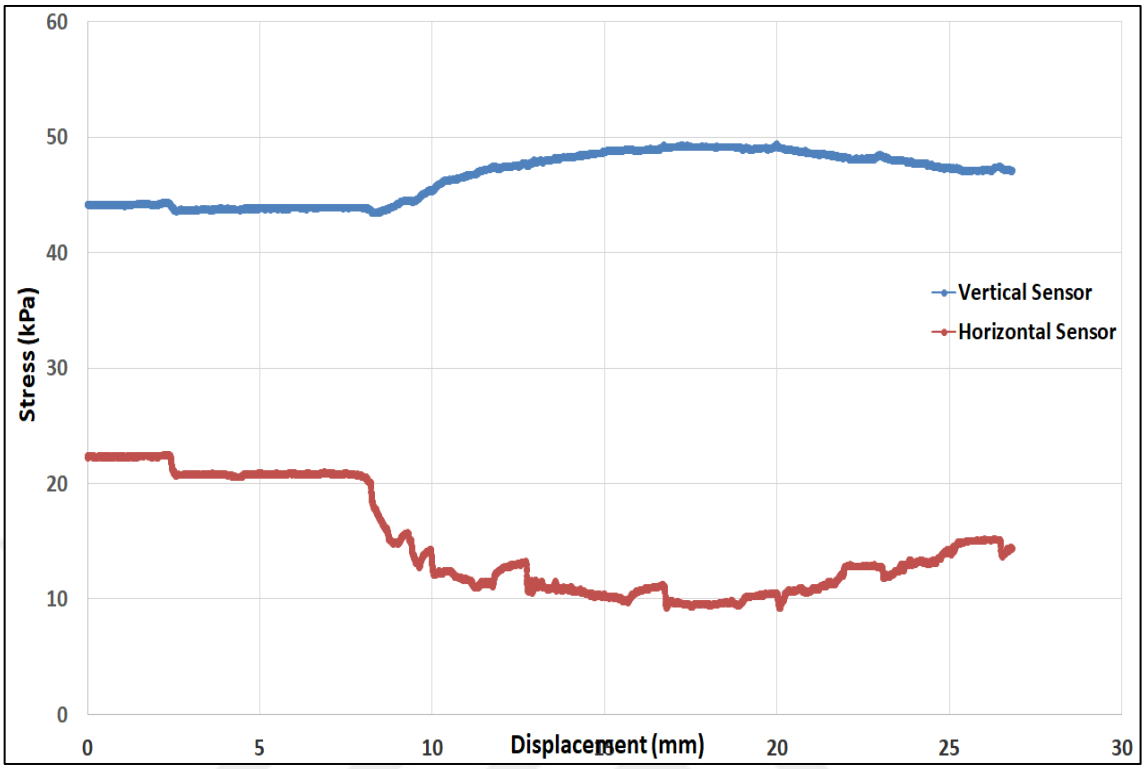


Figure 3.18. Plot of vertical and horizontal sensor readings through wall transition.

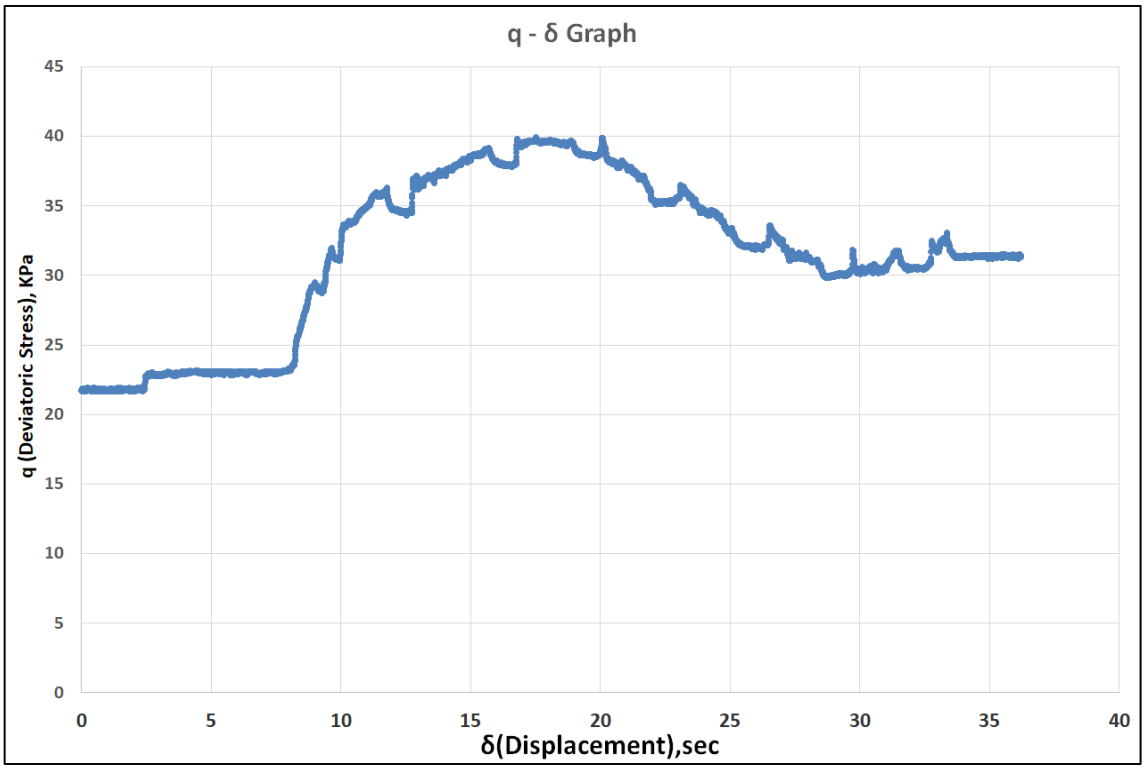


Figure 3.19. Plot of deviatoric stress – displacement graph during wall transition.

To avoid wall-soil interface friction which is also a property effecting the geometry of failure surface, transparent friction reducer lubricant was applied at all inner face of the frame prior to sand placement. Additionally, transparent high-density polyethylene sheets were used on side walls. Direct shear tests were conducted to investigate the effect of polyethylene sheets and silicon lubricant into friction (Figure 3.18). Tests indicated that friction angle between soil and wall averagely reduced from 22^0 to 11^0, therefore soil-wall friction was considerably reduced.

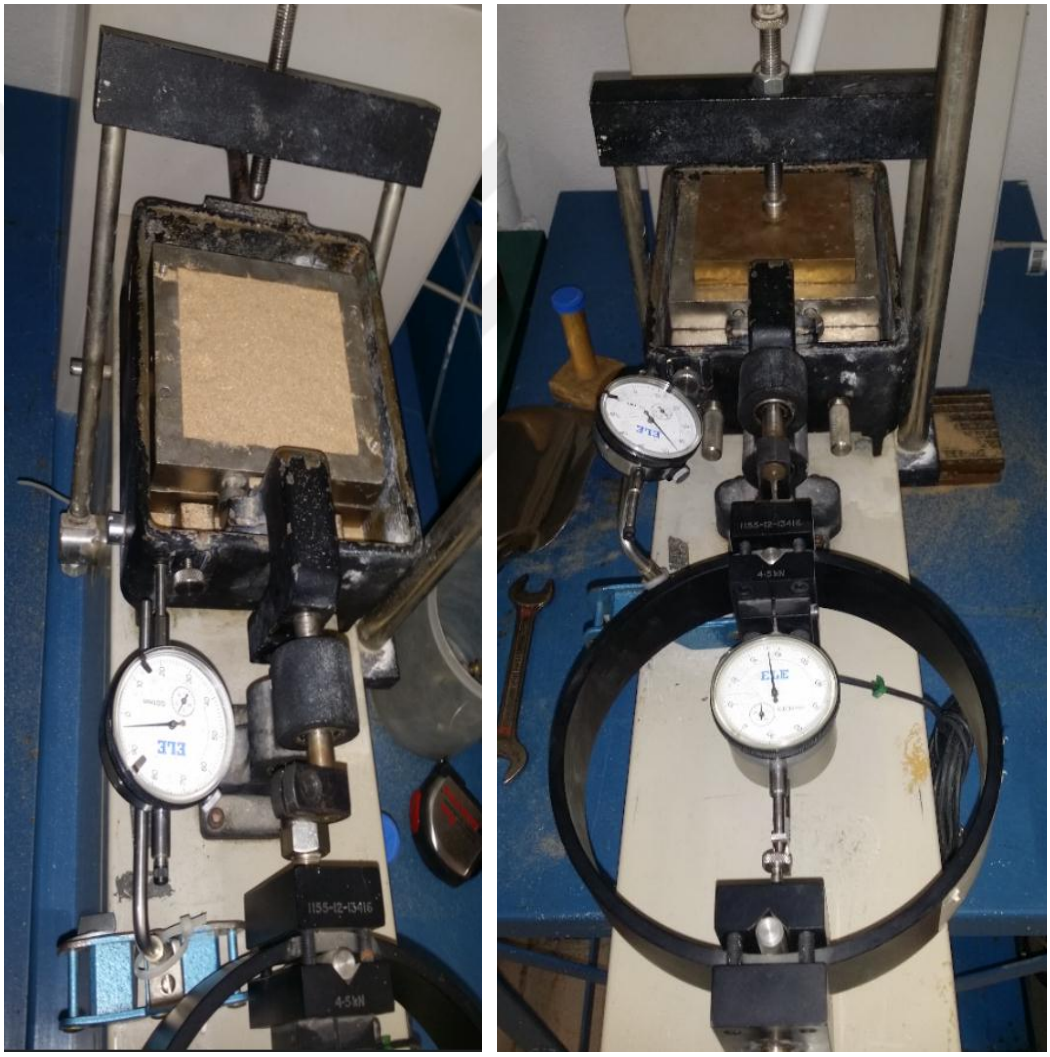


Figure 3.20. Direct shear tests to calculate internal friction between polyethylene sheet and granular soils.

Backfill soil was filled into the frame by air pluvation method so that different relative density ranges can be achieved for each test (D. Presti, 1992). In this method, to obtain

different sand densities, a hopper was used to fill the soil from varying height. To achieve the desired density, the falling height of sand during pluvation was adjusted. After filling, total mass of the granular soil and the volume of the filled area was measured to calculate the relative density of the backfill prior to testing. The relative density of the backfills (I_D) were determined by measuring total mass of the granular soil and the volume of the filled area prior to testing. Due to small model dimensions, it was assumed that dilatancy angle did not change with depth.

During the tests, the retaining wall was laterally displaced manually by the rotating wheel at a constant speed of 0.5 mm/s. During the wall transition, strain localization occurred within a shear band on the backfill soil. From the initial state until active failure state of the backfill, pictures were taken by a 6000 x 4000 high resolution digital camera settled on a tripod and by using a remote control for each 0.1mm of wall transition. Special care was given to keep verticality between camera and physical frame, distance and focus. Figure 3.19 displays the overall view of the physical model used in the study.

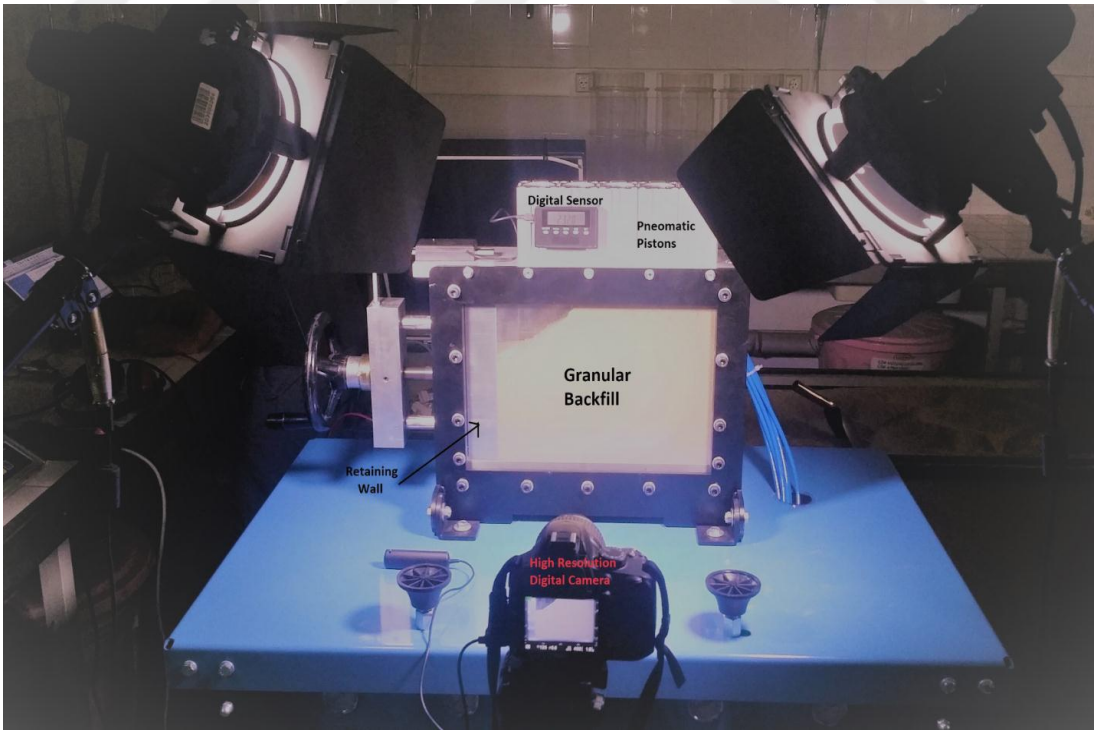


Figure 3.21. The physical test model used in retaining tests.

Tests were conducted at varying density and surcharge values for all the sands and GB to visualize and compare the combined effect of stress and macro-scale physical soil properties. Three different relative density ranges were adopted which represented the loose, medium dense and dense conditions of the soils (Table 3.5). By air pluvation method it was not possible to achieve a certain relative density value for each test therefore the comparisons were done within a 10% density range.

Table 3.5. Testing program of each sand for the physical model experiments

Experiment No	Relative Density Range	Applied Vertical Stress
1	30-40%	0 kPa
2	30-40%	50 kPa
3	30-40%	100 kPa
4	50-60%	0 kPa
5	50-60%	50 kPa
6	50-60%	100 kPa
7	70-80%	0 kPa
8	70-80%	50 kPa
9	70-80%	100 kPa

Same test program was applied for S1, S3, SP-S2, SW-S2 sands and GB respectively. In this way, the obtained failure surface geometries of different granular materials under equal density and/or surcharge values were compared. Since the only intrinsic soil parameter influencing the evaluation of shear band geometry was dilatancy; the effect of grain size and grain shape on failure surface geometry could be investigated by means of this presented premeditative testing program.

The pictures taken during transition of the retaining wall until the active failure state was analyzed by GeoPIV-RG software which is an image analysis module for MATLAB and is capable of sub-pixel measurement resolution for large deformations of soil grains (White *et al*., 2015). Particle image velocimetry (PIV) method examined the difference between a reference image and sequence of deformed images. The initial image was divided into grid of square patches. The GeoPIV searched for a specific zone of deformed image that

had maximum similarity to the patches in the initial image. The reference image in the analysis was chosen to be the initial state of the soil before wall displacement and during the wall displacement the PIV module automatically tracked the difference of the location of soil grains between the reference image and following deformed images until soil failure. The difference between the target patch and the reference patch was measured in pixels and visualized by a displacement vector. The module enabled to visualize the displacements by volumetric and shear strain maps where the strain intensity is embodied by colored pixels. In this way the geometry of the slip surface during wall movement, the localization of strains on shear band and failure surface geometry were visualized. In this study 50 pixel sized square patches were generated by a center-to-center distance of neighboring patches of 25 pixels so that the patches overlap (Figure 3.20). This enabled a more elaborate pixel intensity and displacement vector visualization. In order to increase image texture for adequate correlation, the image contrast was improved by adding seeding to the front surface of the model. In addition, to perform image-object space calibration of the pictures, control points were used on the model frame. These points are shown as black dots on the generated mesh in Figure 3.20. PIV analysis of the pictures taken by digital camera during the physical model experiments revealed the geometry of the slip surfaces. Figure 3.21 presents the shear strain distribution on the backfill at active failure state of the model wall. Blue dots on figures indicate the location of control points.

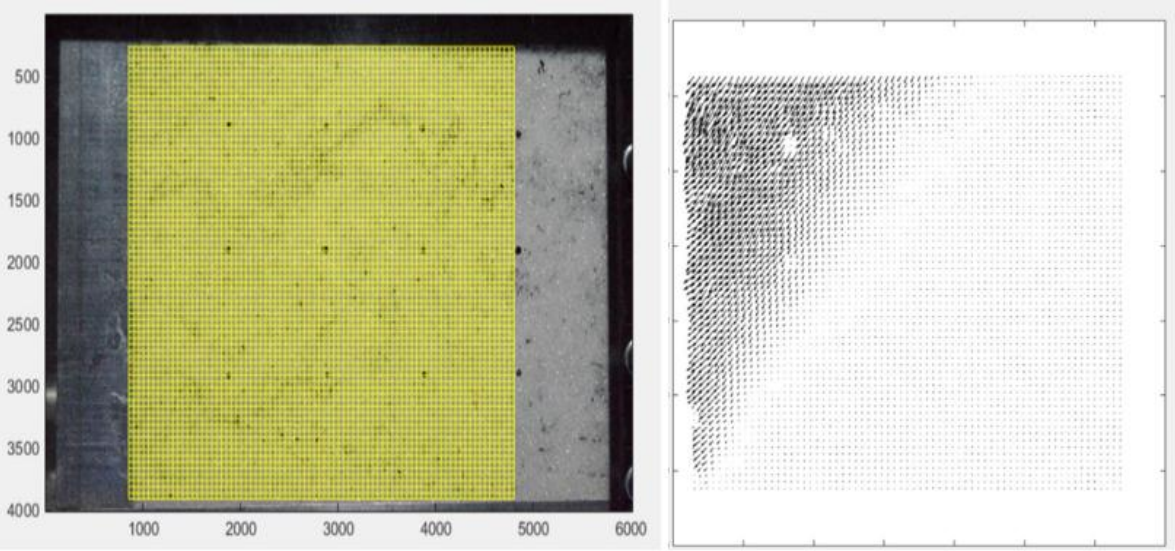
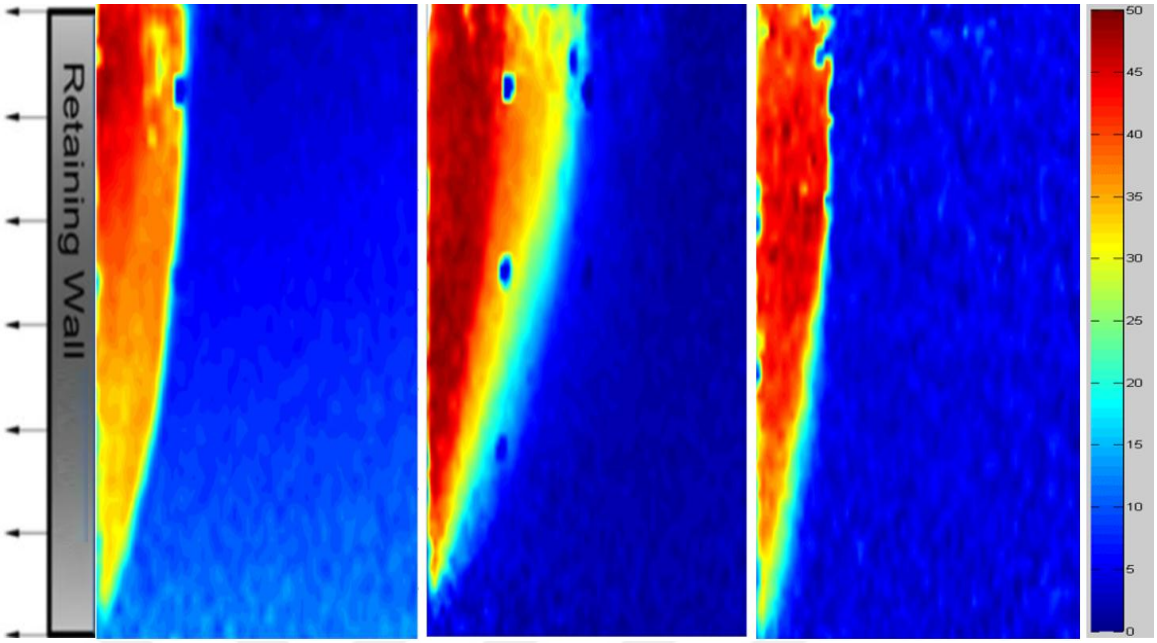


Figure 3.22. View of the generated mesh of square patches and the displacement vector field of the deformed mesh.



a) I_D =31% , σ =0 kPa b) I_D =32% , σ =100 kPa c) I_D =79% , σ =100 kPa

Figure 3.23. Shear strain distribution generated by PIV behind retaining of S2 sand.

PIV analysis displayed the dimensions of x-y axes in pixel coordinates. In order to obtain actual distances in SI units, an image-object space calibration was conducted. The x-y coordinates of the slip surfaces were generated using PlotDigitizer which is a Java program used to digitize scanned plots of functional data (J.A. Huwaldt, 2015). The actual distance between control points in SI units was used to calibrate the measured distances from the digitized plots. As a result, for each picture a specific pixel to cm calibration was generated. Averagely, all results indicated 1 cm = 200 pixels calibration because the camera distance, focus and height were all kept constant and stable during each test. In PlotDigitizer the inputs of the borders of x and y axes (x_{max} and y_{max}) were selected to be SI units so that the actual distance of failure surface to wall was obtained.

The borders of the slip surfaces were picked manually using PlotDigitizer and the obtained x-y coordinate of these points were normalized with the wall height in both axes to obtain unitless parameters. Finally, these points were plotted in to visualize the geometry of the failure surface for each test.

4. EVALUATION OF THE TEST RESULTS

4.1. Triaxial Tests

During the shearing phase stresses reached to a peak value where peak friction angle was evaluated and recorded. Experiments were carried on until axial displacement of the specimen reached to 15%. All data was recorded and $q - p$ relationship, ε_v - ε_a relationship, $q - \varepsilon_a$ relationship and $\psi_p' - \varepsilon_a$ relationships were plotted. From the interpretation of raw test data, mean effective stress at failure (p'_{peak}), deviatoric stress at failure (q_{peak}) and peak friction angle (ϕ_p') values were derived. The peak gradient of volumetric strain – axial strain graph gives peak dilation rate $(d\epsilon_v/d\varepsilon_1)_{max}$. Peak dilation rate values were used to calculate dilatancy angle of the samples using Schanz and Vermeer (1996) formula:

$$sin\psi = -\frac{(^{d\epsilon_v}/_{d\varepsilon_1})_{max}}{2-(^{d\epsilon_v}/_{d\varepsilon_1})_{max}} \tag{4.1}$$

Table 4.1. Calculated peak dilatancy rate, ψ_p' and ϕ_p' for S1 Sand (AC Stress Path)

I_D %	σ_3' (kPa)	p'_{peak}(kPa)	-$(d\varepsilon_v/d\varepsilon_1)_{max}$	ψ_p' (degrees)	ϕ_p' (degrees)
40	150	92.4	0.342	8.4	37.5
32	250	156.2	0.168	4.4	36.0
29	300	314.4	0.132	3.5	35.2
45	250	156.0	0.297	7.4	38.2
67	150	131.6	0.470	11.0	39.4
50	300	231.2	0.423	10.1	38.6
74	150	202.6	0.559	12.6	41.4
50	150	152.3	0.369	9.0	37.3
73	250	163.2	0.432	10.2	39.6
83	300	225.9	0.452	10.6	39.7
37	50	80.4	0.768	16.1	39.3
85	50	71.9	1.453	24.9	44.2

Table 4.2. Calculated peak dilatancy rate, ψ_p' and ϕ_p' for S1 Sand (LE Stress Path)

I_D %	σ_3' (kPa)	p'_{peak}(kPa)	-$(d\varepsilon_v/d\varepsilon_1)_{max}$	ψ_p' (degrees)	ϕ_p' (degrees)
38	150	76.1	0.374	9.1	34.8
53	150	75.6	0.674	14.6	37.0
37	250	129.4	0.118	3.2	34.0
57	250	124.0	0.544	12.3	37.7
51	300	146.6	0.516	11.8	38.0
66	150	73.5	0.724	15.4	38.2
65	250	118.3	0.699	15.0	39.7
65	300	153.3	0.436	10.3	36.1
84	150	75.7	0.770	16.1	37.4
57	250	126.1	0.514	11.8	37.6
88	250	119.7	1.062	20.3	39.3
39	300	151.6	0.497	11.5	36.7
94	150	73.8	0.621	13.7	35.9
92	300	144.5	0.766	16.1	40.1

Table 4.3. Calculated peak dilatancy rate, ψ_p' and ϕ_p' for S3 Sand (AC Stress Path)

I_D %	σ_3' (kPa)	p'_{peak}(kPa)	-$(d\varepsilon_v/d\varepsilon_1)_{max}$	ψ_p' (degrees)	ϕ_p' (degrees)
59	50	149.2	0.879	17.8	42.4
55	300	208.0	0.591	13.2	40.6
43	250	176.3	0.757	15.9	42.0
24	250	154.2	0.355	8.7	37.9
75	150	228.7	0.961	18.9	43.8
60	250	345.7	0.910	18.2	42.5
56	150	241.3	0.861	17.5	41.7
34	150	226.5	0.708	15.2	41.0
45	300	724.3	0.737	15.6	40.9
43	150	228.4	0.786	16.4	41.9
32	300	535.6	0.778	16.3	41.1
60	250	165.1	0.693	14.9	40.1
60	150	194.4	0.941	18.7	42.1

Table 4.4. Calculated peak dilatancy rate, ψ_p' and ϕ_p' for S3 Sand (LE Stress Path)

I_D %	σ_3' (kPa)	p'_{peak}(kPa)	$-(d\varepsilon_v/d\varepsilon_1)_{max}$	ψ_p' (degrees)	ϕ_p' (degrees)
43	150	68.2	0.813	16.8	42.7
57	150	68.7	1.062	20.3	43.8
69	150	67.5	1.170	21.7	43.5
37	250	116.8	0.764	16.0	40.1
58	250	114.2	0.971	19.1	42.9
72	250	110.4	1.202	22.0	44.9
40	300	143.3	0.741	15.7	39.4
60	300	138.2	0.928	18.5	41.0

Table 4.5. Calculated peak dilatancy rate, ψ_p' and ϕ_p' for GB (AC Stress Path)

I_D %	σ_3' (kPa)	p'_{peak}(kPa)	$-(d\varepsilon_v/d\varepsilon_1)_{max}$	ψ_p' (degrees)	ϕ_p' (degrees)
30	50	65.0	0.802	16.6	33.4
30	150	127.4	0.902	18.1	35.4
30	300	278.8	0.881	17.8	34.4
46	50	108.8	0.774	16.2	33.0
33	400	315.5	0.809	16.7	34.2
25	150	133.5	0.904	18.1	35.5
17	50	80.7	0.465	10.9	29.4
48	150	314.7	0.993	19.4	36.2
46	300	644.9	1.000	19.5	36.7
48	50	138.2	1.222	22.3	38.3
28	50	96.7	0.756	15.9	33.0
20	300	572.5	0.823	16.9	33.7

Table 4.6. Calculated peak dilatancy rate, ψ_p' and ϕ_p' for GB (LE Stress Path)

I_D %	σ_3' (kPa)	p'_{peak}(kPa)	$-(d\varepsilon_v/d\varepsilon_1)_{max}$	ψ_p' (degrees)	ϕ_p' (degrees)
30	150	80.4	0.626	13.8	31.7
30	50	26.5	0.466	10.9	29.1
30	300	157.2	0.683	14.7	32.8
48	50	20.3	1.150	21.4	37.5
45	150	75.1	0.769	16.1	34.5
46	300	148.2	1.009	19.6	36.5

Table 4.7. Calculated peak dilatancy rate, ψ_p' and ϕ_p' for SW-S2 (AC Stress Path)

I_D %	σ_3' (kPa)	p'_{peak}(kPa)	$-(d\varepsilon_v/d\varepsilon_1)_{max}$	ψ_p' (degrees)	ϕ_p' (degrees)
46	50	126.8	0.274	6.9	37.5
51	150	198.9	0.288	7.2	38.7
21	50	154.6	0.130	3.5	37.0
46	300	589.3	0.159	4.2	35.4
25	150	264.0	0.063	1.7	38.0
25	300	397.7	0.036	1.0	35.2
72	150	355.2	0.451	10.6	41.0
72	300	308.0	0.440	10.4	41.2

Table 4.8. Calculated peak dilatancy rate, ψ_p' and ϕ_p' for SP-S2 (AC Stress Path)

I_D %	σ_3' (kPa)	p'_{peak}(kPa)	$-(d\varepsilon_v/d\varepsilon_1)_{max}$	ψ_p' (degrees)	ϕ_p' (degrees)
43	50	136.5	0.370	9.0	38.5
57	50	197.7	0.351	8.6	40.5
58	20	18.3	0.512	11.8	47.5
70	50	164.3	0.606	13.4	42.4
42	150	244.6	0.257	6.5	38.1
70	150	356.5	0.490	11.3	40.2
40	300	570.9	0.208	5.4	36.7

Next, peak friction angle – peak dilation angle relationship was plotted for each sand. The friction angle value which corresponds to zero dilatancy evaluated by interpolation of the slope gave the critical state friction angle for each sand type. The graphs for S1 sand AC and LE test respectively are given in Figure 4.1 and Figure 4.2. Figure 4.3 and Figure 4.4 presents the graphs for the S3 sand AC and LE tests. Figure 4.5 and Figure 4.6 present AC and LE tests for the GB of 400μm - 600μm grain size. For SW-S2, AC test results are at Figure 4.7, and finally for SP-S2, results of AC tests are in Figure 4.8.

From the graphs, the constant multiplier of the dilatancy angle which corresponds to the r_{tx} coefficient of Bolton (1986) stress-dilatancy relationship were derived. r_{tx} coefficient represents the influence ratio of dilatancy on soil strength. In Figure 4.9, summary of all the derived relationship is plotted for AC and LE loading conditions respectively.

In this regard, empirical correlation proposed by Nanda and Petra (2015) was used in order to obtain plane strain friction angles and the influence ratio of dilatancy on soil strength for plane strain conditions (r_{ps}):

$$\phi_{p,ps} = \phi_{p,tx}\left[\frac{\frac{A_p}{A_T}(1-K_{\phi T})}{(1-K_{\phi P})}\right] \tag{4.2}$$

To investigate the effect of loading condition on the contribution of dilatant behavior on frictional strength of the soils, samples were prepared under similar density and confining pressure ranges. Results showed that there is only a slight difference on critical state friction angle and contribution of dilatancy on soil strength between axial compression and lateral extension loading conditions.

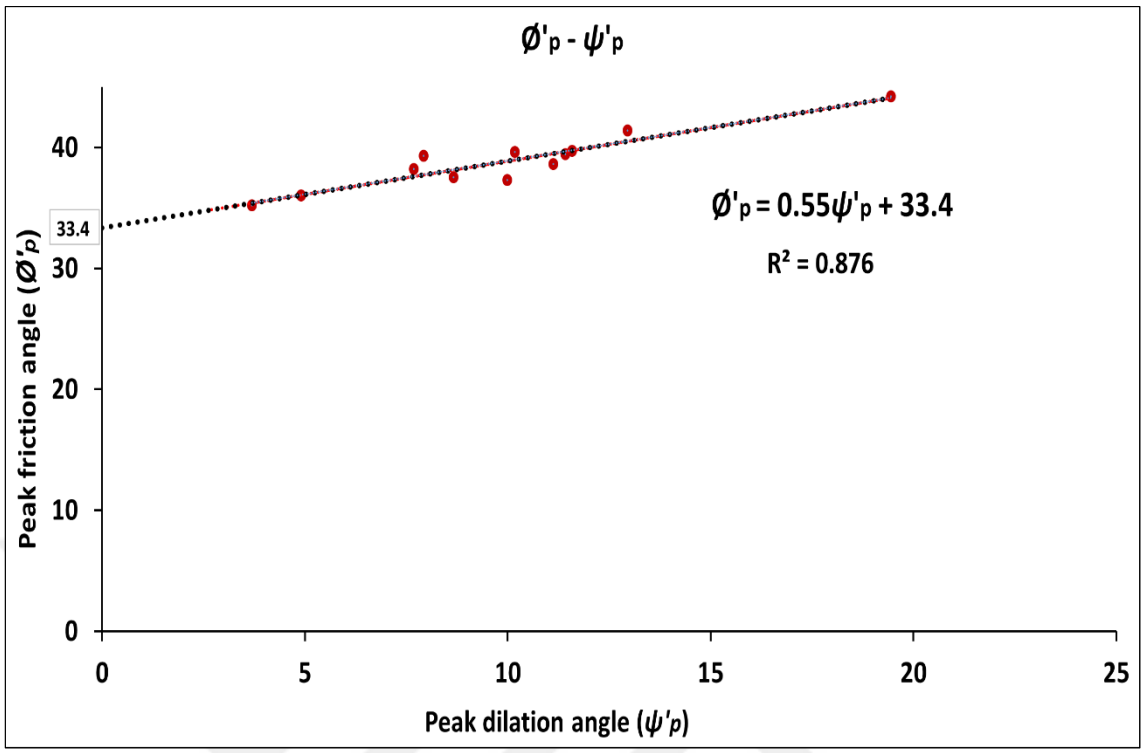


Figure 4.1. ψ_p' and ϕ_p' relationship for AC stress path triaxial testing of S1 sand.

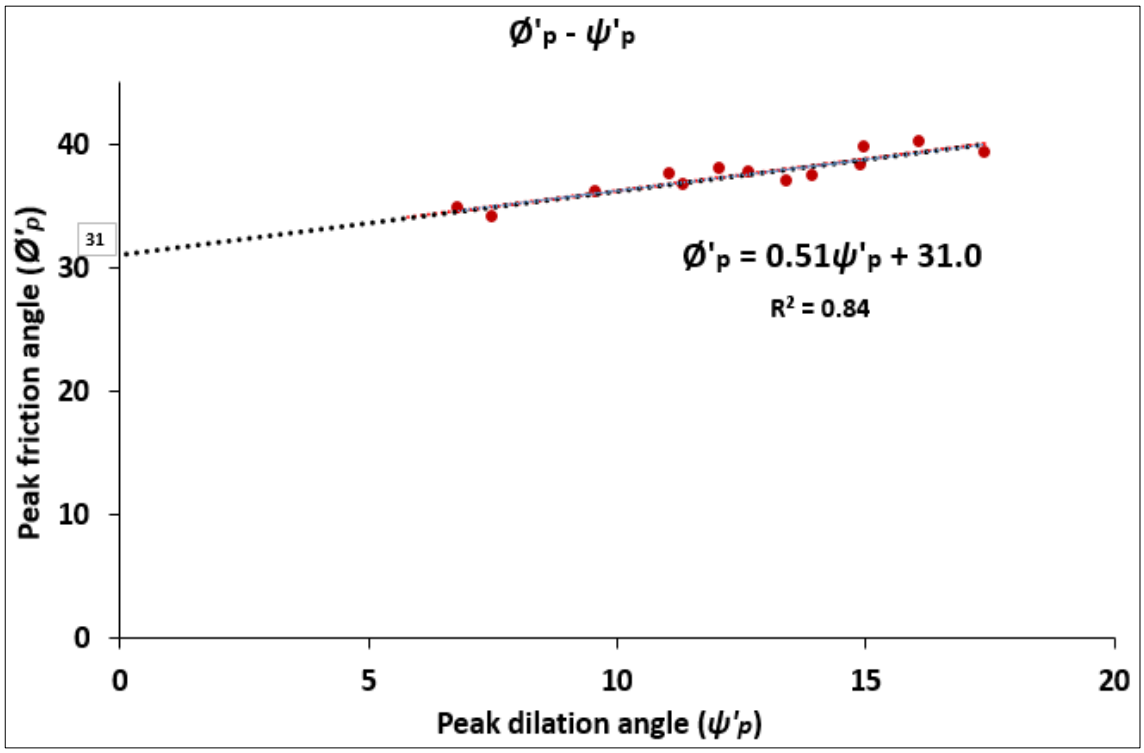


Figure 4.2. ψ_p' and ϕ_p' relationship for LE stress path triaxial testing of S1 sand.

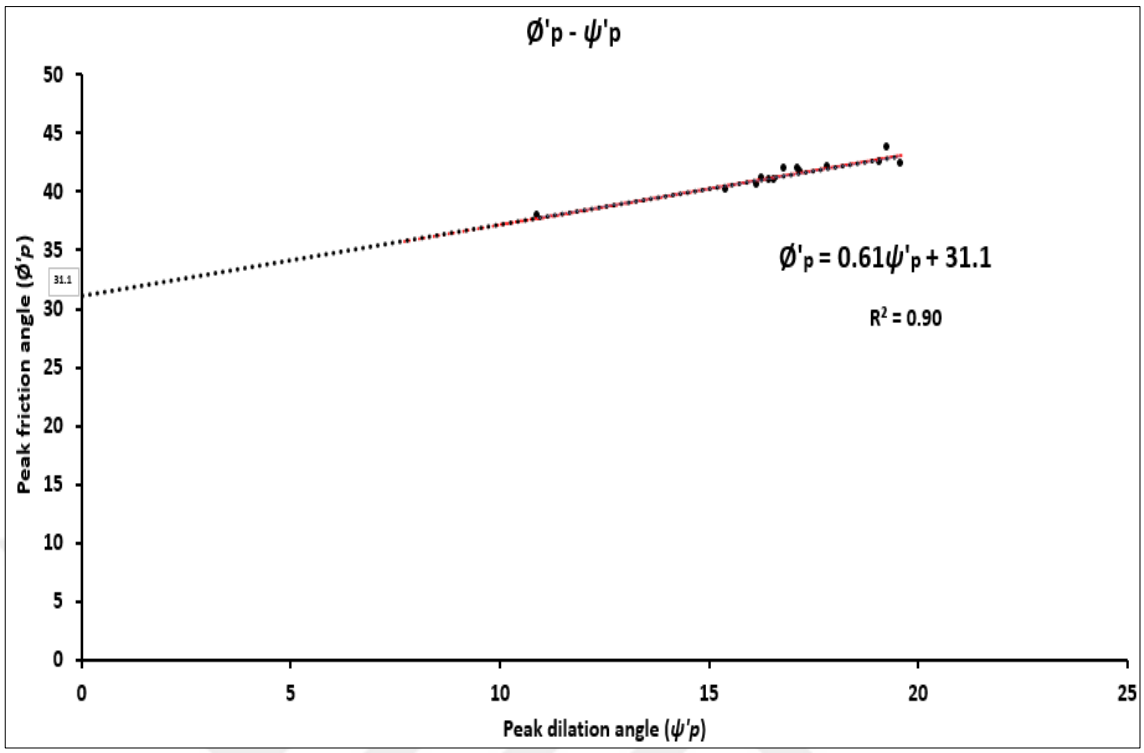


Figure 4.3. ψ_p' and ϕ_p' relationship for AC stress path triaxial testing of S3 sand.

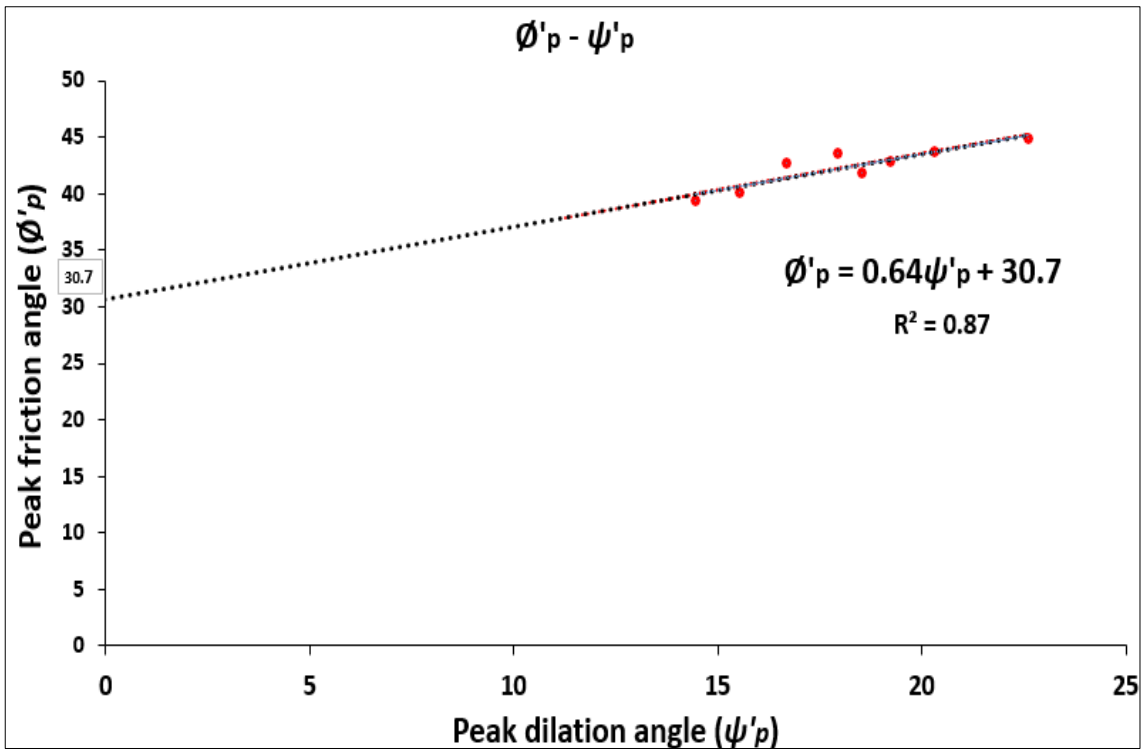


Figure 4.4. ψ_p' and ϕ_p' relationship for LE stress path triaxial testing of S3 sand.

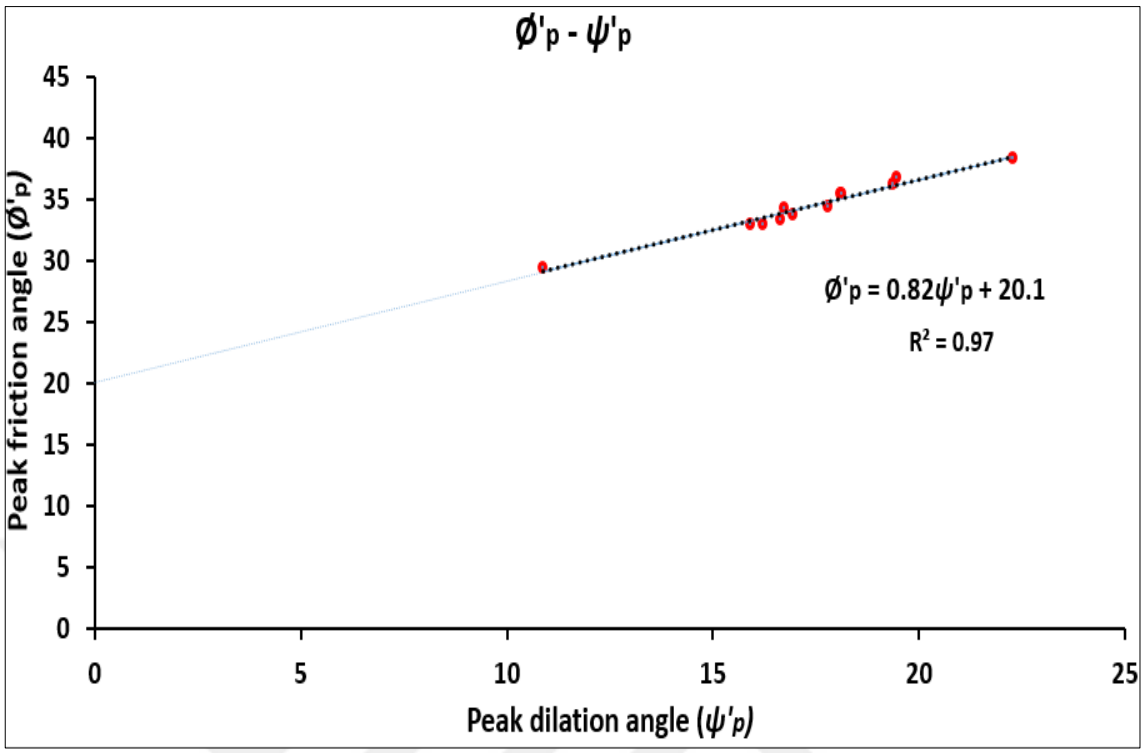


Figure 4.5. ψ_p' and ϕ_p' relationship for AC stress path triaxial testing of GB.

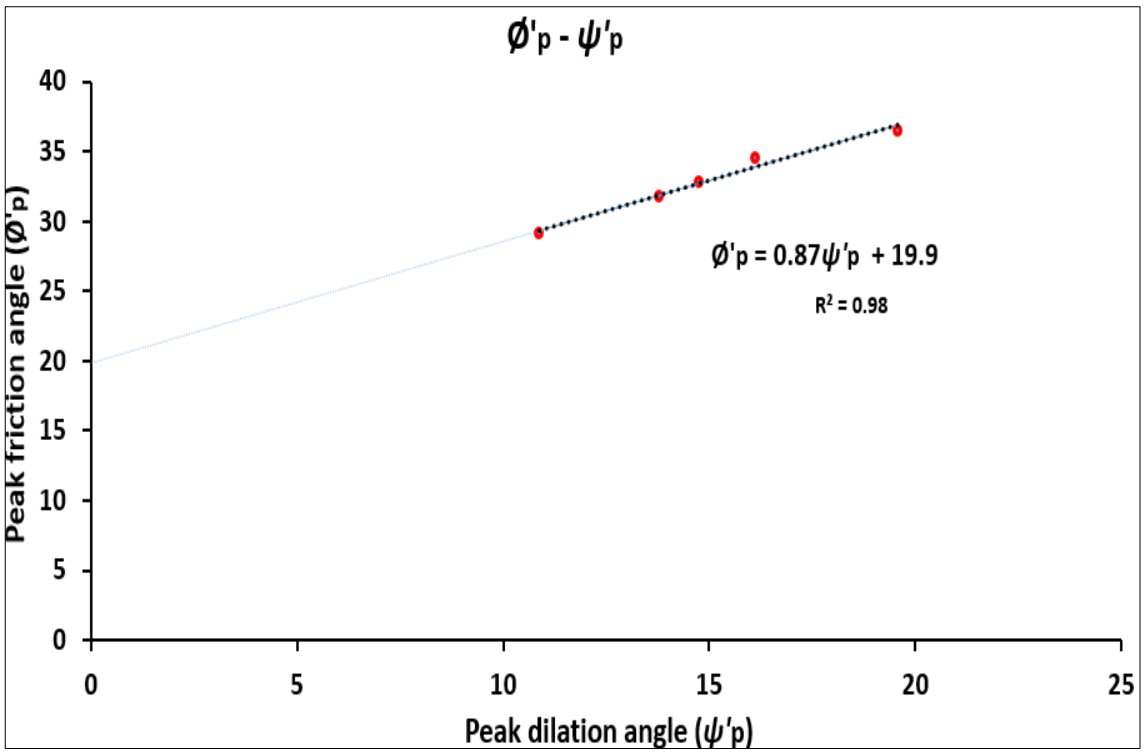


Figure 4.6. ψ_p' and ϕ_p' relationship for LE stress path triaxial testing of GB.

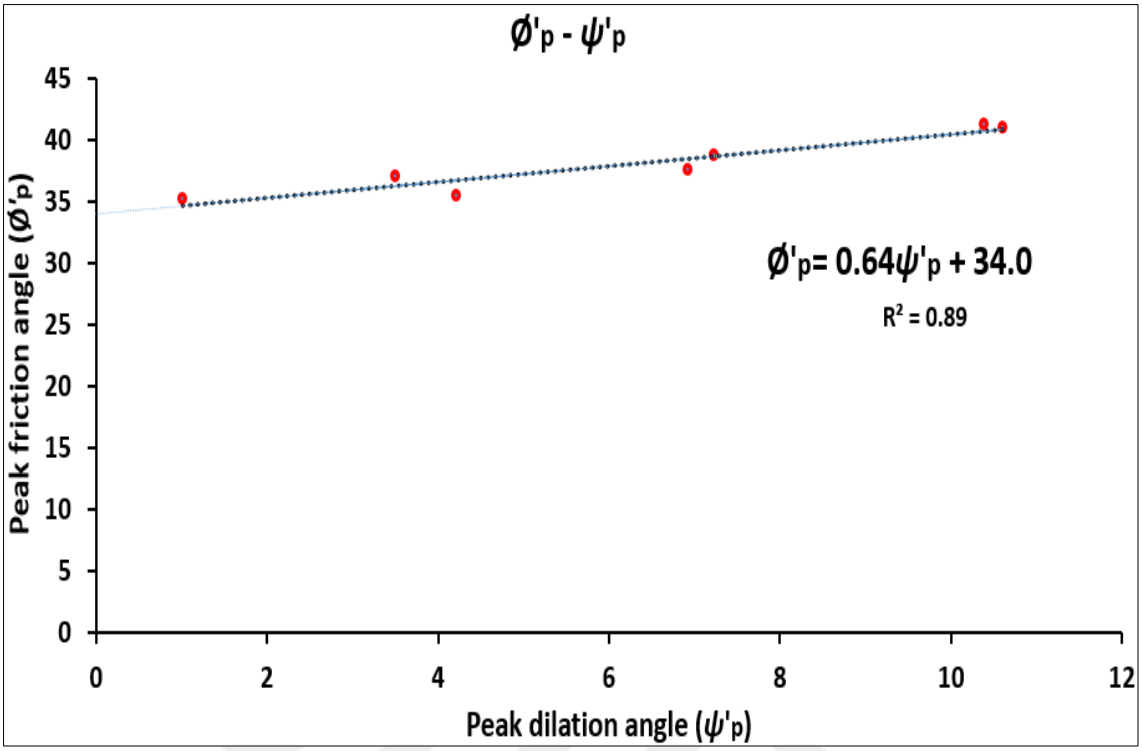


Figure 4.7. ψ_p' and ϕ_p' relationship for AC stress path triaxial tests of SW-S2.

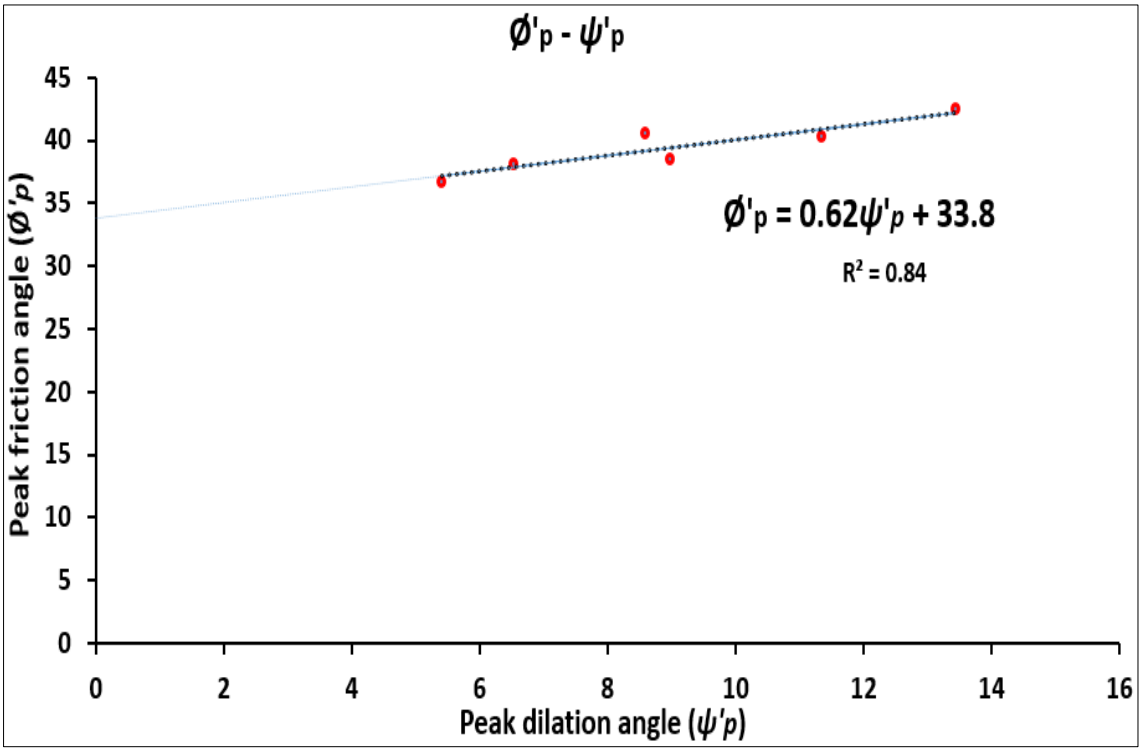
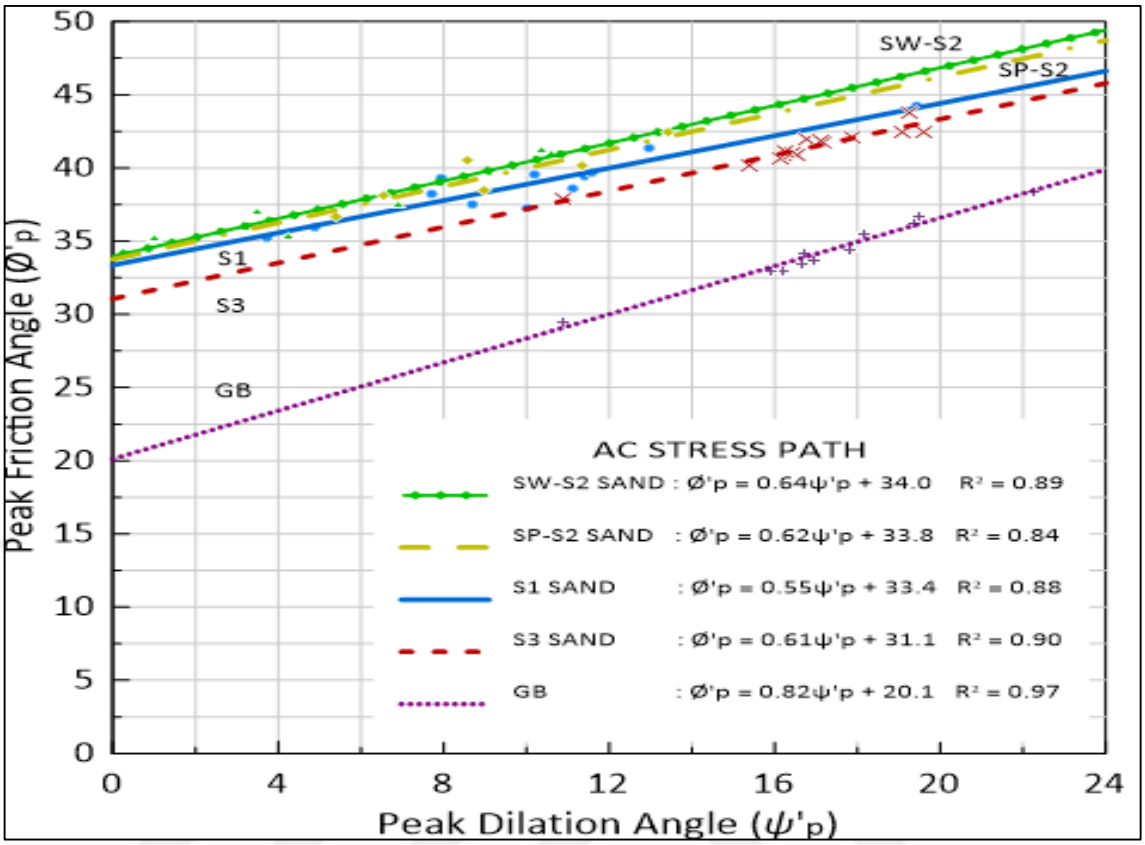


Figure 4.8. ψ_p' and ϕ_p' relationship for AC stress path triaxial tests of SP-S2.



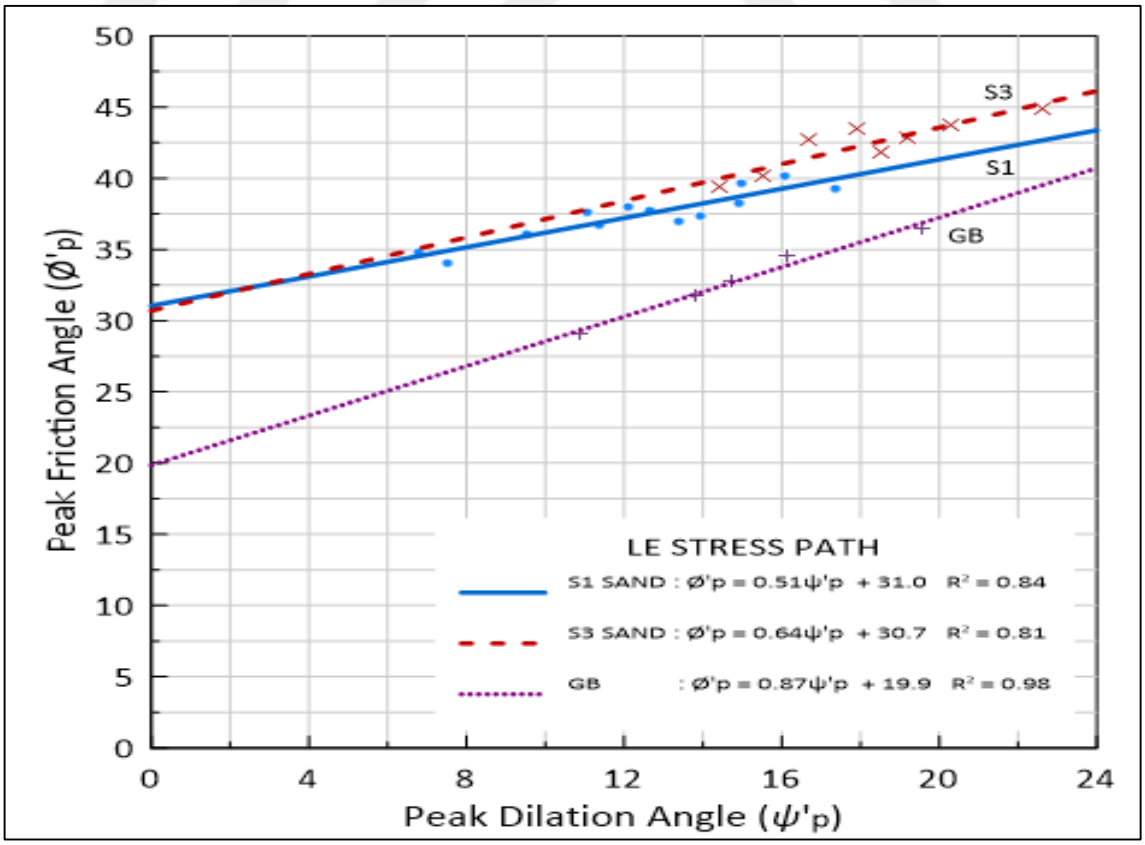


Figure 4.9. Summary of ψ_p' and ϕ_p' relationships for AC - LE conditions.

Based on his triaxial tests, Bolton (1986) recommended that for both axisymmetric and plane strain conditions there has been a linear relationship between dilatancy index value and peak dilation rate, and the dilatancy index constants were Q = 10 and R = 1 for all different density and confining pressure conditions of quartz sand.

However, Chakraborty and Salgado (2010) revealed that Q and R constants are soil-specific line fitting parameters which could be experimentally obtained by triaxial testing. They showed that the influence of initial confining stress (p_i') of the soil affected line-fitting Q and R parameters. Therefore, in this study a wide range of confining stress (50 kPa – 300 kPa) were applied on the specimens to extensionally evaluate line-fitting Q and R parameters. Higher stresses were avoided so that no grain crushing occurs which negatively effects soil strength. Following Chakraborty and Salgado (2010) procedures, soil-specific line fitting Q and R parameters were evaluated for each sand type including GB and are presented in the Figures between 4.10 and 4.17 for each granular material and stress path.

In Figure 4.18, calculated line-fitting parameter Q values when R=1 of each sand for AC and LE loading conditions are summarized respectively.

In addition, the average ratio of peak dilatancy rate to dilatancy index, which is termed as 'a' were derived for each specimen:

$$(-d\varepsilon_v/d\varepsilon_1)_{max} = aI_R \tag{4.3}$$

Finally, the average ratio of the variance between maximum and critical strength to dilatancy index which is termed as 'A_ψ' was also derived for comparison:

$$\phi_p' - \phi_c' = A_\psi I_R \tag{4.4}$$

As a result, all known stress-dilatancy correlation constants (r_{tx}, r_{ps}, Q, R, a, A_ψ, Φ_{cs}) which have been proposed by previous researchers in literature have also been evaluated for the soil samples investigated within this research.

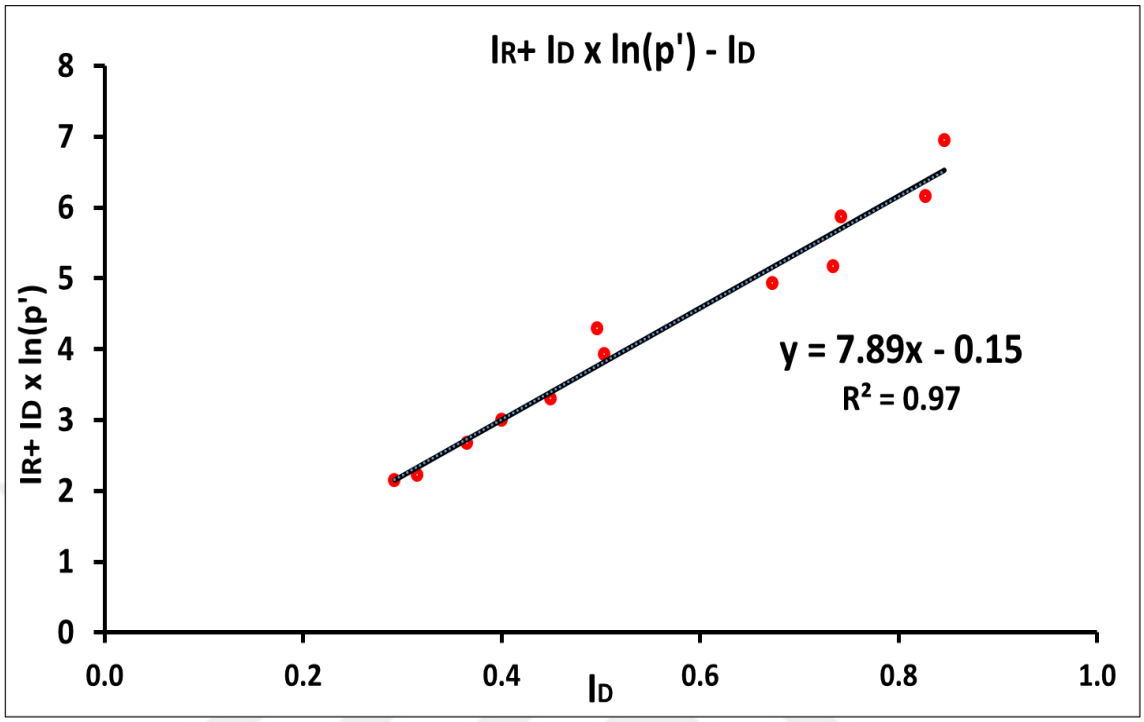


Figure 4.10. Determination of Q and R parameter from AC stress path of S1 sand.

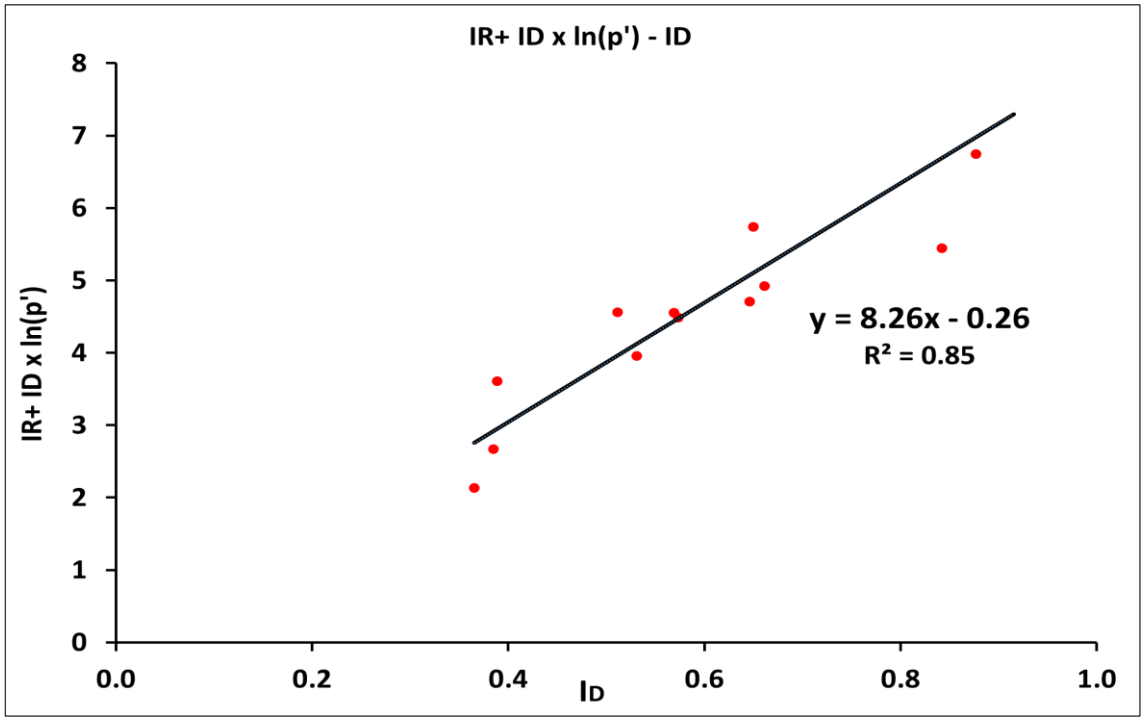


Figure 4.11. Determination of Q and R parameter from LE stress path of S1 sand.

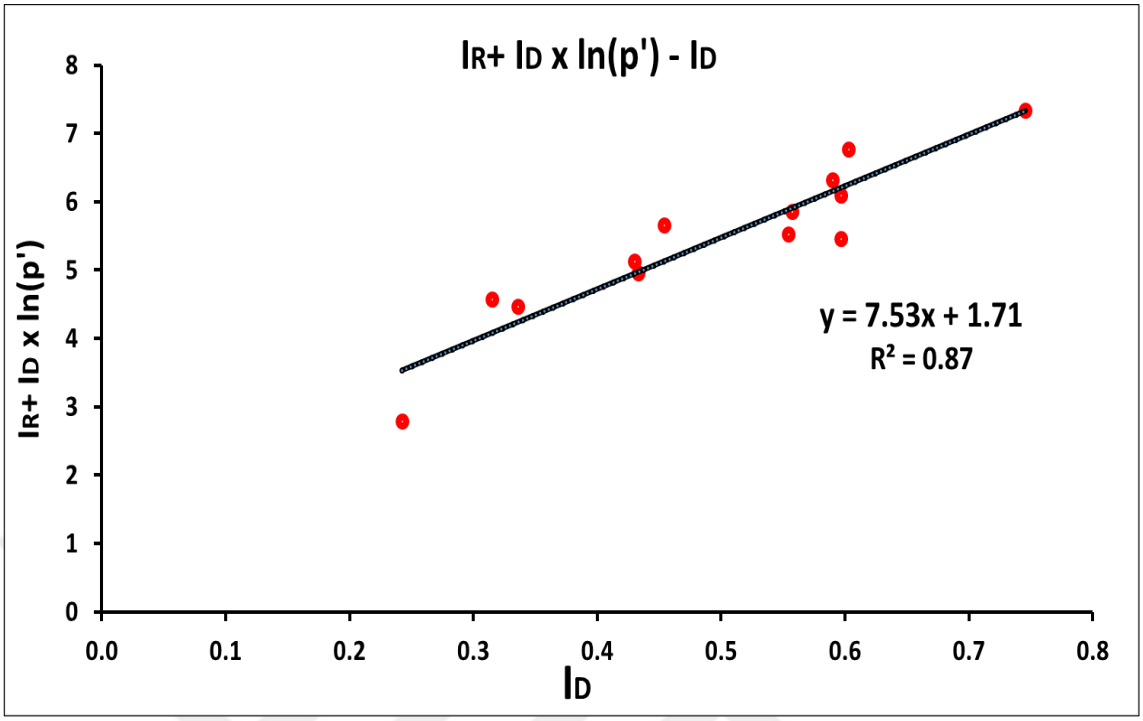


Figure 4.12. Determination of Q and R parameter from AC stress path of S3 sand.

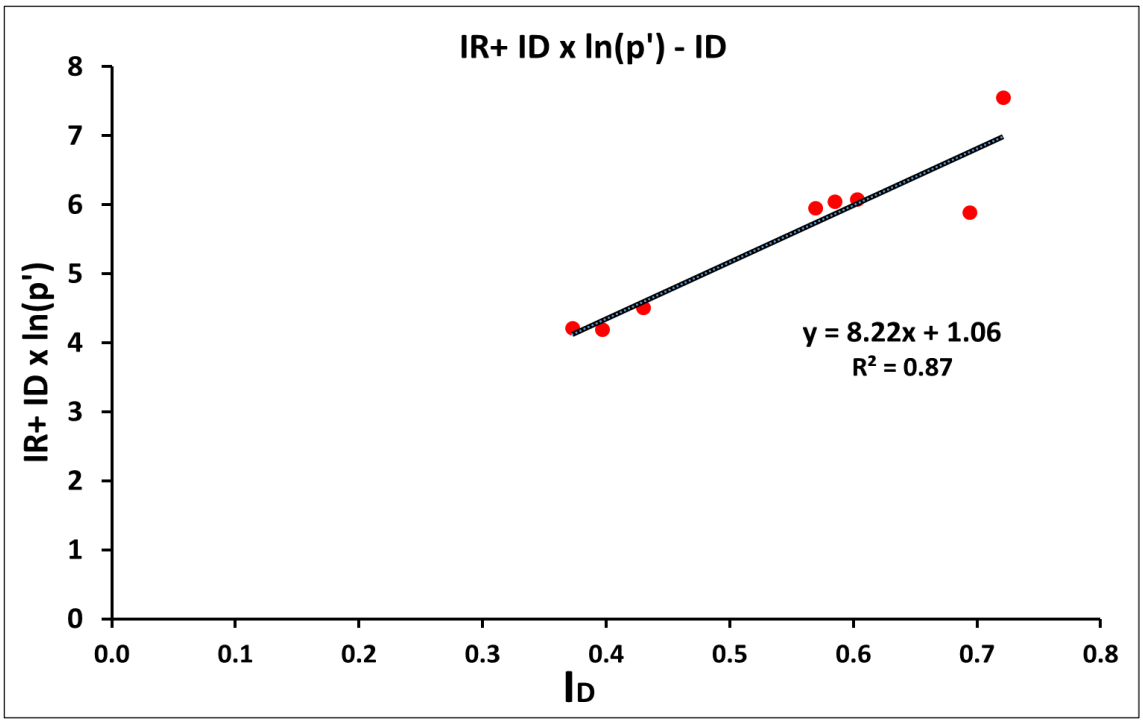


Figure 4.13. Determination of Q and R parameter from LE stress path of S3 sand.

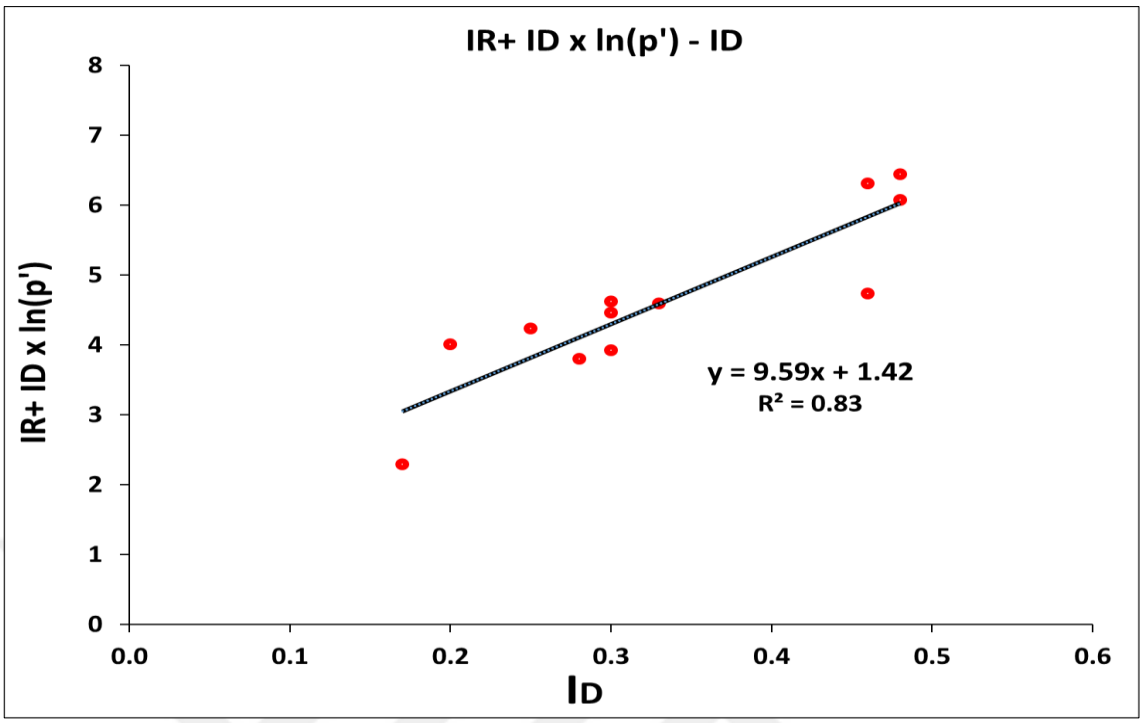


Figure 4.14. Determination of Q and R parameter from AC stress path of GB.

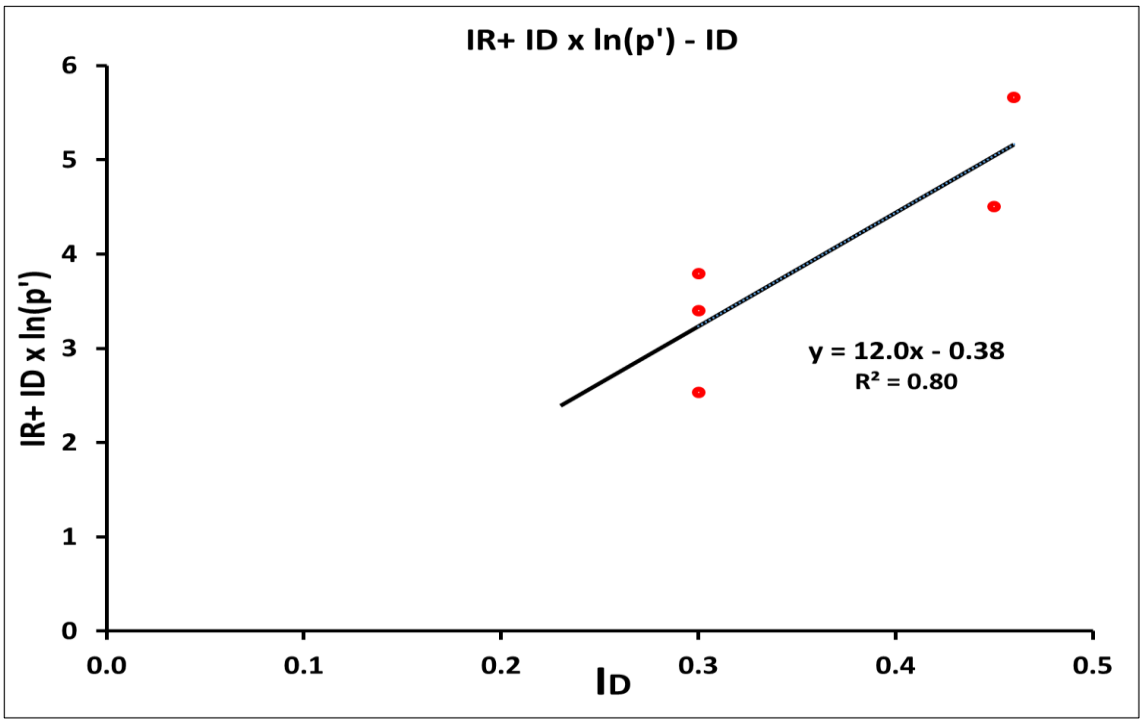


Figure 4.15. Determination of Q and R parameter from LE stress path of GB.

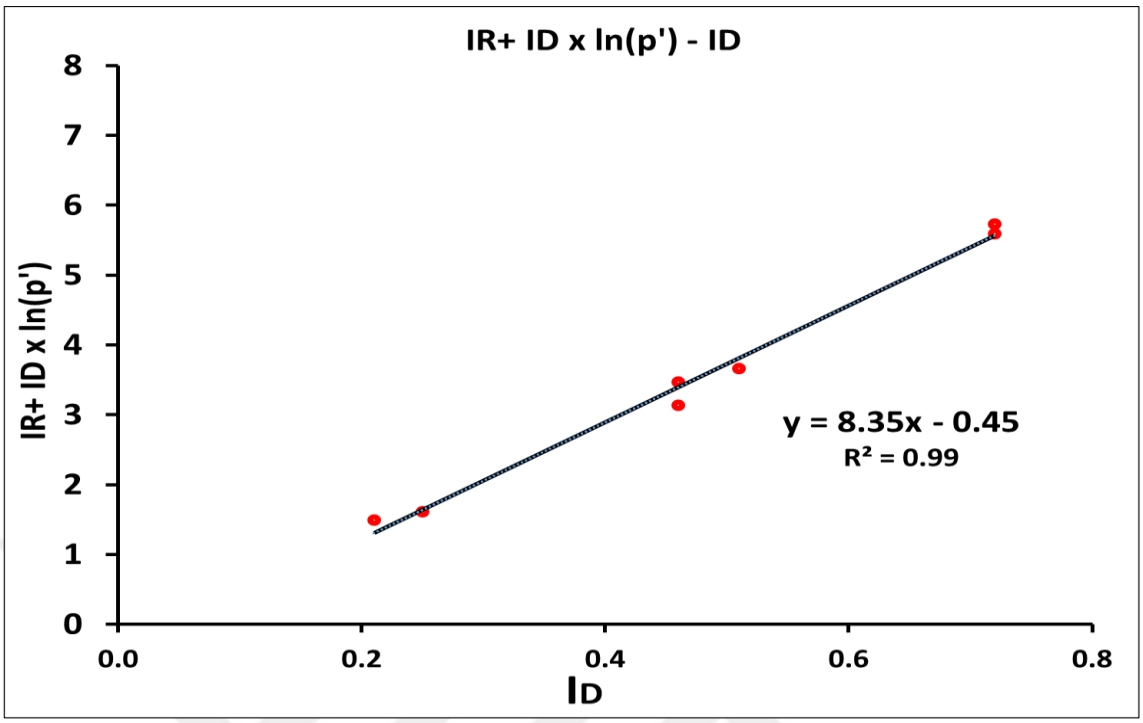


Figure 4.16. Determination of Q and R parameter from AC stress path of SW-S2.

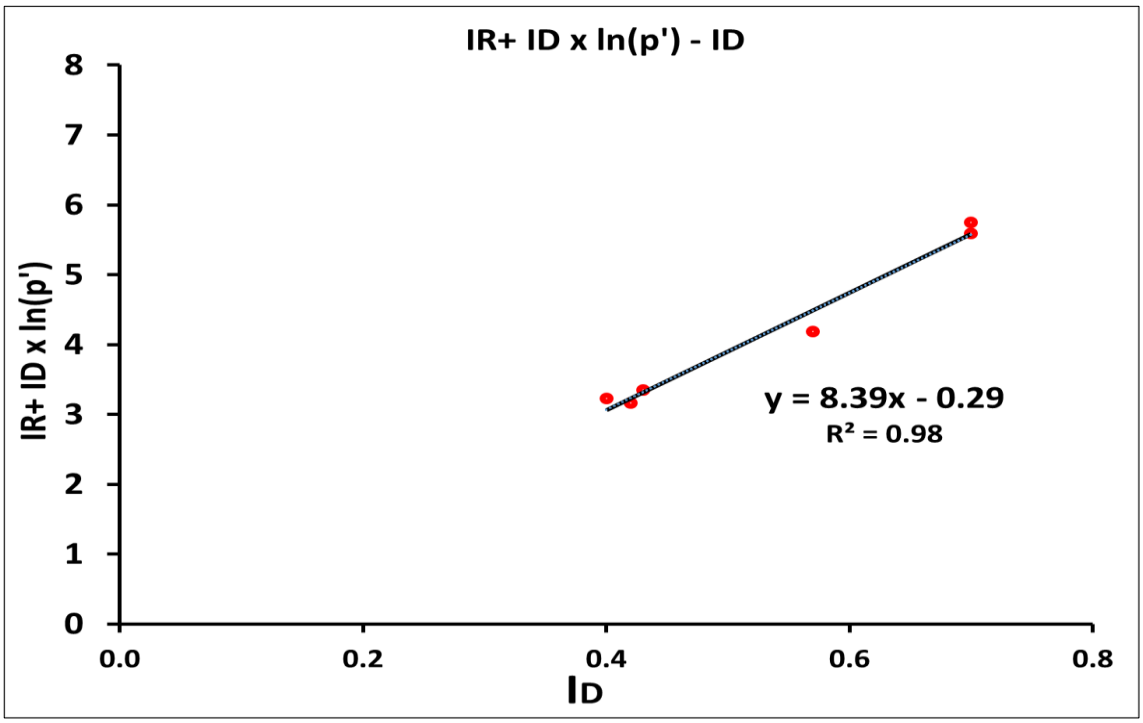


Figure 4.17. Determination of Q and R parameter from AC stress path of SP-S2.

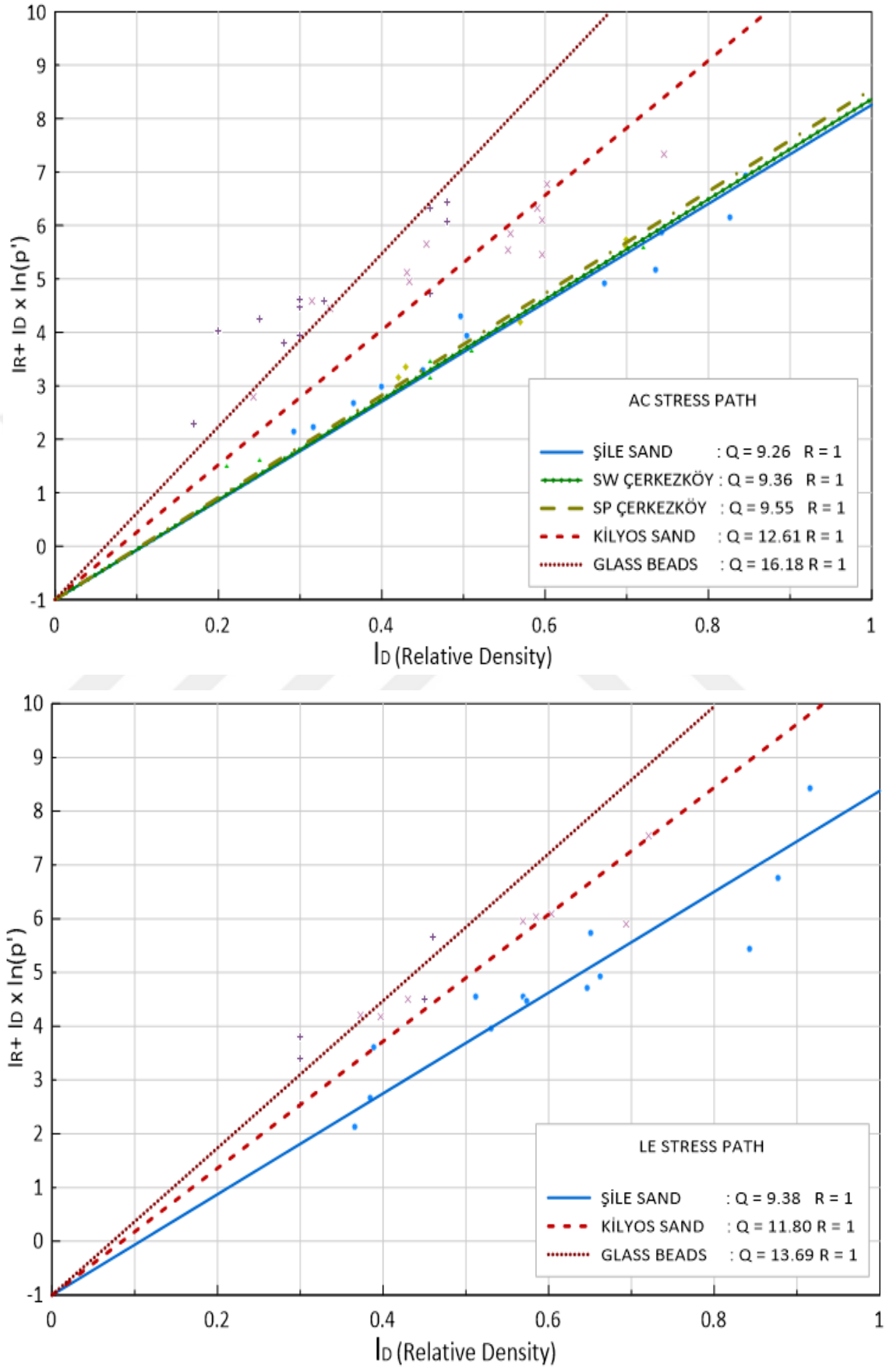


Figure 4.18. Evaluation of line fitting Q parameter when R = 1 for AC-LE conditions.

The coefficients which were used in stress-dilatancy equations calculated for S1, S2, S3 samples and GB under axial compression stress path tests are given in Table 4.9 below. Table 4.10 presents the calculated stress-dilatancy coefficients of the tested soils under lateral extension stress path.

Table 4.9. Stress-dilatancy coefficients calculated for each test under AC stress path

Soil Type	$\mathbf{r_{tx}}$	$\mathbf{r_{ps}}$	**Q**	**Q** *if* **R=1**	**R**	**a**	$\mathbf{A_\psi}$	$\mathbf{Ø'_{cs}}$
S1 Sand	0.55	0.83	7.90	9.26	0.15	0.30	3.88	33.4
S3 Sand	0.61	0.95	7.53	12.61	-1.72	0.30	3.82	31.1
SW S2	0.64	1.12	8.35	9.36	0.45	0.32	5.90	34.0
SP S2	0.62	0.96	8.39	9.55	0.29	0.31	4.58	33.8
GB	0.82	1.24	9.59	16.18	-1.42	0.30	5.06	20.1

Table 4.10. Stress-dilatancy coefficients calculated for each test under LE stress path

Soil Type	$\mathbf{r_{tx}}$	$\mathbf{r_{ps}}$	**Q**	**Q** *if* **R=1**	**R**	**a**	$\mathbf{A_\psi}$	$\mathbf{Ø'_{cs}}$
S1 Sand	0.51	0.76	8.26	9.38	0.26	0.30	3.55	31.0
S3 Sand	0.64	0.96	8.22	11.80	-1.06	0.30	3.85	30.7
GB	0.87	1.30	12.1	13.69	0.38	0.31	5.67	19.9

Triaxial test results reveal that sand specimens having higher initial relative densities possess higher friction angles when sheared under similar confining stress. On the other hand, the specimens having similar relative density but consolidated under higher stress have lower strengths. This experimental outcome agrees with conventional stress-dilatancy theories existing in the literature. Besides, it is also observed that there is a proportional relationship between peak dilatancy rate and friction angle of soils which is in line with Bishop (1966) observations.

It is clear from Tables 4.9 and 4.10 that stress-dilatancy relationship coefficients are different for all tested granular soils. Therefore, a comparison was made in order to seperately investigate the effects of grain characteristics at stress-dilatancy correlation parameters.

4.1.1. Influence of Grain Size on Stress-Dilatancy Coefficients

Grain size parameters, which were investigated within this research are uniformity coefficient (C_u), gradation coefficient (C_c) and median particle size (D_{50}). Table 3.3 reveal that all tested soils possess similar coefficent of gradation (C_c) therefore are excluded from comparison. It was observed that in literature dominantly C_u and D_{50} values of the tested soils are available.

To start with, influence of uniformity coefficient (C_u) on contribution of dilatant behavior on soil strength parameter (r) was investigated for all tested soils for AC and LE loading conditions together with the existing data avaliable from literature. From Figure 4.19, it is realized that there is no countable relationship between C_u and '*r*' parameter.

Next, influence of C_u on line-fitting Q parameter provided that R = 1 is shown on Figure 4.20. C_u - Q relationship is scattered, hence is not countable either.

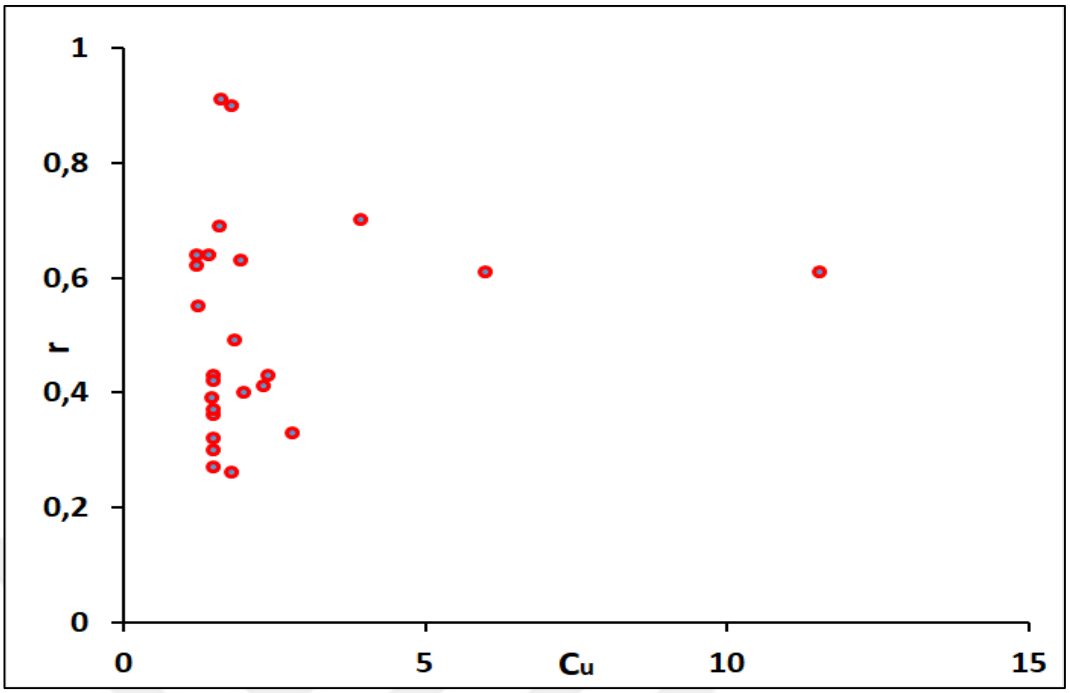


Figure 4.19. C_u – *r* relationship of tested soils together with literature data.

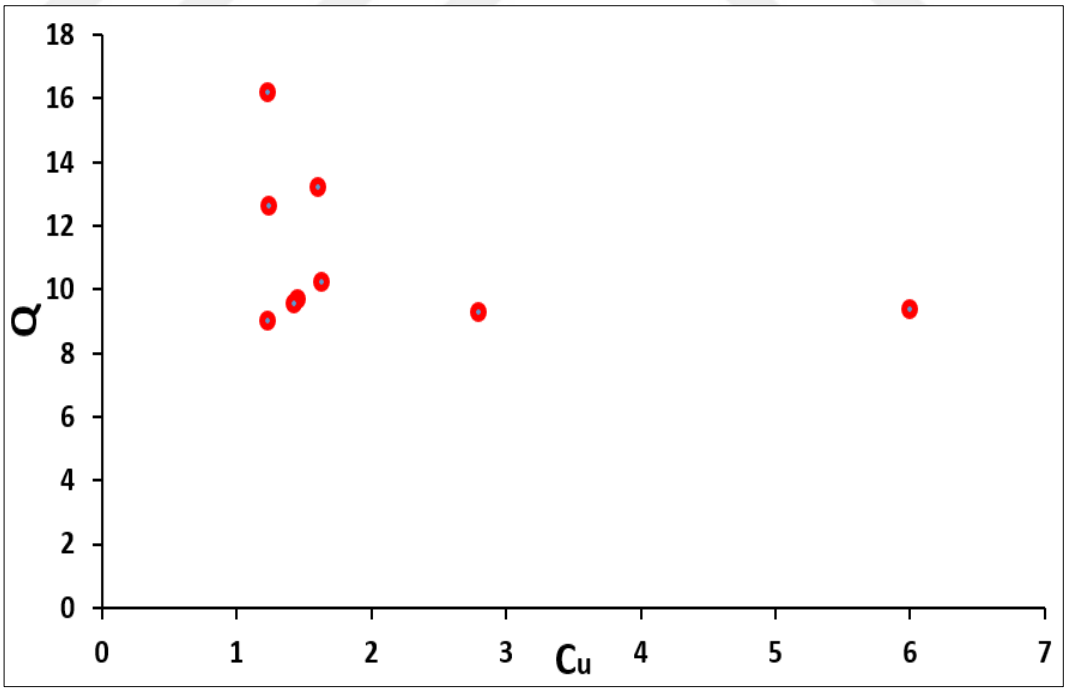


Figure 4.20. C_u - Q relationship of tested soils together with literature data.

In Figure 4.21, the relationship between $Ø_{cs}$ and C_u was investigated. Due to scattered data, the relationship was again uncountable, so the influence of uniformity coefficient (C_u) on constants of stress-dilatancy relationships could not be evaluated.

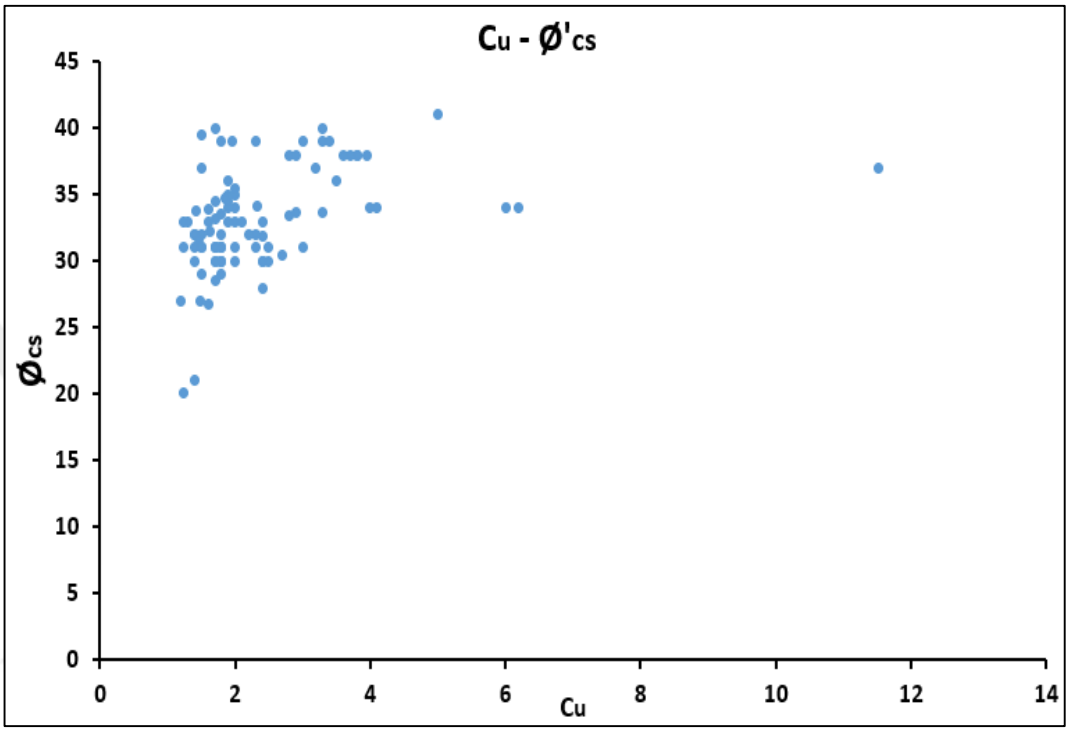


Figure 4.21. C_u – $Ø_{cs}$ relationship.

Effect of median grain size (D_{50}) on stress-dilatancy coefficients was also examined. It was observed that there is a relationship between *r* and D_{50}, as shown in Figure 4.22, however this relationship became only countable when soils consisting of quartz grains and similar grain shapes were compared. Relevantly, this relationship is plotted respectively in Figures 4.23 and 4.24. On the other hand, as seen in Figure 4.25, D_{50} and Q are not related. Finally, the influence of median particle size on critical state strength of soils is presented in Figure 4.26. Both the all available literature data and current study data was used in the comparison. As observed, data is highly scattered, and no countable relationship is oberved, either. D_{50} in the tables are in milimeter units.

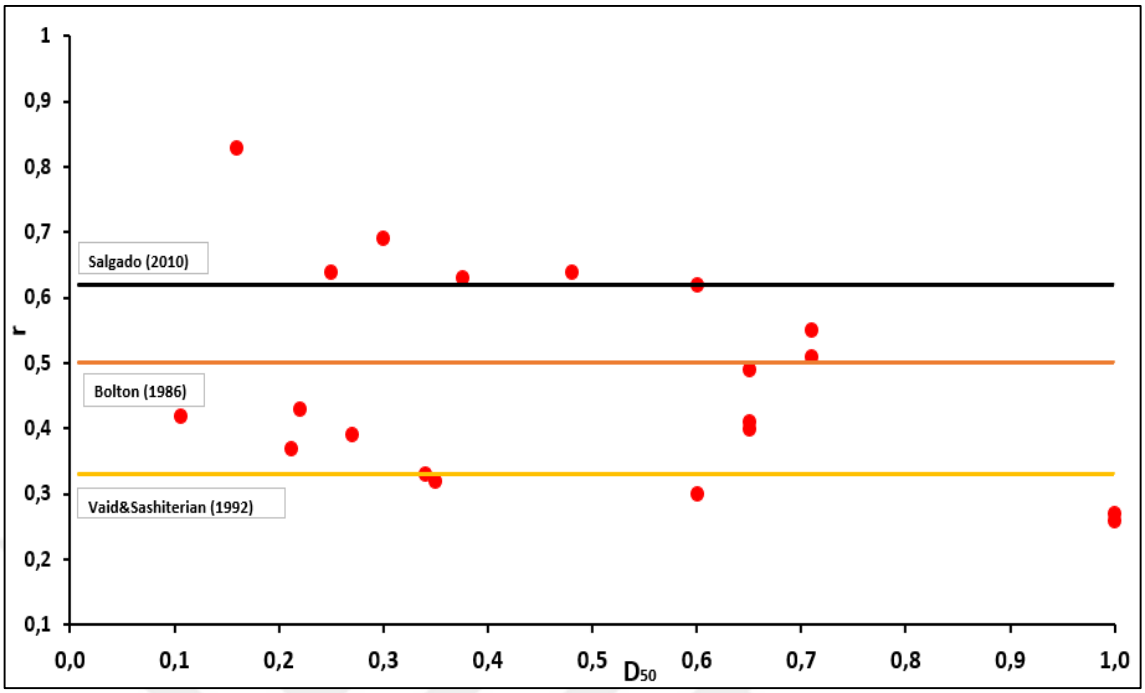


Figure 4.22. D_{50} - *r* relationship for all tested soils in AC and LE stress path and literature.

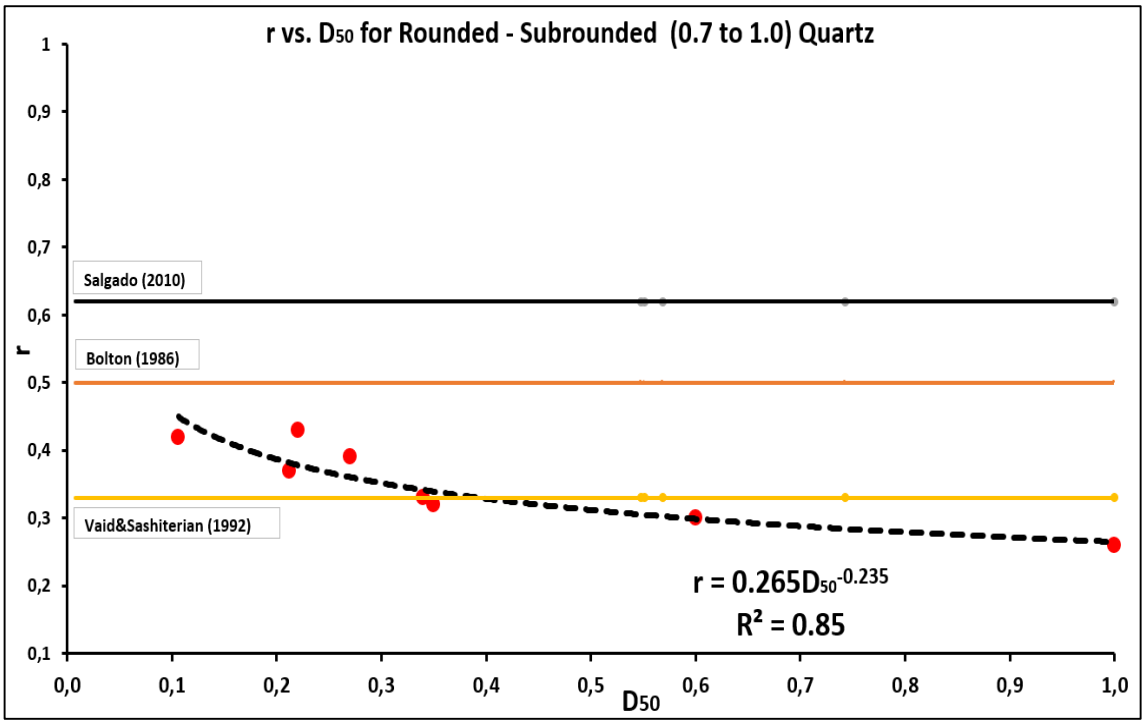


Figure 4.23. D_{50} - *r* relationship for rounded-subrounded quartz sand.

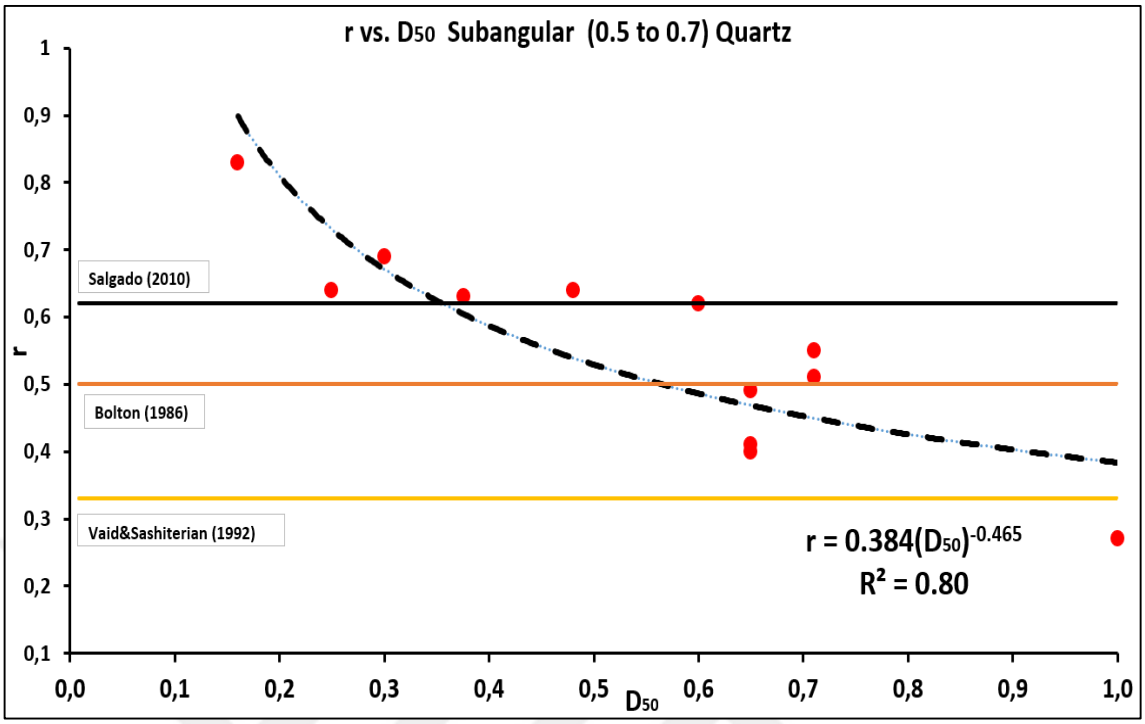


Figure 4.24. D_{50} - *r* relationship for subangular quartz sand.

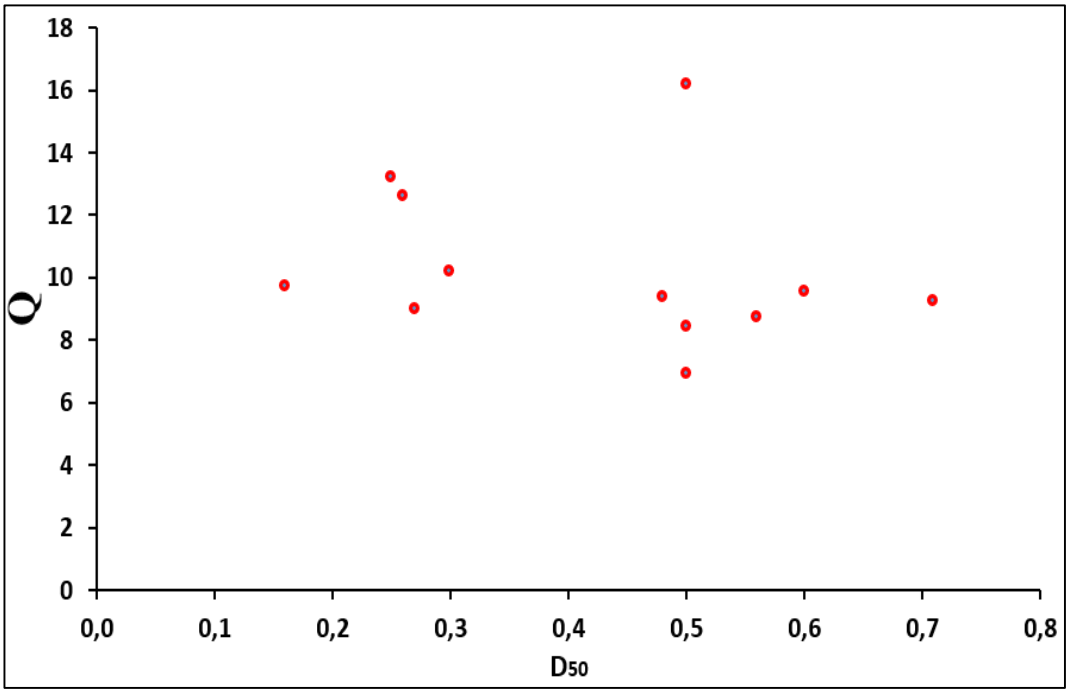


Figure 4.25. D_{50} - Q relationship.

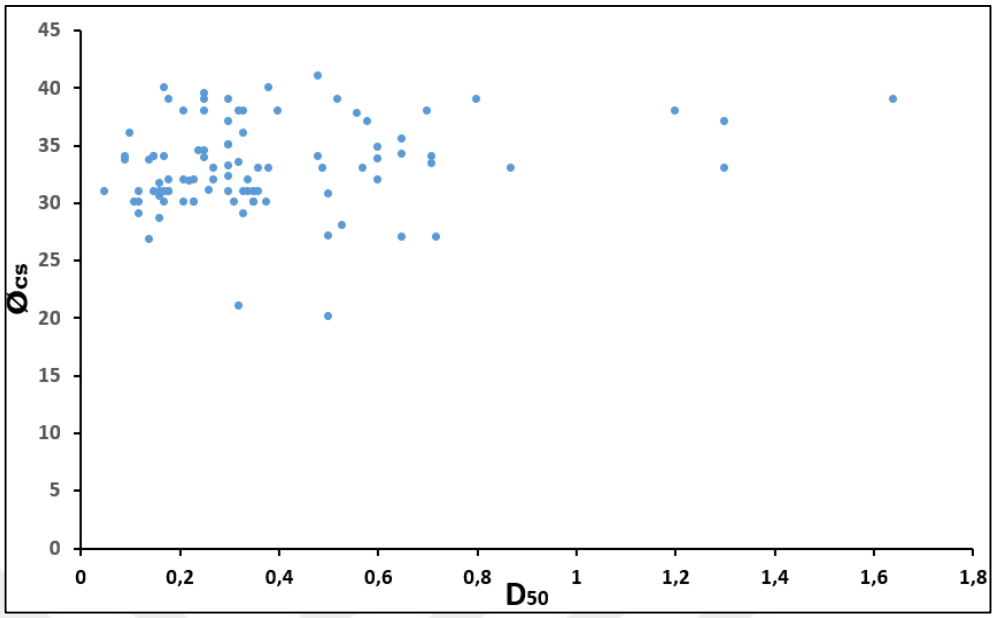


Figure 4.26. D_{50} - $Ø_{cs}$ relationship.

4.1.2. Influence of Grain Shape on Stress-Dilatancy Coefficients

To define grain shape, several empirical constants were derived by researchers, however the most widely accepted parameters are sphericity (S_{ave}) and roundness (R_{ave}). Within this research, it was observed from Table 3.3 that all tested soils tend to consist of similar roundness values. Therefore to provide comparability, S_{ave} was selected as the parameter which represents grain shape of a particular granular soil. To start with, as plotted in Figure 4.27, S_{ave} and '*r*' is not directly related. However as presented in Figures 4.23 and 4.24, in order to count the relationship between grain size and '*r*', empirical correlations are close to the fitted regression line only when the data is grouped under different grain shape ranges. Next, the influence of grain shape on Bolton (1986)'s line-fitting Q and R parameters were investigated. Provided that R = 1 as presented in Figure 4.28, there is a unique relationship between S_{ave} and Q. However, the available data in literature is scarce. As presented in Table 2.2, excluding current research data Q values were only avaliable from the research of Chakraborty and Salgado (2010), Lee *et al.* (2013) and Bradshaw *et al.* (2017). It is noted that only the data of quartz sand was used in S_{ave} – Q comparison because the relationship becomes only countable when soils apart from quartz are excluded from comparison. Also, the relationship is countable for particle sphericity values more than 0.5.

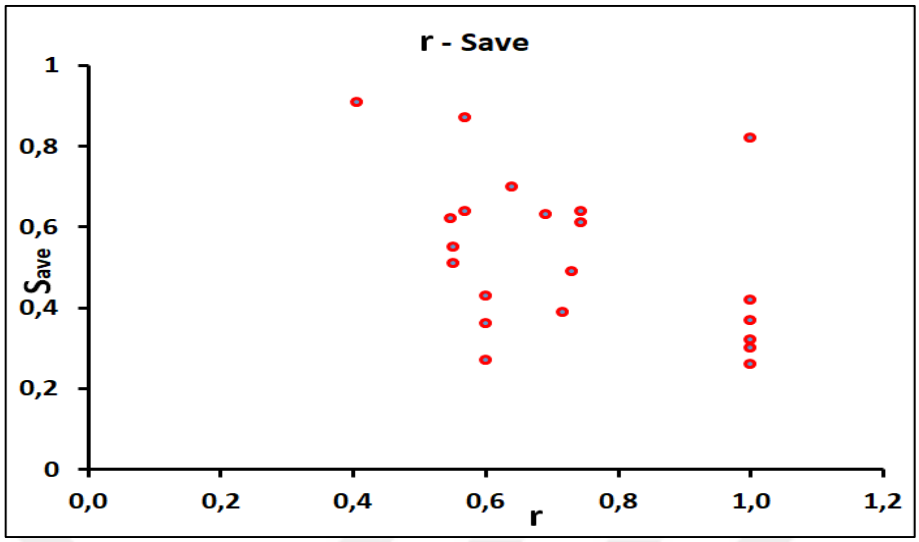


Figure 4.27. S_{ave} - r relationship.

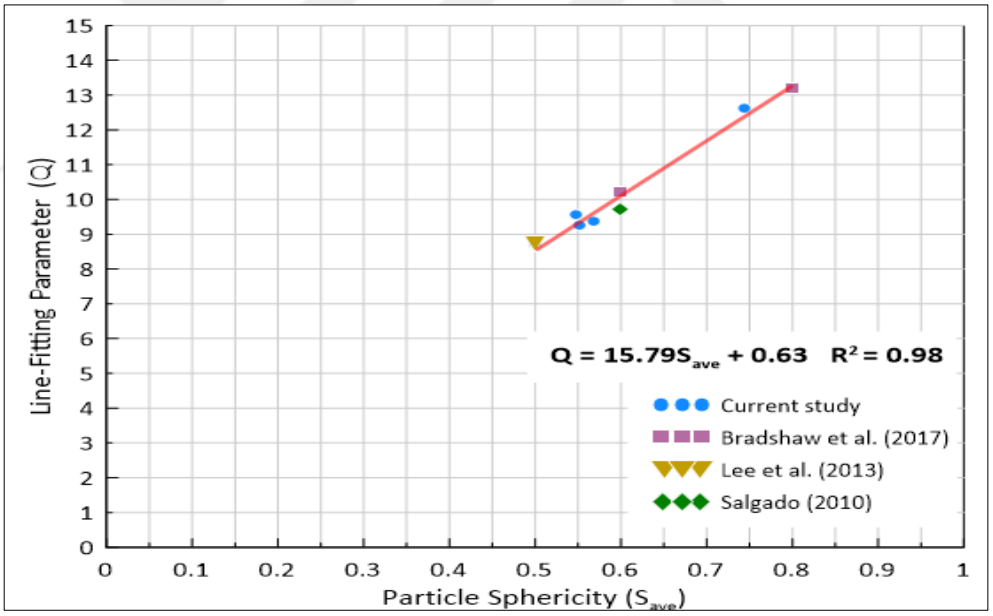


Figure 4.28. S_{ave} – Q relationship provided that R =1.

Finally, due to the presence of high variabilty on literature data, the influence of both sphericity and roundness on critical state friction angle of granular soils were seperately investigated, and presented respectively in Figure 4.29. For both S_{ave} and R_{ave} relationships, combination of avaliable data in literature and tested soils in current research is very scattered, therefore a countable relationship can not be proposed. However, graphs indicate

that if the grains are less angular (higher sphericity-roundness), critical state friction angle of granular soils is less. Although the coefficient is determination is too low, correlation between S_{ave} and $Ø'_{cs}$ is presented. Uniformity coefficient (C_u) of soils were also included in the comparison, and it is revealed that well graded soils have higher critical strengths.

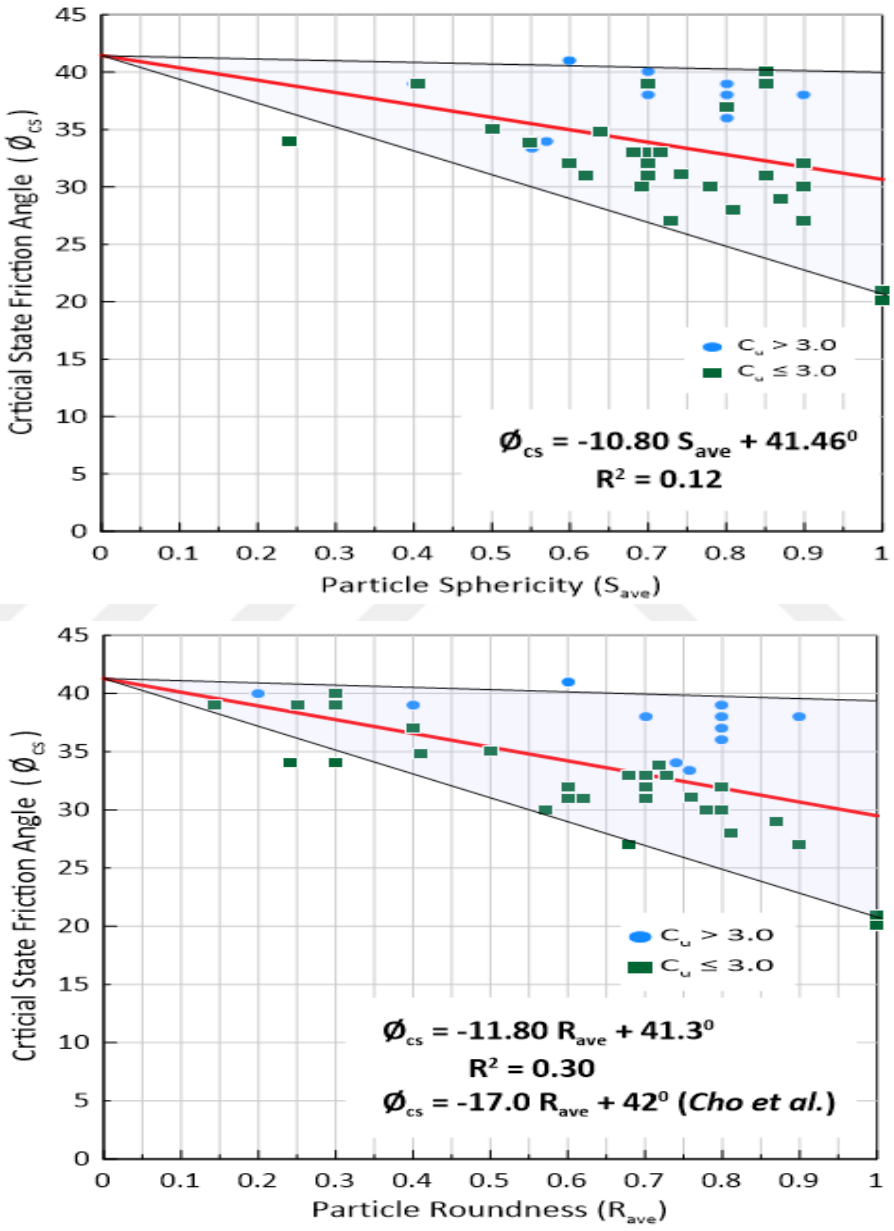


Figure 4.29. S_{ave} – $Ø_{cs}$ and R_{ave} – $Ø_{cs}$ relationship.

Equation proposed by Cho *et al.* (2006) was modified with current test results and avaliable up-to-date research data. Hence, $Ø_{cs}$ - R relationship proposed by Cho *et al.* (2006) was revised.

$$\emptyset'_{cs} = -10.8S_{ave} + 41.5^0 \text{ (proposed in this study)} \quad (4.5)$$

$$\emptyset'_{cs} = -17.0R_{ave} + 42.0^0 \text{ (Cho } et\ al.\text{, 2006)} \quad (4.6)$$

$$\emptyset'_{cs} = -11.8R_{ave} + 41.3^0 \text{ (proposed in this study)} \quad (4.7)$$

In Figure 4.30, both grain sphericity and roundness were merged into a single equation for predicting the critical state friction angle. However, it came out that again the coefficient of determination is very low for a linear relationship to be proposed, but the correlation well fits between S_{ave} - $\emptyset_{cs}$ and R_{ave} - $\emptyset_{cs}$ relationships.

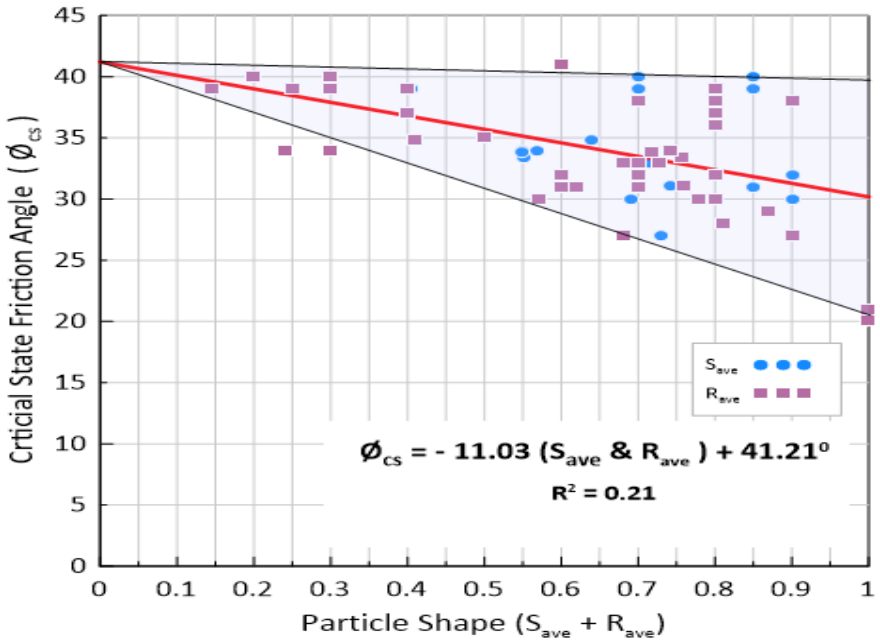


Figure 4.30. Grain shape – $Ø_{cs}$ relationship.

In conclusion, interpretation of triaxial tests conducted within this research with avaliable data in literature deducts the below given outcome:

(i) To count the influence of grain size on stress-dilatancy correlation coefficients, median grain size (D_{50}) is the most comparable parameter. However, to empirically propose a relationship, different ranges of grain angularity should be taken into account. Morover, equation is only valid for quartz sand. Consequently, for quartz sand:

$$r = 0.265\ (D_{50})^{-0.235} \text{ if } S_{ave} \geq 0.7 \ (D_{50} \text{ in mm}) \quad (4.8)$$

$$r = 0.384\ (D_{50})^{-0.465} \text{ if } S_{ave} \leq 0.7 \ (D_{50} \text{ in mm}) \quad (4.9)$$

Additionally, it is observed that soils consisting of larger grain sizes and better gradation (higher D_{50} and C_u values) tend to have higher ciritcal frictional strength.

(ii) Grain angularity both influences the contribution of dilatant behavior on soil strength (r) and Bolton's (1986) line-fitting Q and R dilatancy index parameters and critical state friction angle ($Ø_{cs}$). Granular soils consisting of more angular grains possess lower Q but higher '*r*' and higher ($Ø_{cs}$) values. However, only the relationship between grain shape and Q parameter is countable when R = 1 for simplicity. Consequently, it is proposed that:

$$Q = (15.79 \times S_{ave}) + 0.63 \quad (4.10)$$

Where S_{ave} is the average sphericity of the granular soil. The proposed equation is valid for different loading conditions provided that $S_{ave} > 0.5$ and samples are predominantly quartz. However, the literature data variability is scarce; and to strengthen the propsoed equation it is recommended to collate with more granular soil data.

(iii) Although the literature data is very extensive, it is not possible to propose a countable relationship between critical state friction angle and grain size/shape due to the scattered data. However, in this research, empirical correlation of $Ø'_{cs} = -17.0R_{ave} + 42.0^0$ proposed by Cho *et al.* (2006) between $Ø_{cs}$ and grain shapes (R_{ave} , S_{ave}) was modified as given in equations (4.5) and (4.7).

(iv) Regardless of soil type and loading condition, average '*a'* values which define the rate of dilation are strain-independent and almost equal to 0.30, as given in Tables 4.9 and 4.10. This observation fits well with Bolton (1986) and Salgado (2010) proposals.

$$\left(-\frac{d\varepsilon_v}{d\varepsilon_1}\right)_{max} = aI_R \ \rightarrow a \approx 0.30 \quad (4.11)$$

(v) Results also reveal that loading condition of the specimens do not considerably affect the critical state friction angle and the stress-dilatancy coefficients which is in well agreement with theory. However, for lateral extension tests, peak dilatancy angles and peak friction angles are slightly higher than axial compression tests (Figure 4.31). This finding is coherent with Lambe and Whitman (1969) and Tang-Tat Ng (2005).

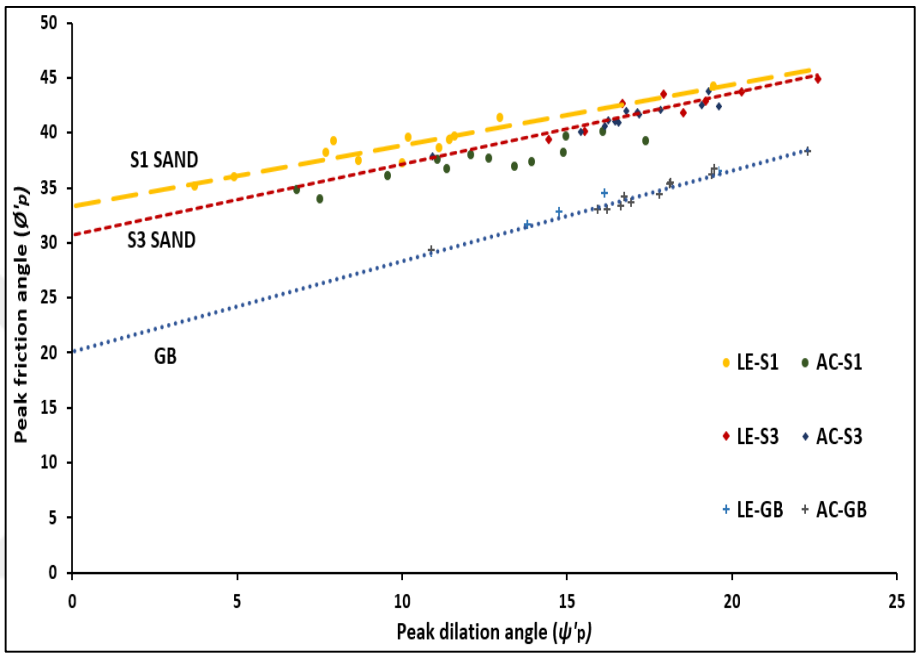


Figure 4.31. Effect of loading condition on strength properties.

Therefore, it is concluded that triaxial test results and the variance of the effect of grain characteristics such as median grain size, grain shape and grain size distribution on dilatant behavior are comparable with existing research results available in literature. This strenghtens the reliability and accuracy of test results. However, conducting CD tests are difficult and time consuming, but is the only exact method to define strength parameters of granular soils. Proposed correlations in this research are only an evidence that mechanical properties of engineering materials are considerably affected by grain characteristics, and can be used as data of further research.

4.2. Physical Model Tests

Particle image velocimetry analysis displays are given in Figures 4.32 to 4.36 respectively for the small-scale physical retaining wall model experiments conducted with S1, S3, SW-S2, SP-S2 sands and GB.

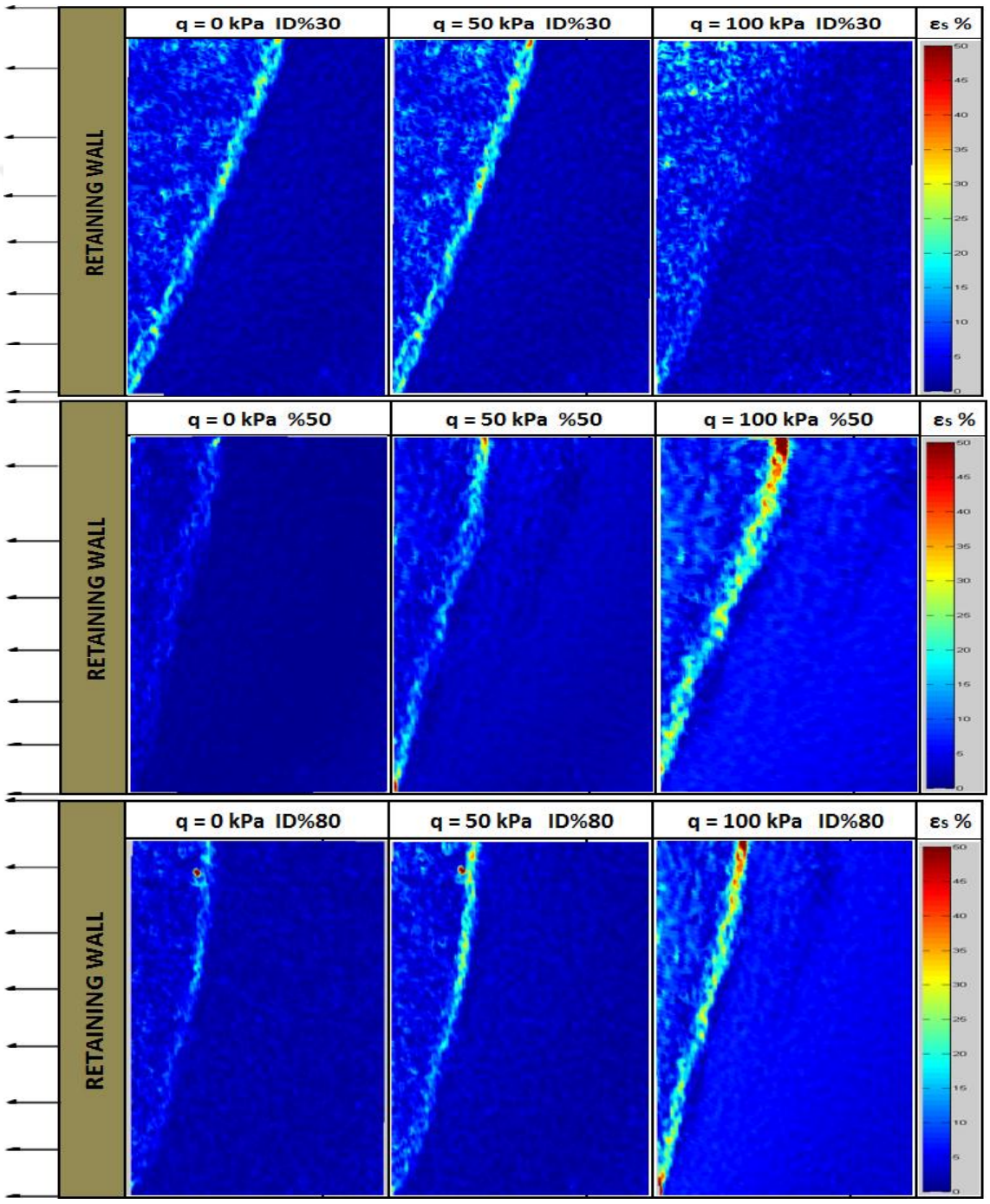


Figure 4.32. PIV analysis results for S1 sand.

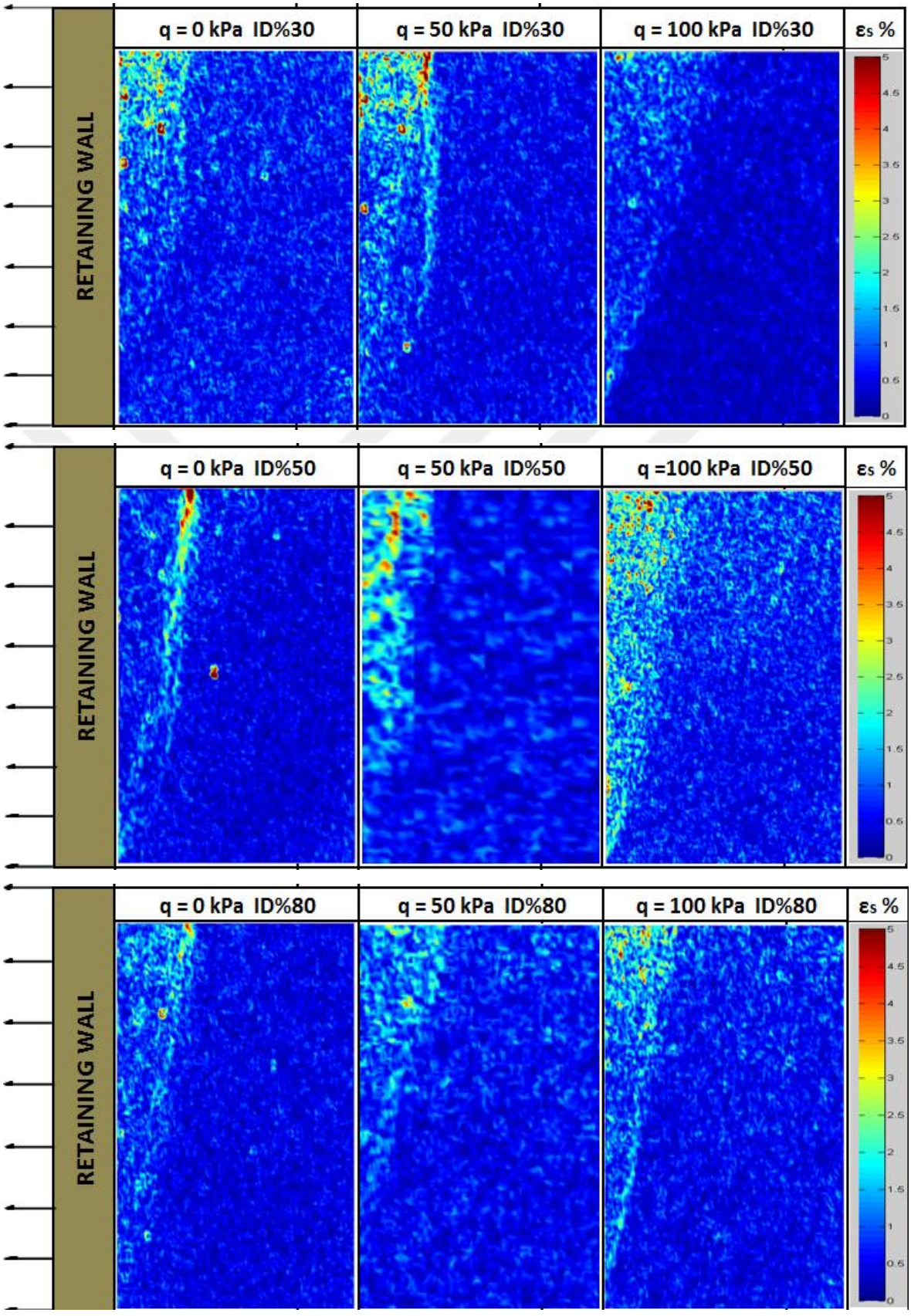


Figure 4.33. PIV analysis results for S3 sand.

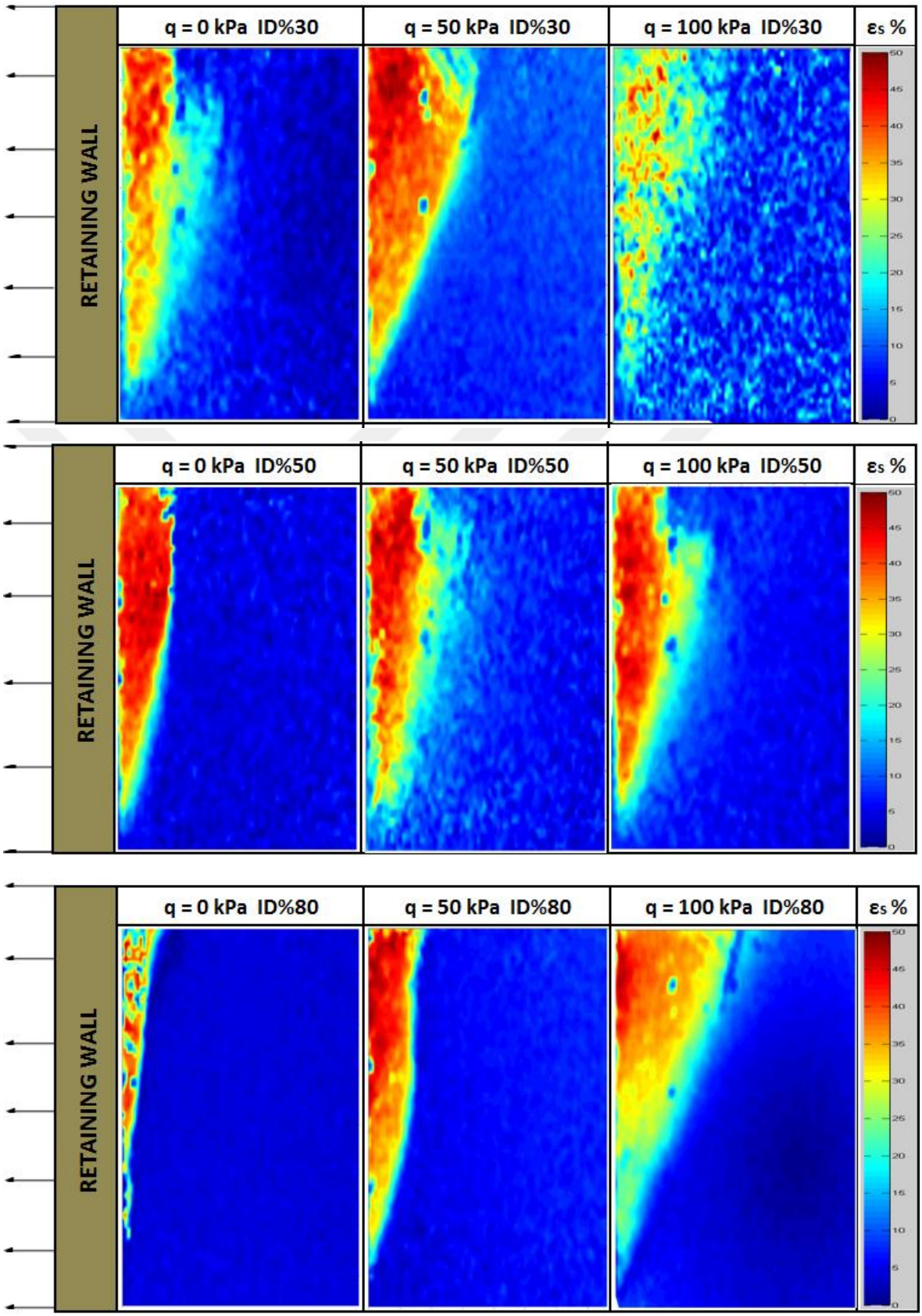


Figure 4.34. PIV analysis results for SW-S2.

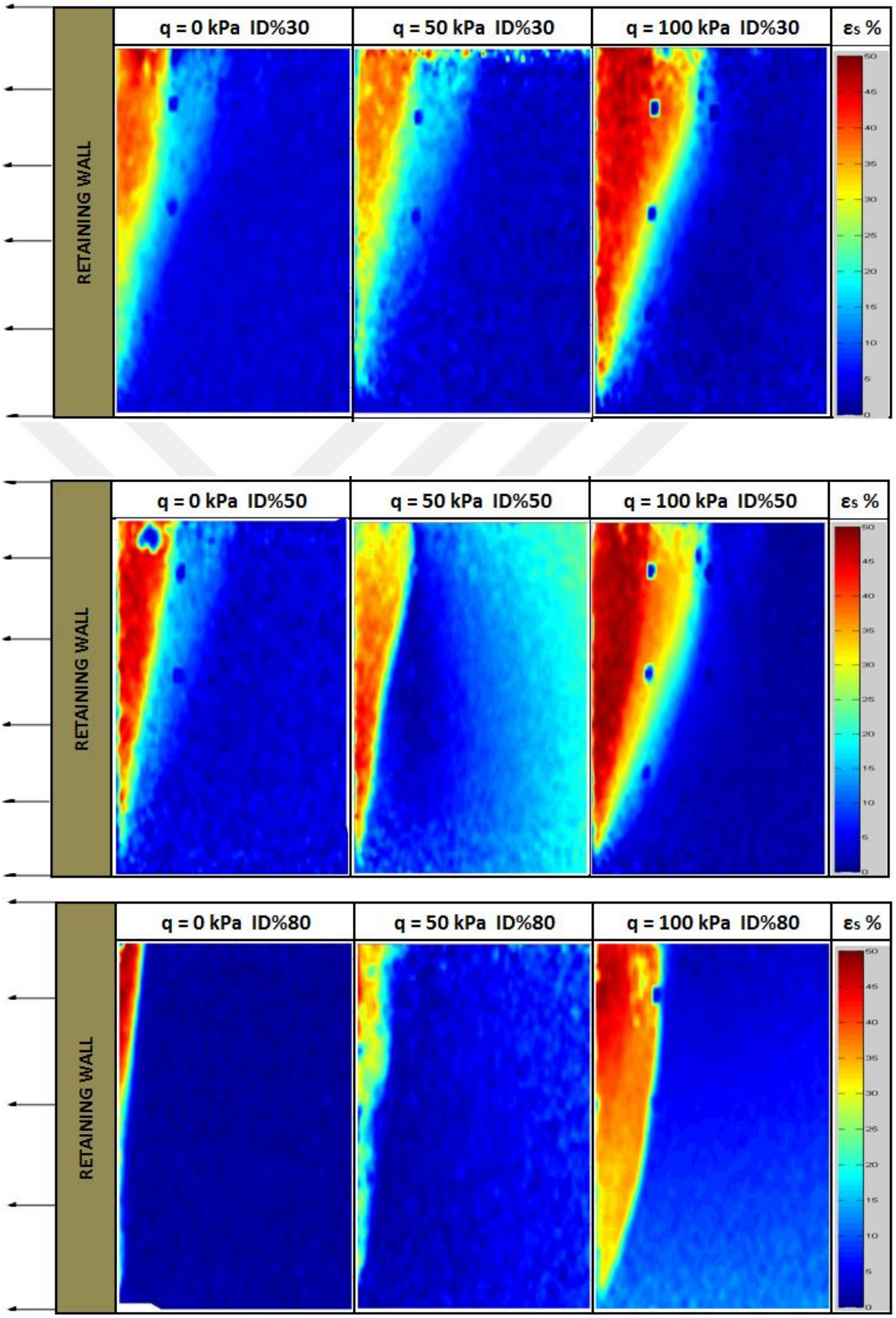

q = 0 kPa ID%30
q = 50 kPa ID%30
q = 100 kPa ID%30
εs %
RETAINING WALL
q = 0 kPa ID%50
q = 50 kPa ID%50
q = 100 kPa ID%50
εs %
RETAINING WALL
q = 0 kPa ID%80
q = 50 kPa ID%80
q = 100 kPa ID%80
εs %
RETAINING WALL

Figure 4.35. PIV analysis results for SP-S2.

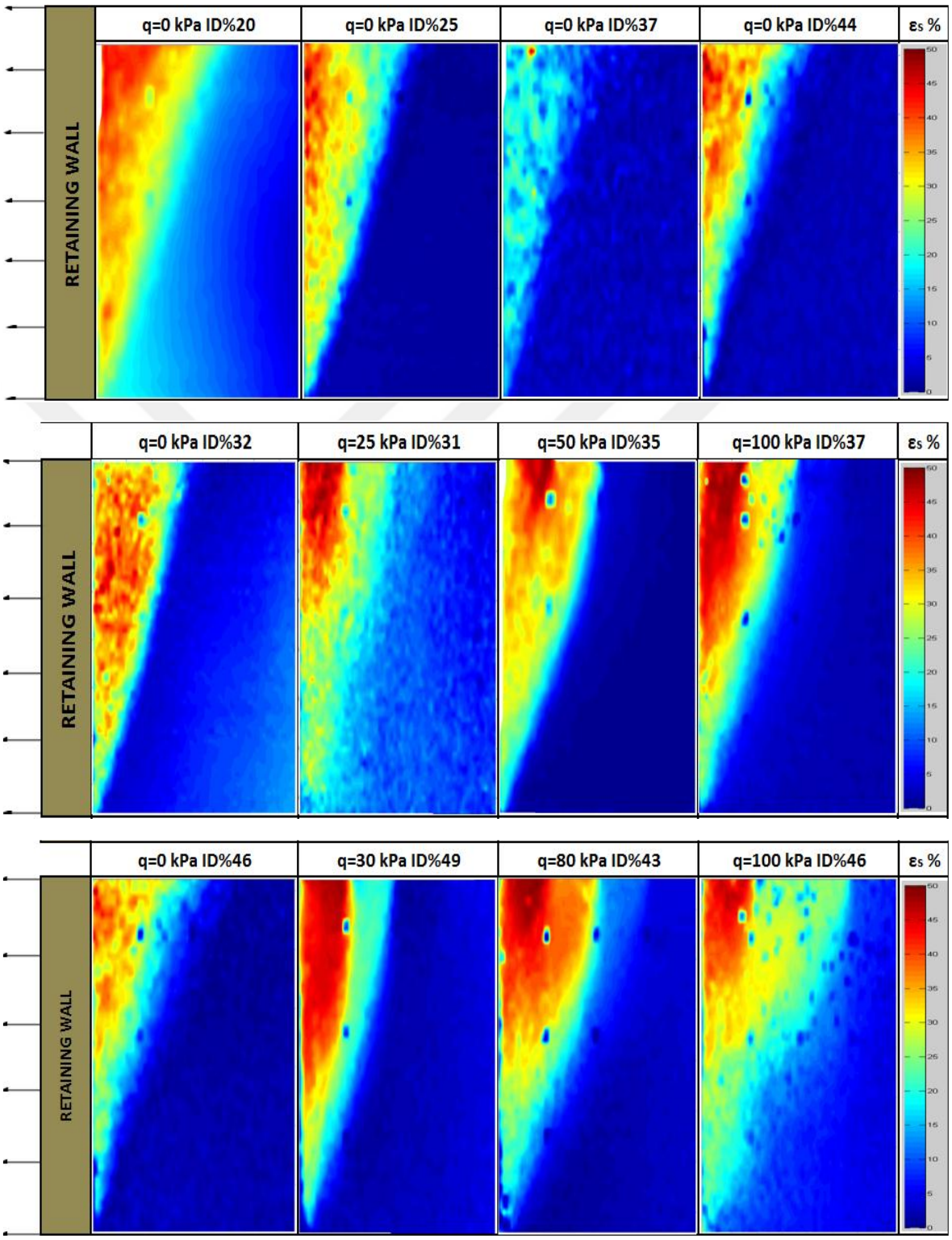


Figure 4.36. PIV analysis results for GB.

The analysis results indicate that for all sand classes increasing initial density results in steeper shear bands for the same stress levels. On the other hand, the sands exhibit lower strengths under high surcharge pressures at similar density ranges since the dilatant behavior is suppressed. This outcome fits well with conventional stress-dilatancy theories available in literature. The observed shear bands correspond to large shearing strains where dilatant behavior at its peak state influences the evaluation of the shear bands.

In order to investigate the influence of dilatancy on shear band geometry, peak friction angle and peak dilation angle of the backfills at the failure state for each physical model test were calculated using Bolton (1986) stress-dilatancy relationship. To evaluate peak dilatancy, mean effective stresses at failure (p'_f) were calculated for each test. Due to the frictional forces at side wall-soil interface and the geometry of model frame, the physical model represents true triaxial conditions with three dimensions where:

$$p'_f = \left(\sigma'_{1f} + \sigma'_{2f} + \sigma'_{3f}\right)/3 \tag{4.13}$$

$$\sigma'_{1f} = \sigma'_{vf} \tag{4.14}$$

$$\sigma'_{2f} \times A_{sw} = K_0 \sigma'_{vf} A_{sw} - K_0 \sigma'_{vf} \tan\delta A_p \tag{4.15}$$

$$\sigma'_{3f} = \sigma'_{hf} \tag{4.16}$$

Here, A_{sw} represents the side frame area of the physical model box, A_p is the area of the shear wedge and δ is side wall-soil friction angle measured by simple shear tests.

Stress-displacement relationship was plotted by using the values read by pressure and displacement sensors during wall transition. Vertical stresses and horizontal stresses at failure state were recorded. Next, the failure point was located and selected as the maximum stress value which did not increase with any additional wall displacement (Figure 4.37).

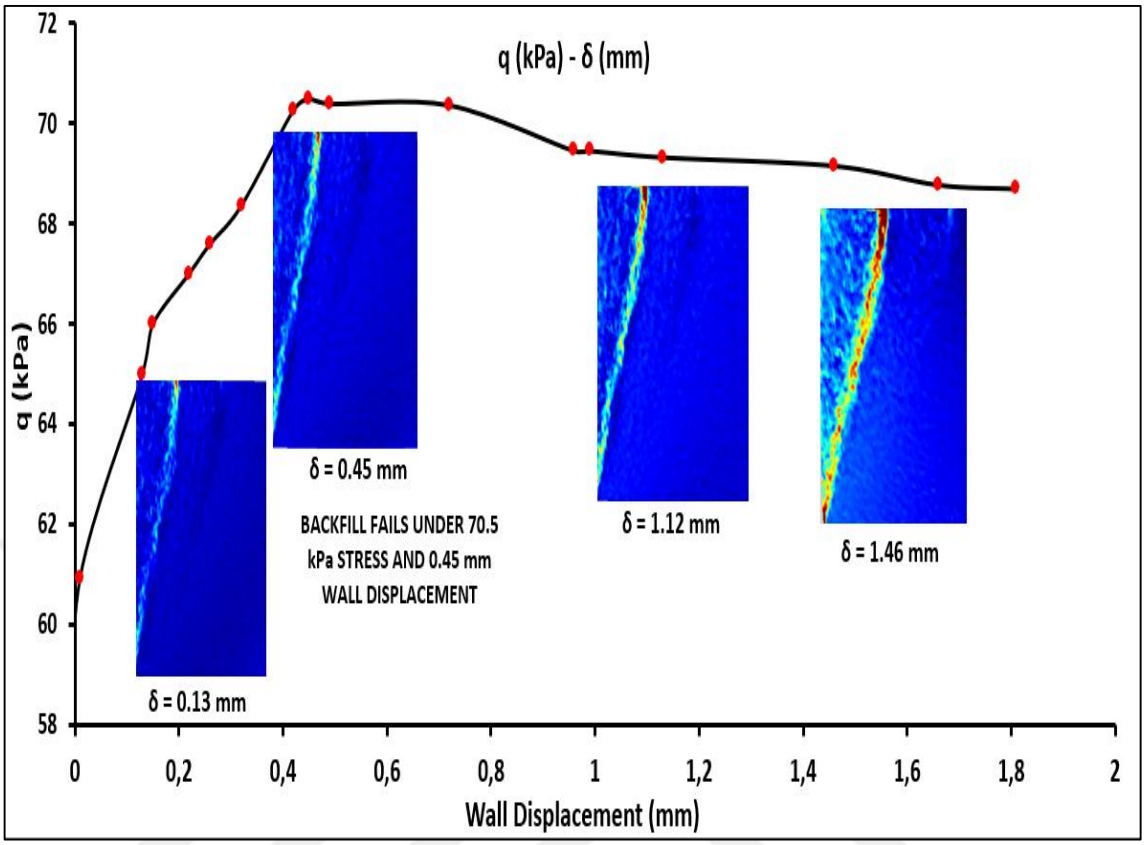


Figure 4.37. Deviatoric stress – wall displacement graph for a particular physical model experiment.

The pressures recorded by the sensors during physical retaining wall model tests do not equally represent the actual vertical ($\sigma_{1,act}$) and actual horizontal ($\sigma_{3,act}$) stresses which were generated at wall surfaces. The reason for this difference is that at failure state the soil wedge moves downward, mobilizing friction at the slip surface, between plexiglass frame and shear wedge, and between retaining wall and shear wedge. These additional stresses due to friction should be excluded from the measured stress values by pressure sensors so that the actual vertical and horizontal stress at failure state on a soil element within the shear wedge could be evaluated. In this way, the principal stresses at failure state would be excluded from frictional effects, hence the influence of pure dilatant behavior on peak strength would be evaluated within physical model tests. This situation is demonstrated in Figure 4.38 below.

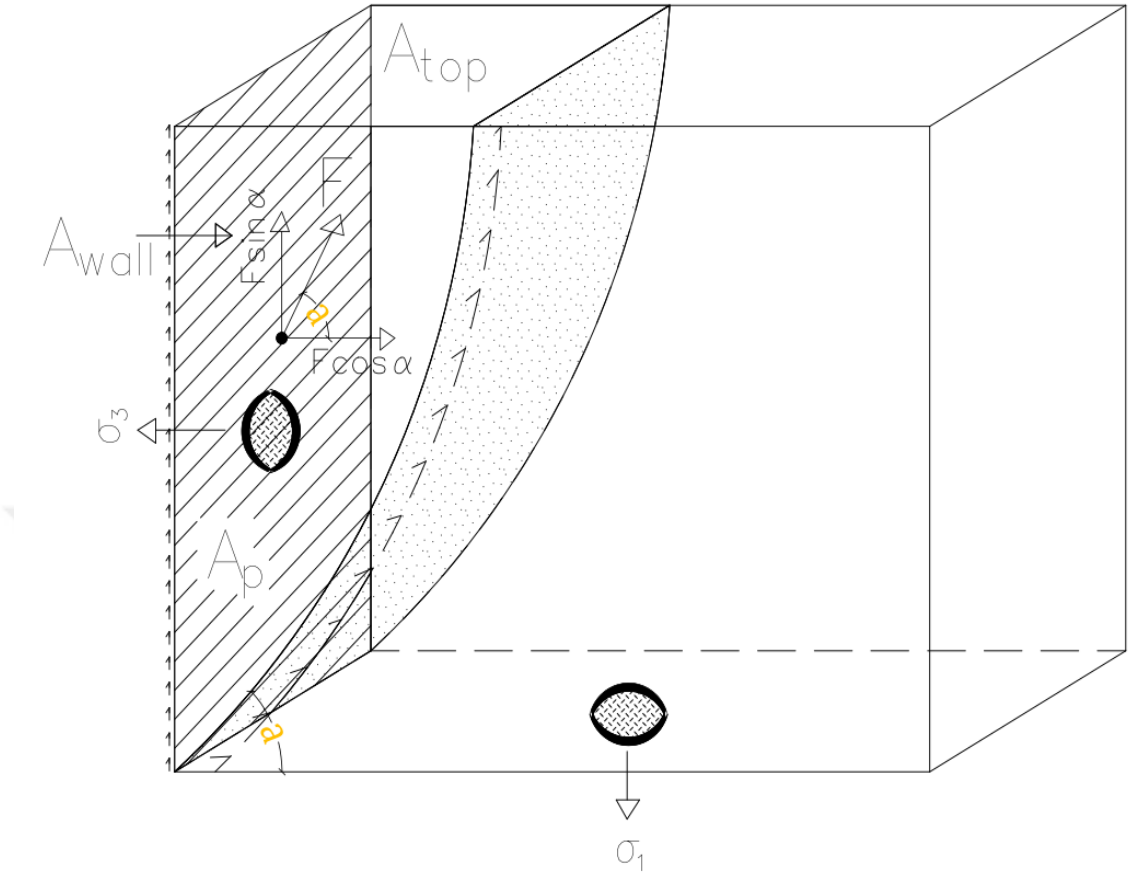


Figure 4.38. Visualization of friction forces between shear wedge and model frame.

Accordingly,

$$\sigma_{1,act} = \frac{\sigma_1 A_{top} - 2\sigma_1 K_0 tan\delta A_p sin\alpha - \sigma_3 tan\mu A_{wall}}{A_{top}} \quad (4.17)$$

$$\sigma_{3,act} = \frac{\sigma_3 A_{wall} - 2\sigma_1 K_0 tan\delta A_p cos\alpha}{A_{wall}} \quad (4.18)$$

where, the symbols stand for the following:

A_{top} : Area of the top of frame between retaining wall and slip surface

A_{wall} : Area of the translating retaining wall

A_p : Area of the shear wedge

δ: Interface friction angle between soil and plexiglass frame

α : Inclination angle of slip surface from horizontal axis

The relative density of the backfills (I_D) were determined by measuring total mass of the granular soil and the volume of the filled area prior to testing. Bolton (1986) stress-dilatancy relationship coefficients (Q, R, r) which were calculated for each sand by consolidated drained triaxial tests were used in the Bolton's (1986) stress-dilatancy correlation in order to calculate the dilatancy index (I_R) values for each test. In this line, dilation and friction angles of the backfill soils were calculated.

$$sin\psi'_{p,calc} = \frac{aI_R}{2+aI_R} \tag{4.19}$$

$$r_{act} = \frac{\emptyset'_{p,act} - \emptyset'_{cs}}{\psi'_p} \tag{4.20}$$

Within the scope of this research, friction angles which were calculated using the existing modified stress-dilatancy relationship of Bolton (1986) were compared with the experimentally quantified actual friction angles of the granular soils evaluated by stress distribution in the physical retaining wall model at active failure state. Peak friction angle of the backfills at the failure state for each physical model test was calculated using Mohr-Coulomb failure criterion. Actual vertical and horizontal stresses at failure of the backfill were used to draw Mohr's circle and evaluate the peak friction angle.

$$\emptyset'_{p,act} = sin^{-1}\frac{(\sigma'_{1,act} - \sigma'_{3,act})}{(\sigma'_{1,act} + \sigma'_{3,act})} \tag{4.21}$$

Tables 4.11 to 4.20 below summarize the measured actual vertical and horizontal stresses, lateral earth pressure coefficients at active conditions, calculated peak dilatancy angle and friction angle values using Bolton's (1986) stress-dilatancy coefficients, evaluated actual peak friction angles by Mohr-Coulomb criterion using the measured actual stresses from the physical model tests and stress-dilatancy correlation coefficients from physical model tests for each sand type respectively.

Table 4.11. Measured vs. actual principal stresses of S1 sand

Test No.	ID_{av} %	σ'_{1f} *(measured)*	σ'_{3f} *(measured)*	K_0	p'_0 *(kPa)*	σ'_{1f} *(actual)*	σ'_{2f} *(actual)*	σ'_{3f} *(actual)*	K_a	p'_a *(kPa)*
1	**40**	**1,5**	**3,9**	**0,39**	**2,3**	**3,52**	**1,45**	**0,63**	**0,18**	**2,01**
2	**40**	**13,5**	**38,0**	**0,36**	**21,7**	**34,51**	**12,98**	**7,37**	**0,21**	**19,69**
3	**40**	**32,5**	**89,8**	**0,36**	**51,6**	**81,22**	**31,11**	**18,09**	**0,22**	**46,89**
4	**51**	**1,5**	**4,0**	**0,38**	**2,3**	**3,61**	**1,46**	**0,64**	**0,18**	**2,04**
5	**51**	**11,8**	**40,0**	**0,30**	**21,2**	**37,04**	**11,55**	**7,32**	**0,20**	**19,98**
6	**51**	**44,2**	**95,8**	**0,46**	**61,4**	**84,18**	**42,56**	**17,95**	**0,21**	**52,92**
7	**61**	**1,5**	**4,0**	**0,38**	**2,3**	**3,66**	**1,47**	**0,62**	**0,17**	**2,05**
8	**61**	**15,3**	**45,2**	**0,34**	**25,2**	**41,54**	**15,03**	**7,75**	**0,19**	**23,11**
9	**61**	**36,5**	**89,5**	**0,41**	**54,2**	**80,40**	**35,53**	**16,16**	**0,20**	**47,84**
10	**80**	**1,7**	**4,2**	**0,41**	**2,5**	**3,78**	**1,67**	**0,60**	**0,16**	**2,17**
11	**80**	**21,0**	**44,4**	**0,47**	**28,8**	**39,66**	**20,76**	**6,80**	**0,17**	**24,45**
12	**80**	**50,8**	**94,6**	**0,54**	**65,4**	**82,31**	**49,62**	**15,55**	**0,19**	**54,21**

Table 4.12. Actual vs. calculated strength – dilatancy parameters of S1 sand

Test No.	$Ø'_{p,act}$ (Eq. 4.21)	$\psi'_{p,act}$ (Eq. 4.20)	I_R (Eq. 2.8)	$\psi'_{p,calc}$ (Eq. 4.19)	$Ø'_{p,calc}$	*r (act)* (Eq. 4.20)	a *(act)* (Eq. 4.19)
1	**44,1**	**19,4**	**2,7**	**16,9**	**42,7**	**0,63**	**0,36**
2	**40,4**	**12,7**	**1,8**	**12,4**	**40,2**	**0,57**	**0,31**
3	**39,5**	**11,0**	**1,5**	**10,4**	**39,1**	**0,58**	**0,32**
4	**44,4**	**19,9**	**3,5**	**20,2**	**44,5**	**0,54**	**0,29**
5	**42,1**	**15,8**	**2,4**	**15,1**	**41,7**	**0,57**	**0,32**
6	**40,4**	**12,8**	**1,9**	**12,6**	**40,3**	**0,56**	**0,31**
7	**45,4**	**21,8**	**4,2**	**22,8**	**46,0**	**0,52**	**0,28**
8	**43,3**	**18,0**	**2,8**	**17,0**	**42,7**	**0,58**	**0,32**
9	**41,7**	**15,1**	**2,3**	**14,9**	**41,6**	**0,56**	**0,30**
10	**46,4**	**23,7**	**5,6**	**27,0**	**48,3**	**0,48**	**0,24**
11	**45,0**	**21,1**	**3,6**	**20,6**	**44,7**	**0,56**	**0,31**
12	**43,0**	**17,5**	**3,0**	**18,0**	**43,3**	**0,54**	**0,29**
						avg. = 0.56	**avg. = 0.31**

Calculated Stress-Dilatancy Coefficients of S1 sand (From Table 4.9)				
Q	**R**	**r**	**$Ø_{cs}$**	**a**
7.90	**0.15**	**0.55**	**33.4**	**0.30**
$$I_R = I_D(Q - lnp') - R$$				

Table 4.13. Measured vs. actual principal stresses of S2-SW sand

Test No.	ID_{av} %	σ'_{1f} *(measured)*	σ'_{3f} *(measured)*	K_0	p'_0 *(kPa)*	σ'_{1f} *(actual)*	σ'_{2f} *(actual)*	σ'_{3f} *(actual)*	K_a	p'_a *(kPa)*
1	**31**	**2,53**	**3,35**	**0,76**	**2,8**	**2,81**	**2,70**	**0,56**	**0,20**	**2,4**
2	**51**	**1,81**	**3,13**	**0,58**	**2,3**	**2,79**	**1,78**	**0,51**	**0,18**	**1,8**
3	**79**	**3,95**	**5,05**	**0,78**	**4,3**	**4,35**	**3,70**	**0,75**	**0,17**	**3,1**
4	**34**	**21,42**	**52,79**	**0,41**	**31,9**	**48,33**	**21,32**	**9,77**	**0,20**	**29,0**
5	**51**	**30,15**	**50,32**	**0,60**	**36,9**	**43,32**	**30,98**	**8,17**	**0,19**	**31,5**
6	**80**	**29,17**	**50,15**	**0,58**	**36,2**	**43,61**	**31,88**	**7,69**	**0,18**	**32,6**
7	**32**	**50,43**	**100,04**	**0,50**	**67,0**	**91,06**	**53,82**	**18,79**	**0,21**	**62,6**
8	**52**	**48,84**	**98,66**	**0,50**	**65,4**	**88,36**	**50,09**	**17,34**	**0,20**	**58,8**
9	**75**	**44,55**	**96,25**	**0,46**	**61,8**	**87,65**	**49,97**	**16,45**	**0,19**	**60,4**

Table 4.14. Actual vs. calculated strength – dilatancy parameters of S2-SW sand

Test No.	$Ø'_{p,act}$ (Eq. 4.21)	$\psi'_{p,act}$ (Eq. 4.20)	I_R (Eq. 2.8)	$\psi'_{p,calc}$ (Eq. 4.19)	$Ø'_{p,calc}$	*r (act)* (Eq. 4.20)	a *(act)* (Eq. 4.19)
1	**41,9**	**12,4**	**1,9**	**13,3**	**42,5**	**0,59**	**0,29**
2	**43,6**	**15,0**	**3,5**	**21,0**	**47,5**	**0,46**	**0,20**
3	**45,1**	**17,3**	**5,3**	**27,2**	**51,4**	**0,41**	**0,16**
4	**41,6**	**11,9**	**1,2**	**9,6**	**40,1**	**0,79**	**0,42**
5	**43,1**	**14,1**	**2,0**	**14,3**	**43,1**	**0,63**	**0,32**
6	**44,4**	**16,3**	**3,4**	**20,8**	**47,3**	**0,50**	**0,23**
7	**41,1**	**11,2**	**0,9**	**7,2**	**38,6**	**0,99**	**0,53**
8	**42,2**	**12,8**	**1,8**	**12,8**	**42,2**	**0,64**	**0,32**
9	**43,2**	**14,3**	**2,7**	**17,7**	**45,3**	**0,52**	**0,24**
						avg. = 0.61	**avg. = 0.30**

Calculated Stress-Dilatancy Coefficients of S2-SW sand (From Table 4.9)				
Q	**R**	**r**	**$Ø_{cs}$**	**a**
8.35	**0.45**	**0.64**	**34.0**	**0.32**
$$I_R = I_D(Q - lnp') - R$$				

Table 4.15. Measured vs. actual principal stresses of S2-SP sand

Test No.	ID_{av} %	σ'_{1f} *(measured)*	σ'_{3f} *(measured)*	K_0	p'_0 *(kPa)*	σ'_{1f} *(actual)*	σ'_{2f} *(actual)*	σ'_{3f} *(actual)*	K_a	p'_a *(kPa)*
1	**33**	**0,77**	**2,31**	**0,33**	**1,3**	**2,15**	**0,86**	**0,43**	**0,20**	**1,3**
2	**51**	**1,15**	**3,18**	**0,36**	**1,8**	**2,96**	**1,23**	**0,58**	**0,19**	**1,8**
3	**79**	**1,81**	**4,33**	**0,42**	**2,7**	**4,01**	**1,72**	**0,73**	**0,18**	**2,2**
4	**29**	**18,95**	**43,01**	**0,44**	**27,0**	**38,90**	**19,10**	**8,03**	**0,21**	**24,3**
5	**50**	**23,84**	**46,81**	**0,51**	**31,5**	**41,29**	**25,74**	**8,21**	**0,20**	**29,2**
6	**76**	**22,36**	**44,11**	**0,51**	**29,6**	**39,41**	**23,14**	**7,42**	**0,19**	**26,5**
7	**31**	**45,05**	**96,63**	**0,47**	**62,2**	**87,83**	**45,47**	**18,48**	**0,21**	**56,0**
8	**52**	**52,57**	**96,08**	**0,55**	**67,1**	**84,71**	**52,01**	**17,21**	**0,20**	**57,3**
9	**79**	**39,61**	**97,23**	**0,41**	**58,8**	**89,76**	**39,29**	**17,32**	**0,19**	**53,1**

Table 4.16. Actual vs. calculated strength – dilatancy parameters of S2-SP sand

Test No.	$Ø'_{p,act}$ (Eq. 4.21)	$\psi'_{p,act}$ (Eq. 4.20)	I_R (Eq. 2.8)	$\psi'_{p,calc}$ (Eq. 4.19)	$Ø'_{p,calc}$	*r (act)* (Eq. 4.20)	a *(act)* (Eq. 4.19)
1	**42,0**	**13,2**	**2,4**	**15,7**	**43,5**	**0,52**	**0,25**
2	**42,4**	**13,9**	**3,7**	**21,4**	**47,0**	**0,40**	**0,17**
3	**43,8**	**16,1**	**5,7**	**28,0**	**51,2**	**0,36**	**0,13**
4	**41,1**	**11,8**	**1,2**	**9,1**	**39,5**	**0,80**	**0,42**
5	**41,9**	**13,1**	**2,2**	**14,8**	**43,0**	**0,55**	**0,27**
6	**43,1**	**15,0**	**3,6**	**21,0**	**46,8**	**0,44**	**0,19**
7	**40,7**	**11,2**	**1,1**	**8,1**	**38,8**	**0,85**	**0,45**
8	**41,5**	**12,4**	**2,0**	**13,5**	**42,2**	**0,57**	**0,28**
9	**42,6**	**14,1**	**3,2**	**19,4**	**45,8**	**0,45**	**0,20**
						avg. = 0.55	**avg. = 0.26**

Calculated Stress-Dilatancy Coefficients of S2-SP sand (From Table 4.9)				
Q	**R**	**r**	**$Ø_{cs}$**	**a**
8.39	**0.29**	**0.62**	**33.8**	**0.31**
$$I_R = I_D(Q - lnp') - R$$				

Table 4.17. Measured vs. actual principal stresses of S3 sand

Test No.	ID_{av} %	σ'_{1f} *(measured)*	σ'_{3f} *(measured)*	K_0	p'_0 *(kPa)*	σ'_{1f} *(actual)*	σ'_{2f} *(actual)*	σ'_{3f} *(actual)*	K_a	p'_a *(kPa)*
1	**39**	**0,73**	**3,10**	**0,24**	**1,5**	**2,93**	**0,71**	**0,74**	**0,25**	**1,53**
2	**39**	**30,58**	**72,77**	**0,42**	**44,6**	**65,5**	**29,09**	**17,43**	**0,27**	**39,76**
3	**38**	**78,06**	**187,33**	**0,42**	**114,5**	**168,5**	**75,74**	**46,99**	**0,28**	**104,7**
4	**50**	**0,34**	**3,20**	**0,11**	**1,3**	**3,12**	**0,33**	**0,77**	**0,25**	**1,44**
5	**49**	**24,41**	**60,25**	**0,41**	**36,4**	**54,59**	**23,37**	**13,95**	**0,26**	**32,55**
6	**49**	**69,58**	**176,68**	**0,39**	**105,3**	**160,4**	**67,31**	**42,55**	**0,27**	**96,25**
7	**60**	**0,28**	**3,30**	**0,08**	**1,3**	**3,24**	**0,27**	**0,78**	**0,24**	**1,45**
8	**59**	**22,52**	**55,41**	**0,41**	**33,5**	**50,20**	**21,68**	**12,36**	**0,25**	**29,92**
9	**59**	**60**	**167,69**	**0,36**	**95,9**	**153,8**	**58,92**	**39,59**	**0,26**	**90,10**
10	**69**	**0,37**	**3,40**	**0,11**	**1,4**	**3,32**	**0,36**	**0,78**	**0,23**	**1,52**
11	**69**	**26,91**	**48,42**	**0,56**	**34,1**	**42,47**	**25,99**	**10,13**	**0,24**	**28,33**
12	**69**	**62,26**	**163,54**	**0,38**	**96,0**	**149,3**	**61,38**	**37,31**	**0,25**	**88,93**

Table 4.18. Actual vs. calculated strength – dilatancy parameters of S3 sand

Test No.	$Ø'_{p,act}$ (Eq. 4.21)	$\psi'_{p,act}$ (Eq. 4.20)	I_R (Eq. 2.8)	$\psi'_{p,calc}$ (Eq. 4.19)	$Ø'_{p,calc}$	*r (act)* (Eq. 4.20)	a *(act)* (Eq. 4.19)
1	**36,7**	**9,2**	**2,0**	**13,2**	**39,1**	**0,42**	**0,19**
2	**35,4**	**7,1**	**0,7**	**5,5**	**34,4**	**0,79**	**0,40**
3	**34,3**	**5,3**	**0,3**	**2,4**	**32,6**	**1,33**	**0,69**
4	**37,3**	**10,2**	**2,8**	**17,1**	**41,5**	**0,36**	**0,15**
5	**36,4**	**8,6**	**1,2**	**8,7**	**36,4**	**0,61**	**0,30**
6	**35,5**	**7,2**	**0,7**	**5,1**	**34,2**	**0,86**	**0,44**
7	**37,7**	**10,9**	**3,5**	**20,1**	**43,4**	**0,33**	**0,13**
8	**37,2**	**10,0**	**1,6**	**11,4**	**38,0**	**0,54**	**0,26**
9	**36,2**	**8,4**	**1,0**	**7,4**	**35,6**	**0,69**	**0,34**
10	**38,4**	**12,0**	**4,1**	**22,4**	**44,8**	**0,33**	**0,13**
11	**37,9**	**11,2**	**2,1**	**13,8**	**39,5**	**0,50**	**0,23**
12	**36,9**	**9,5**	**1,3**	**9,4**	**36,8**	**0,62**	**0,30**
						avg. = 0.61	**avg. = 0.30**

Calculated Stress-Dilatancy Coefficients of S3 sand (From Table 4.9)				
Q	**R**	**r**	**$Ø_{cs}$**	**a**
7.53	**0.80**	**0.61**	**31.1**	**0.30**
$$I_R = I_D(Q - lnp') - R$$				

Table 4.19. Measured vs. actual principal stresses of GB sand

Test No.	ID_{av} %	σ'_{1f} *(measured)*	σ'_{3f} *(measured)*	K_0	p'_0 *(kPa)*	σ'_{1f} *(actual)*	σ'_{2f} *(actual)*	σ'_{3f} *(actual)*	K_a	p'_a *(kPa)*
1	20	2,50	4,39	0,57	3,1	3,77	2,49	1,24	0,33	2,82
2	25	2,74	4,61	0,59	3,4	4,00	2,68	1,20	0,30	2,92
3	37	2,03	4,61	0,44	2,9	4,26	1,99	1,22	0,29	2,66
4	44	3,18	4,40	0,72	3,6	3,72	3,17	0,99	0,27	2,96
5	32	2,71	4,6	0,59	3,3	3,96	2,62	1,12	0,28	2,84
6	31	16,15	25,22	0,64	19,2	21,38	15,25	6,38	0,30	15,82
7	37	55,98	85,20	0,66	65,7	72,26	56,36	22,91	0,32	57,45
8	32	75,64	123,17	0,61	91,5	104,8	73,52	34,89	0,33	79,48
9	46	2,03	4,23	0,48	2,8	3,78	1,97	0,90	0,24	2,42
10	49	16,86	29,06	0,58	20,9	25,22	18,21	6,47	0,26	19,43
11	43	57,84	79,27	0,73	65,0	65,30	56,10	17,38	0,27	52,44
12	46	67,03	89,44	0,75	74,5	71,18	62,03	19,46	0,27	57,87
13	49	55,54	126,03	0,44	79,0	109,5	54,79	30,30	0,28	73,73

Table 4.20. Actual vs. calculated strength – dilatancy parameters of GB sand

Test No.	$Ø'_{p,act}$ (Eq. 4.21)	$\psi'_{p,act}$ (Eq. 4.20)	I_R (Eq. 2.8)	$\psi'_{p,calc}$ (Eq. 4.19)	$Ø'_{p,calc}$	*r (act)* (Eq. 4.20)	a *(act)* (Eq. 4.19)
1	30,3	12,5	1,7	11,8	29,8	0,87	0,32
2	32,5	15,1	2,1	14,0	31,6	0,88	0,33
3	33,7	16,6	3,2	18,9	35,6	0,72	0,25
4	35,5	18,8	3,7	21,1	37,4	0,73	0,25
5	33,9	16,9	2,7	16,9	34,0	0,82	0,30
6	32,7	15,4	2,1	13,9	31,5	0,91	0,34
7	31,2	13,6	2,0	13,6	31,3	0,82	0,30
8	30,0	12,1	1,7	11,5	29,6	0,86	0,32
9	37,9	21,7	4,0	22,0	38,2	0,81	0,29
10	36,3	19,7	3,2	19,1	35,8	0,85	0,31
11	35,4	18,7	2,4	15,5	32,8	0,99	0,39
12	34,8	17,9	2,5	16,0	33,3	0,92	0,35
13	34,5	17,6	2,6	16,3	33,4	0,89	0,33
						avg. = 0.85	avg. = 0.32

Calculated Stress-Dilatancy Coefficients of GB (From Table 4.9)				
Q	R	r	$Ø_{cs}$	a
9.59	-1.42	0.82	20.1	0.30
$I_R = I_D(Q - lnp') - R$				

Figure 4.39 below plots the variance of '***r***' parameter calculated from triaxial tests (r_{calc}) and physical model tests (r_{act}) which are taken as the average of test results. 'r' defines the contribution of dilatant behavior on soil strength and is considered as a stress-dilatancy correlation coefficient.

Additionally, Figure 4.39 presents the variance of '***a***' parameter which defines the ratio between peak dilatancy rate and dilatancy index and is considered as a stress-dilatancy correlation coefficient.

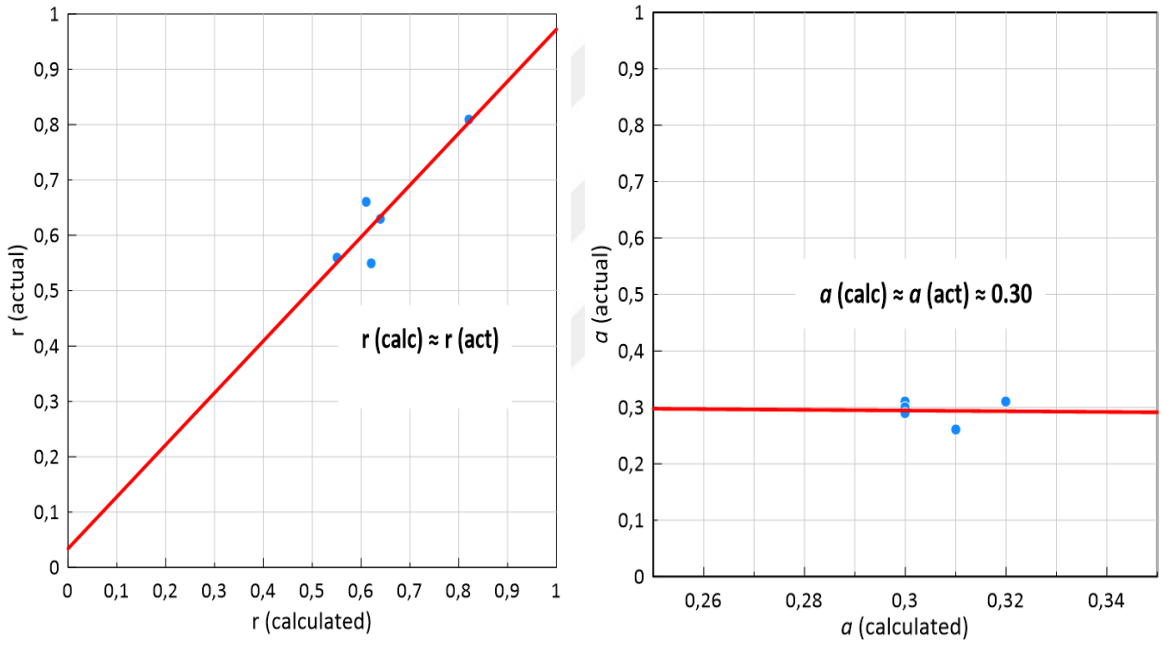


Figure 4.39. Comparison of calculated 'r' and 'a' stress-dilatancy coefficients from triaxial tests and actual 'r' and 'a' from physical model tests.

Figure 4.39 proves that peak friction angles of the tested soils in the physical model calculated using actual stresses almost match with friction angles evaluated using stress-dilatancy correlation constants which are derived from CD triaxial tests. On Figure 4.40 the relationship between calculated peak friction angle and relative density under equal surcharge pressure of 100 kPa is plotted for each tested granular soil.

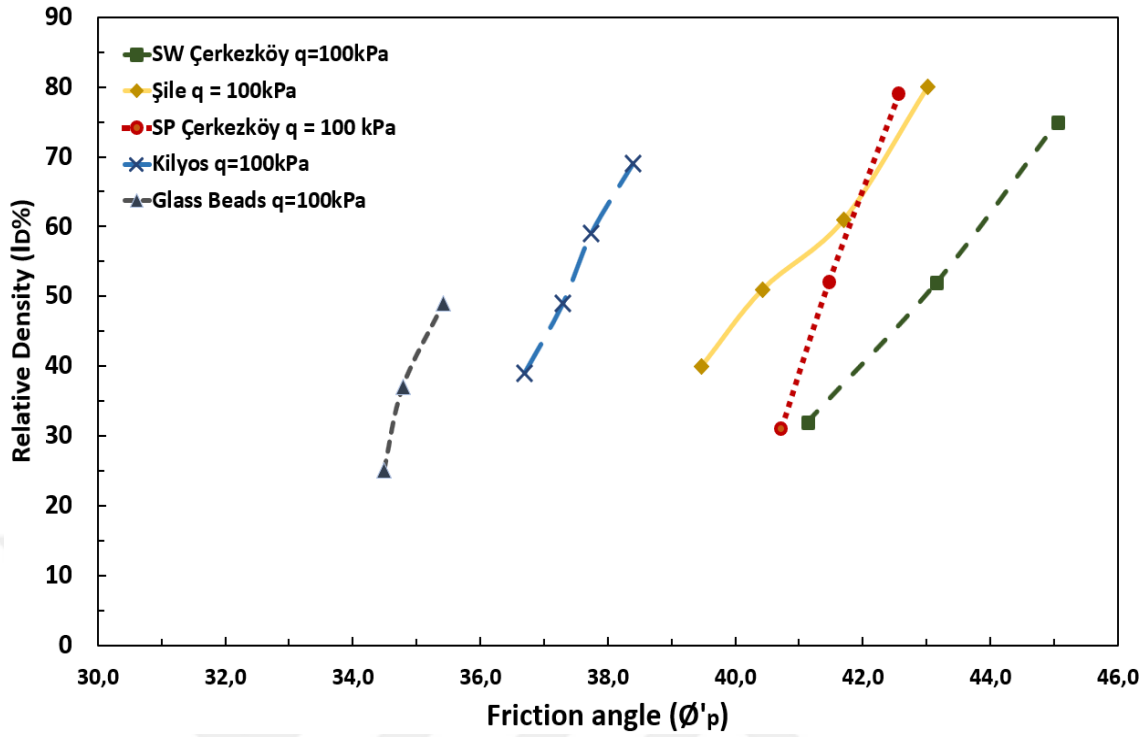


Figure 4.40. Relative density – Friction angle relationship at 100 kPa surcharge pressure for tested soils.

Figure 4.40 clearly demonstrates that strength properties of the granular soils are influenced by grain size and shape. To start with, as presented in Table 3.3, S2 and S1 sand have similar grain shapes; however well graded S2 has wider variability of grain sizes and have higher coefficient of uniformity. As a result, well graded S2 exhibit higher strength when sheared. Another effect of grain size distribution is that uniform graded specimens (GB, S3 sand, S2-SP) are less compressible, therefore there is less increase on shear strength when densely packed, as compared with well graded samples of S1 sand and S2-SW sand.

When the soils are compared according to grain shape, S1 and S2 sands are the most angular. S3 sand grains are more sphere compared with S1 and S2. Lastly, GB are totally circular and sphere. When calculated, shear strengths of the tested sands were compared, it was detected that sands consisting of angular grains comprise higher dilatant behavior, therefore exhibit higher internal peak friction angle. This result is reasonable since circular, sphere, and uniform graded soil grains have less void ratio and their compressibility decreases with uniformity (Apollonia and Holubec, 1973).

Since there is a proportional relationship between friction and dilation angle which are both an intrinsic soil property; it was concluded that grain size distribution and grain shape characteristics of granular materials effectively influence their peak frictional strengths. Another outcome from the interpretation of physical model test results was that, peak shear strength and dilatant behavior is proportional provided that arching effects are suppressed. Strength parameters and stress-dilatancy coefficients calculated by physical retaining wall model tests and triaxial tests were almost equal, provided that horizontal and vertical stresses measured by pressure sensors at failure state during model tests were rectified from frictional effects. A final outcome of the study was that loading condition does not considerably affect the stress-dilatancy correlation coefficients because triaxial tests and retaining wall tests yield approximate dilatant behavior.

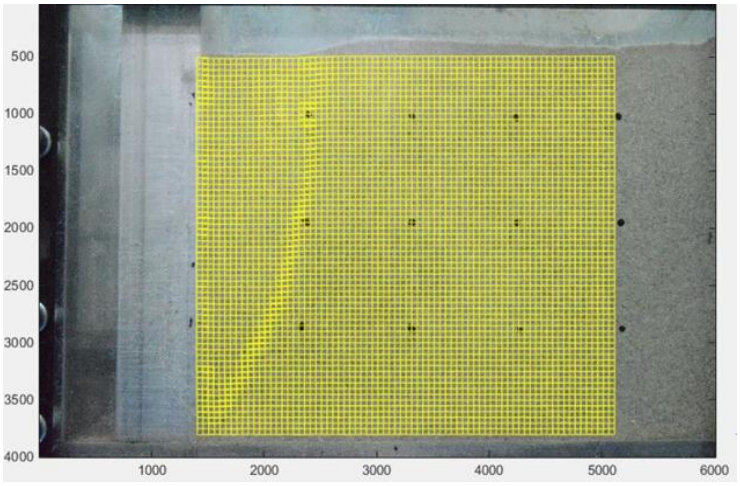
4.2.1. Experimental Visualization of Active Failure Surfaces

In order to quantify the geometry of the failure surfaces, PlotDigitizer program was used. This program enables the engineer to obtain actual X-Y coordinates of the failure band by using the output of GeoPIV-RG software (Figure 4.41). First, the initial bottom part of failure surface was selected to be the origin X,Y=[0,0]. Next, actual dimensions of the model frame were given as the input for X_{max} and Y_{max} data points. Finally, minimum five points were located at the outside border of the observed shear band. The software automatically gives the actual coordinates of these points located on the slip surface. Using these coordinates, actual failure surface geometries of all tests were plotted. In graphs, horizontal distance of any point located on the slip surface from the retaining wall was termed as 'B_f' and vertical distance of any point from the top of the wall was termed as 'h'. Both values were normalized with wall height (H) in order to become unitless.

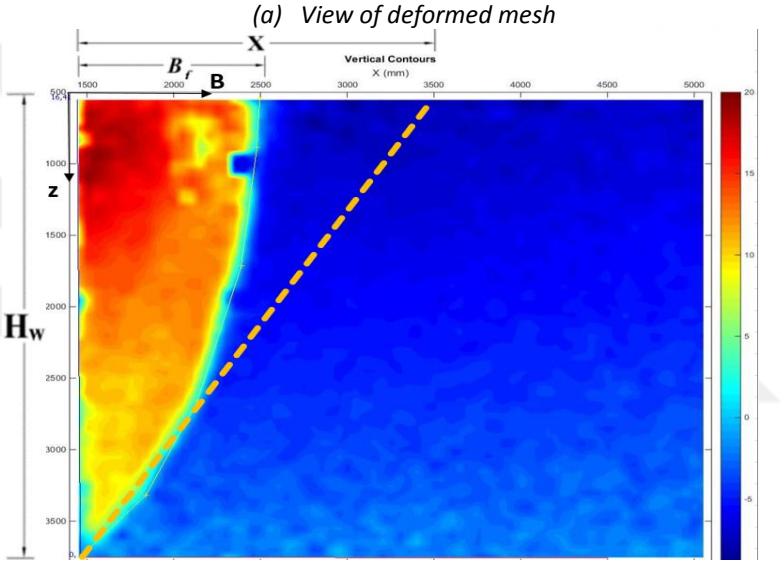
In Figures 4.42 to 4.46, comparison of obtained actual failure surface geometries are presented for the tested granular materials for;

(i) varying relative densities of similar surcharge pressures,

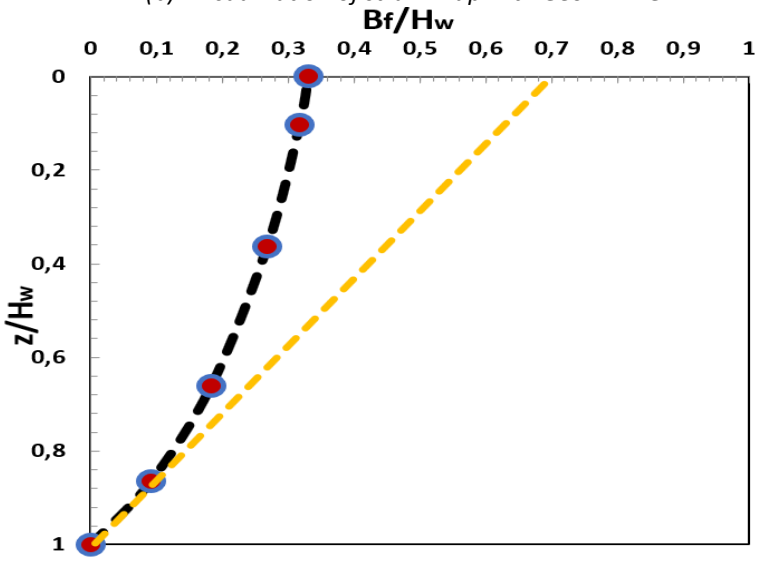
(ii) varying surcharge pressures of similar relative density ranges.



(a) View of deformed mesh

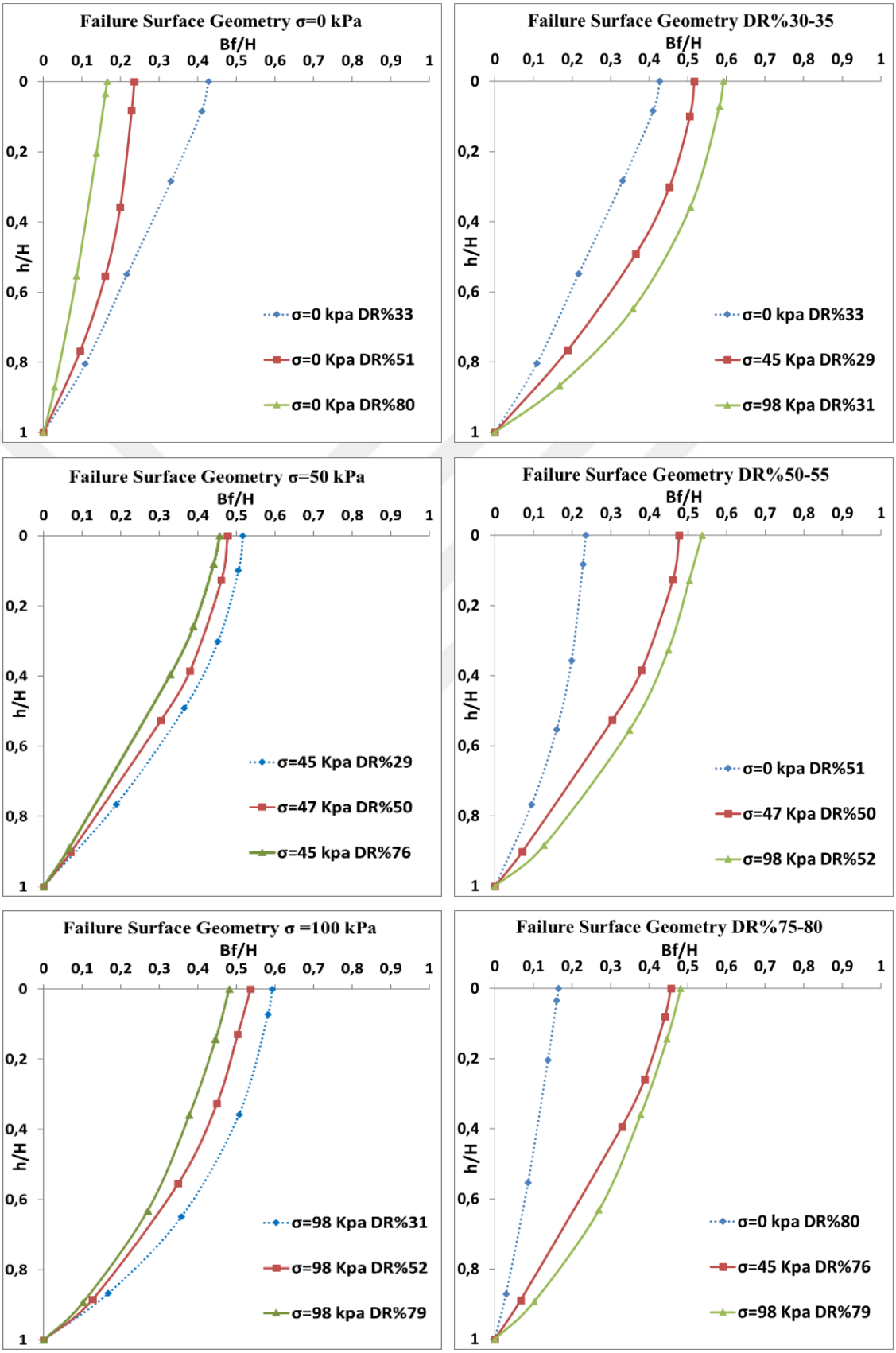


(b) Visualization of strain map with GeoPIV-NG



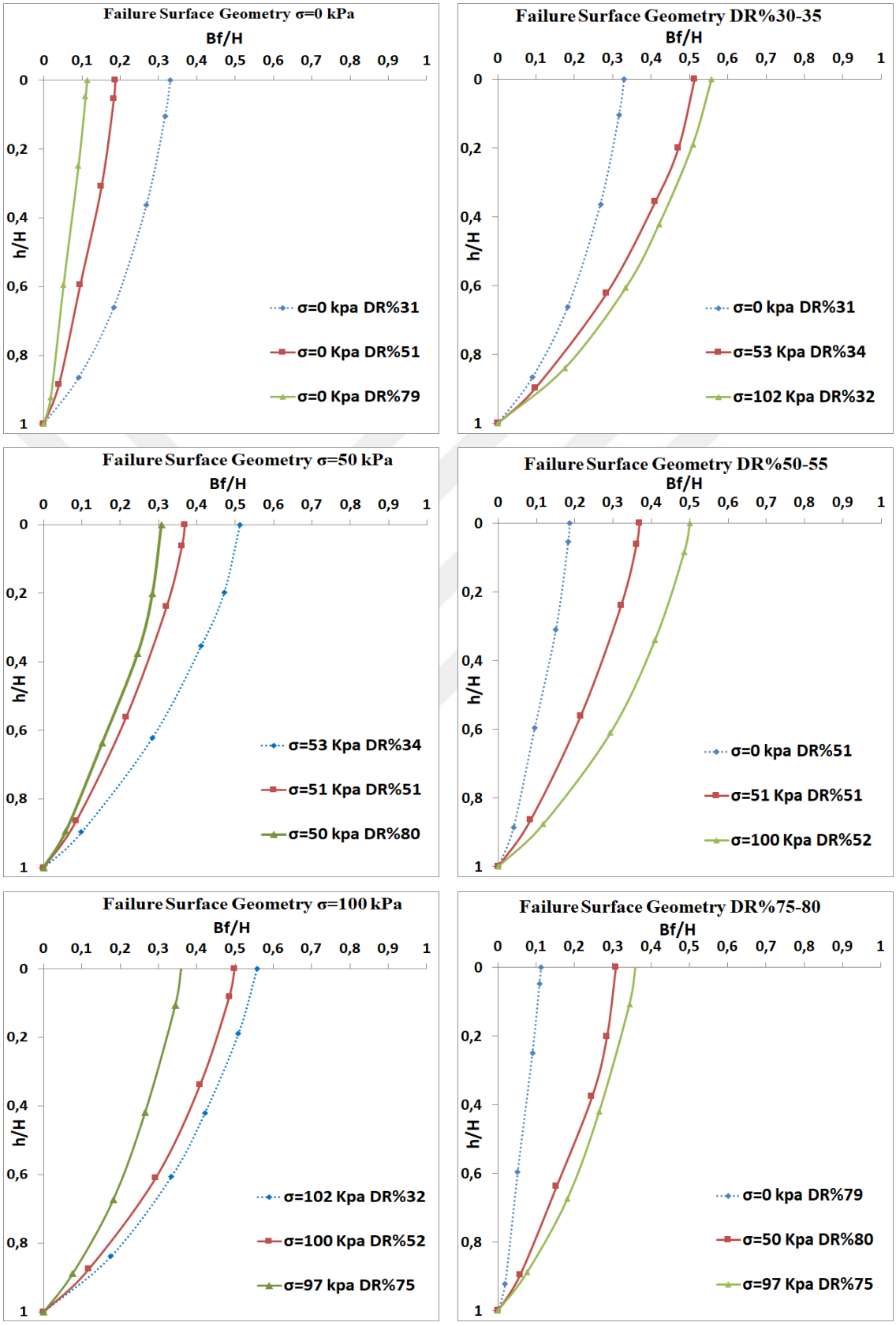
(c) *Generation of actual x-y coordinates located on failure surface by PlotDigitizer*

Figure 4.41. Selection of X-Y coordinate points using PlotDigitizer software.



(a) varying densities of similar surcharge *(b) varying surcharge of similar relative density*

Figure 4.42. Active failure surface geometries of SW- S2 sand.



(a) varying densities of similar surcharge *(b) varying surcharge of similar relative density*

Figure 4.43. Active failure surface geometries of SP- S2 sand.

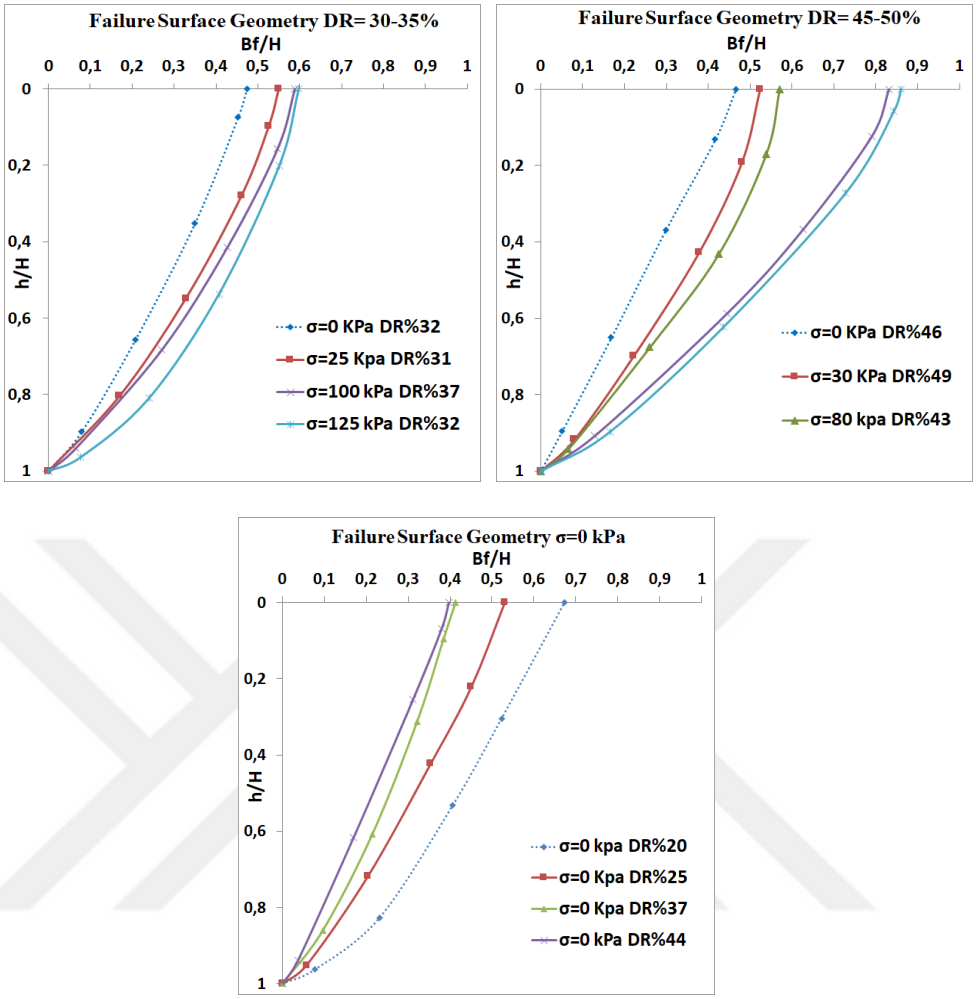


Figure 4.44. Active failure surface geometries of GB at varying surcharge and densities.

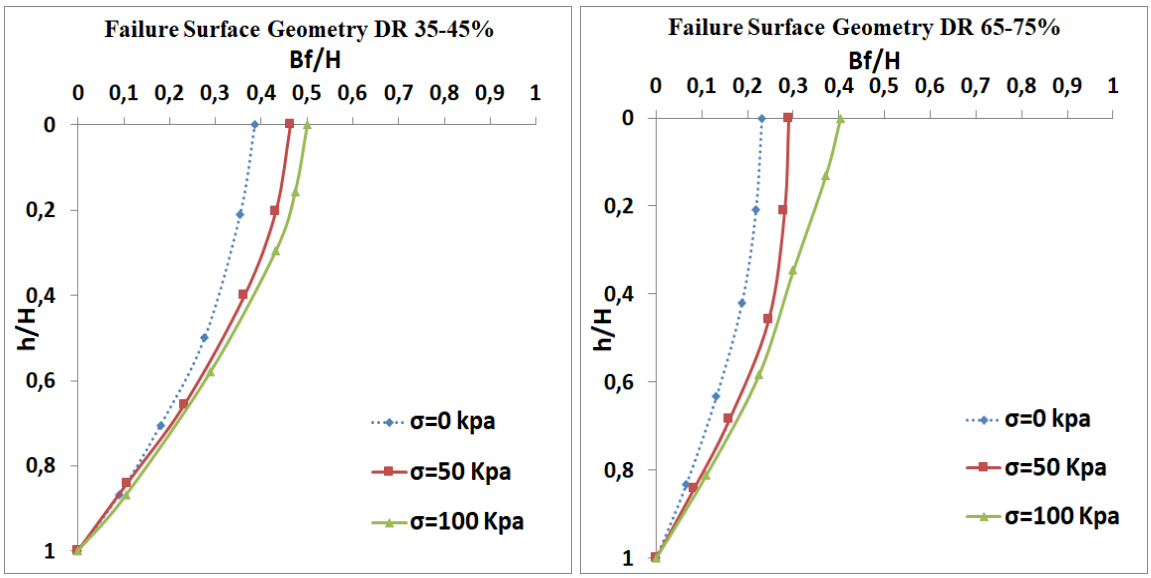


Figure 4.45. Active failure surface geometries of S1 at varying surcharge and densities.

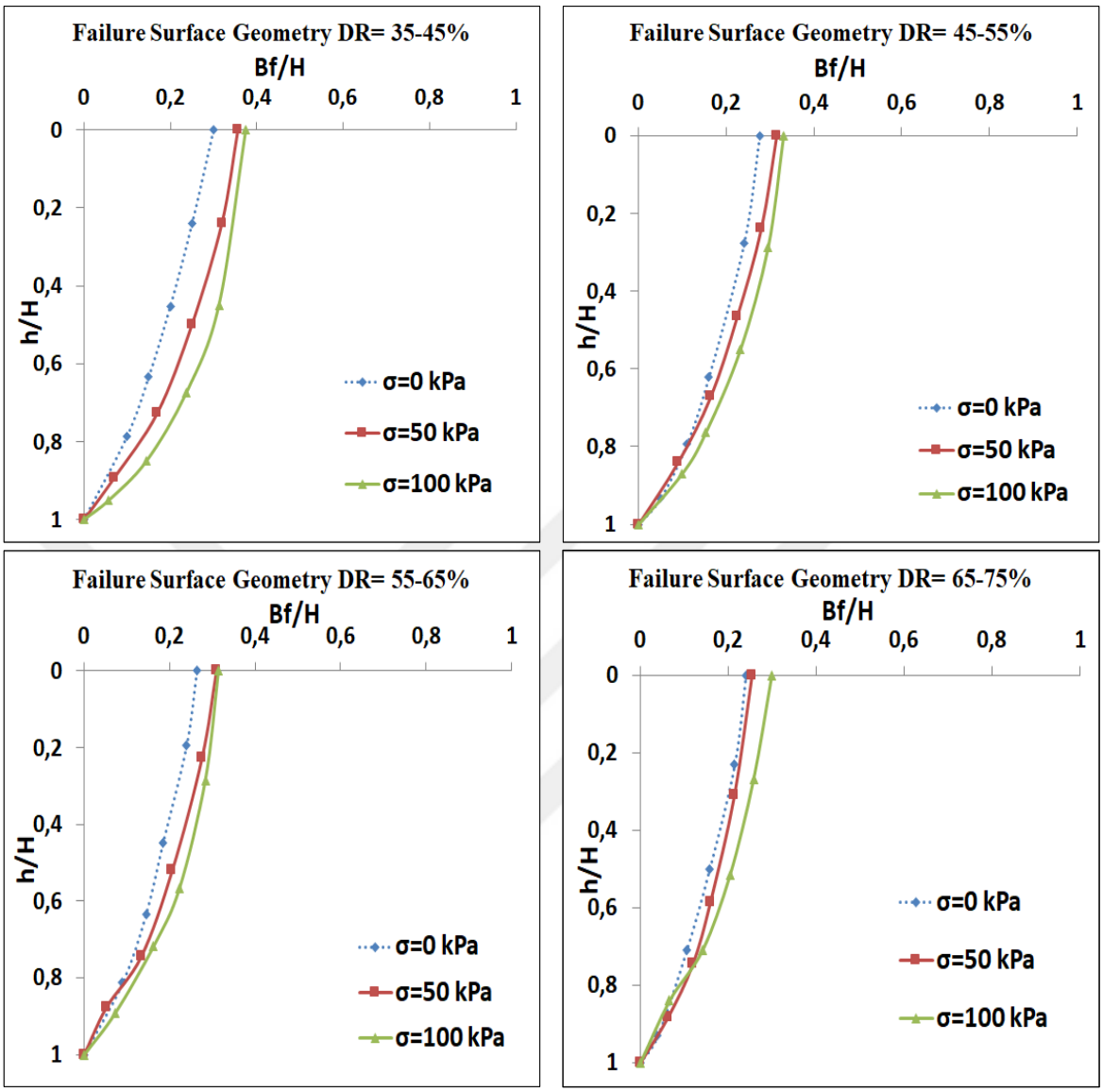


Figure 4.46. Active failure surface geometries of S3 at varying surcharge and densities.

Regardless of soil type, all physical model tests yield two specific results:

(i) If granular soils are tested under equal vertical stress, the inclination of the failure surface to horizontal increases and the geometry of the shear band gets steeper and closer to retaining wall when initial relative density value of the backfill soil behind the retaining wall is increased.

(ii) If granular soils are tested under equal initial relative density range, the inclination of the failure surface to horizontal decreases and the geometry of the shear band gets further from the retaining wall when initial stress state of the soil is increased.

These outcomes are coherent with the existing stress-dilatancy theories in which dilatancy is related to density and stress state of granular soil. According to Bolton's (1986) stress-dilatancy theory, which is widely accepted in literature, relative density and dilatancy index are proportional whereas there is an inverse proportion between stress and dilatancy. This is due to the fact that dilatancy of soil grains, which is higher at denser soils, increases the internal friction, however if the soil is under high confining pressure, the dilatant behavior of the soil is suppressed (Figure 4.47). Consequently, dilatant behaviour affects the volumetric strains which modify the slip surface, resulting in a parabolic shaped shear band geometry. On the other hand, existing Rankine and Coulomb theories propose a linear failure surface since dilatant behavior is not considered in their approach.

In order to visualize the influence of dilatant behaviour on shear band geometry, graphs are prepared for each sand which show the comparison of actual failure surface geometries revealed by GeoPIV-RG analysis with calculated dilatancy and friction angles at Figure 4.48. In the graphs, 'z' is the vertical distance of any point on the failure surface to the top of the retaining wall. Similarly, 'B_f' indicates the horizontal distance. 'σ' is the surcharge pressure applied on the backfill soil by pneumatic pistons. 'ID' represents the relative density and 'ψ_p' is the peak dilatancy angle of the tested soil.

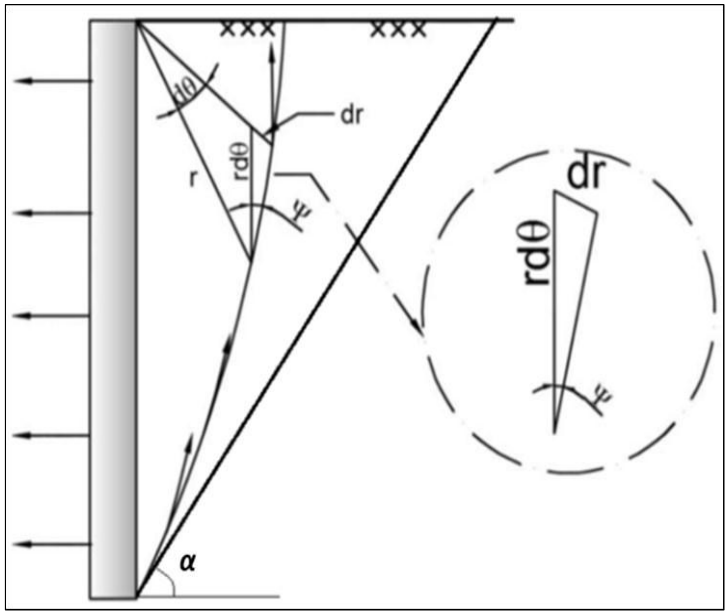
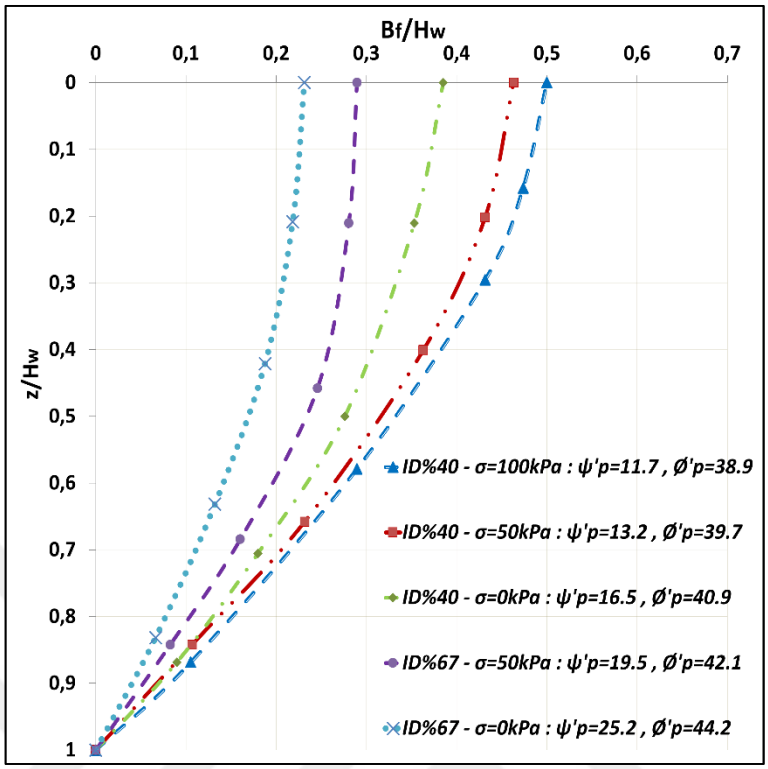
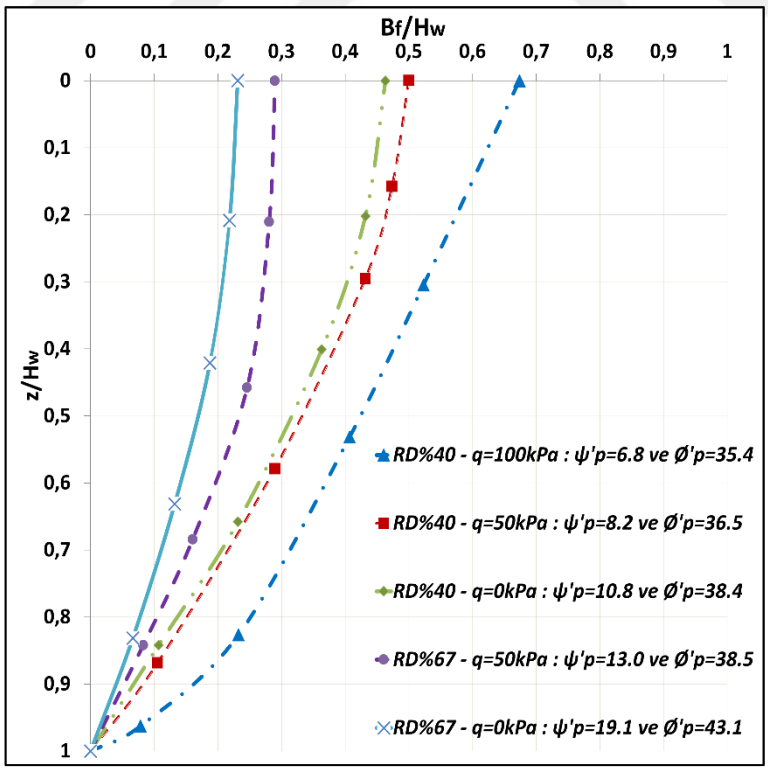


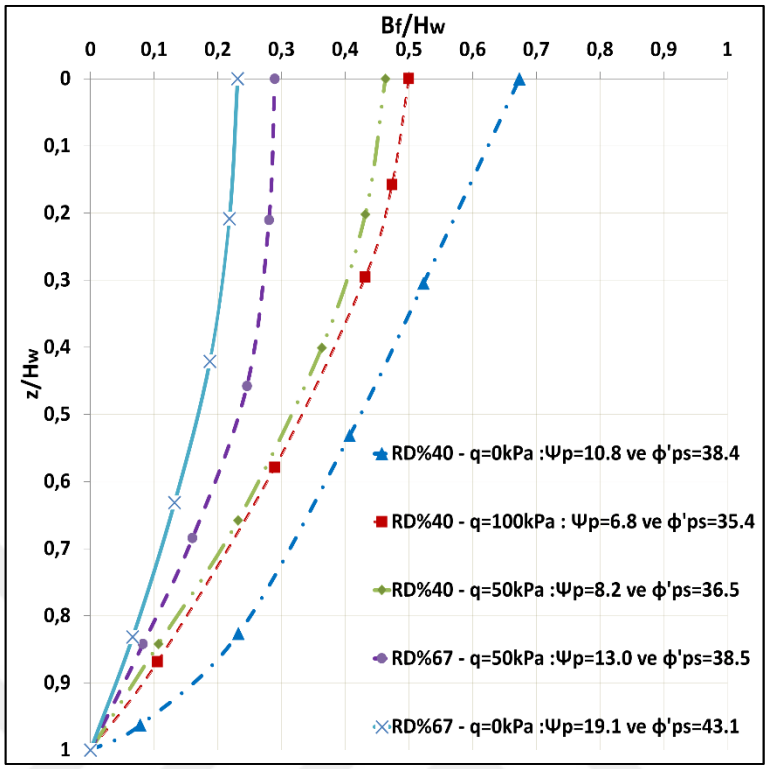
Figure 4.47. Influence of dilatancy on slip surface geometry.



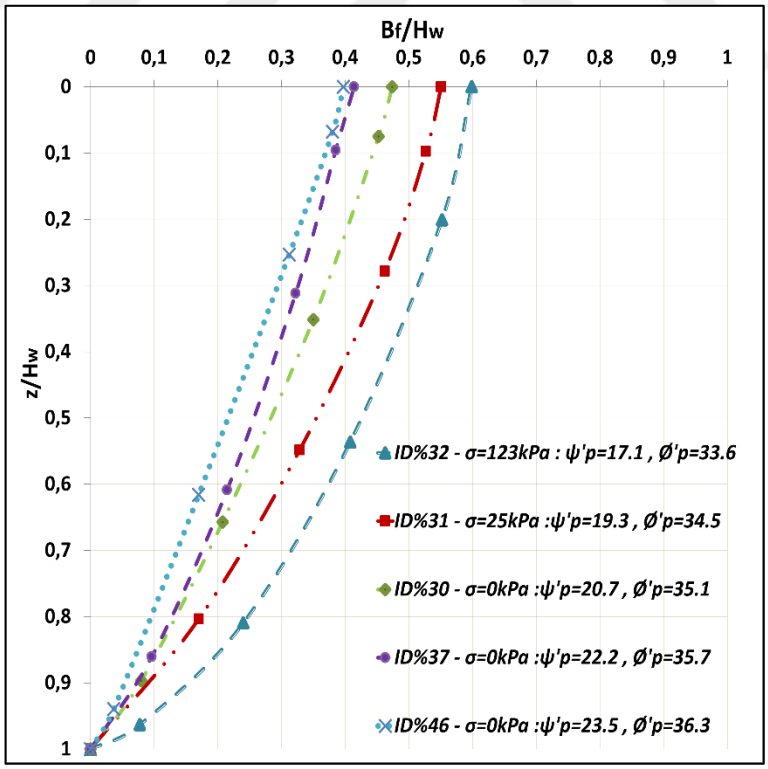
(a) S1 sand



(b) S2 sand



(c) S2 sand



(d) Glass Beads

Figure 4.48. Comparison of failure surface geometries of tested granular materials at varying dilatancy angle values.

The graphs clearly indicate that regardless of soil type, if dilatancy angle of a granular soil sample is higher, friction angle is higher and the initial inclination of the slip surface to horizontal (α) is steeper. Moreover, GB, which consist of totally circular and sphere particles possess lowest frictional strengths and consequently lower initial inclination angles to horizontal. On the other hand, steeper active slip surface inclinations were observed on the tests conducted with angular and well graded S1 and S2-SW sands. Therefore, plotting dilatancy-failure surface geometry relationship for each sand has revealed the influence of grain shape and grain size on dilatant behaviour. Figure 4.49 below shows the relationship between the inclination of the initial part of the slip surface (α) with calculated peak friction angles for the tested granular backfills.

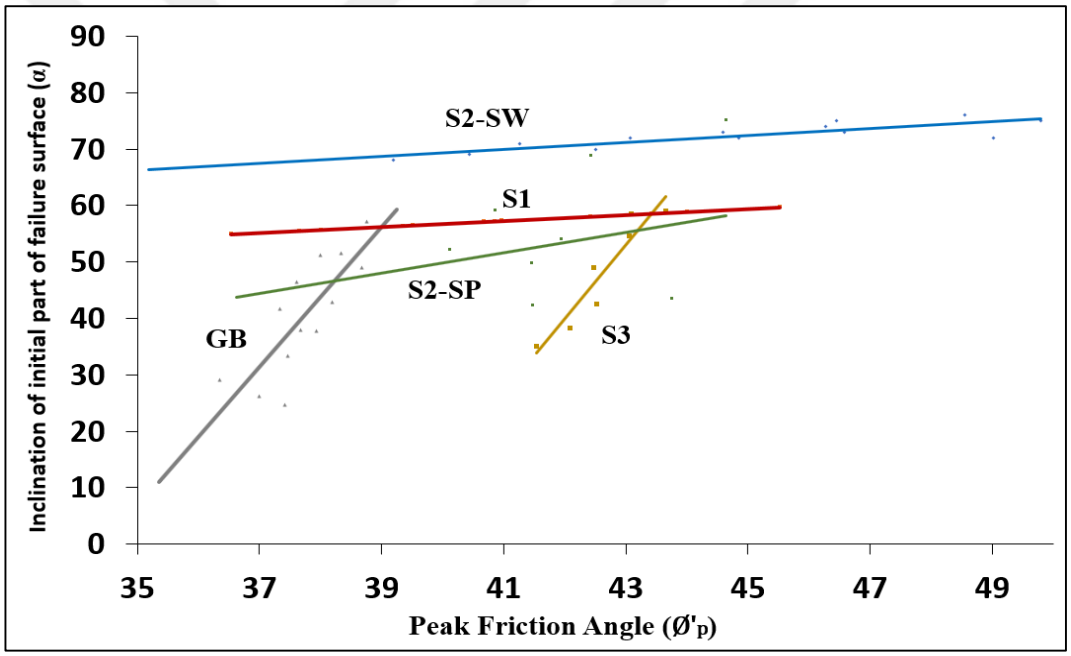


Figure 4.49. Relationship between inclination of initial part of the failure surface and peak friction angle for tested granular backfills.

From Figure 4.49, increment at the inclination on the initial part of failure surface with increasing peak friction angle is clearly figured out. In addition, steeper shear bands form behind retaining walls backfilled with well graded, angular sands such as S2-SW and S1 sand. However, the ratio of increment in the failure surface inclination is higher with increased soil strength for uniform graded soils consisting of more rounded particle shapes.

Figures 4.50 to 4.53 below plot a_b – tanψ'_p relationship for the failure surface geometry of the granular soils used in the research at each surcharge pressure level respectively.

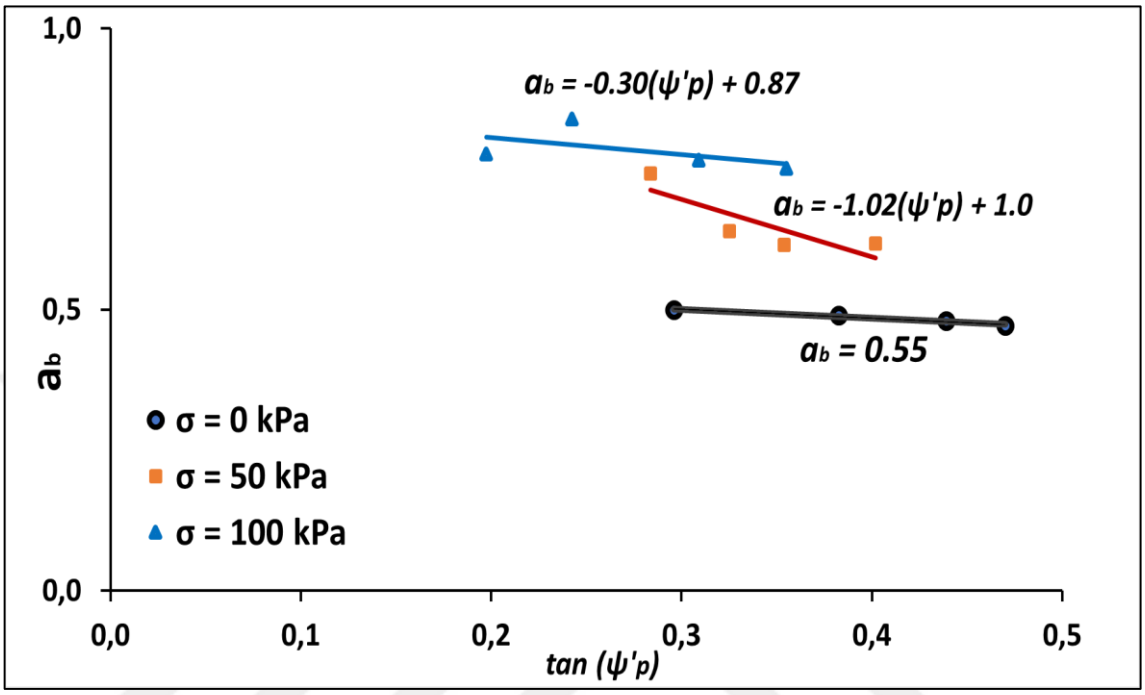


Figure 4.50. Influence of dilatancy on experimentally measured values of a_b for S1 Sand.

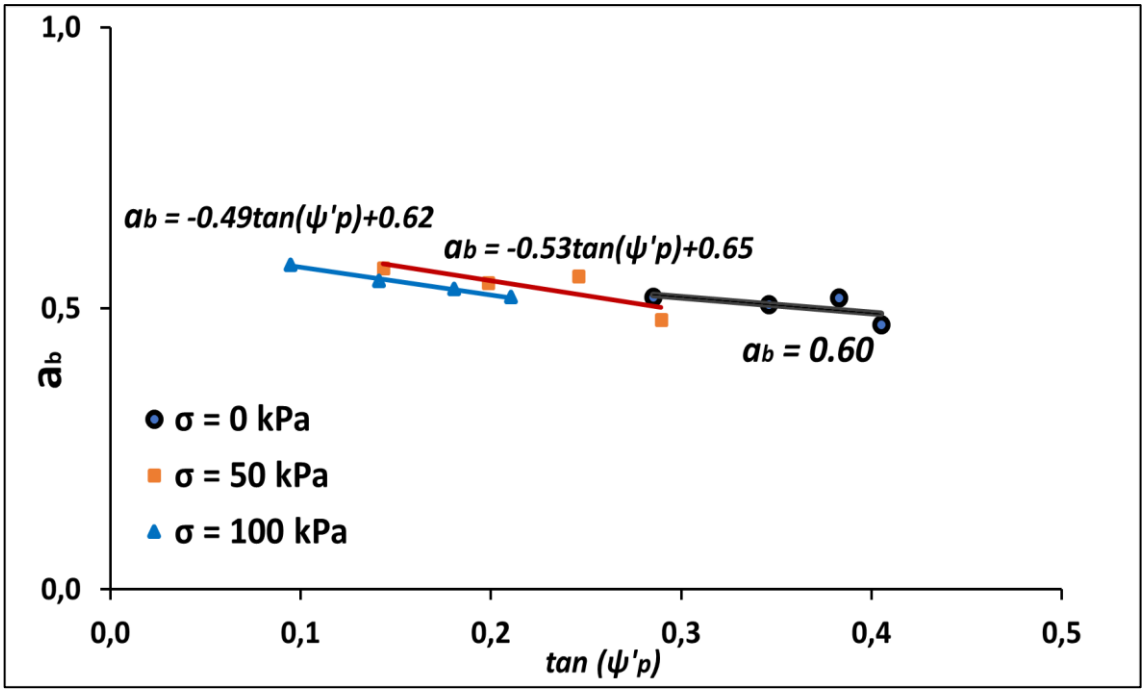


Figure 4.51. Influence of dilatancy on experimentally measured values of a_b for S3 Sand.

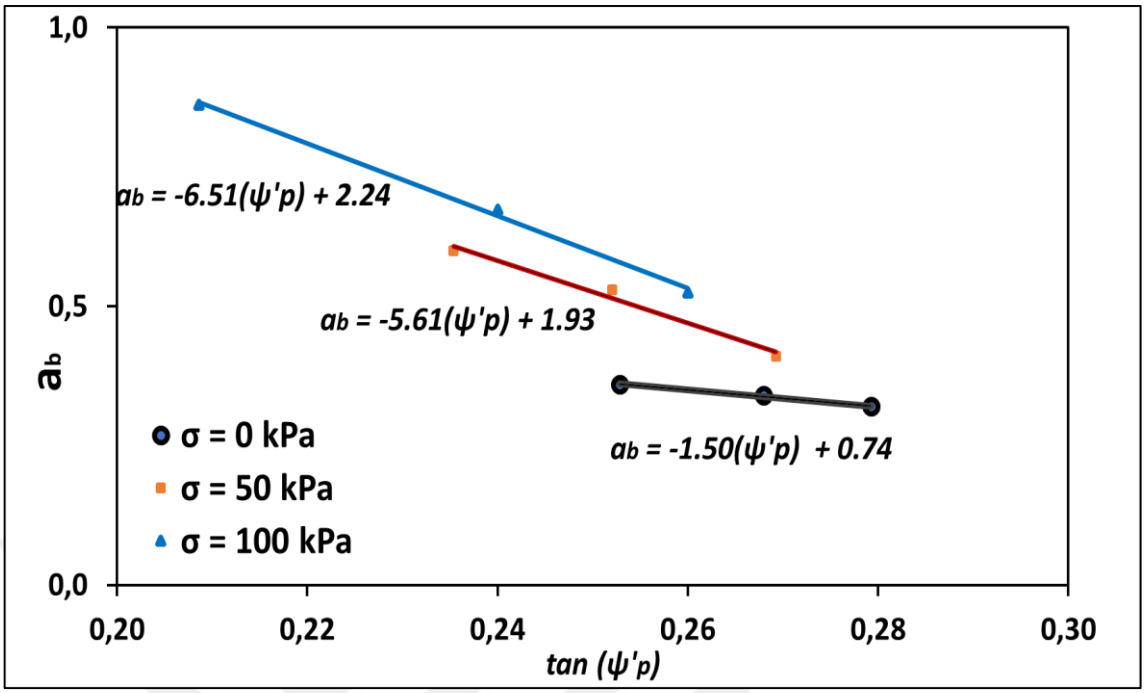


Figure 4.52. Influence of dilatancy on experimentally measured values of a_b for S2-SW.

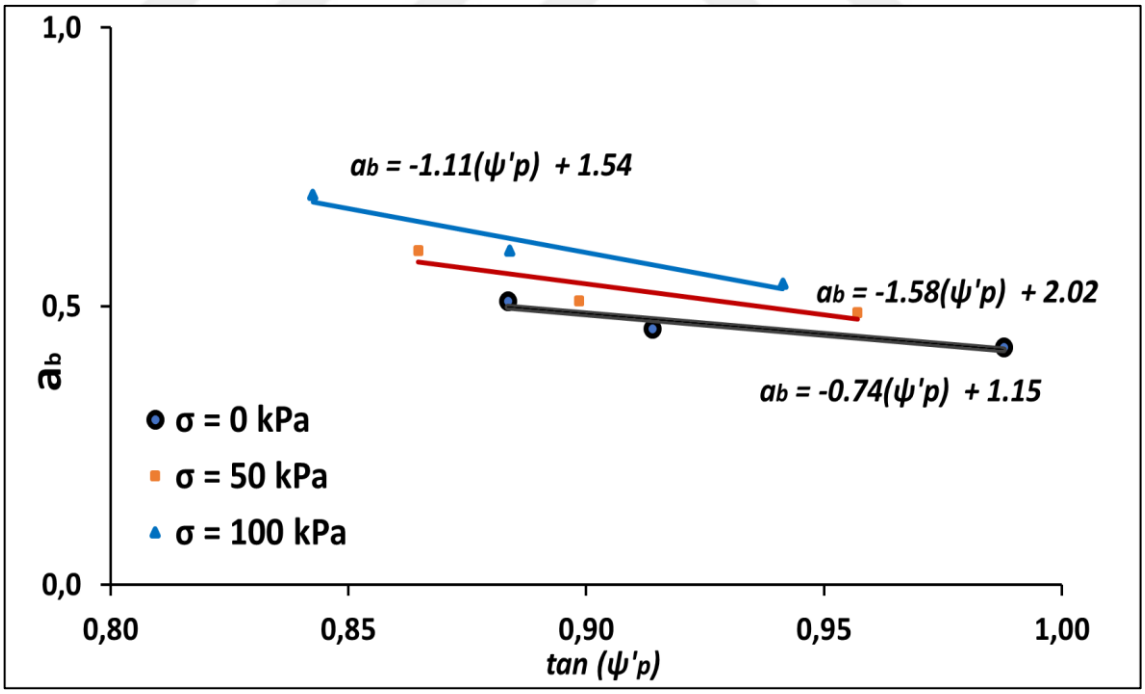


Figure 4.53. Influence of dilatancy on experimentally measured values of ab for S2-SP.

Graphs indicate that the normalized horizontal distance of the point of emergence of the failure plane on ground surface (a_b) to the wall is only constant when no surcharge is applied to backfill soil in physical model experiments. On the other hand, when the initial

stress state of the soil behind the retaining wall is increased by applying surcharge, a_b values differ with any variance in dilatancy of the soil and its gradient is different for each sand type.

According to the results, it can be proposed that for angular and well graded soils, the influence of surcharge on dilatant behavior and failure surface geometry is more intense. Because, for S1 sand and SW-S2 which consists of angular and well graded grains, a_b value and the slope of a_b-tanψ_p relationship considerably increase if initial stress state of the sand is increased. On the other hand, the variance in S3 sand is obviously slight, which is constituted of uniform and round particles.

4.2.2. Proposing an Equation to Define Failure Surface Geometry

Prior to proposing a geometrical correlation to calculate the coordinates of any point located on the shear band, the geometry of observed actual failure surfaces during physical modelling is compared with existing theories available in the literature which estimates slip surface geometries. In geotechnical practice, Coulomb's equation to define the inclination of linear active failure wedge (α) is widely used and is only dependent on the internal friction angle of the granular soil.

$$\alpha = 45^o + \frac{\emptyset_p}{2} \tag{4.22}$$

According to experimental studies of Arthur *et al.*, (1977) and Vardoulakis (1980) as presented in literature review section, the orientation of rupture layers forming the shear band at active failure state are roughly inclined with an angle of

$$\alpha = \frac{\pi + \emptyset'_p + \psi'_p}{4} \tag{4.23}$$

with the horizontal.

Finally, based on physical model tests, Altunbas *et al*., (2017) proposed a parabolic function to define the actual shear geometry as:

$$z = aB^2 + bB + c \tag{4.24}$$

where,

$$a = [(a_b - 1)/(a_b^2 H_w)]tan^2(\alpha) \tag{4.25}$$

$$b = -\tan(\alpha) \tag{4.26}$$

$$c = H_w \tag{4.27}$$

The geometric variables of the failure surface presented by Altunbas *et al*., (2017) are the wall height (H_w), distance of shear band to wall at ground surface (B_f), distance of the linear extrapolated line to wall at ground surface (X) which is tangent to initial part of shear band at toe level and the inclination of the initial section of the shear band at the toe level (α). *'z'* defines the vertical coordinate and 'B' defines the horizontal distance from the retaining wall to the failure surface at a particular depth *z*. The positions of these variables are presented in Figure 4.54. To derive a unitless parameter to be used in the comparison of failure geometry of backfills consisting of various dilatancy angles, B_f / X ratio is selected as the 'a_b' parameter.

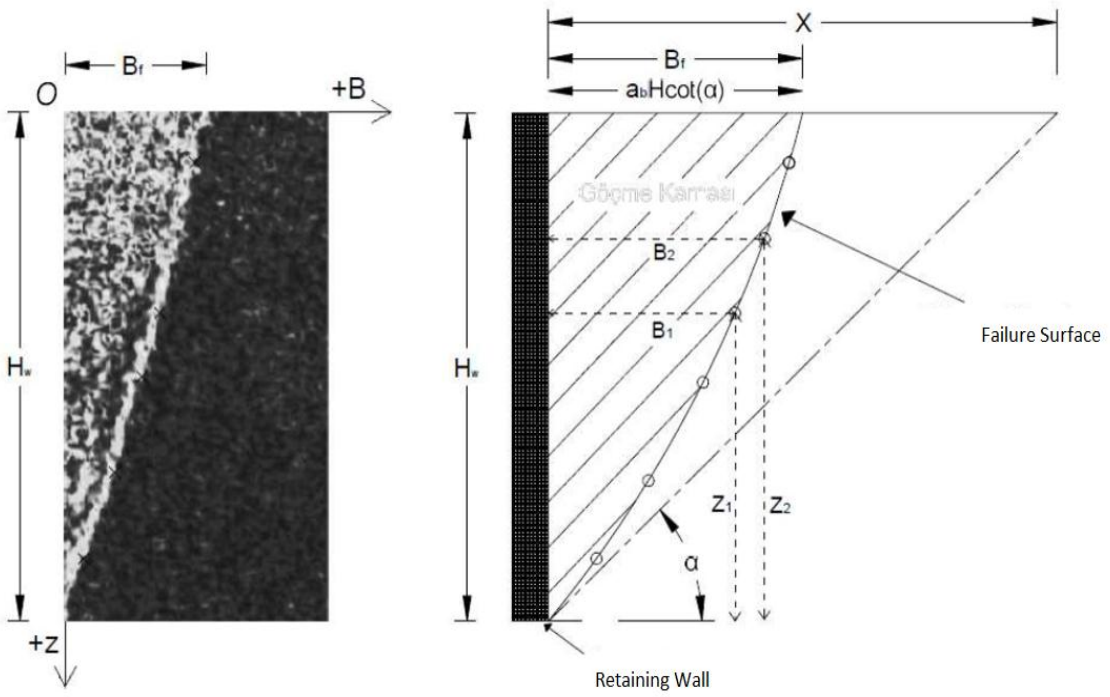


Figure 4.54. Geometric properties of failure surface geometry.

According to physical model experiments conducted by Altunbas *et al*., (2017), failure surface geometry calculated by above equation which predicts active failure planes fit exactly with actual geometries obtained by PIV analysis. However, the test box used in their study did not include pneumatic pistons, therefore tests were conducted at very low confining pressure ranges. Moreover, only one particular type of granular soil was used in the work, therefore any possible effect of macro-scale physical soil property such as grain size and shape could not be investigated.

In this study the actual inclination 'α' is derived from PIV analysis and has been used in the geometrical correlation proposed by Altunbas *et al*., (2017) in order to obtain vertical and horizontal coordinates (X, Y) of any point located on the active failure surface behind the model retaining wall. Coordinates of six points have been calculated using the equation and has been used to geometrically plot the failure surface geometry forming behind the retaining wall during active failure state. Next, Arthur *et al.,* (1977) correlation was used to calculate 'α' angle and plot the estimated linear failure surface. Finally, the slip surface geometries were plotted on the same graph with the experimentally visualized, actual failure surface geometry which was generated by GeoPIV-RG software. Comparisons are given in Figures 4.55 to 4.59 respectively.

Actual 'α' angles obtained by PIV analysis and estimated values proposed by Arthur *et al.,* (1977) correlation are approximate and stand between upper $45^0+1/2\emptyset'$ and lower $45^0+1/2\psi'$ limit states as proposed by Arthur *et al.,* (1977). Therefore, the initial inclination of active failure surfaces (α) can approximately be estimated well using either Arthur *et al.,* (1977) correlation or Altunbas *et al., (*2017) correlation. However, results reveal that linear failure surface geometry evaluated by using Arthur *et al.,* (1977) correlation is slightly an overestimate of actual failure surface generating behind retaining walls for all king of granular materials. Actual failure is parabolic shaped and is generally well aligned with Altunbas *et al*., (2017) correlation. However, there are still slight differences between experimentally visualized and theoretically estimated failure surface geometries forming behind the middle section of the wall.

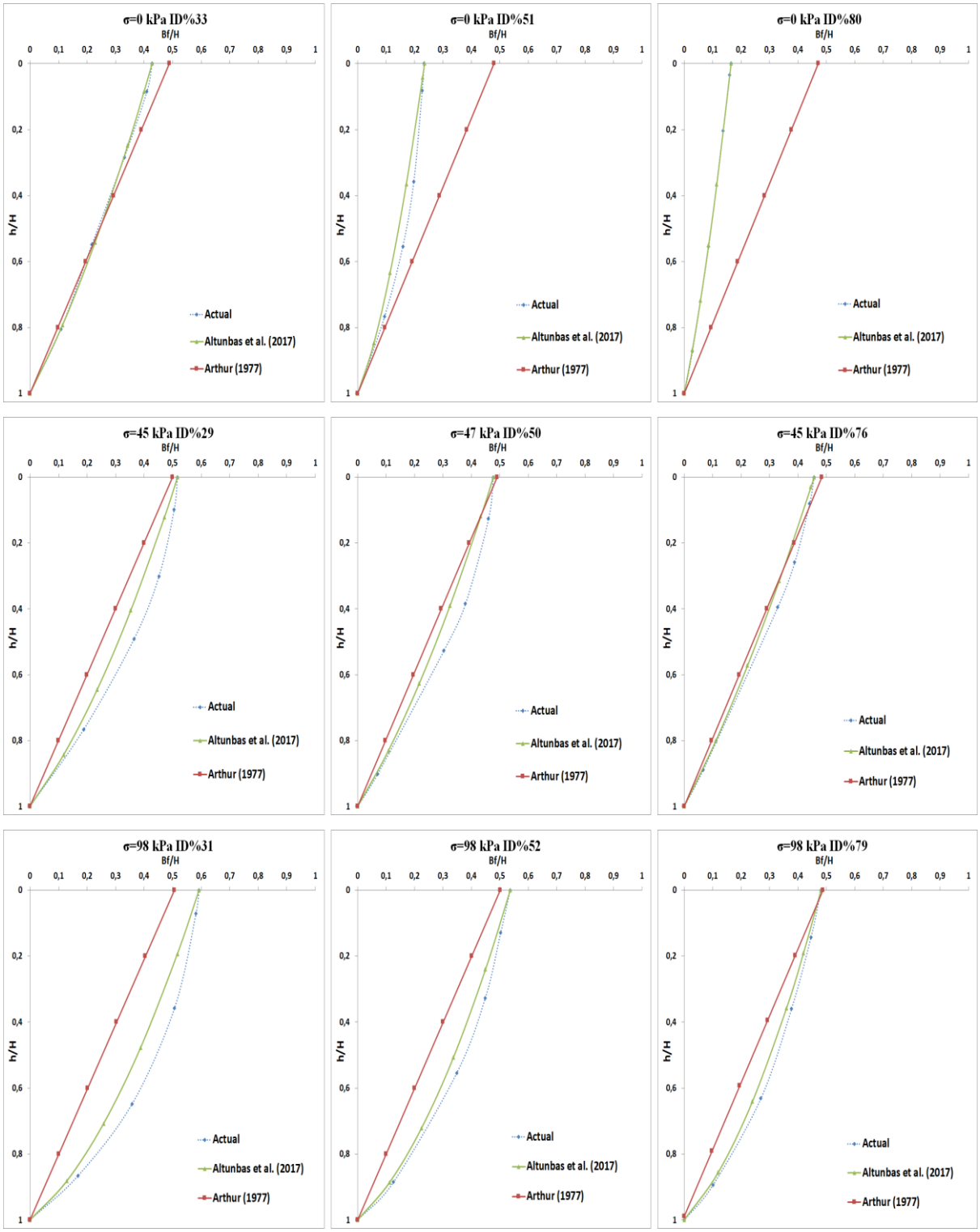


Figure 4.55. Comparison between plots of estimated and actual failure surfaces on normalized coordinate system for varying dilatancy values of physical model experiment data of SW-S2.

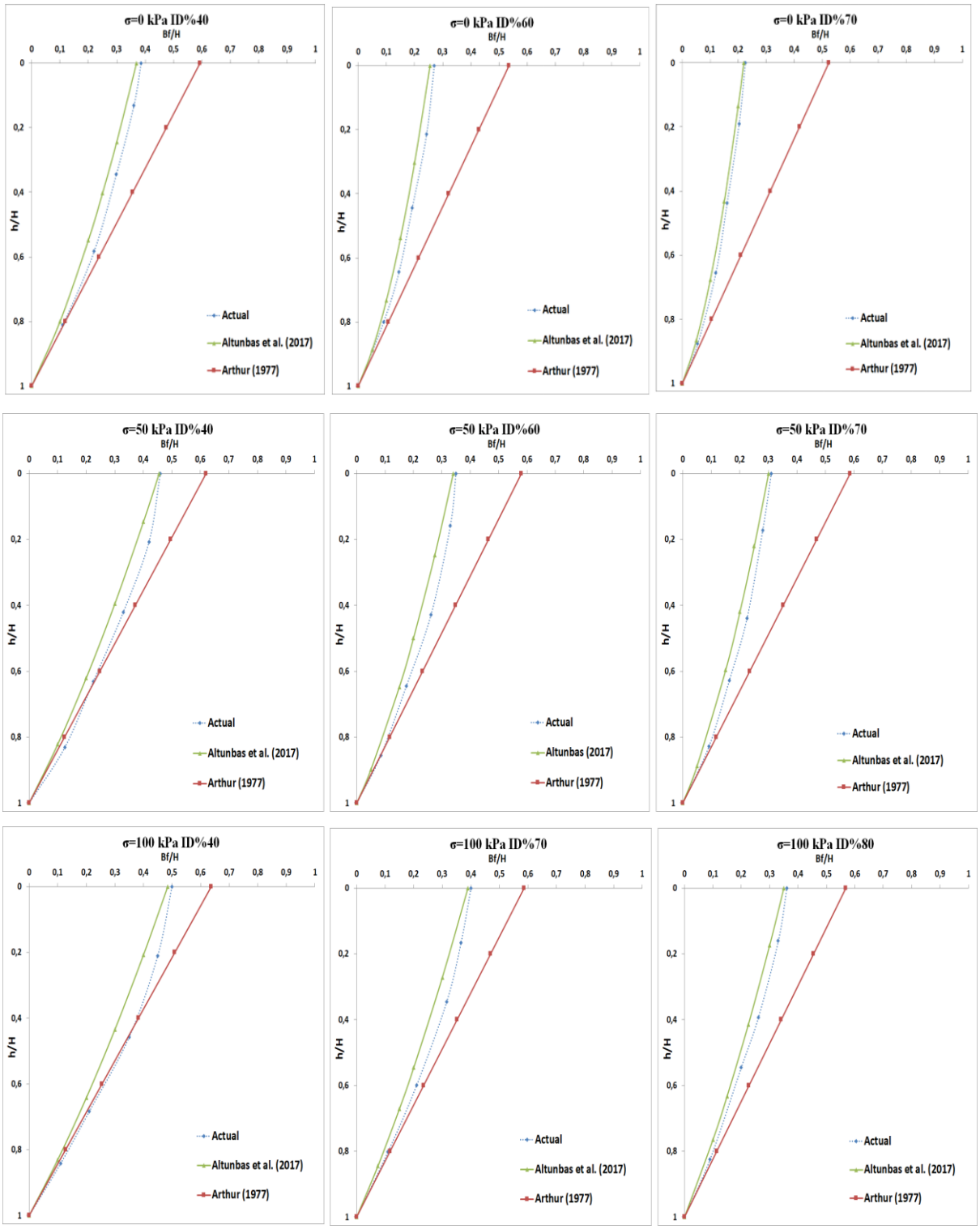


Figure 4.56. Comparison between plots of estimated and actual failure surfaces on normalized coordinate system for varying dilatancy values of physical model experiment data of S1 Sand.

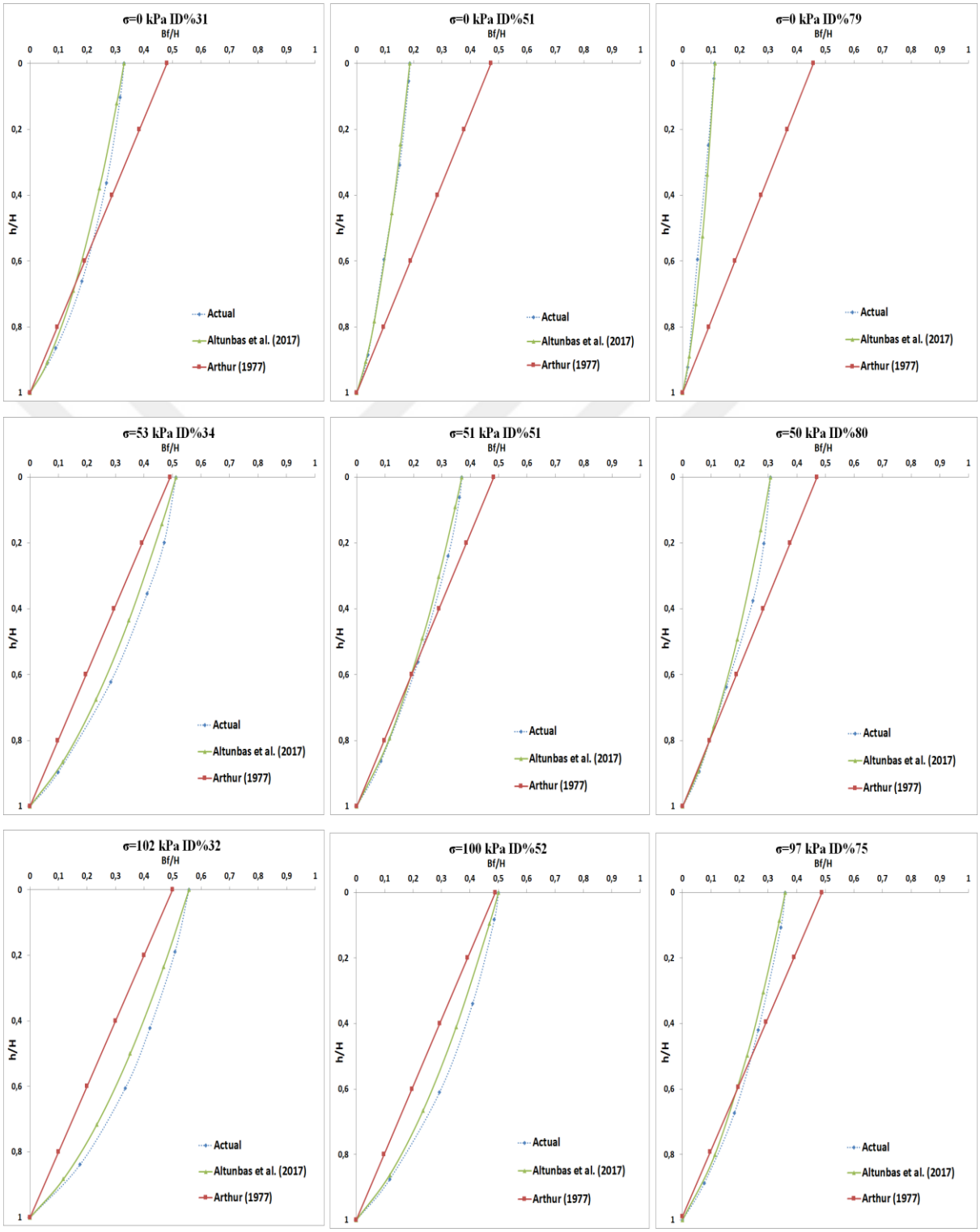


Figure 4.57. Comparison between plots of estimated and actual failure surfaces on normalized coordinate system for varying dilatancy values of physical model experiment data of SP-S2.

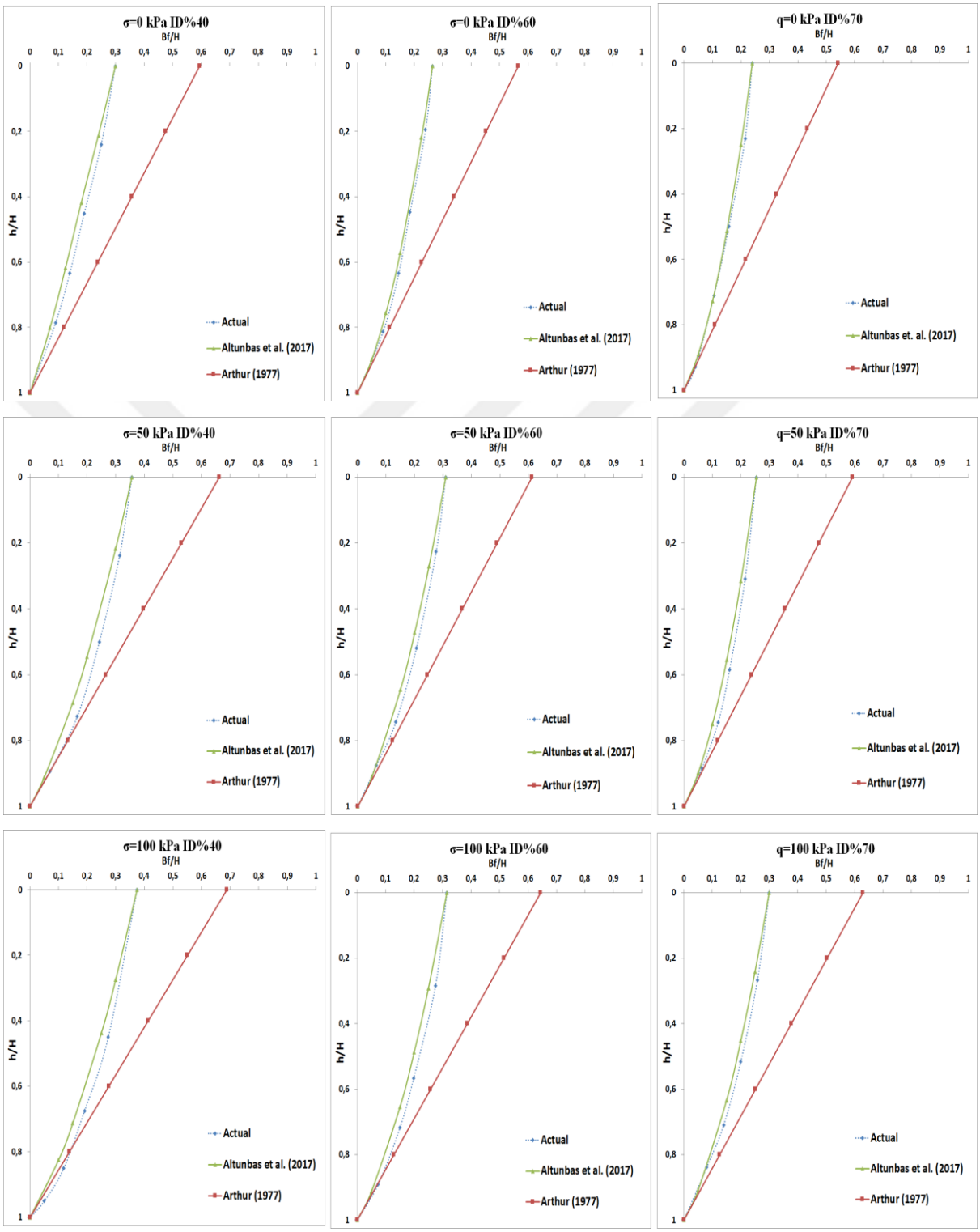


Figure 4.58. Comparison between plots of estimated and actual failure surfaces on normalized coordinate system for varying dilatancy values of physical model experiment data of S3 Sand.

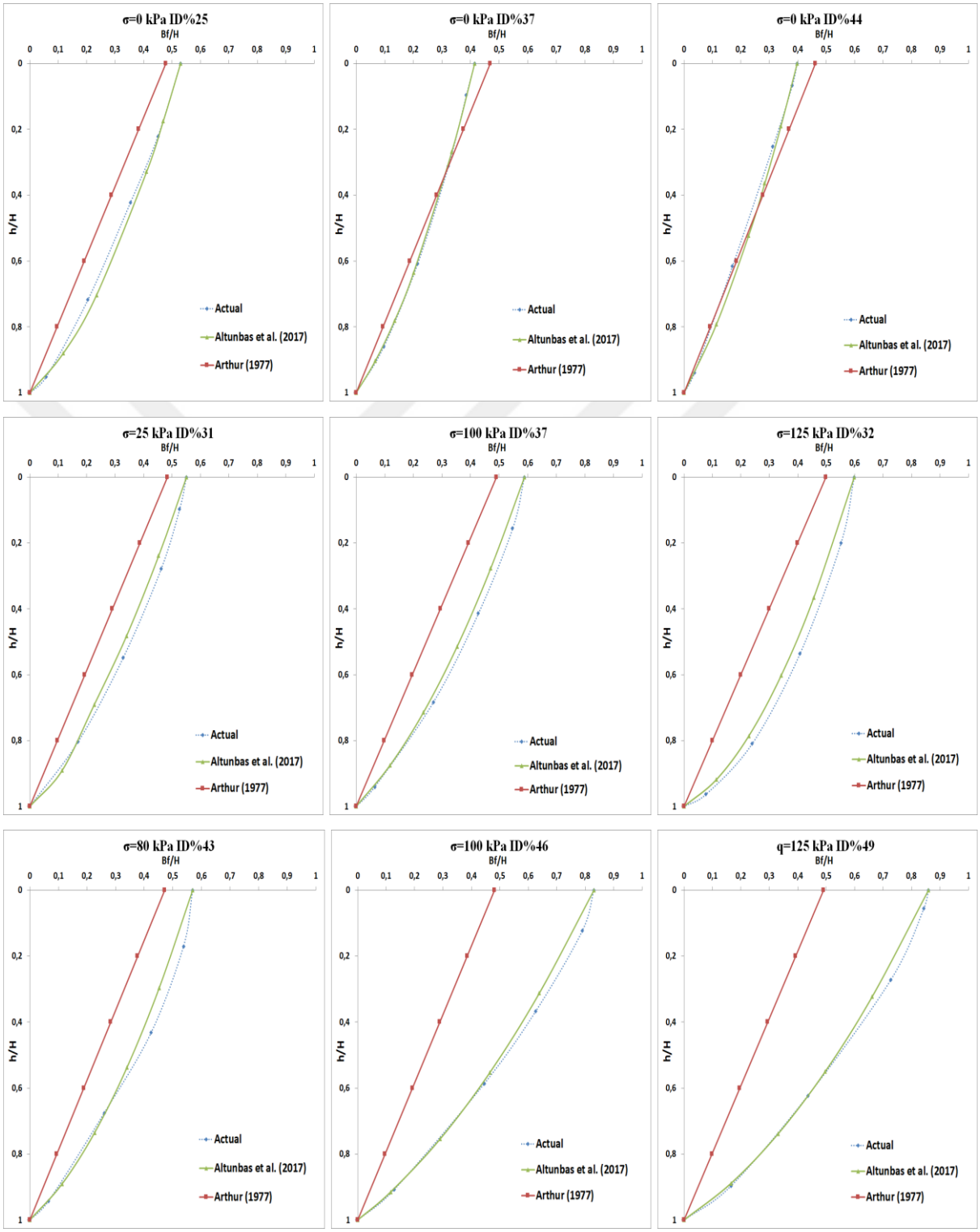


Figure 4.59. Comparison between plots of estimated and actual failure surfaces on normalized coordinate system for varying dilatancy values of physical model experiment data of GB.

The graphs show that when the influence of dilatant behavior reduces (low initial density and high surcharge), the center part of failure surface behind the center of retaining wall is more inclined and there is more difference between actual failure surface geometry and the proposed geometry using Altunbas *et al.,* (2017) correlation. The difference becomes more obvious if the granular soil is well graded. Next, grain shape considerably affects the geometry of failure surface, because for GB which consist of totally circular and spherical particles, the failure surfaces evaluated by Altunbas *et al.,* (2017) correlation and visualized experimentally nearly coincide with each other.

Subsequently, it appears that when GB are used as a backfill soil behind retaining wall, as proposed by Altunbas *et al.,* (2017), correlation gives a good estimate to calculate the coordinates of the points located on the actual failure surface geometry. Moreover, similar geometry is observed for physical retaining wall experiments where no surcharge pressure is applied. However, with increasing surcharge proposed geometry differs from the actual. In addition, if the angularity of the granular soil particles increase, proposed and actual coordinates differ from each other. Finally, when geometries of SP-S2 and SW-S2 are compared, it is observed that uniformity of grains also influence the geometry; actual failure surface geometry of the well graded soil consisting of higher uniformity coefficient is considerably different from estimated geometries. These observations visualize the influences of initial stress state, particle angularity, and grain size distribution on shear band geometry.

These observations are better visualized by comparing the geometry of actual slip surfaces at active failure state behind physical retaining wall models with empirically evaluated parabolic geometries using Altunbas *et al.,* (2017) equation for different granular materials and equal density or confining pressure ranges (Figures 4.60 and 4.61). Figure 4.60 indicates that Altunbas *et al*., (2017) correlation generally gives a good estimate to evaluate the slip surface provided that no surcharge is applied on tested soils. However for both S3 and S2 sands, a 100 kPa increase at the initial stress state of soils due to surcharge pressure obviously influences the convexity of the shear geometry and consequently the proposed quadratic function.

The variance between the actual and the proposed geometry by Altunbas *et al.,* (2017) equation is apparently different at each sand type due to grain size and grain shape effects. Primarily, for GB particles which are completely circular and spherical, proposed formula is the most accurate in defining the actual geometry. However, as the angularity of sands increase, the difference becomes more obvious.

Another major outcome of the interpretation of test data is given in Figure 4.61. The difference between experimentally visualized and the estimated geometry by Altunbas *et al.,* (2017) equation increases when the dilatant behavior is reduced. In addition, actual failure surface geometries of SP-S2 and SW-S2 consisting of equal angularity are slightly different, even if both are under equal initial stress state and density range. This is possibly caused by the difference in their granulometry. According to existing data it can be proposed that higher uniformity coefficient (C_u) causes a more convex shaped slip surface.

Figure 4.60 and 4.61 prove that granular backfill possesses a steeper shear band behind a transiting retaining wall through active state when it:

- acquires higher dilatancy,
- consists of more angular particles,
- has better gradation.

In addition, the difference between actual and calculated geometry is higher when:

- dilatancy of granular materials is low,
- granular material consists of less angular particles,
- granular material is uniform graded.

As a result, it is concluded that existing geometrical correlations which estimate the coordinates of slip surface geometries are not sufficient and applicable for different graded granular materials consisting of different particle shapes and under varying confining stress. Therefore, in order to embody all known physical variables for a granular soil element existing in nature, existing parabolic Altunbas *et al*., (2017) equation was modified.

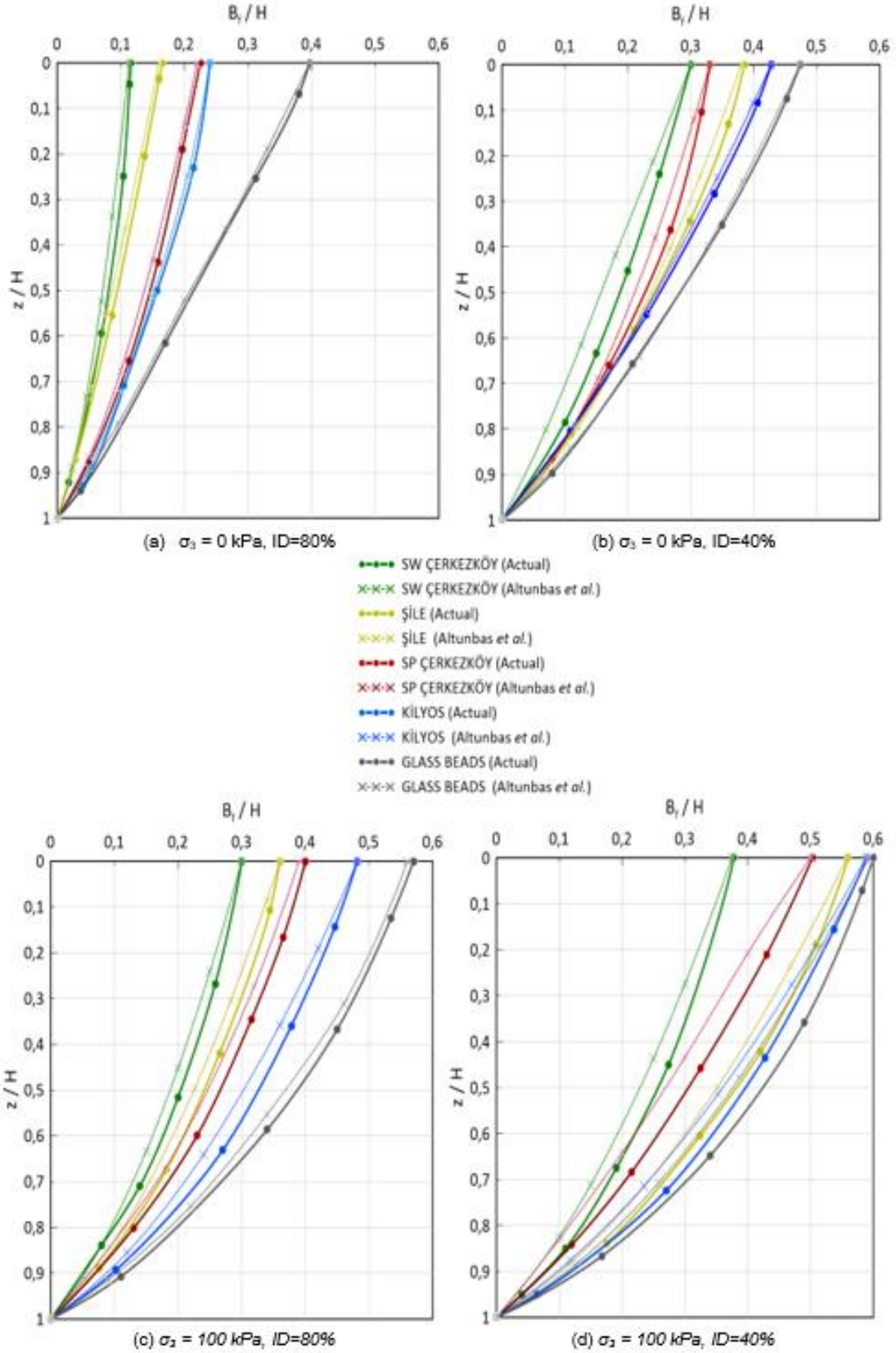


Figure 4.60. Comparison of actual failure surface geometries with empirical method (Altunbas *et al*., 2017) of tested soils.

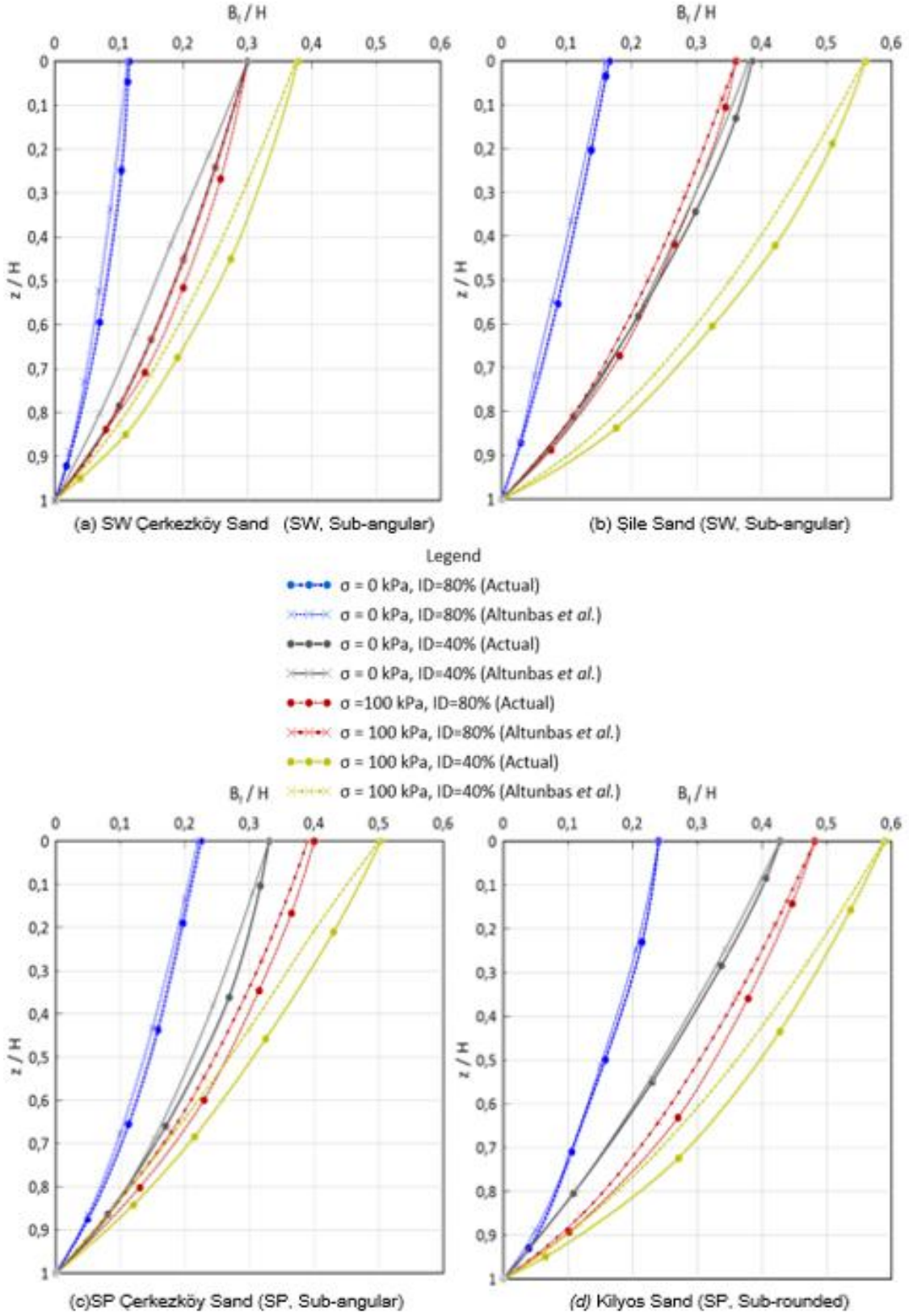


Figure 4.61. Actual - empirical failure surface geometry relationship of different sands at similar initial conditions.

Therefore, the variables of the proposed function should at least include grain size and shape soil constants; C_u (uniformity coefficient), S_{ave} (average sphericity) and R_{ave} (average roundness). In order to extend the applicability of Altunbas *et al.,* (2017) geometrical correlation to define failure surface geometry, IBM SPSS Statistics software was used. This software program enables to conduct data analysis of the input values of an existing function and correlate the variables of a particular function into the existing function in order to generate a unique equation. Accordingly, a new unique correlation was derived which includes grain shape and grain size coefficients so that experimentally visualized failure surfaces and the coordinates calculated by the proposed new function yield to approximate geometries.

$$Actual = \frac{z}{H_w} + [\, n \cdot \left(\frac{(S_{ave}+R_{ave})}{2}\right) \cdot (C_u) \cdot B] \tag{4.28}$$

Equation best fits with the actual failure surface geometry for all sands, where

$$z = aB^2 + bB + c$$

being as,

$$a = [(a_b - 1)/(a_b^2 H_w)]tan^2(\alpha)$$

$$b = -\tan(\alpha)$$

$$c = H_w$$

S_{ave} is the average sphericity and R_{ave} is the average roundness of the soil (grain shape parameters). C_u is the coefficient of uniformity and is added to the formula in order to consider the effects of gradation, and *B* is the apsis on the horizontal (x) axis.

The equation enables to calculate the coordinates of the actual, parabolic slip surface forming behind the retaining wall translating laterally through the active state for all the different variety of granular materials tested within the study. These coordinates at varying horizontal (B) and vertical (z) directions can be used to plot the failure surface geometry at coordinate system normalized with the wall height (H) where the origin is the initial inclination of the shear band originated at the bottom of the wall.

The '*n*' values obtained by statistical analysis differ at varying density and surcharge ranges and are presented below in Table 4.21.

Table 4.21. '*n*' coefficient derived by SPSS analysis for varying density and surcharge

	σ_v =0 kPa	σ_v =50kPa	σ_v = 100 kPa
	n	***n***	***n***
Loose	0.040	0.087	0.091
Medium Dense	0.029	0.072	0.073
Dense	0.011	0.045	0.050

Note: All the analysis results give >0.90 R^2 values

The '*n*' values in Table 4.22 are the average estimates of the upper and lower bound values obtained from SPSS parameter estimation results. On Table 4.22, the standard deviations of the estimations according to SPSS analysis are presented.

Table 4.22. Standard deviations of '*n*' for different density and surcharge ranges

	σ = 0 kPa (no surcharge)	σ = 50kPa surcharge	σ = 100 kPa surcharge
	Standard Deviation of '*n*'	**Standard Deviation of '*n*'**	**Standard Deviation of '*n*'**
Loose	0.029	0.011	0.010
Medium Dense	0.064	0.007	0.017
Dense	0.017	0.013	0.011

Hence, within this PhD study the existing Altunbas *et al.*, (2017) parabolic function has been modified to comprise surcharge, grain size and grain shape effects while evaluating the effect of dilatant behavior on failure surface geometry for any granular soil. Consequently, the applicability and usability of the parabolic function have been enhanced.

Commenting about the results, regardless of the applied surcharge pressure on the soil, the ‘n’ coefficient tends to decrease as the relative density of the soil increases. Additionally, for a specified relative density state (loose, medium dense or dense) the increase in the applied surcharge pressure leads to an increase in the “*n*” coefficient. While there is a rapid increase between the 0-50 kPa stress region, the rate of increase drops afterwards.

Results indicate that there is an inverse proportion between the ‘*n*’ coefficient and dilatancy.

The variation of ‘*n*’ coefficient with the stress state of soil is presented as a chart in Figure 4.62 for practicality. The slope of the graph points that for high stresses there is not a major change in ‘*n*’ coefficient. This attitude is presumed to the fact that the effect of dilatant behavior is already considerably suppressed at low stresses so that no further stress influences the formation of shear band geometry.

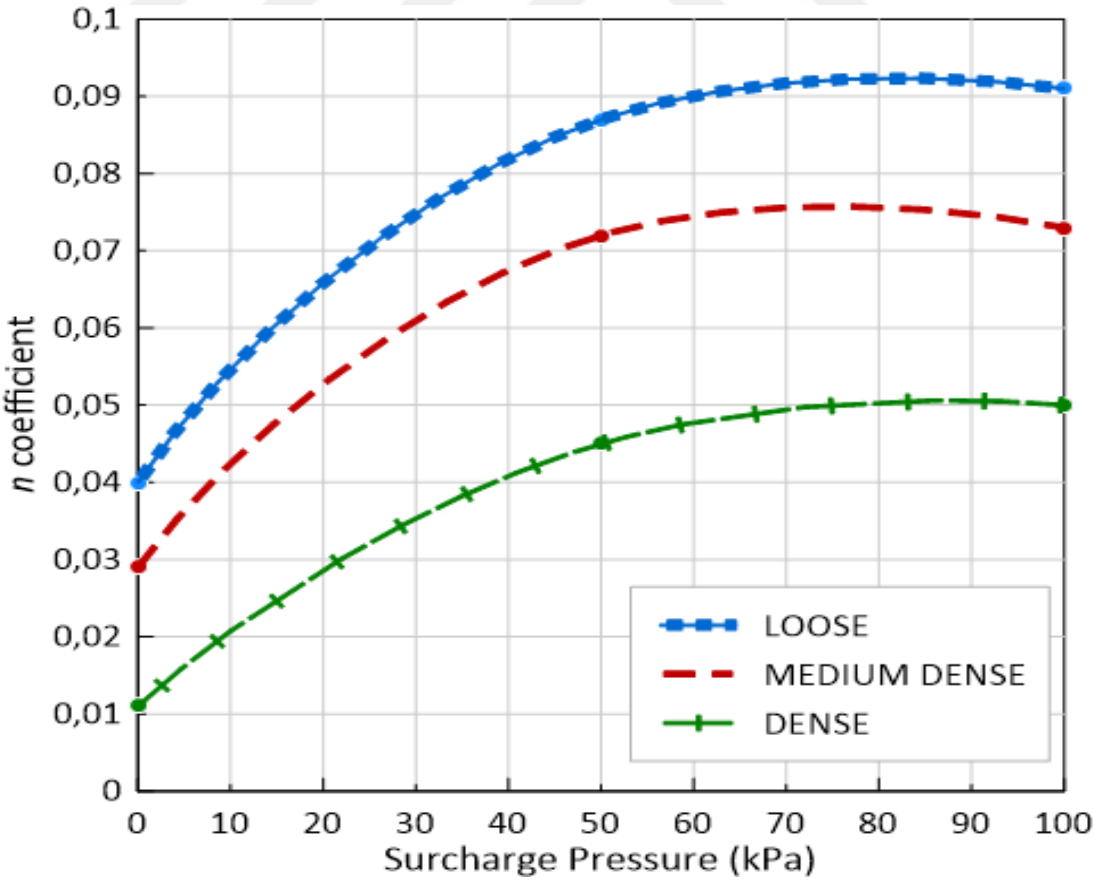


Figure 4.62. Change of “*n*” coefficient with respect to surcharge pressure.

5. CONCLUSION

In this research, the first main objective was to conduct a wide range of experimental work initially in order to investigate the influences of both grain characteristics and stress path on strength-dilation correlation constants such as the critical state friction angle ($Ø_{cs}$), effect of dilatancy on soil strength (r), and Bolton's line fitting parameters of Q and R. For this purpose, a total of 80 triaxial tests were conducted on five different graded granular material consisting of varying grain shapes. Tests were conducted under different confining pressures, relative density ranges, and loading conditions.

In spite of existing fixed coefficients suggested by Bolton (1986), Vaid and Sashiterian (1992) and Salgado (2010); interpretation of current research and literature revealed that median grain size and particle angularity apparently influence both interlocking and stress-dilatancy behavior of granular soils. Observations of current study are well in accordance with the results revealed by recent studies which consider grain characteristics (Amirpour *et al*., 2017 and 2018). In this research, both well graded and uniform graded materials were used to extend the applicability of proposed correlations between grain characteristics and empirical strength-dilation parameters. Moreover, it was also observed that proposed equations are also valid for different stress paths. To summarize, it is observed that soils with better gradation (higher C_u) and consisting of more angular particles (lower S_{ave} and R_{ave}) possess higher mechanical properties when sheared. On the other hand, dilatant behavior of soils with higher median grain size (higher D_{50}) have less contribution on soil strength due to less ratio of particle interlocking between soil grains. So; when sheared, more particle interlocking mechanism will occur in well graded engineering materials consisting of smaller grain size and higher particle angularity, leading to higher dilatant behavior and higher frictional strength. No countable relationship was observed between grain angularity and critical strength due to low coefficient of determination of linear regression curves, however it was detected that soils with lower coefficient of uniformity (C_u) and lower angularity (S_{ave} and R_{ave}) had lower critical state friction angles. However, equations were suggested between grain shape parameters and critical state friction angle.

On Table 5.1 the suggested equations are summarized which correspond to related empirical strength-dilatancy parameter. It should be noted that although the proposed functions corroborate numerically the effect of grain characteristics on stress-dilatancy and strength properties of granular materials, due to the scarcity of laboratory data and low coefficient of determination values, the suggested equations cannot be replaced by shear test data to evaluate mechanical soil properties of engineered materials such as friction and dilation angles.

Table 5.1. Summary of proposed correlations between grain characteristics and stress-dilatancy and strength parameters

Strength-Dilatancy Constant	**Proposed Relation**
$\emptyset_{cs} \rightarrow \emptyset'_p = \emptyset'_{cs} + r\psi'_p$	$\emptyset_{cs} = -10.8S_{ave} + 41.46$ $\emptyset_{cs} = -11.8R_{ave} + 41.29$ $\emptyset_{cs} = -11.0(S_{ave} + R_{ave}) + 41.21$
r $\rightarrow \emptyset'_p = \emptyset'_{cs} + r\psi'_p$	$r = 0.265D_{50}^{-0.235}$ ($S_{ave} \geq 0.7$) ($D_{50} \rightarrow$ mm) $r = 0.384D_{50}^{-0.465}$ ($S_{ave} \leq 0.7$) ($D_{50} \rightarrow$ mm)
Q and R $\rightarrow I_R = I_D(Q - lnp') - R$	$Q = (15.79S_{ave}) + 0.63$ R = 1
a $\rightarrow \left(-\frac{d\varepsilon_v}{d\varepsilon_1}\right)_{max} = aI_R$	a = 0.30

The second main objective of the research was to investigate the applicability of existing empirical functions in literature which estimates the coordinates of the failure surface geometry forming behind laterally displacing retaining walls through the active side.

In the design of soil-retaining structures, the most-widely accepted theories are Coulomb and Rankine. These theories are based on limit-equilibrium method which do not consider wall interface, soil arching and dilatant behavior. On the other hand, provided that the effects of wall-soil interface and soil arching due to model geometry is eliminated, the

only function that influences the shear band geometry becomes dilatancy. Therefore, researchers like Arthur *et al.,* (1977) and Vardoulakis (1980) proposed parabolic geometrical functions in order to define failure surface geometry by considering dilatancy effects. However in the present century by means of recent advances in computational geomechanics and particle image velocimetry software, physical model tests became a more convenient and appropriate tool to visualize and reveal the actual slip surface geometries during wall transition. Therefore, many researchers adopted physical model studies to investigate the parameters effecting shear band evaluation. Subsequently, Altunbas *et al.,* (2017) proposed a quadratic equation to define the slip surface geometry. However, physical model experiments conducted so far failed to comprise all variables influencing the formation of shear bands due to either physical restrictions of the model box or the variety of soil samples. As proposed by stress-dilatancy theories available in the literature, soil relative density and the stress at failure state are the two main functions of dilatancy. However, recent research revealed that macro-scale physical properties such as grain size and shape also have an important influence on dilatant behavior.

Therefore, in this study a physical retaining wall model was manufactured which included pneumatic pistons so that surcharge pressure could be applied to backfill. The geometry of the physical retaining wall model was inspired from the test box manufactured by Lesniewska and Wood (2009) who examined the advantages of photoelastic technique (PIV) on the analysis of incremental stress, displacement, and strain fields for model retaining walls. Next, tests were conducted on glass beads and sands of different grain shape or granulometry so that the coupled influence of physical soil properties into dilatant behavior were quantified. Finally the pictures taken during wall transition were analyzed by geoPIV-RG and obtained failure surface geometries under varying initial density and stress state ranges were presented. By installing pressure sensors on physical model frame, the lateral earth pressures and peak internal friction angle of soils at failure state were calculated for each test. The results showed that even at high initial stress states, soil density and strength were proportional. Next, well graded and angular soils had higher dilation and friction angles, where effect of grain angularity on soil strength was considerably higher. It was observed that gradation did not considerably influence the rate of increase on friction angle values with increasing relative density since well graded and poorly graded S2 sand had both the same strength increment rates. Also it was observed that packing density affects

the contribution of angularity on shear band geometry. Provided that actual failure surfaces and soil-wall friction forces were well obtained, physical model apparatus used in the study was an efficient tool to calculate internal friction angle of granular soils and results were in well accordance with consolidated-drained triaxial test results.

The actual failure surface geometries determined by PIV analysis were compared with Altunbas *et al.*, (2017) equation existing in the literature which estimates the coordinates of parabolic shaped slip surface geometry by a quadratic function. Results indicated that surcharge pressure, grain size and grain shape notably influence the convexity of slip surface geometry. For high surcharge pressures the difference was more obvious because dilatant behavior decreased. Therefore, Altunbas *et al.*, (2017) equation was modified into a more comprehensive correlation using IBM SPSS Statistics software which grain shape and size effects also represented as a constant function of vertical coordinate on x-axis. In the modified equation, the only coefficient which had different values depending on initial density and stress state of the soil was termed as '*n*'. Finally, a chart was proposed where '*n*' value can practically be selected as a function of surcharge pressure and density.

As a further research, it is recommended to work with granular soils mixed with up to 5% fine content to examine the influence of fine fraction on the results, so that the study embodies the in-situ engineering materials. Because perfectly granular soils are very rare in-situ. Next, granular materials used in the study consisted of very similar coefficient of gradation ranges (C_c), and were dominantly quartz. So, it is recommended to work with soils consisting of different mineral fractions than quartz to enhance the applicability of proposed stress-dilatancy coefficients and line-fitting parameters. Finally, formation of shear bands behind retaining walls is also a function of dilatancy provided that frictional and arching effects are suppressed. In this study, existing geometrical equations which calculates the active slip surface are modified to consider grain characteristics and high pressures. However, the equations are only valid for laterally translating, rigid retaining walls through active failure state. More advanced physical retaining wall models which provides wall inclination, passive failure state and higher surcharge pressures are recommended to enhance the applicability of proposed quadratic function which calculates the coordinates of shear band geometry.

REFERENCES

1. Abadkon, A., *Strength and Dilatancy of Anisotropic Cohesionless Soils*, Ph.D. Thesis, Boğaziçi University, Istanbul, 2012.

2. Ahmadabadi, M. and Faghirizadeh, M. K., ‘‘Design Diagrams for the Analysis of Active Pressure on Retaining Walls with the Effect of Line Surcharge’’, *Advances in Civil Engineering*, Hindawi, 2017.

3. Alshibli, K.A. and Alsaleh, M.I., ‘‘Characterizing Surface Roughness and Shape of Sands Using Digital Microscopy’’, *J. Comput. Civ. Eng.*, Vol. 18(1), pp. 36-45, 2004.

4. Alshibli, K.A. and Sture, S., ‘‘Shear Band Formation in Plane Strain Experiments of Sand’’, *Journal of Geotechnical and Geoenvironmental Engineering*, pp. 495-503, June 2000.

5. Altuhafi, F.N., Coop, M.R. and Georgiannou, V.N., ‘‘Effect of Particle Shape on the Mechanical Behavior of Natural Sands’’, *J. Geotech. Geoenviron. Eng., ASCE*, Vol. 142, No. 12, 2016.

6. Altunbas, A., Soltanbeigi, B. and Cinicioglu, O., ‘‘Determination of Active Failure Surface Geometry for Cohesionless Backfills’’, Geomechanics and Engineering, Vol.12, No.6, 983-1001, 2017.

7. American Society for Testing and Materials, ‘‘Standard Test Methods for Maximum Index Density and Unit Weight of Soils Using a Vibratory Table’’, *ASTM Standards: D4253*, 2006.

8. American Society for Testing and Materials, ‘‘Standard Test Methods for Minimum Index Density and Unit Weight of Soils and Calculation of Relative Density’’, *ASTM Standards: D4254*, 2006.

9. American Society for Testing and Materials, ‘‘Standard Test Methods for Specific Gravity of Soil Solids by Water Pycnometer’’, *ASTM Standards: D854-14*, 2014.

10. American Society for Testing and Materials, ‘‘Standard Test Methods for Particle-Size Analysis of Soils’’, *ASTM Standards: D422-63*, 2007.

11. American Society for Testing and Materials, ‘‘Standard Test Methods for Consolidated Drained Triaxial Compression Test for Soils’’, *ASTM Standards: D7181-11*, 2011.

12. Amirpour, S., Karray, M. and Hussien, M.N., ‘‘Influence of Particle-Size and Gradation on the Stress-Dilatancy of Granular Materials During Drained Triaxial Compression’’, *International Journal of Geomechanics*, Vol. 17, No. 9, 04017077, February 2017.

13. Amirpour, S., Hussien, M.N., Karray, M., Roubtsova, V. and Chekired, M., ‘‘Influence of Particle-Size and Gradation on Shear Strength-Dilation Relation of Granular Materials’’, *Canadian Geotechnical Journal*, https://doi.org/10.1139/cgj-2017-0468, 2018.

14. Arthur, J.R., Dunstan, T., Al-Ani, Q.A. and Assadi, A., ‘‘Plastic Deformation and Failure in Granular Media’’, *Geotechnique,* Vol. 27, Issue 1, pp. 53-74, 1977.

15. Bang, S., ‘‘Active Earth Pressure Behind Retaining Walls’’, *J. Geotech. Eng*., Vol. 111, pp. 407-412, 1985.

16. Barden, L. and Khayatt, A.J., ‘‘Incremental Strain Rate Ratios and Strength of Sand in the Triaxial Test’’, *Geotechnique,* Vol.16 Issue 4, pp. 338-357, 1966.

17. Bardet, J.P. and Proubet, J., ‘‘Shear-Band Analysis in Idealized Granular Material’’, *Journal of Engineering Mechanics*, Vol.118, No.2, 1992.

18. Been, K. and Jefferies, M.G., ‘‘A State Parameter for Sands’’, *Geotechnique,* Vol. 35, Issue 2, pp. 99-102, 1985.

19. Been, K., Jefferies, M.G. and Hachey, J., ‘‘The Critical State of Sands’’, *Geotechnique,* Vol. 41, Issue 3, pp. 365-381, 1991.

20. Bell, J.M., *Stress-Strain Characteristics of Cohesionless Granular Materials Subjected to Statically Applied Homogenous Loads in an Open System,* Ph.D. Thesis, California Institute of Technology, 1965.

21. Bishop, A.W., ‘‘The Use of Pore-Pressure Coefficients in Practice’’, *Geotechnique,* Volume 4 Issue 4, pp. 148-152, 1954.

22. Bishop, A.W., ‘‘The Strength of Soils as Engineering Materials’’, *Geotechnique,* Volume 16 Issue 2, pp. 91-130, June 1966.

23. Bjerrum, L., *Theoretical and Experimental Investigations on the Shear Strength of Soils*, Ph.D. Thesis, The Swiss Federal Institute of Technology, Zürich, 1954.

24. Bolton, M.D., ‘‘The Strength and Dilatancy of Sands’’, *Geotechnique,* Vol. 36, Issue 1, pp. 65-78, 1986.

25. Chakraborty, T. and Salgado, R., ‘‘Dilatancy and Shear Strength of Sand at Low Confining Pressures’’, J. Geotech. Geoenviron. Eng., Vol.136, No. 3, pp. 527-532, 2010.

26. Chang, C.S. and Yin, Z., ‘‘Modeling Stress-Dilatancy for Sand under Compression and Extension Loading Conditions’’, *Journal of Engineering Mechanics, ASCE,* June 2010.

27. Chen, L., ‘‘Active Earth Pressure of Retaining Wall Considering Wall Movement’’, *European Journal of Environmental and Civil Engineering,* Vol.18, No.8, pp. 910-926, 2014.

28. Cho, G.C., Dodds, J. and Santamarina, J.C., ‘‘Particle Shape Effects on Packing Density, Stiffness and Strength: Natural and Crushed Sands’’, *J. Geotech. Geoenviron. Eng.,* Vol. 132, No. 5, pp. 591-602, 2006.

29. Chu, J., Kim, S.R., Oh, Y.N., Balasubramaniam, A.S. and Bergado, D.T., ‘‘An Experimental and Theoretical Study on the Dilatancy of Sands and Clays’’, *New Zealand Geotechnical Society,* January 2004.

30. Cox, M.R.B., *The Influence of Grain Shape on Dilatancy,* PhD Thesis, The University of Arizona, 2008.

31. Cubrinovski, M. and Ishihara, K., ‘‘Maximum and Minimum Void Ratio Characteristics of Sands’’, *Soils and Foundations, Japanese Geotechnical Society*, Vol.42, No. 6, pp. 65-78, December 2002.

32. Cuccovillo, T. and Coop, M.R., ‘‘On the Mechanics of Structured Sands’’, *Geotechnique,* Vol. 49, No. 6, pp. 741-760, 1999.

33. Çinicioğlu, Ö. and Abadkon, A., ‘‘Variation of Friction Angle and Dilatancy for Anisotropic Cohesionless Soils’’, *Proceedings of the 18th Int. Conf. on Soil Mech. and Geotech. Eng.*, Paris, 2013.

34. Çinicioğlu, Ö. and Abadkon, A., ‘‘Dilatancy and Friction Angles Based on Insitu Soil Conditions’’, *J. Geotech. Geoenviron. Eng*., ISSN 1090-0241, 2014

35. De Josselin de Jong, G., ‘‘Rowe’s Stress-Dilatancy Relation Based on Friction’’, *Geotechnique,* Vol. 26, No.3, pp. 527-534, 1976.

36. Ehrlich, R. and Weinberg, B., ‘‘An Exact Method for Characterization of Grain Shape’’, *Journal of Sedimentary Petrology*, Vol. 40, No.1, pp. 205-212, March 1970.

37. Ertuğrul, N.A., *Effect of Soil Arching on Lateral Soil Pressures Acting Upon Rigid Retaining Walls*, MS Thesis, Middle East Technical University, 2013.

38. Frossard, E., ‘‘Effect of Sand Grain Shape on Interparticle Friction; Indirect Measurements by Rowe’s Stress Dilatancy Theory’’, *Geotechnique,* Vol. 29, No.3, pp. 341-350, 1979.

39. Fonseca, J., *The Evolution of Morphology and Fabric of a Sand During Shearing*, Ph.D. Thesis, Imperial Collage, London, April 2011.

40. Giampa, J.R. and Bradshaw, A.S., ‘‘A Simple Method for Assessing the Peak Friction Angle of Sand at Very Low Confining Pressures’’, *Geotechnical Testing Journal*, Vol. 41, No.4, pp. 639-647, 2018.

41. Gezgin, A.T. and Cinicioglu, O., ‘‘Dilatancy Based Calculation of Passive Earth Thrust and the Locked-in Stress Concept’’, *Proceedings of the 24th European Young Geotechnical Engineers Conference (EYGEC)*, Durham, UK, 2015.

42. Guo, P. and Su, X., ‘‘Shear Strength, Interparticle Locking and Dilatancy of Granular Materials’’, *Canadian Geotechnical Journal,* Vol. 44, pp. 579-591, 2007.

43. Hanna, A., ‘‘Determination of Plane-Strain Shear Strength of Sand From the Results of Triaxial Tests’’, *Canadian Geotechnical Journal*, p.1231, Dec. 2001.

44. Herle, I. and Gudehus, G., ‘‘Determination of Parameters of a Hypoplastic Constitutive Model from Properties of Grain Assemblies’’, *Mechanics of Cohesive-Frictional Materials,* Vol. 4, No. 5, pp. 461-486, 1998.

45. Holubec, I. and Appolonia, E., ‘‘Effect of Particle Shape on the Engineering Properties of Granular Soils’’, *American Standard of Testing Materials, STP523*, 1973.

46. Horn, H.M. and Deere, D.U., ‘‘Frictional Characteristics of Minerals’’, *Geotechnique,* Volume 12 Issue 4, pp. 319-335, 1962.

47. Horne, M.R., The Behaviour of an Assembly of Rotund, Rigid, Cohesionless Particles. I, *Proc. R. Soc. Lond.*, Vol. 286, pp. 62-78, 1965.

48. Horne, M.R., The Behaviour of an Assembly of Rotund, Rigid, Cohesionless Particles. II, *Proc. R. Soc. Lond.*, Vol. 286, pp. 79-97, 1965.

49. Jiang, M.J., Niu, M.Y. and He, J., ‘‘DEM Analysis of Small-Displacement Earth Pressure Against a Rigid Retaining Wall with the Wall Moving Towards Structured Sand’’, The 7th Conference on Discrete Element Methods, China, 2016.

50. Jensen, R.P., Edil, T.B., Bosscher, P.J., Plesha, M.E. and Kahla, N.B., ‘‘Effect of Particle Shape on Interface Behavior of DEM-Simulated Granular Materials’’, *The International Journal of Geomechanics*, Volume 1, Number 1, pp. 1-19, 2001.

51. Khosravi, M.H., Pipatpongsa, T. and Takemura, J., ‘‘Theoretical Analysis of Earth Pressure Against Rigid Retaining Walls Under Translation Mode’’, *Soils and Foundations*, Vol. 56, No. 4, pp. 664-675, The Japanese Geotechnical Society, 2016.

52. Kowalska, M., ‘‘Influence of the Ratio Between Dilatancy Angle and Internal Friction Angle on Stress Distribution Behind a Gravity Retaining Wall’’, *Architecture Civil Engineering Environment*, No.1, pp. 77-82, 2015.

53. Krumbein, W. and Sloss, L., ‘‘*Stratigraphy and Sedimentation’’*, W.H. Freeman and Co., San Francisco, p. 660, 1963.

54. Kuhn, M.R., ‘‘Structured Deformation in Granular Materials’’, *Mechanics of Materials*, Vol. 31, pp. 407-429, 1999.

55. Lade, P.V. and Duncan, J.M., ‘‘Stress Path Behavior of Cohesionless Soil’’, *Journal of the Geotechnical Engineering Division*, January 1976.

56. Lade, P.V. and Tsai, J., ‘‘Effects of Localization in Triaxial Tests on Clay’’, *Proceedings of the 11th International Conference on Soil Mechanics and Foundation Engineering*, San Francisco, 1985.

57. Lambe, T.W. and Whitman, R.V., *Soil Mechanics*, Massachusetts Institute of Technology, John Wiley & Sons, New York, 1969.

58. Latha, G.M. and Sitharam, T.G., ‘‘Effect of Particle Size and Gradation on the Behaviour of Granular Materials Simulated Using DEM’’, *Indian Geotechnical Journal*, Vol. 38, No. 1, pp. 68-88, 2008.

59. Lee, J., Yun, T.S., Lee, D., and Lee, J., ‘‘Assessment of K_o correlation to strength for granular materials’’, *The Japanese Geotechnical Society, Soils and Foundations*, Vol. 53, pp. 584-595, 2013.

60. Lesniewska, D., ‘‘Analysis of Shear Band Pattern Formation in Soil’’, Institute of Hydro-Engineering of Polish Academy of Sciences, Gdansk, 2000.

61. Lesniewska, D. and Mroz, Z., ‘‘Limit Equilibrium Approach to Study Evaluation of Shear Band Systems in Soils’’, *Geotechnique*, Vol. 50, No.5, pp. 521-536, 2001.

62. Lesniewska, D. and Sklodowski, M., ‘‘Photoelastic Investigation of Localization Phenomena in Granular Materials’’, *Powders and Grains*, pp. 69-72, 2005.

63. Lesniewska, D. and Wood, D.M., ‘‘Observations of Stresses and Strains in a Granular Material’’, *Journal of Engineering Mechanics*, September 2009.

64. Lindenberg, J. and Koning, H.L., ‘‘Critical Density of Sand’’, *Geotechnique,* Vol. 31, No.2, pp. 231-245, 1981.

65. Mair, K., Frye, K.M. and Marone, C., ‘‘Influence of Grain Characteristics on the Friction of Granular Shear Zones’’, *Journal of Geophysical Research*, Vol. 107, No. B10, p. 2219, 2002.

66. Matsuoka, H., ‘‘A Microscopic Study on Shear Mechanism of Granular Materials’’, *Japanese Society of Soil Mechanics and Foundation Engineering*, Vol.14, No.1, March 1974.

67. Matsuoka, H., Liu, S., Ueno, Y. and Kodama, H., ‘‘A Microscopic Study on Shear Mechanism of Granular Materials in Simple Shear Simulated by DEM’’, *Dobuku Gakkai Ronbunshu,* Volume 1994, Issue 487, pp. 167-175, 1994.

68. McDowell, G.R. and Bolton, M.D., ‘‘On the Micromechanics of Crushable Aggregates’’, *Geotechnique*, Vol. 48, No.5, pp. 667-679, 1998.

69. Miura, K., Maeda, K., Furukawa, M. and Toki, S., ‘‘Mechanical Characteristics of Sands with Different Primary Properties’’, *Soils and Foundations,* Japanese Geotechnical Society, Vol. 38, No.4, pp. 159-172, Dec. 1998.

70. Nanda, S. and Patra, N.R., ‘‘Determination of Soil Properties for Plane Strain Condition From the Triaxial Tests Results’’, *Int. Journal for Numerical and Analytical Methods in Geomechanics,* Vol. 39, pp. 1014-1026, 2015.

71. Ng, T.T., ‘‘Behavior of Ellipsoids of Two Sizes’’, *J. Geotech. Geoenviron. Eng.*, Vol. 130, No. 10, pp. 1077-1083, 2004.

72. Ng, T.T., ‘‘Behavior of Gravity Deposited Granular Material Under Different Stress Paths’’, *Can. Geotech. J.*, Vol. 42, pp. 644-1655, 2005.

73. Niedostatkiewicz, M., Lesniewska, D., and Tejchman, J., ‘‘Experimental Analysis of Shear Zone Patterns in Cohesionless for Earth Pressure Problems Using Particle Image Velocimetry’’, *Strain: An International Journal for Experimental Mechanics,* Vol. 47 (Suppl. 2), pp. 218-231, 2011.

74. Oda, M., ‘‘Initial Fabrics and Their Relations to Mechanical Properties of Granular Material’’, *Japanese Society of Soil Mechanics and Foundation Engineering,* Vol.12 No.1, March 1972.

75. Oda, M. and Kazama, H., ‘‘Microstructure of Shear Bands and its Relation to the Mechanisms of Dilatancy and Failure of Dense Granular Soils’’, *Geotechnique,* Vol. 48, No.4, pp. 465-481, 1998.

76. Olarte, A.A.P., *Influence of Particle Shape on the Global Mechanical Response of Granular Packings: Micromechanical Investigation of the Critical State in Soil Mechanics*, PhD Thesis, Stuttgart University, Germany, 2008.

77. Paik, K.H. and Salgado, R., ‘‘Estimation of Active Earth Pressure Against Rigid Retaining Walls Considering Arching Effects’’, *Geotechnique,* Vol. 53, No. 7, pp. 643-653, 2003.

78. Penman, A.D., ‘‘Shear Characteristics of a Saturated Silt, Measured in Triaxial Compression’’, *Geotechnique,* Volume 3, Issue 8, pp. 312-328, December 1953.

79. Peters, J.F., Lade, P.V., and Bro, A., ‘‘Shear Band Formation in Triaxial and Plane Strain Tests’’, *Advanced Triaxial Testing of Soil and Rock,* ASTM STP 977, pp. 604-627, 1988.

80. Pietrzak, M. and Lesniewska, D., ‘‘Failure Evaluation in Granular Material Retained by Rigid Wall in Active Mode’’, *Studia Geotechnica et Mechanica,* Vol. 34, No.4, 2012.

81. Powers, M.C., ‘‘A new roundness scale for sedimentary particles*.’’ J. Sediment. Petrol.,* Vol. 23, No. 2, pp. 117-119., 1953.

82. Presti, C.F., Pedroni, S., and Crippa, V., ‘‘Maximum Dry Density of Cohesionless Soils by Pluvation and by ASTM D4253-83: A Comparative Study’’, *Geotechnical Testing Journal*, Vol.15, No.2, June 1992.

83. Procter, D.C. and Barton, R.R., ‘‘Measurements of the angle of interparticle friction’’, *Geotechnique,* Vol. 24, No.4, pp. 581-604, 1974.

84. Potticary, M., Zervos, A., and Harkness, J., ‘‘The Effect of Particle Elongation on the Strength of Granular Materials’’, *Proc. 24th UK Conference of the Assoc. for Comp. Mechanics in Engineering*, Cardiff University, 2016.

85. Ramamurthy, T. and Tokhi, V.K., *Plane Strain Strength from Triaxial Test*, 1989, https://www.issmge.org/uploads/publications/1/33/1989_01_0167.pdf, accessed at April 2019.

86. Rankine, W. J., ‘‘On the Stability of Loose Earth’’, *Phil. Trans. R. Soc. Lond.*, 1857.

87. Rao, P.P, Chen, Q., Zhou, Y., Nimbalkar, S., and Chiaro, G., ‘‘Determination of Active Earth Pressure on Rigid Retaining Wall Considering Arching Effect in Cohesive Backfill Soil’’, *International Journal of Geomechanics*, 04015082, September 2015.

88. Reades D.W. and Green, G.E., ‘‘Independent Stress Control and Triaxial Extension Tests on Sand’’, *Geotechnique,* Vol. 26, No.4, pp. 551-576, 1976.

89. Reynolds, O., ‘‘On the Dilatancy of Media Composed of Rigid Particles in Contact’’, *Phil. Magazine and Journal of Science*, December 1885.

90. Rittenhouse, G., & Thorp, E. M., ‘‘Heavy minerals in sediment-transportation studies’’, *Transactions, American Geophysical Union*, Vol. 24, No. 2, p. 524, 1943.

91. Roscoe, K.H., ‘‘The Influence of Strains in Soil Mechanics’’, *Geotechnique*, Vol. 20, No.2, pp.129-170, 1970.

92. Rowe, P.W., ‘‘A Stress-Strain Theory for Cohesionless Soil with Applications to Earth Pressures at Rest and Moving Walls’’, *Geotechnique,* Volume 4, Issue 2, pp. 70-88, June 1954.

93. Rowe, P.W., ‘‘ The Stress-Dilatancy Relation for Static Equilibrium of an Assembly of Particles in Contact’’, *Proc. R. Soc. Lond.*, Vol. 269, pp. 500-527, 1962.

94. Rowe, P.W., ‘‘The Relation Between the Shear Strength of Sands in Triaxial Compression, Plane Strain and Direct Shear’’, *Geotechnique,* No.1, pp. 75-86, 1969.

95. Santamarina, J.C. and Cho, G.C., ‘‘Determination of Critical State Parameters in Sandy Soils-Simple Procedure’’, *Geotechnical Testing Journal*, June 2001.

96. Santamarina, J.C. and Cho, G.C., ‘‘Soil Behaviour: The Role of Particle Shape’’, *Proc. Skempton Conf.,* London, March 2004.

97. Santamarina, J.C. and Shin, H., ‘‘Friction in Granular Media’’, Technical Report, *Georgia Institute of Technology*, September 2009.

98. Sazzad, M. and Suzuki, K., ‘‘A Comparison Between Conventional Triaxial and Plane-Strain Compression on a Particulate System Using 3D DEM’’, *Acta Geotechnica Slovenica*, 2012.

99. Schanz, T. and Vermeer, P.A., ‘‘Angles of Friction and Dilatancy of Sand’’, *Geotechnique,* Vol. 46, No.1, pp. 145-151, 1996.

100. Schofield, A. and Wroth, P., ‘‘*Critical State Soil Mechanics’’*, Cambridge University, London, 1968.

101. Schofield, A.N., ‘‘Interlocking, Peak and Design Strengths’’, *Geotechnique,* Vol. 56, No.5, pp. 357-358, 2006.

102. Shin, H. and Santamarina, C., ‘‘Role of Particle Angularity on the Mechanical Behavior of Granular Mixtures’’, *J. Geotech. Geoenviron. Eng.*, Vol. 139, pp. 353-355, 2013.

103. Siang, A.J.M., Wijeyesekera, D.C., Zainorabidin, A. and Bakar, I. ‘‘The Effects of Particle Morphology (Shapes and Sizes) Characteristics on its Engineering Behaviour and Sustainable Engineering Performance of Sand’’, *International Journal of Integrated Engineering*, Vol. 4, No.3, pp. 27-37, 2012.

104. Skempton, A.W. and Bishop, A.W., ‘‘The Measurement of the Shear Strength of Soils’’, *Geotechnique,* Volume 2, Issue 2, pp. 90-108, December 1950.

105. Skinner, A.E., ‘‘A Note on the Influence of Interparticle Friction on the Shearing Strength of a Random Assembly of Spherical Particles’’, *Geotechnique,* Volume 19, Issue 1, pp. 150-157, March 1969.

106. Soltanbeigi, B., Altunbas, A., and Cinicioglu, O., ‘‘Influence of Dilatancy on Shear Band Characteristics of Granular Backfills’’, *European Journal of Environmental and Civil Engineering,* 2019.

107. Stainer, S.A. and White, D.J., ‘‘Improved Image-Based Deformation Measurement in the Centrifuge Environment’’, *Geotechnical Testing Journal*, Vol.36, No.6, 2013.

108. Stanier, S.A., ‘‘Improved Image-based Deformation Measurement for Geotechnical Applications’’, *Canadian Geotechnical Journal*, Vol. 53, pp. 727-739, 2016.

109. Sukumaran, B. and Ashmawy, A.K., ‘‘Quantitative Characterization of the Geometry of Discrete Particles’’, *Geotechnique*, Vol. 51, No.7, pp. 619-627, 2001.

110. Taylor, D.W., ‘‘*Fundamentals of Soil Mechanics’’*, John Wiley & Sons, New York, 1948.

111. Tatsuoka, F., Sakamoto, M., Kawamura, T., and Fukushima, S., ‘‘Strength and Deformation Characteristics of Sand in Plane Strain Compression at Extremely Low Pressures’’, *Japanese Society of Soil Mechanics and Foundation Engineering*, Vol.26 No.1, pp. 65-84, March 1986.

112. Tehrani, F.S., Arshad, M.I., Prezzi, M., and Salgado, R., ‘‘Visualization of Active Mode of Failure Behind Flexible Walls Under Pure Rotation Using Digital Image Correlation’’, *Geo-Congress Technical Papers*, pp. 3393-3402, ASCE, 2014.

113. Tsomokos, A. and Georgiannou, V.N., ‘‘Effect of Grain Shape and Angularity on the Undrained Response of Fine Sands’’, *Canadian Geotechnical Journal*, Vol. 47, pp. 539-551, 2010.

114. Toulios, M. and Freund, L.B., ‘‘Initiation and Propagation of Shear Bands in Antiplane Shear Deformation’’, *Technical Report, Division of Engineering,* Brown University, March 1984.

115. Vaid, Y.P. and Negussey, D., ‘‘Relative Density of Pluviated Sand Samples’’, *Japanese Society of Soil Mechanics and Foundation Engineering*, Vol.24 No.2, pp. 101-105, June 1984.

116. Vaid, Y.P. and Sasitharan, S., ‘‘The Strength and Dilatancy of Sand’’, *Canadian Geotechnical Journal,* Vol. 29, pp. 522-526, 1992.

117. Vardoulakis, I., ‘‘Shear Band Inclination and Shear Modulus of Sand in Biaxial Tests’’, *International Journal for Numerical and Analytical Methods in Geomechanics,* Vol.4, pp. 103-119, 1980.

118. Wan, R.G. and Guo, P.J., ‘‘A Pressure and Density Dependent Dilatancy Model for Granular Materials’’, *Soils and Foundations,* Japanese Geotechnical Society, Vol.39, No.6, pp. 1-11, Dec.1999.

119. Wanatowski, D. and Chu, J., ‘‘A New Plane-Strain Apparatus and Plane-Strain Tests on Sand’’, *Proc. The 16th Southeast Asian Geotechnical Conference,* Malaysia, 2007.

120. Wentworth, C.K., ‘‘The Shapes of Beach Pebbles’’, *Shorter Contributions to General Geology*, 1922.

121. Wroth, C.P. and Bassett, R.H., ‘‘A Stress-Strain Relationship for the Shearing Behaviour of a Sand’’, *Geotechnique,* Volume 15, Issue 1, pp. 32-56, March 1965.

122. White, D.J., Take, W.A., and Bolton, M.D., ‘‘Soil Deformation Measurement Using Particle Image Velocimetry and Photogrammetry’’, *Geotechnique,* Vol. 53, No.7, pp. 619-631, 2003.

123. Yang, H.J., ‘‘Assess Cohesionless Soil Behavior under Drained Lateral Extension from Drained Axial Shear Test’’, *Journal of Geotechnical and Transportation Engineering*, Volume 2, Issue 2, 2016.

124. Yasin, S.J.M. and Safiullah, A.M.M., ‘‘Effect of Particle Characteristics on the Strength and Volume Change Behaviour of Sand’’, *Journal of Civil Engineering, The Institution of Engineers, Bangladesh*, Vol. CE31, No.2, 2003.

125. Youd, T. L., ‘‘Factors Controlling Maximum and Minimum Densities of Sands’’, *American Standard of Testing Materials, STP523*, pp. 98-112, 1973.